Solution Chemistry and Aging of Perovskite Precursor Solutions

Mary E. O'Kane

Department of Physics and Astronomy
University of Sheffield

Sept 2022

A thesis submitted in partial fulfilment of the requirements for the degree of Doctor of Philosophy

List of Publications

---

1. *As Chapter 4* - **Mary E O'Kane**, Joel A Smith, Tarek I Alanazi, Elena J Cassella, Onkar Game, Sandra van Meurs, David G Lidzey. *Perovskites on Ice: An Additive-Free Approach to Increase the Shelf-Life of Triple-Cation Perovskite Precursor Solutions*, ChemSusChem, **2021**, 14, 12. DOI:10.1002/cssc.202100332
2. *As Chapter 7* - **Mary E O'Kane**, Joel A Smith, Rachel C Kilbride, Emma LK Spooner, Chris P Duif, Thomas E Catley, Adam L Washington, Stephen M King, Steven R Parnell, Andrew J Parnell. *Exploring Nanoscale Structure in Perovskite Precursor Solutions Using Neutron and Light Scattering*, Chem. Mater., **2022**, 34, 16, DOI:10.1021/acs.chemmater.2c00905
3. Elena J Cassella, Emma LK Spooner, Timothy Thornber, **Mary E O'Kane**, Thomas E Catley, James E Bishop, Joel A Smith, Onkar S Game, David G Lidzey. *Gas-Assisted Spray Coating of Perovskite Solar Cells Incorporating Sprayed Self-Assembled Monolayers*, Advanced Science, **2022**, 9, DOI:10.1002/advs.202104848
4. Kirsty E McGhee, Anton Putintsev, Rahul Jayaprakash, Kyriacos Georgiou, **Mary E O'Kane**, Rachel C Kilbride, Elena J Cassella, Marco Cavazzini, Denis A Sannikov, Pavlos G Lagoudakis, David G Lidzey. *Polariton condensation in an organic microcavity utilising a hybrid metal-DBR mirror* Scientific Reports, **2021**, 11, DOI:10.1038/s41598-021-00203-y
5. Timothy Thornber, Onkar S Game, Elena J Cassella, **Mary E O'Kane**, James E Bishop, Thomas J Routledge, Tarek I Alanazi, Mustafa Togay, Patrick JM Isherwood, Luis C Infante-Ortega, Deborah B Hammond, John M Walls, David G Lidzey. *Nonplanar Spray-Coated Perovskite Solar Cells*, ACS Applied Materials & Interfaces, **2022**, 14, 33, DOI:10.1021/acsami.2c05085
6. Dominic Blackburn, Thomas J Routledge, **Mary E O'Kane**, Onkar Game, Thomas E Catley, Christopher J Wood, Trevor McArdle, David G Lidzey. *Low-temperature, scalable, reactive deposition of tin oxide for perovskite solar cells.* Solar RRL, **2022**, 6, DOI:10.1002/solr.202200263
7. Baocai Du, Renyong Geng, Wei Li, Donghui Li, Yuchao Mao, Mengxue Chen, Xue Zhang, Joel A Smith, Rachel C Kilbride, **Mary E O'Kane**, Dan Liu, David G Lidzey, Weihua Tang, Tao Wang. *13.9% efficiency ternary nonfullerene organic solar cells featuring low-structural order*, ACS Energy Lett., **2019**, 4, 10, DOI:10.1021/acsenergylett.9b01630
8. Donghui Li, Xiaolong Chen, Jinglong Cai, Wei Li, Mengxue Chen, Yuchao Mao, Baocai Du, Joel A Smith, Rachel C Kilbride, **Mary E O'Kane**, Xue Zhang, Yuan Zhuang, Pang Wang, Hui Wang, Dan Liu, Richard AL Jones, David G Lidzey, Tao Wang. *Non-fullerene acceptor fibrils enable efficient ternary organic solar cells with 16.6% efficiency*, Science China Chemistry, **2020**, 63, DOI:10.1007/s11426-019-9681-8

List of Conference Presentations

1. Oral Presentation - **Mary E. O'Kane**, Joel A. Smith, Tarek I. Alanazi, Elena J. Cassella, Onkar Game, Sandra van Meurs, David G. Lidzey. *Extending the Lifetime of Perovskite Precursor Solutions.* UK Semiconductors 2022.
2. Oral Presentation - **Mary E. O'Kane**, Joel A. Smith, Tarek I. Alanazi, Elena J. Cassella, Onkar Game, Sandra van Meurs, David G. Lidzey. *How to Keep your Triple Cation Perovskite Precursors Looking Young, Fresh and Fabulous*, Supersolar/PVSAT 2021
3. Poster Presentation - **Mary E. O'Kane**, Joel A. Smith, Tarek I. Alanazi, Elena J. Cassella, Onkar Game, David G. Lidzey. *Further Understanding the Solution Chemisty of Perovskite Precursor Solutions*, HOPV22.

Note on Thesis Format

This thesis is written in an alternative format. Chapter 4 and 7 are published works that have been previously peer-reviewed. For ease-of-reading, these have been adapted to the style of this thesis although the content is unchanged, and the accompanying chapters have been written in a similar format.

The papers of Chapter 4 and 7 have a number of collaborating authors. In each case the experimental work, analysis of the data, and writing of the manuscript was primarily completed by the author (Mary E. O'Kane), and the co-authors listed below have been contacted and agree to this.

Tarek I. Alanazi

Elena J. Cassella

Thomas E. Catley

Chris P. Duif

Onkar S. Game

Rachel C. Kilbride

Stephen M. King

David G. Lidzey

Andrew J. Parnell

Steven R. Parnell

Joel A. Smith

Emma L.K. Spooner

Sandra van Meurs

Adam L. Washington

Acknowledgements

First of all, I would like to thank my supervisor David Lidzey for giving me the opportunity to join this incredible group of researchers. Thank you for taking a chance on me and for helping me steer the course through this PhD, especially through some muddy waters. To Joel Smith, thank you for your guidance, your support, your advice and your compassion - you have helped shape the researcher I am and for that I will always be grateful. To Elena Cassella, I am so lucky to have you as my battle buddy. Thank you for putting up with my clumsy chemistry questions, for your brilliant insight and drive which inspires me daily and most importantly thank you for your friendship, which has made even the most difficult days of the PhD so much brighter. Thank you to Emma Spooner, who is not only a brilliant researcher but an extraordinary leader - and I'm glad to say a great friend. A big thank you to Matt Wright for fixing everything all of the time - and for being so kind when things are quickly unfixed! Thank you to all the researchers who have since left the group - Claire Greenland, Tom Routledge, James Bishop, Onkar Game, Mike Wong-Stringer, Kirsty McGhee and Tarek Alanazi - for answering every question and weathering every crisis, and showing me that passion, curiosity and a great sense of fun are some of the most important components of a PhD researcher. These are traits which I'm glad to say have continued throughout EPMM - thanks to Timothy Thornber, Peter Claronino, Ibrahim Albariqi, Yan Chen and Dominic Blackburn for continually inspiring me, helping me and often drinking with me. I would particularly like to thank Ibrahim for his help with the $CsFAPbI_3$ devices in this thesis, without which I wouldn't have been able to get this crucial result - thank you so much!

I now have to thank the Polymer group, who have really taken me in as one of their own and helped me navigate the wild world of scattering. Thank you especially to Rachel Kilbride for helping me wrangle with those crazy neutrons and for always making me laugh. You are a hard-core scientist, and I am so lucky to call you a friend! Thank you to Andy Parnell introducing me to SANS in the first place. Thank you for your continued support and for sharing your fantastic scattering brain with a clueless device maker.

Thank you to my mom, dad, brother and all my friends and family for reminding me there is more to life than perovskites, and confirming that the world doesn't end with a shorted pixel. Special thanks to Afeefah Malik, Emma Bennett, Emily Griffin, Josh Everett, Polly Lisa Loftus, Kate Munro, Jess Hall, Leah Morgan, Harriet Hanson, Alex Davis, Lianne Gahan, Mitch Perry, Alex Brown, Spencer Moore and Ethan Mclaughlin.

And lastly to Tom, to say I wouldn't have done this without you, is an understatement. You are not just my partner, you are my inspiration and my joy, my motivation and my calm. Thank you for always being there and for always supporting me. You are a brilliant man, thank you for spending all of your time with me.

Abstract

The efficiencies of perovskite solar cells (PSCs) have increased dramatically over the past 15 years, with a record power conversion efficiency (PCE) of 25.7% achieved in 2022, and device stability is continuously improving. Due to these recent developments, more and more attention is being devoted to the scalability of PSCs. One of the attractive properties of PSCs is they can be solution processed, making them compatible with many roll-to-roll processing techniques, commonly used in industrial manufacturing. In order to ensure reliable performances of devices made from solution processing, perovskite precursor ink shelf life must be accurately measured and extended. We also note that by understanding the intermediate complexes which form within solution, we can improve the crystallisation and subsequent quality of perovskite films.

This work aims to find the usable lifetime of several perovskite precursor solutions, particularly for inks which commonly produce high performing PSCs devices. Specifically, we identify a particular degradation mechanism in a stoichiometric $CsFAMAPb(I_xBr_{1-x})_3$ ink over a period of several months. We find that the main degradation pathway is due to a reaction between the organic cation, methylammonium (MA^+), and formamidinium iodide (FAI), which leads to the formation of non-perovskite polytypes in perovskite films. Interestingly, we find that solvent choice also has an effect on this reaction. Solutions dissolved in DMSO show a slower rate of reaction than those dissolved in a DMF/DMSO blend. We also explore the affect of precursor age on device stability and find that a photo-induced degradation mechanism occurs in devices made from aged inks. Importantly however, we find that we can delay all these effects, for several weeks at least, by storing precursor solutions at low temperatures ($\sim 4°C$). Following on from this work, we investigate the solution stability of methylammonium-free perovskite solutions, namely a $CsFAPbI_3$ precursor ink. We find that devices made from this ink perform consistently for up to 6 weeks after ink creation. We believe this confirms the conclusions of the earlier work, that the reaction between FAI and MA^+ is the most significant degradation pathway in these mixed-cation systems.

Finally, we analyse the methods used to study colloid sizes within PSC solutions. We find that results from dynamic light scattering (DLS) measurements on these inks can be useful - but sometimes misleading. We therefore expand on how DLS data is presented in order to accurately represent the colloid size distribution, emphasizing that volume-weighted data should always be presented over intensity-weighted data for PSC solutions. Additionally, we find that small-angle neutron scattering (SANS) and spin-echo SANS can be very useful in confirming particle size measurements and solute volume % within these inks. Excitingly, we also find that the SANS data can be modelled in such a way that not only size. but composition of the intermediate complexes within PSC solutions can be probed. We use this model to study the evolution of intermediate complexes within a Pb-excess $CsFAMAPb(I_xBr_{1-x})_3$ solution and a $MAPbI_3$ solution. We here find that a noticeable change in $MAPbI_3$ film morphology correlates with a change in composition and size of the $MAPbI_3$ colloids. Studying these intermediate complexes could unlock key information about the crystallisation mechanics of the perovskite film.

Contents

1 Introduction **17**

1.1 Thesis Motivation 19

1.2 Thesis Overview 19

2 Background **21**

2.1 Atomic Properties 21

2.2 Band Structure of Solids 22

2.3 Photovoltaics 23

2.3.1 Photovoltaic Principle 23

2.3.2 p-n Junction Solar Cells and the Equivalent Circuit Model 25

2.3.3 Solar Cell Measurement 28

2.3.4 Solar Irradiance Spectrum and Solar Cell Limits 29

2.4 Perovskite Solar Cells 31

2.4.1 Crystal Structure 31

2.4.2 The Origins of Perovskite Solar Cells 32

2.4.3 PSC Device Structure 33

2.4.4 Common Compositions 34

2.4.5 Solution Processing 36

2.4.6 Solvent Engineering 39

2.4.7 Solution Aging 42

2.5 Summary 44

3 Experimental Methods **45**

3.1 Perovskite Devices 45

3.1.1 Materials 45

3.1.2 Solution Deposition Techniques 46

3.1.3 Device Fabrication 47

3.1.4 Device Characterisation 50

3.1.5 Stability Measurements 50

3.2 Film Characterisation 50

3.2.1 UV-Vis Absorption and PL 50

3.2.2 Scanning Electron Microscopy 50

3.2.3 X-Ray Diffraction 51

3.3 Precursor Characterisation 52

3.3.1 Nuclear Magnetic Resonance 52

3.3.2 Dynamic Light Scattering 57

3.3.3 Neutron Scattering 59

4 Perovskites On Ice: An Additive-Free Approach to Increase the Shelf Life of Triple-Cation Perovskite Precursor Solutions 67
4.1 Paper Foreword 68
4.2 Author Contributions 68
4.3 Main Paper Body 68
  4.3.1 Abstract 68
  4.3.2 Introduction 68
  4.3.3 Results And Discussion 71
  4.3.4 Conclusions 79
  4.3.5 Experimental Details 81
4.4 Supplementary Information 83
  4.4.1 Spin-Coating Parameters Used for Perovskite Films 83
  4.4.2 Arrhenius Relationship Note 83
  4.4.3 NMR: Experimental Details and Molarities 83

5 Stability of Devices from Aged Precursor Solutions 107
5.1 Abstract 107
5.2 Introduction 107
5.3 Experimental Details 109
5.4 Results and Discussion 112
  5.4.1 Intrinsic Stability 112
  5.4.2 Light Soaking Effects 113
  5.4.3 ATLAS Aging 115
  5.4.4 Film Study 117
5.5 Conclusions 119
5.6 Supplementary Information 121

6 Methylammonium-Free Precursors - The Perfect Solution? 125
6.1 Abstract 125
6.2 Introduction 125
6.3 Experimental Details 126
6.4 Results and Discussion 128
  6.4.1 Film study 128
  6.4.2 Solution Chemistry 131
  6.4.3 Device Study 135
6.5 Conclusions 139
6.6 Supplementary Information 140

7 Exploring Nanoscale Structure in Perovskite Precursor Solutions Using Neutron and Light Scattering 143
7.1 Paper Foreword 144
7.2 Authors Contributions 144
7.3 Main Paper Body 144
  7.3.1 Abstract 144
  7.3.2 Introduction 145
  7.3.3 Experimental Methods 147
  7.3.4 Results and Discussion 149
  7.3.5 Conclusions 156

7.4 Supplementary Information 159
7.4.1 Film Calculations 159
7.4.2 Tuebner Strey Model 160

8 Conclusions and Future Work 169

8.1 Summary of Results 169
8.2 Future Work 170

List of Figures

1.1 Installed PV Technology and % Contribution of Solar Power in UK 18

2.1 Band Levels of Atoms, Molecules and Solids. 22
2.2 Diagram Illustrating the Absorption of a Photon with Various Energies. . . 24
2.3 Examples of Photon Excitation in Direct and Indirect Bandgap Semiconductors. 25
2.4 Schematic Showing p-n Junctions Under Forward and Reverse Bias 26
2.5 Schematic showing p-n Junction Solar Cells 27
2.6 Equivalent Circuit Model Representing a Solar Cell 28
2.7 Example of Current-Voltage Sweep 29
2.8 AM 1.5 Solar Irradiance Spectrum 30
2.9 Shockley-Queisser Limit 31
2.10 Perovskite Unit Cell and Crystal Structure 32
2.11 Different Lead-Halide Polytypes 33
2.12 Common PSC Device Architectures 34
2.13 Lamer Nucleation Theory 38
2.14 Hansen Parameters and Donor Numbers of Perovskite Solvents 41

3.1 Diagram Illustrating Spin Coating 47
3.2 Diagram Illustrating Spray Coating 48
3.3 Regular Achitecture Device Fabrication 49
3.4 Principles of Nuclear Magnetic Resonance 52
3.5 Precession of Magnetic Moments in Pulsed Nuclear Magnetic Resonance . . 54
3.6 NMR Equipment Diagram 55
3.7 Example of Peak Deconvolution and Ratio Integrations in NMR 56
3.8 Principles of Dynamic Light Scattering 57
3.9 Principles of Small-Angle Neutron Scattering 60
3.10 Scattering Event Away from Origin Point 61
3.11 SLD Variation in Real Space and Accompanying Fourier Transforms 62
3.12 Principles of Spin-Echo Small-Angle Neutron Scattering 64

4.1 Chemical Degradation Pathways within TC-Mixed Solutions 71
4.2 Device data for Room-Temperature and Low-Temperature Aged Triple Cation Solutions in DMF/DMSO 73
4.3 Film Characterisation of Films made from RT- and LT-aged Triple Cation Solution in DMF/DMSO 75
4.4 X-ray Diffraction data of Films made from RT-aged Triple Cation Solution in DMF/DMSO 76

4.5 Comparison of XRD data of Films made from RT- and LT-aged Triple Cation Solution in DMF/DMSO 77
4.6 ^1H NMR analysis of TC solutions dissolved in DMF/DMSO aged over a 28 day period 78
4.7 Comparison of Relative Molarities of Cations in Various TC Solutions from ^1H NMR Spectra 80
4.8 Deconvolution and Integration Methods for NMR 85
4.9 Device Metrics for Control Devices 86
4.10 Accelerated Aging Device Metrics 87
4.11 Boxplots of V_{OC}, J_{SC} and FF for LT and RT Aged Inks 88
4.12 Device data for RT-aged TC-DMSO Inks 89
4.13 Device data for LT-aged TC-DMSO Inks 90
4.14 Images of Films made from Aged TC Inks 93
4.15 AFM of Films prepared from 115-day Aged TC Inks 94
4.16 Film Characterisation of Films made from Aged TC-DMSO Inks 95
4.17 XRD measurements of Films made from Aged TC-DMSO Inks 95
4.18 Thicknesses of Films made from Aged Precursor Solutions 96
4.19 XRD spectra for TC-mixed and TC-DMSO, compared with Simulated Perovskite Polytypes 97
4.20 XRD spectra for films made from aged TC-DMSO ink 98
4.21 ^2H NMR Spectra for TC-mixed and TC-DMSO solutions before and after aging 98
4.22 TC-mixed full NMR spectra: 7 days 99
4.23 TC-mixed full NMR spectra: 14 days 100
4.24 TC-mixed full NMR spectra: 21 days 101
4.25 TC-mixed full NMR spectra: 28 days 102
4.26 TC precursor dissolved in DMSO NMR spectra: 7 days 103
4.27 TC precursor dissolved in DMSO NMR spectra: 28 days 104
4.28 TC precursor dissolved in DMF NMR spectra: 7 days 105
4.29 TC precursor dissolved in DMF NMR spectra: 28 days 106

5.1 Normalised Device Metrics for Device made from 2 week Aged Inks, and Stored in Dark Inert Conditions 112
5.2 Normalised Device Metrics for Device made from Aged Inks, and stored in Inert Conditions under Constant Illumination 113
5.3 J-V Sweeps for Devices made from 2 week Aged Inks, and stored in Inert Conditions under Constant Illumination 114
5.4 Normalised Device Metrics for Devices made from 1-week Aged Inks, and stored in an ATLAS Lifetime Tester 115
5.5 J-V Sweeps for Devices made from Aged Inks, and stored in an ATLAS Lifetime Tester 116
5.6 Normalised Device Metrics for Devices made from 2-week Aged Inks, and stored in an ATLAS Lifetime Tester 117
5.7 PL and absorption data of films from aged inks, before and after film aging 118
5.8 Device data of Device made from Aged Inks, and stored in Dark Inert Conditions 121
5.9 Device data of Devices made from Aged Inks, and stored in Inert Conditions under Constant Illumination 122

5.10 Device data of Devices made from Aged Inks, and aged in an ATLAS Lifetime Tester 122

6.1 Absorption and PL data of Films made from Aged $CsFAPbI_3$ Inks 129
6.2 XRD data of Films made from Aged $CsFAPbI_3$ Ink 130
6.3 Ratio of PbI_2:Perovskite XRD Peaks 131
6.4 SEM data of Films made from Aged $CsFAPbI_3$ Inks 132
6.5 FA^+ Molecular Structure 133
6.6 ^1H NMR spectra of Aged $CsFAPbI_3$ Solutions 134
6.7 ^{13}C and ^{207}Pb NMR spectra of Aged $CsFAPbI_3$ Inks 136
6.8 Device metrics for devices made from aged $CsFAPbI_3$ inks 137
6.9 Comparison of Devices made from Aged TC and Aged $CsFAPbI_3$ Inks . . 138
6.10 ^1H NMR of Aged FAI Inks 140
6.11 ^1H NMR of Aged MAI Inks 141

7.1 Tyndall scattering and DLS studies on PSC Precursor Solutions 149
7.2 Optical microscope and SEM Image of PSC Films Compared to Representative Colloid Sizes 151
7.3 SANS Data on PSC Precursor Solutions Fit with a Lorentzian Peak Model 152
7.4 SANS Data on PSC precursor Solutions Fit with a Teubner-Strey Model . . 153
7.5 SESANS Data on PSC Precursor Solutions 157
7.6 Schematic Aid to Explain Volume % and Colloid Concentration Calculations 159
7.7 Individual DLS Intensity-Weighted Measurements 160
7.8 DLS Intensiity-weighted Measurement Before and After Filtration 161
7.9 Physical Representation of Teubner-Strey model in PSC Precursors 162
7.10 UV-Vis Absorption and XRD Spectra of Films Made from PSC Precursors Aged for Various Lengths of Time 162
7.11 SEM and AFM Measurements of Films Made from Fresh and Aged $MAPbI_3$ Precursors 163
7.12 Height Histogram of Films made from Fresh and Aged $MAPbI_3$ Solutions . 164
7.13 Bearing Analysis of Films made from Fresh and Aged $MAPbI_3$ Solutions . 165
7.14 SEM and AFM Measurements of Films made from Fresh and Aged TC Precursors 166
7.15 SANS Data on $MAPbI_3$ Solutions dissolved in DMF/DMSO 167

List of Tables

2.1 Instrinsic Spin of Atoms and Isotopes 21

3.1 Differential Cross Section Dependence on Colloid Shape within SANS . . . 64

4.1 Spin coating parameters for Chapter 4 83
4.2 Device Parameters of Aging DMF/DMSO TC Precursors 91
4.3 Device Parameters of Aging DMF/DMSO TC Precursors stored at LT . . . 91
4.4 Device Parameters of Aging DMSO TC Precursors 92
4.5 Device Parameters of Aging DMSO TC Precursors stored at LT 92
4.6 Molarity of A-cations within aging TC solutions in DMF/DMSO 96
4.7 Molarity of A-cations within aging TC solutions in DMSO 103
4.8 Molarity of A-cations within aging TC solutions in DMF 104

5.1 Comparison of Device Aging Conditions to ISOS standards 111
5.2 Device metrics before Device Aging in Dark, Inert Conditions 121
5.3 Device Metrics after Device Aging in Dark, Inert Conditions 123
5.4 Device Metrics before Device Aging in Inert Conditions under Constant Illumination 123
5.5 Device Metrics after Device Aging in Inert Conditions under Constant Illumination 124
5.6 Device Metrics before Device Aging in an ATLAS Lifetime Tester 124
5.7 Device Metrics after Device Aging in an ATLAS Lifetime Tester 124

6.1 Molar Concentrations of FAI as Solution Ages 140
6.2 Molar Concentrations of MAI as Solution Ages 142

7.1 Teubner-Strey Model Parameters, Fitted to SANS Data 154
7.2 Scattering length densities of various molecules 164

Chapter 1

Introduction

Reducing the severity of global warming is one of the most important issues that humanity faces at this time. Even after enduring a global pandemic in 2020 and with current economic instabilities, the World Economic Report 2022 claims that effects of climate change (Climate action failures, extreme weather and biodiversity loss) are the top three most severe risks the world faces over the next 10 years[1] - beating social cohesion erosion, livelihood crises and debt crises. In the long term, extreme weather events and increased global temperatures will lead to food instabilities and increased disease risk, not to mention the devastating loss to biodiversity in all ecosystems.[2] Unfortunately, it has also been shown that these impacts will hit the most vulnerable people and societies first.[3] However, it is suggested that these damages can be mitigated by limiting the raise in global temperature as much as possible, as a lot of these damages scale with increased temperature. In order to reduce this scale of the destruction that will be caused around the world, we clearly need to make serious changes throughout the world.

Solar power is one of the largest natural resources we have at our disposal. As we try to eliminate our dependence on fossil fuels, we must effectively utilise this asset. Over the past 5 years, there has been a large investment in photovoltaic (PV) production throughout Asia, where there has been a substantial increase in production capacity for c-Si PV. This has allowed solar modules to be produced at a fraction of their previous costs, which has meant that the levelized cost of electricity (LCOE) for solar technology has dropped by 88% between 2010 and 2020. [4] For this reason, the installation of solar PV is increasing both throughout the UK and generally worldwide (for example see Figure 1.1). Nevertheless, there is still huge scope to increase this amount, and there are many areas in which new solar devices could contribute a great amount (for example indoor PV, internet of things, etc).

Currently, silicon-wafer based solar cells account for 95% of solar cell production worldwide [6] with current record performances of 26.7% power conversion efficiency (PCE) for single-crystalline PV cells [7]. Despite this, silicon has a few qualities which are not ideal for use in solar cells (such as an indirect band gap) meaning that relatively thick layers are needed in order to acheive such high PCEs. This means high performing c-Si PV modules are inherently heavy, which makes retrofitting to roofs more complex. Furthermore, it is not possible to produce high efficiency c-Si devices that are also flexible, or semi-transparent. Additionally, even with lower production costs, the process of producing c-Si PV is complex and energy-intensive. For these reasons and more, there has been a growing interest in what

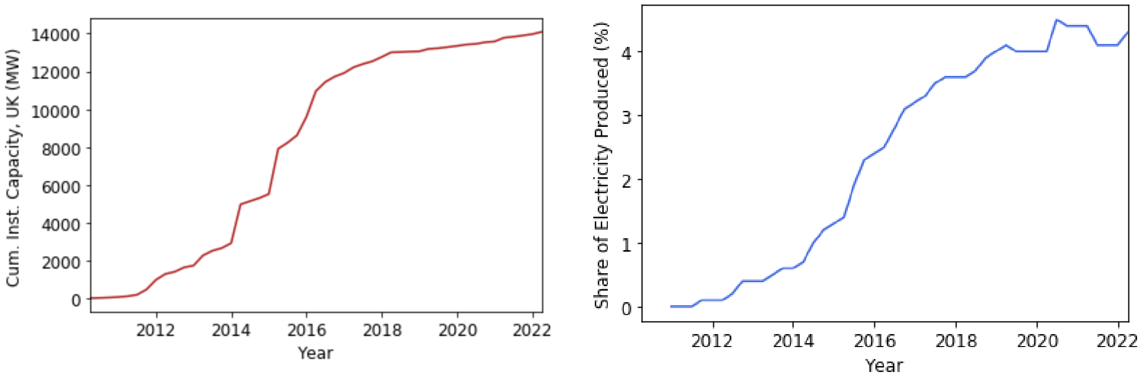

Figure 1.1: Cumulative installed PV technology (left) and share of UK electricity produced by PV technology (right). Share of UK electricity produced in average over the previous 12 months for each time point shown. Data from [5].

are now known as 3^{rd} generation photovoltaics. This includes technologies such as organic photovoltaics (OPV), dye-sensitized solar cells (DSSC) and more recently perovskite solar cells (PSCs).

OPVs and DSSCs are promising thin-film solar technologies, acheiving certified efficiencies of 18.4% and 13.0% respectively as of 2022.[7] However, whilst these devices are still improving, these PCEs are still well below the best c-Si PV performance. Notably, OPVs and DSSCs are potentially easier than C-Si to mass produce through methods such as solution processing, and their material properties can be modified by changing their chemical composition. This is in stark contrast to silicon PV, which is limited by the properties of Si.

Perovskites first emerged in 3^{rd} generation solar technology as sensitizers in DSSCs. A perovskite refers to any crystal with an ABX_3 crystal structure, but in solar technology, it tends to refer to hybrid organic-inorganic PV materials. After their use in DSSCs, it was soon realised that they have many intrinsic properties that make them ideal thin-film PV materials. Since their first use in 2009, they have rapidly improved in order to achieve impressive device efficiencies of up to 25.7%. [7] Like OPVs and DSSCs, they can also be synthesised and processed through cheap and low-energy deposition methods such as solution processing, and devices can be thin and lightweight due to their high absorption at visible wavelengths. Another reason for the excitement in the solar landscape is the potential for application of perovskites in perovskite-silicon tandem PVs. The current record efficiency for a PSC-Si tandem device is a jaw-dropping 31.3%.[7]

Despite these impressive qualities, there are issues with PSCs which need to be addressed and much research to be done before high efficiency modules are commercially available. There are inherent stability issues with high-performing PSCs, as well as extrinsic vulnerabilities to atmospheric moisture and high temperatures. Additionally, many worry about the large quantities of water-soluble lead-halides used in most PSC devices, and it is necessary to ensure that these materials do not pose an ecological threat to the environment. On top of this, the production of large-area devices should be as cheap and safe as possible in order to compete (or complement) the ever growing c-Si market. This goal introduces a wealth of new criteria. For example, devices should ideally be made using scalable, roll-to-roll compatible techniques. Another goal for large scale manufacturing is that the materials used in every layer of a PSC be abundant, cheap and environmentally friendly. Despite these numerous challenges, perovskites have proven to be adaptable and capable of producing high efficiency PV solar cells. With proper encapsulation and appropriate life-cycle assessment, there remains great hope that PSCs can contribute in a meaningful way to the growing energy crisis.

1.1 Thesis Motivation

The ability to process PSCs from solution is one of their largest advantages, both in term of small-scale laboratory research and for R2R large-area manufacturing. On both scales, understanding the complex solution chemistry that occurs prior to film crystallization is an invaluable part of optimizing perovskite quality. Additionally, knowing the usable lifetime of these perovskite precursor inks will help reduce time and material wastage in research and commercial environments. This thesis hereby explores the stability of several perovskite precursors under various conditions, and outlines the aging pathways that occur within these inks, which can lead to poor film quality and subsequently poor devices. We also explore the methods used to study these solutions and evaluate some of their strengths and limitations.

1.2 Thesis Overview

- **Chapter 2** discusses the relevant physics and solar cell theory related to thin film PV technology. Additionally, a brief history of PSCs is discussed and common perovskite compositions are outlined. Various solution chemistry topics are explored in relation to PSC devices, including solution processing methods, nucleation theory, solvent engineering research and precursors solution aging studies.

- **Chapter 3** summarises the various techniques used in this work. Following Chapter 2, we describe the compositions and techniques used in Chapters 4-7 and we outline specific device fabrication methodology. We also discuss the various thin film characterisation methods used and explain the theory behind some of the solution characterisation techniques used to probe perovskite precursor solutions.

- **Chapter 4** details a study on the aging processes of a highly performing triple-cation mixed-halide PSC precursor solution. Stock solutions of this perovskite composition are made from two different solvent systems and the chemical reactions within them are studied with ^1H NMR. Devices and films are routinely made from this stock. Films are characterised with UV-Vis absorption, XRD and SEM, and device performance over this time is measured. Through low-temperature storage of this solution ($\sim 4°C$), the usable lifetime of this ink was extended, and through solvent engineering we explore how solvent choice affects this solution aging. We identified the main degradation pathway in this solution to be due to a reaction between the organic cations in solution.

- **Chapter 5** expanded on the work of Chapter 4 and investigates whether device stability is reduced by aging of triple-cation inks. The stability of devices made from various aged inks were tracked throughout their storage in dark, inert conditions. Additionally, devices made from the aged solutions were studied whilst under constant illumination in inert conditions. Finally, devices are stressed under constant illumination in high-temperature ambient conditions while being held at open-circuit voltage, representing a extremely high stress environment. These studies reveal that devices made from inks stored at low-temperature show similar device stability to controls under all stress conditions. This finding agrees with the results of Chapter 4. We also identify a photodegradation effect in devices made from some of the aged inks, which we speculate may be linked to an increase in trap state density.

- **Chapter 6** expand upon the results in Chapter 4 and 5. A methylammonium-free ink ($CsFAPI_3$) is aged at room temperature, and the activity of the organic and Pb components are tracked with ^1H NMR, alongside ^{13}C and ^{207}Pb NMR. The aim of this experiment was to explore other reactions that may occur without the presence of MA^+. Interestingly, we find that this solution appears to be stable for the duration of our experiment. This work confirms the results of Chapter 4 and proves that a reaction between organic cations seems to be the main degradation pathway leading to poor solution stability.

- **Chapter 7** examines several methods of probing the complexes that form within a PSC precursor. Several measurements of colloid sizes were taken using dynamic light scattering, and the limitation and physical interpretations of these results are discussed. Small-angle neutron scattering is then used to probe colloid size. In this work, we suggest a model which could describe the composition of such “colloids” as well as their size. We also used spin-echo small-angle neutron scattering to prove there is an extremely small amount of larger colloids present within these perovskite precursor solutions.

- **Chapter 8** summarises the results of this thesis and suggests future work that could be done to further the conclusions made here.

Chapter 2

Background

In this chapter, we will briefly discuss the relevant solid state physics and provide an apt background to thin film semiconductors. We then outline fundamental principles of solar cell theory and device measurement. We also provide a general review of perovskite solar cells (PSCs) - including a brief history of their development, various device architectures and common perovskite compositions. The theory and mechanisms of PSC solution processing is briefly outlined and recent research regarding solvent engineering and precursor aging studies is discussed.

2.1 Atomic Properties

Within an atom, electrons occupy positions in specific orbitals around a nucleus. The Pauli Exclusion Principle states that no two identical electrons can occupy the same quantum state within a quantum system. This quantum state is governed by four quantum numbers which define the electron orbital shell (n), the orbital angular momentum (l), the magnetic quantum number (m_l) and the electron spin quantum number (m_s). Electrons fill these orbitals from a level closest to the nucleus, outwards. The shape and occupancy of these orbitals determine the properties of the atom.

Mass Number	# of Protons	# of Neutrons	Spin	Atoms
Even	Even	Even	0	^{12}C
Even	Odd	Odd	Integer (1,2,3)	^{2}H
Odd	Even	Odd	Half Integer ($\frac{1}{2}$,$\frac{3}{2}$)	^{13}C
Odd	Odd	Even	Half Integer ($\frac{1}{2}$,$\frac{3}{2}$)	^{1}H

Table 2.1: A general rule for defining the intrinsic spin in an atom or isotope.

Much as electrons have an intrinsic spin defined by their angular momentum m_s, protons and neutron also have intrinsic spin (I). Electrons, neutrons and protons are all spin 1/2 particles. The nucleus of different atoms will comprise of different amounts of protons and neutrons. As a result, the nucleus as a whole can have a range of angular momentum values. Therefore, we define spin an intrinsic value for each individual atom and isotope. An atoms intrinsic spin depends on a number of factors but in general it does follow the following basic rule defined in Table 2.1. These values of intrinsic spin can be utilised to study various atoms within a material without causing any material damage. Methods that use this principle include nuclear magnetic resonance and spin-echo small-angle neutron scattering, which will be discussed in more detail in Chapter 3.

2.2 Band Structure of Solids

As previously mentioned, the Pauli Exclusion Principle states that two identical electrons cannot occupy the same quantum state simultaneously. Therefore as two atoms are brought towards one another to form a molecule, their energy levels split to accommodate both electrons (see Figure 2.1). As more atoms are brought together to form a solid, the energy level splitting becomes continuous forming energy bands rather than individual orbitals.

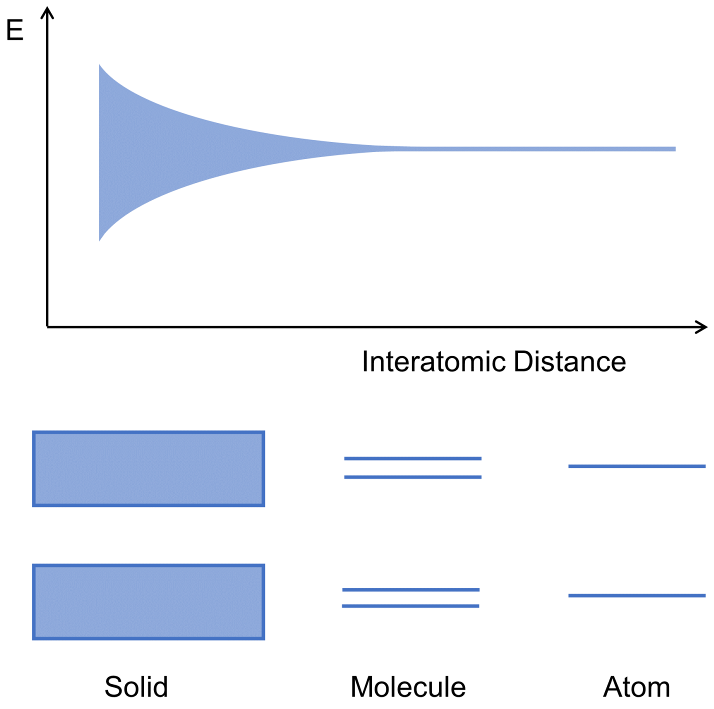

Figure 2.1: Band levels of atoms, molecules and solids.

For a given material, the highest energy band that contains electrons is termed the valence band. The lowest unoccupied energy level is the conduction band, and the gap (if any) between these two levels is called the band gap or energy gap (E_g).[8] In a metal, the highest occupied energy band is not completely filled, or these conduction and valence bands overlap. In this case, electrons can easily move through the material, so metals will readily conduct heat or energy. If the valence band is filled and there is an significant gap between the valence and conduction band, this energy level becomes much more important. The movement of electrons though such a material relies on the electrons in the valence band being excited into the conduction band as shown in Figure 2.2. If the band gap is large, it is very difficult for an electron to move into this higher orbital state. Therefore these electrons are localised in the valence band and such a material will not conduct electricity easily. These materials are insulators. However if the band gap of a material is between 0.5-3eV, this is considered a semiconductor as this energy gap is such that $E_g > k_B T$. For such materials, an electron at finite temperatures can be excited into the conduction band through a variety of processes.[8, 9]

Here, we introduce a concept known as the Fermi level (E_F) of a material. This is the energy level which has a 50% chance of being occupied by an electron. The probability that a state of energy E contains an electron is described by the Fermi-Dirac distribution:

$$f(E) = \frac{1}{e^{\frac{(E-E_F)}{k_b T n}} + 1} \tag{2.1}$$

where E_F is the Fermi energy of the material, k_B is the Boltzmann constant and T is temperature in Kelvin. In a metal, the Fermi level is likely within a band, where there are many electrons that can move freely. In contrast for an insulator or an undoped semiconductor, E_F will lie within the energy gap.

2.3 Photovoltaics

2.3.1 Photovoltaic Principle

A photovoltaic material is one which acts to convert incident solar energy into electrochemical potential energy. In semiconductors, valence electrons can be excited into the conduction band through the absorption of a photon with $E > E_g$. Moving this electron into the conduction band leaves behind a vacancy in the valence band in place of the electron. This is often referred as a “hole”, and is treated as a pseudo-particle which moves as a positive charge would in the material. If this electron and hole exist for a significant period before recombining, they are known as an exciton. An exciton is a bound electron-hole pair which acts as a single particle. They are bound due to the Coulombic force between the electron and hole. Such bound charges can recombine releasing a photon of energy equal to the band gap of the material or, in some materials, an exciton can move throughout the material, for example in a crystal.

In order to be utilised for photovoltaic purposes, this exciton must dissociate to its component free charges (an individual electron and hole carrier). These free electron and hole charges can be harvested at into an external circuit. The energy needed to separate the exciton is the exciton binding energy. In most inorganic photovoltaic materials, this binding energy is on the scale of a few mV, so can be readily overcome at room temperature. In organic photovoltaics, excitons can disassociate into free charge carriers at the interface between two different semiconductor materials with an energy level offset greater than the binding energy. Once this binding energy is overcome, the electron and hole can move freely

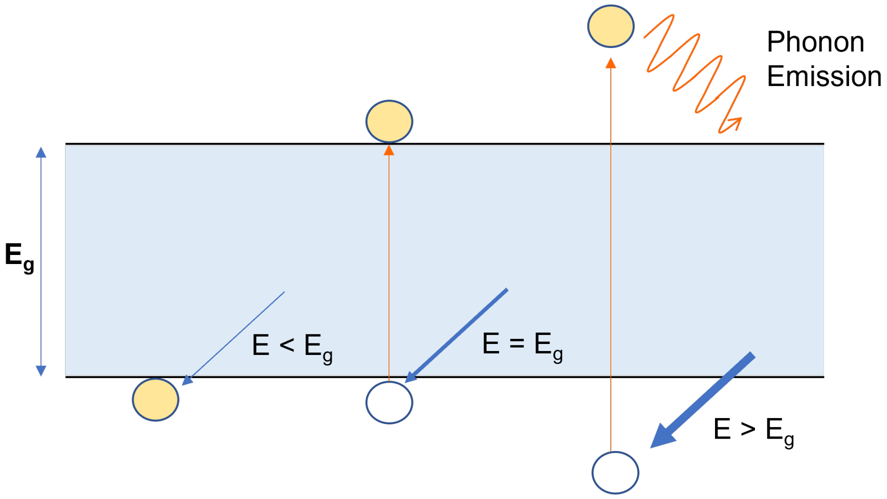

Figure 2.2: Diagram illustrating the absorption of a photon with various energies.

as individual charge carriers throughout the crystal. Here, selective contacts can be useful to extract charges to an external circuit. Factors such as the exciton binding energy and free charge diffusion length determine the optoelectronic properties of the semiconductor and therefore its most suitable application.

The energy of an incident photon compared to E_g of the semiconductor material is important (see Figure 2.2). If the incident photon has $E < E_g$, it is not absorbed as there is not sufficient energy to promote an electron to the conduction band. Alternatively, if a photon has $E > E_g$, an electron will be excited to a hot state in the conduction band. It will then quickly lose energy through phonon emission until it reaches the conduction band edge. Therefore, the maximum energy that can be extracted by a semiconductor is directly related to the materials band gap. This is a fundamental limitation for solar cells and is discussed in more detail later.

Another factor that can affect an absorption process is whether the material is a direct or indirect semiconductor. By using Bloch functions to solve the Schrödinger equation, band formations can be explained in terms of an electrons energy and its crystal momentum vector (k-vector). Direct and indirect semiconductors are defined by the relative position of the conduction band minimum and the valence band maximum point in wavevector k-space. Representative band diagrams are shown in Figure 2.3. For direct band gaps, the minima of the conduction band aligns with the maxima of the valence band in k-space. Therefore, an electron can be easily excited across the bandgap. However for indirect band gaps in a semiconductor, an additional phonon is required to assist the transition of the electron. Both indirect and direct band gap semiconductors can be used in photovoltaic devices, but indirect band gap materials require a thicker active layer to facilitate maximum photon absorption.

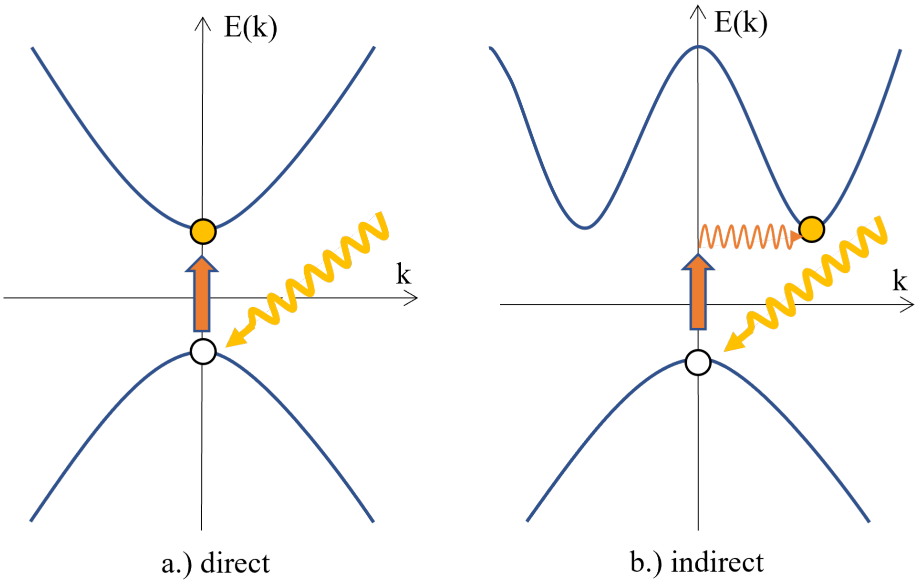

Figure 2.3: Examples of photon excitation in (a) direct and (b) indirect bandgap semiconductors.

2.3.2 p-n Junction Solar Cells and the Equivalent Circuit Model

One example of how semiconductor materials can be used to extract electric potential is via a p-n junction. Here, a semiconductor is doped with impurities to manipulate its electronic properties. It can be doped with donor (n-type) impurities to create an excess of electrons within a material - creating an n-type semiconductor. Likewise, it can be doped with acceptor (p-type) impurities, creating a scarcity of electrons. Layering a p-type and an n-type semiconductor next to one another creates p-n junction. N-type doping shifts the Fermi level towards the conduction band while p-type doping shifts it towards the valence band. At equilibrium, the Fermi levels in the p- and n-type materials must align. This causes a shift of band levels to align E_F, which hereby manifests itself in a built-in potential within the solar cell, inducing the movement of charge carriers.

There are two phenomena which determine the movement of carriers in a p-n junction – drift and diffusion. Diffusion is the movement of charges towards areas of lower concentration (electrons towards the p-doped region and vice versa). Drift current describes the movement of carriers in the direction of the inherent electric field, which opposes the direction of diffusion. At the p-n junction interface, the “depletion region” is formed which contains no free charges, as the positive and negative charge carriers at the interface recombine. This creates positive and negative ions in the n- and p-doped depletion regions respectively. At thermal equilibrium, any carriers that move across the depletion region due to diffusion are matched by an amount of carriers driven in the opposite direction due to the intrinsic electric field.

When a reverse bias is applied across a p-n junction (as shown in Figure 2.4a), free electrons in the n-doped region will be pulled be toward the positive terminal of applied bias,

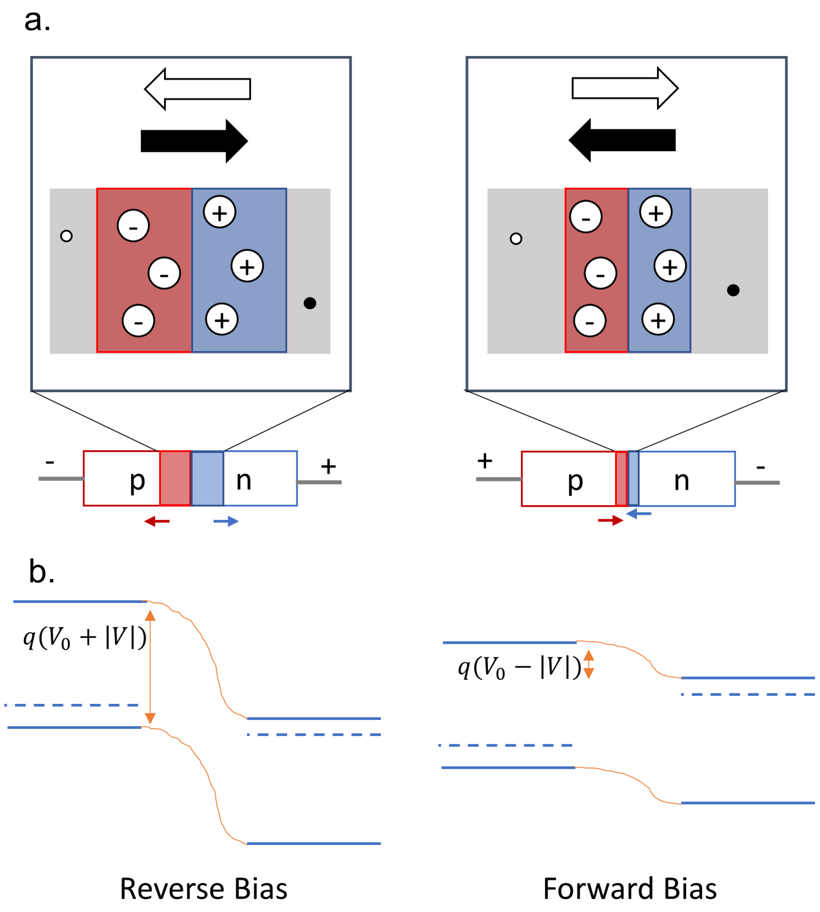

Figure 2.4: a.) Change in depletion region size under reverse and forward bias. Insets show the forces experienced by electron and hole majority carriers where arrows represent the force on the carrier due to the applied bias (black and white show the force on electrons and holes respectively) b.) Change in the potential barrier accross the p-n junction under reverse and forward bias. Here V_0 is the potential bias accross the p-n junction in equilibrium conditions and $|V|$ is the applied bias across the p-n junction.[8]

away from the depletion region. Free hole carriers in the p-doped region will experience a force pulling them towards the negative terminal. This movement of carriers will act to increase the depletion region, and it is therefore harder for any free majority carriers to diffuse accross this. Carrier movement can still occur due to the drift current, so over time there is a net increase in the amount of electrons in the n doped region and holes in the p-doped regions. This leads to a greater potential barrier at the p-n junction (see Figure 2.4b).

Alternatively, when a forward bias is applied, free electrons will experience a force towards the positive terminal which is connected to the p-doped region. Free holes are pulled towards the negative terminal which is connected to the n-doped region. This encourages majority charge carriers to move across the depletion region in the same direction as diffusion. As an electron moves into the p-doped region, it is likely to neutralise an positive ion in the depletion region. This will have the effect of decreasing the size of the depletion region as more ions are neutralised. As this depletion region decreases, it is easier for majority carriers to diffuse across this region, resulting in an increased flow of electrons from the n-doped region to the p-doped region and holes in the p-doped region to the n-doped region. This acts to reduce the built in potential at the p-n junction.

This provides a useful model for depicting a solar cell. Incoming photons can excite electrons across the band-gap in both p- and n-doped regions (see Figure 2.4). Electrons in the conduction band of the p-doped region can easily move into the n-doped region, and holes created in the n-doped region can drift into the p-doped region. However, this flow cannot be reversed due to the potential barrier created by V_0. This increases the number of majority carriers in the n- and p-doped regions which in turn splits the electron and hole quasi-Fermi levels. [8] If an external circuit is connected to this p-n junction, this flow of electrons will create a small current.

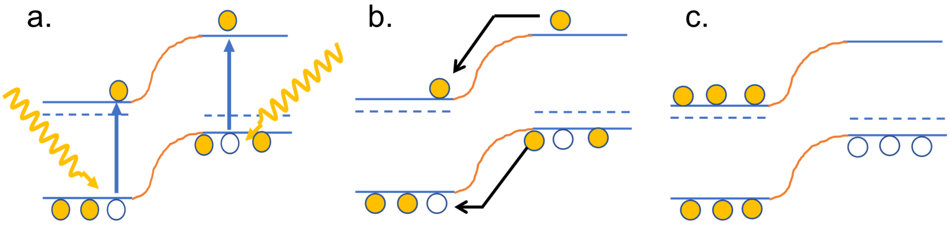

Figure 2.5: a) Electrons are excited into the conduction band by incoming photons in both p- and n-doped regions. b) Due to the potential energy barrier, electrons can move from the p-doped to the n-doped regions easily and holes from the n-doped to p-doped regions. c) There is a resulting excess of electrons in the n-doped region and holes in the p-doped region inducing reverse bias conditions.

An equivalent circuit for a solar cell is as shown in 2.6. This consists of an ideal current source in parallel with a diode. The ideal current source produces a current proportional to light intensity, and this current flows through either the diode or the load. If resistance accross the load is larger than the resistance across the diode, the produced current will flow through the diode, increasing the potential difference between the terminals. However, this results in a reduced current flowing through the load. This balance must be carefully optimised to achieve maximum power output from the cell. We must also consider parasitic losses in the device. These are represented in the equivalent circuit model by a series (R_S) and shunt (R_{Sh}) resistance. R_S represents any non-radiative losses such as recombination at interfaces in the device or charge build up between layers, and should therefore be reduced as much as possible. Shunts represent leakage of current through the cell via pinholes or defects, and therefore R_{Sh} should be maximised.

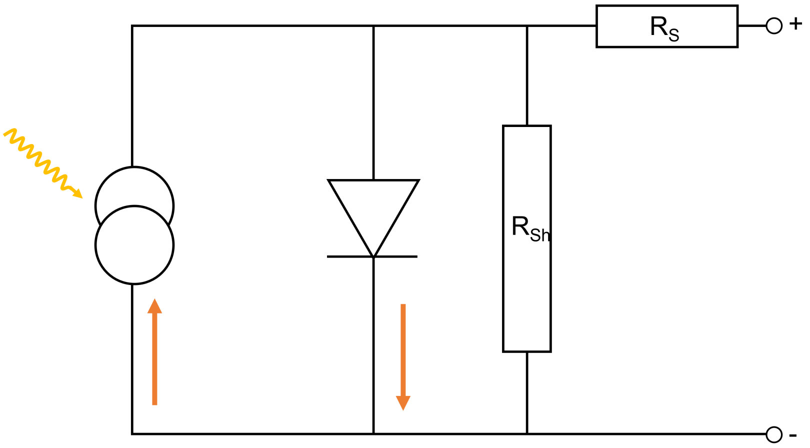

Figure 2.6: Equivalent Circuit Model for a Solar Cell

2.3.3 Solar Cell Measurement

Solar cell metrics are extracted from current-voltage (J-V) sweeps like the one shown in Figure 2.7. Here, current from a solar cell driven at different voltages is measured. This current is expressed in terms of current density, J, in order to ensure results are comparable regardless of device area. J_{SC} is the short-circuit current and is measured when V=0. This is a measurement of the maximum available current from a device and depends on the incident flux density on the device (b_S), and the absorber materials quantum efficiency for a particular photon energy, $QE(E)$:

$$J_{SC} = q \int b_S(E) QE(E) dE \tag{2.2}$$

$QE(E)$ can also be defined as the probability that an incident photon will be converted into an extracted charge carrier. J_{SC} therefore depends on the absorption of photons throughout the cell and the ability of the solar cell to separate and then extract charge. J_{dark} quantifies the current that flows under an applied bias, without illuminating the device. This depends on the applied voltage V and can be expressed using the ideal diode equation:

$$J_{dark} = J_0(e^{(qV/k_bT)} - 1) \tag{2.3}$$

where J_0 is the saturation current density, V is voltage, T is temperature in Kelvin, and k_B is Boltzmanns constant. [8] J(V) can be described as the summation of the J_{SC} and the opposing J_{dark} and is known as the superposition approximation.

$$J(V) = J_{SC} - J_{dark} = J_{SC} - J_0(e^{(qV/k_BT)} - 1) \tag{2.4}$$

Another important metric is the open circuit voltage (V_{OC}). V_{OC} is the voltage across the illuminated device when no current is drawn. When $V = V_{OC}$, the absorbed photon

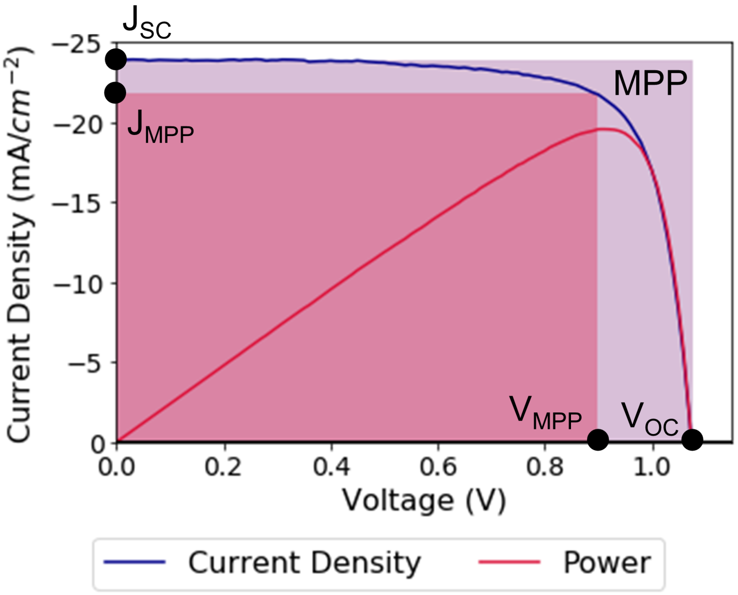

Figure 2.7: An example of a J-V sweep of a solar cell, and the power resulting power density.

flux is matched by the recombination flux, and therefore the net current is zero extracted from the device is zero. This value is the maximum voltage at which the device can produce a positive photocurrent.

An example of a typical J-V sweep is shown in Figure 2.7, along with the calculated power density at each voltage point. Here, the smaller shaded area represents the maximum achievable power density ($J_{MPP} \times V_{MPP}$) with the larger shaded area being the area which lies within $J_{SC} \times V_{OC}$. The fill factor (FF) is a metric that describes the squareness of a J(V) curve and represents how similar these two "squares" are. FF can be expressed using

$$FF = \frac{J_{MPP}V_{MPP}}{J_{SC}V_{OC}} \tag{2.5}$$

As power is a product of both voltage and current, they both must be optimised to achieve maximum device efficiency. The power conversion efficiency (PCE) is the metric commonly used to describe solar cell efficiency and is a product of V_{OC}, J_{SC} and FF, and is given by

$$PCE = \frac{V_{OC}J_{SC}FF}{P_{int}} \tag{2.6}$$

Where P_{int} is the power density of incident light.

2.3.4 Solar Irradiance Spectrum and Solar Cell Limits

The Sun's spectral radiation can be approximated as that of a black body at 5760K. Figure 2.8 shows the solar irradiance at the top of the Earth's atmosphere (AM0) and at the Earth

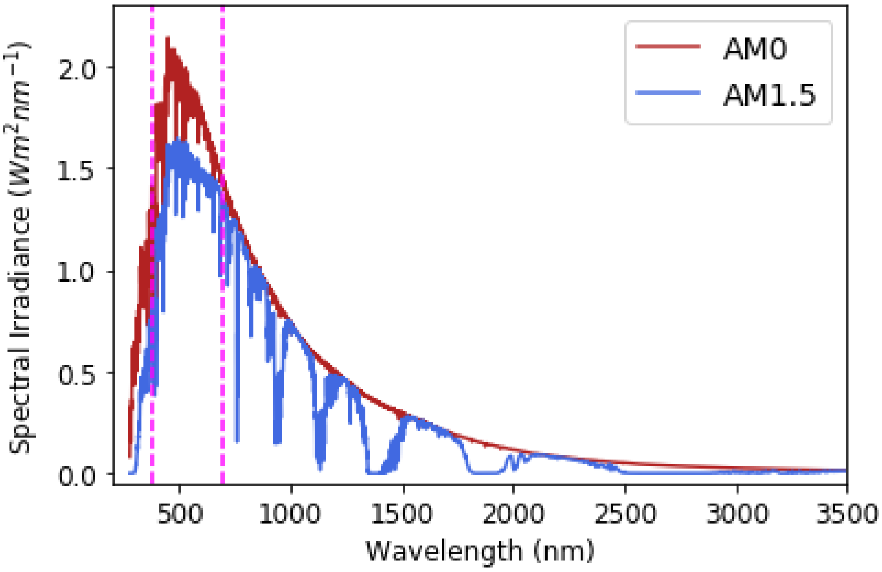

Figure 2.8: Solar Irradiance Intensity at various wavelengths assuming an Air Mass of 0 and 1.5. These correspond to the solar intensity at the edge of the Earth's atmosphere and at the Earth's surface respectively. Here we see the majority of irradiance lies at visible wavelengths (dashed vertical lines). Graph plotted from data in [10]

surface, assuming an Air Mass of 1.5 and a global tilt of 37° (AM1.5G). [10] AM1.5G is considered the standard for solar cell testing. This intensity spectrum integrates to $1000Wm^{-2}$, and Fig. 2.8 shows that in both cases, the highest levels of irradiance are within the visible light region. However, not all of this power can be harnessed for energy conversion.

As discussed earlier, there is a balance to be achieved between optimising voltage and current in order to maximise power output from a solar cell. Photons can only be absorbed by a semiconductor when $E > E_g$, so a larger band gap will mean fewer photons will provide enough energy to excite electrons into the conduction band. Therefore, J_{SC} decreases with increasing band gap as the flow of electrons is reduced. However, V_{OC} increases with increasing band gap as the potential energy gained from recombination is higher. Therefore, there is an optimum E_g for which the $V_{OC} \times J_{SC}$ is maximised, and the largest quantum efficiency can be achieved. This is known as the radiative efficiency limit (or the Shockley-Queisser limit), and Figure 2.9 shows the maximum achievable PCE as a function of E_g for a single heterojunction solar cell. This approximation assumes that that all incident photons with $E > E_g$ are converted into usable charge carriers, and there are no other losses of energy other than radiative recombination.

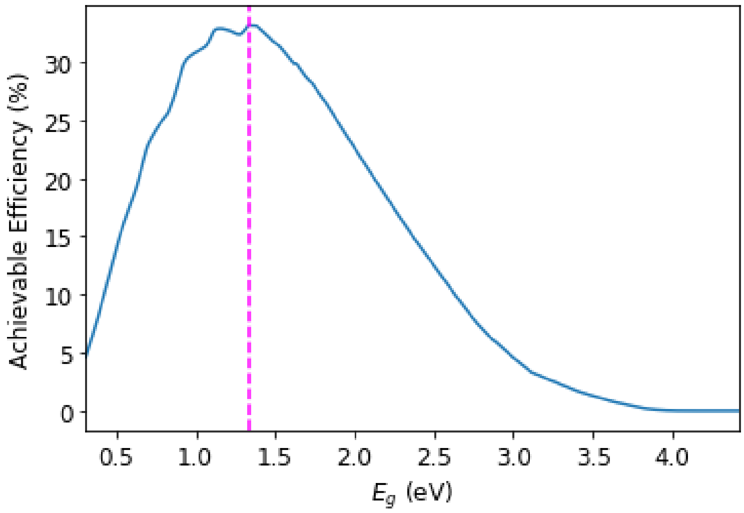

Figure 2.9: Maximum achievable PCE dependence on E_g. Maximum efficiency band gap (1.34eV) plotted with dashed line. Graph plotted from data from [11] .

2.4 Perovskite Solar Cells

2.4.1 Crystal Structure

Perovskites have a characteristic ABX_3 crystal structure where positively charged A and B cations are balanced in charge by three anions (X) to form a lattice structure. The first observed perovskite crystal was $CaTiO_3$ and was discovered by the minerologist, L.A. Perovski. Since then, many examples of this crystal structure have been observed in nature and synthesised in research. Two ways of representing this crystal structure are shown in Figure 2.10. In the unit cell structure (Figure 2.10a) A cations occupy the corners of the lattice structure, while a metal-halide octahedra occupies the body-centre of the unit cell. Another visualisation of the crystal lattice is shown in Figure 2.10b. Here, the B cations of the BX_6 octahedra occupy corner regions of the lattice centred around the A cation in the body-centred position. These visualisations are equivalent ways to represent the overall crystal structure.

An "ideal" 3D perovskite structure will have a cubic or tetragonal lattice as shown in Figure 2.10. The lattice structure of a perovskite crystal depends on the ionic radii of each ion, and mismatched ion radii can encourage lower symmetry structures to form, such as orthombic or hexagonal crystal structures. [12, 13] This dependence of crystal structure on ionic radii in ABX_3 crystal structures can be defined by the Goldschmidt tolerance factor:

$$t = \frac{r_A + r_X}{\sqrt{2}(r_B + r_X)} \tag{2.7}$$

Here r_A, r_B and r_X are the ionic radii of A, B and X ions.[14] For an ideal cubic structure t=1 - however for a stable perovskite phase to form, t must be between $0.8 \leq t \leq 1.0$. Perovskite structures with a tolerance factor outside these limits (t≥1) will likely encourage the formation of non-perovskite polytypes. The most commonly reported phases are

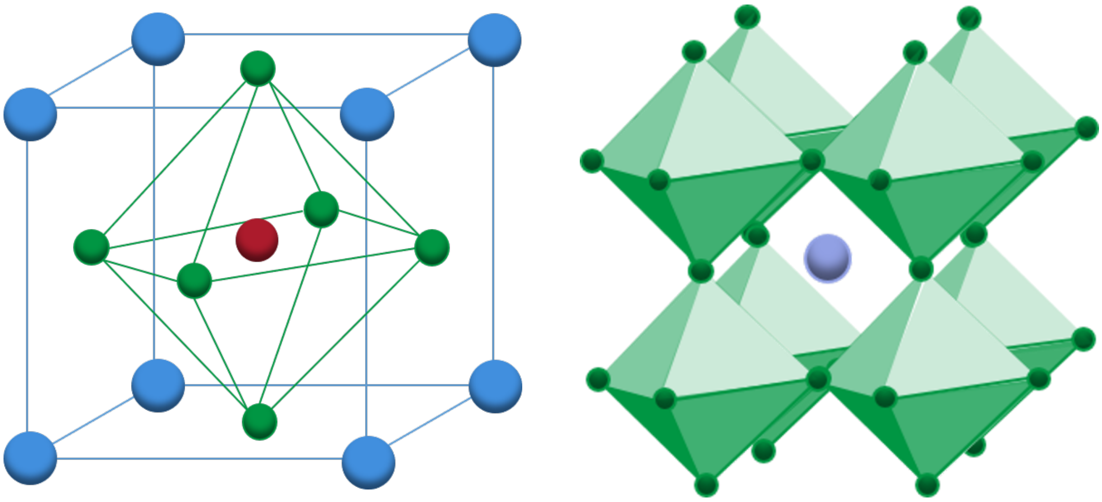

Figure 2.10: a.) Unit cell structure of a perovskite. b.) Equivalent crystal structure - BX_6 octahedra occupying the corner spaces surrounding an A cation. A and B cations are shown as blue and red spheres respectively, and X anions are shown in green.

the perovskite α-phases and non-perovskite δ-phases. An α phase consists of cubic close-packed stacking of AX_3, where B^+ occupy the corner-lattice spaces as shown in Figure 2.10b and 2.11. Alternatively, the δ-polytype phase contains hexagonally closed-packed 1-D structures, in the form of long chains of face-sharing PbX_6 octahedra. These α and β phases have been labelled in literature as 3D and 2H phases (see Figure 2.11). An example of the formation of multiple polytypes within a crystal structure is seen within $FAPbI_3$ perovskites. Here, δ-phases are particularly common due to the large ionic radius of the formamidinium cation.[15–19] It is thought that these long chains of PbI_6 hinder electron transport through the material.[16] Gratia et al. identified phases which contain a combination of both face-sharing and corner-sharing octahedra (identified as 4H and 6H), and demonstrated that these can act as intermediate pathways in the formation of MAFA-based perovskites. These phase patterns are also depicted in Figure 2.11.

The Goldschmidt tolerance factor can be a useful tool to predict the stability of a perovskite crystal. However, it is limited in how well it can predict this, as it has been shown to accurately predict the stability of 3D perovskites in only 74% of cases.[20] Therefore, a tolerance factor of 1.0 does not necessarily guarantee the creation of a stable perovskite.

2.4.2 The Origins of Perovskite Solar Cells

Organic-inorganic PSCs often consist of an organic A cation such as CH_3NH_3 (methylammonium, MA^+) or $CH_3(NH_2)_2$ (formamidinium, FA^+), or an inorganic Cs^+ ion, with a heavy metal B cation (Pb^{2+} or Sn^{2+}) and halide X anion (I^-, Br^-, Cl^-) forming the ABX_3 photovoltaic material. The interesting optoelectronic qualities of a metal-halide perovskite material were first demonstrated in 2009, where $CH_3NH_3PbX_3$ or $MAPbX_3$ - where X is either I^- or Br^- - was used as a sensitizer layer on top of mesoporous TiO_2 in dye-sensitised solar cells. [21] In 2012, it was demonstrated that entirely solid-state PSCs could

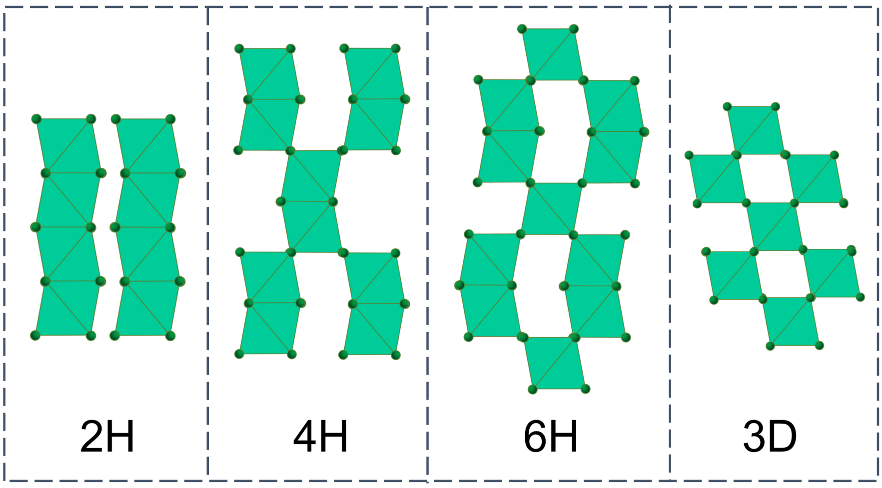

Figure 2.11: Polytype formations of the Pb-halide complexes.

be created using mesoporous TiO_2 as an “electron transport layer” and Spiro-OMeTAD as a “hole transport layer”. Using this formation, a PCE of 9.7% was achieved.[22, 23]. In 2013, the introduction of two-step deposition resulted in a uniform perovskite layer, and subsequently a jump to a PCE of 15.0% was reported.[24] Through extensive optimisation of perovskite compositions and deposition techniques, the performance of PSCs has soared over the past 10 years, reaching highest single junction efficiencies of 25.7%.[7]

2.4.3 PSC Device Structure

Rather than the traditional p-n semiconductors discussed earlier in this chapter, perovskites have the ability to transport both holes and electron effectively, making them “intrinsic” semiconductors. Therefore, in order to maximise photovoltaic performance, charge extraction layers are necessary to aid in the transport of charge carriers to the relevant electrode, and to block electron/hole transport at the undesired electrode. These are known as electron transport layers (ETL) and hole transport layers (HTLs), and are typically materials that have appropriate band alignment with the conductor or valence band of the perovskite material.

Three different device architectures are shown in Figure 2.12. Initially n-i-p mesoporous PSCs were the most common architecture as they most closely resembled a dye-sensitized solar cell. These commonly involve a TiO_2 ETL with a Spiro-OMeTAD HTL. [22] Here, the mesoporous layer acts to aid the transport of negative carriers to the planar ETL, helped by the larger surface area of the mesoporous layer. The charge transport potential of perovskite materials was demonstrated via a mesoporous layer. It was shown that devices using an insulating Al_2O_3 mesoporous layer were more efficient than those using an electron transporting mesoporous layer, TiO_2[23]. This proved that electrons could be transported more efficiently through the perovskite layer than the TiO_2 ETL layer. The Al_2O_3 layer in these solar cells acted only as a scaffold for the perovskite material. The formation of mesoporous layers is costly both in terms of time and energy, and the high temperatures

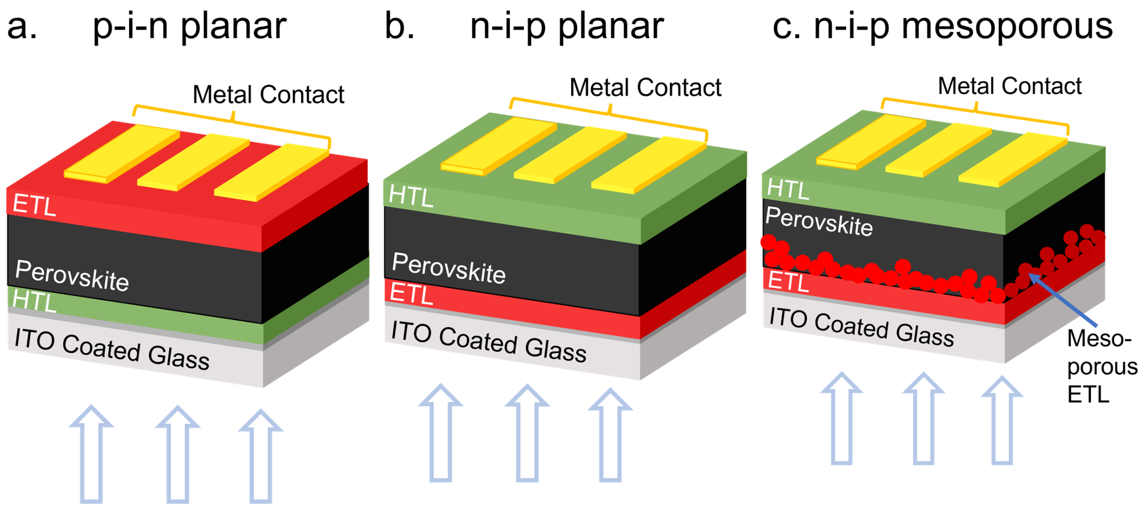

Figure 2.12: Common device architectures for PSCs. a.) Inverted planar structure (p-i-n) b.) Regular planar structure (n-i-p) and c.) Mesoporous regular architecture. All these architectures are illuminated from the substrate side.

needed to synthesise a mesoporous layer limits the substrates that can be used. It was also found that trap-states can be introduced by the mesoporous layer. Therefore, the field has generally moved towards planar architecture structures such as can be seen in Figure 2.12a and 2.12b. These consist of thin, dense HTL and ETL layers in a regular (n-i-p) or inverted (p-i-n) architecture. It has been shown that carrier lifetimes of electrons and holes within the perovskite layers are long enough to ensure efficient charge transfer through to the selective contact layers. Regular (n-i-p) architecture devices often consist of a SnO_2 or TiO_2 ETL layer and use Spiro-OMeTAD as a HTL.[25–27] Inverted (p-i-n) architecture have historically had lower efficiencies than n-i-p devices [28]. However, the introduction of self-assembly monolayers as HTLs has improved charge extraction within p-i-n devices. This has lead to p-i-n devices regularly achieving PCEs exceeding 20%. [29–31]

2.4.4 Common Compositions

The material properties of a perovskite layer can be easily altered by changing its composition. This makes perovskites an extremely useful material for use in many different applications. Here , we will discuss different perovskite compositions used in PSCs and their benefits and limitations.

A-site Cations

Initially, PSCs achieved impressive PCEs using MA^+ as the organic A-cation. However, MA^+ has been shown to be vulnerable to moisture [32–35], light [36, 37] and high temperature degradation.[38] FA^+ is another A-site cation which is often used in PSCs. Perovskites using FA^+ as the primary A-cation have much better temperature resistance and do not undergo as much degradation under light. For these reasons FA^+ is considered in some ways more resistant than MA^+ to external degradation factors.[17] Additionally, the band gap for $FAPbI_3$ is 1.48eV [39, 40] which is closer to the optimal band gap for a solar cell (see Figure 2.9) than $MAPbI_3$ (E_g=1.59eV). It has also been shown that $FAPbX_3$ single crystals have longer carrier lifetimes compared to $MAPbX_3$ crystals.[41] However, FA has a larger Goldschmidt tolerance factor than MA, which can encourage a non-photoactive δ-phase to form in the perovskite.[13, 18] As discussed previously, this polytype is a hexagonal, yellow, non-perovskite phase. High-temperatures ($\geq$150°C) are required in order to convert $FAPbI_3$ into the α-perovskite phase, and even after this, the $FAPbI_3$ perovskite is not phase stable and will form δ-phase polytypes over time. [42, 43] Cs^+ can be also used as an inorganic A-cation. $CsPbX_3$ are extremely resilient at high temperatures and have impressively low rates of non-radiative recombination and an optimal absorbance range in the visible region.[44] For example, $CsPbI_3$ perovskites recently achieved 14.4% PCE synthesised completely in air.[45] However, $CsPbI_3$ PSCs tend to have relatively low PCEs compared to their organic counterparts. Furthermore, the ionic radium of Cs^+ is very small compared to FA^+ and MA^+, and this may be in part due to t being too low to form a stable cubic structure. Also, high temperatures of 300°C are required to create a photoactive $CsPbI_3$ phase and like $MAPbI_3$, these material have serious moisture instabilities.

In 2015, it was first reported that $FAPbI_3$ perovskites could maintain α-perovskite phase in combination with small amounts of $MAPbBr_3$, with no evidence of the δ-$FAPbI_3$ phase formation.[18, 19] It has also been demonstrated that by including a small amount of Cs^+ in $FAPbI_3$ perovskites, not only can the α-phase of $FAPbI_3$ be stabilised [13], but devices become more resistant to light- and moisture-degradation. [17] As both MA and Cs have smaller ionic radii than FA, the incorporation of these in small quantities reduces the Goldschmidt tolerance factor enough that the α-perovskite phase can be stabilised. In 2016, "Triple Cation" perovskites (TCs) using a combination of these three cations (Cs, MA and FA) demonstrated impressive device efficiencies of 21.1% which maintained ~18% PCE after 250 hours operational use.[46] It has also been demonstrated that triple-cation perovskites can achieved PCEs of ~18% without annealing or post-treatment.[47]. Therefore, multiple cation perovskites are often used within PSCs in order to improve the stability of devices.

Halides

Due to the ionic radii of I^- and Br^-, $MAPbI_3$ perovskites are more likely to form a tetragonal crystal structure and $MAPbBr_3$ is more stable in a cubic structure.[48] In 2013, Noh et al. showed by tuning the ratio of halides in $MAPb(I_xBr_{1-x})_3$ perovskites, the band gap could be adjusted between 1.5eV-2.3eV covering almost the entire visible region. This is an especially important property in relation to tandem perovskite solar cells, where tuning the band gap of PSCs to ~1.75eV is optimum for perovskite-silicon tandem cells. [49] Similar band-gap tuning behaviours have been seen in $FAPb(I_xBr_{1-x})_3$ perovskites.[40] Additionally, $MAPb(I_{0.8}Br_{0.2})_3$ exhibited better stabilility under 30% relative humidity compared to $MAPbI_3$. It has also been shown that mixed-halide perovskite $MAPb(I_{3-x}Cl_x)_3$ exhibited an increased carrier diffusion length of nearly 1μm compared to roughly 100nm for $MAPbI_3$ perovskite.[50] However, these mixed-halide materials can undergo phase separation under illumination, splitting into iodine-rich and bromine-rich regions. These iodine rich regions act as trap states, reducing the effective band gap of the perovskite. Although this effect reverses once illumination stops, V_{OC} is ultimately limited by such trap states.[51] Interestingly, it has been demonstrated that mixed cation PSCs (for example, CsFA-perovskites) are more resistant to halide segregation than MA-based perovskites. Knight et al [52] showed that $MAPb(I_xBr_{1-x})_3$ has "fast" ionic pathways that facilitate halide segregation, whereas $CsFAPb(I_xBr_{1-x})_3$ appears to be resistant to halide segregation. Rehman et al. suggested that with optimal addition of Cs^+ into the $FAPb(I_xBr_{1-x})_3$) crystal, the lattice strain within the mixed halide crystal can be reduced. With optimised Cs^+/FA^+ ratios highly crystalline perovskites can be created with high carrier mobility compared to $FAPb(I_xBr_{1-x})_3$ perovskites. [53] In fact, McMeekin et al. demonstrated that with an optimised Cs:FA and I:Br ratio, both halide segregation and δ-phase transition could be supressed and an optimum band gap of 1.74eV could be achieved in CsFA-based perovskites.[49]

2.4.5 Solution Processing

Perovskites can be deposited via solvent-free methods such as thermal evaporation [54], but are usually deposited via solution processing. Solution processing techniques have been adopted by most laboratories as these methods do not require large start-up costs or very specific conditions (vacuum, inert, etc). Additionally when solution processing, perovskite compositions can be easily changed by changing the precursor solutions, and additives can be used to alter the crystallisation process. It should be noted that even small changes in the precursor concentrations can significantly affect device performance, so particular care should be taken when preparing these precursor solutions. [55] In most research, PSCs are spin-coated as this allows for a high level of control over crystallisation. However, PSCs have been deposited using many solution processing techniques that are compatible with roll-to-roll (R2R) processing, such as spray-coating [31, 56–58], blade-coating [59], ink-jet printing and slot-die coating [60, 61]. The successful deposition of perovskite materials and transport layers with these techniques is vital if the industrial potential of solution-processed PSCs is to be realised.

In 2021, Vesce et al. demonstrated 17.9% PCE in a $9cm^2$ device, where both the perovskite and antisolvent were blade coated.[59] Additionally, blade-coated PSCs with a PCE of 15.9% were achieved over areas of $42.9cm^2$ using an air-blade quench. [62, 63] Simultaneously, it was shown that all active PSCs layers (ETL, triple-cation perovskite, HTL) can be deposited via spray coating to achieve a champion PCE of 12.7% over a $1.08cm^2$ active area [57]. PSC modules with a PCE of 16.7% have been achieved over a combined active area of $20.77cm^2$ where the perovskite was deposited via slot-die coating[60], while Bu et al. details a slot-die coated $CsFAPbI_3$ module with a PCE of 19.5% over an active area of $65.0cm^2$. [64] Interestingly, by using a unique “hot-press” style deposition method, 12.1% modules of $36cm^2$ were fabricated and, although there was a liquid phase of perovskite, this method was technically both solvent and vacuum-free.[63, 65]. These promising results all demonstrate that there is potential for scalable solution-processing of PSCs. However, there is still much work to be done in order to ease this conversion and ensure high PCEs are maintained over these large areas.

Nucleation

When considering solution processing in PSCs, it is important first to consider nucleation theory. Homogenous nucleation refers to a situation in which there are no preferred nucleation sites. One example of this is spontaneous nucleation occurring within a nanoparticle solution. Here, whether the monomers in the solution will begin to form "clusters" will depend on the concentration of solute compared to the overall solubility of the particle in the solvent. This is often called supersaturation (S) and can be defined as:

$$S = \frac{C}{C_S} \tag{2.8}$$

Here, C is the concentration of the solute, and C_S is the solubility limit of the solute in that solvent.[66] Homogenous nucleation also depends on the Gibbs Free energy of the large particle, and also on the radius of the particle. For a given solute in a solvent, there is a critical radius, r_c. If a particle is below r_c, it will likely dissolve - but if it reaches $r \geq r_c$, it will continue to grow. [66] This is of particular importance when considering the formation of colloids in solution.

Heterogenous nucleation on the other hand usually has preferred nucleation sites. One example of this type of nucleation is when a solution is placed onto a substrate and undergoes crystallisation as solvent evaporates. While this nucleation also depends on S and r_c, it is also dependent on surface energy between a surface, the solution and its surrounding medium. For this reason, contact angle is very important for heterogeneous nucleation. During perovskite solution processing, thermal annealing is often used to achieve supersaturation in the perovskite film, which instigates crystal nucleation on a substrate surface.

The nucleation of a perovskite film can be described with LaMer nucleation theory. This theory describes how a thin film can grow from a solution. Here, we consider a solution as comprised of two components; a solvent which continually evaporates, and a solute which makes up the bulk of the film. There are three distinct stages of film formation which depend on the concentration of the solution. The concentration of solution changes as solvent continually evaporates from the wet film, which drives nucleation. In Stage 1, the concentration of monomers in solution exceeds the supersaturation point (Equation 2.8). However, there is an threshold concentration that must be reached before nucleation begins, C_{min}. Once this threshold concentration is exceeded due to solvent evaporation, spontaneous nucleation occurs and the nucleation sites then begin to grow. This is phase 2. As the solvent keeps evaporating, the concentration of solution keeps increasing, driving further nucleation. However at a certain point, a large proportion of solute is consumed by the growing nucleation sites, decreasing the concentration of the remaining solute. This drives the concentration down. At some point, the concentration reduces to below C_{min} and no more nucleation can occur, only growth.

By considering this nucleation theory, we can identify some important factors to consider when designing a precursor solution. Firstly, we note that solvent choice plays a vital role in the crystallisation process. Solvent volatility and the strength of co-ordination to solute molecules will drastically affect the amount of time spent in Phase 2 and Phase 3 of LaMer nucleation. Notably, the initial precursor concentration will also affect this. The solution must also have appropriate wettability on the chosen substrate/layer in order to coalesce into a uniform film. There are several techniques that can be used to drive solvent from a wet film, speeding up this nucleation or growth at key points. This is especially important when considering methods such as spray or slot-die coating where the deposition process is less controlled. These methods often use high temperatures, anti-solvent quenches or a

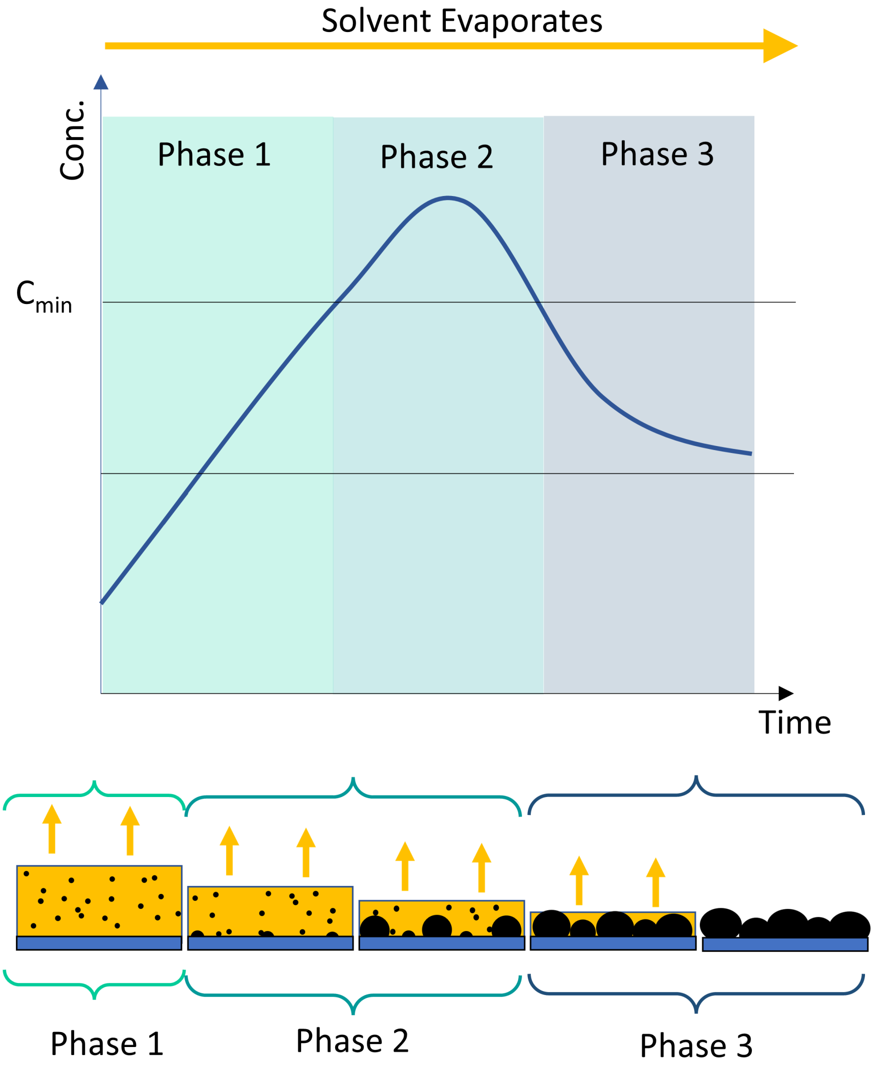

Figure 2.13: LaMer nucleation theory in relation to the formation of perovskite films. During stage 1, sponaneous nucleation occurs but no growth happens while the concentration remains below the threshold concentration, C_{min}. In Stage 2, $C > C_{min}$ and nucleation begins at the substrate surface, and these nucleation sites grow continuously. As more solute is consumed by the nucleation sites, and the solvent continues to evaporate, $C < C_{min}$ and any new nucleation stops. As the remaining solvent evaporates, only growth continues until all the solvent is gone. Adapted from [67].

controlled flow of air or N_2 gas to drive remaining solvent from a film.

The bulk of the work in this thesis will focus on one step deposition of perovskite material. This consists of mixing the precursor materials (lead halides PbX_2 and cation salts AX where A is an A-cation and X is halide atom) in one solvent or a solvent blend, which is then deposited onto the substrate. Some solvent leaves the film during deposition, but solvent is mainly removed during post-deposition annealing. During this process, other mechanisms are often used to control the crystallisation of perovskite films, such as anti-solvent quenching or air blading.

Spin-Coating

Spin coating is a technique that ensures extremely uniform coating of a thin film on a smooth substrate. This involves depositing a small amount of precursor solution in the centre of a substrate, before or whilst spinning the substrate at substantial speed (several thousand rotations per minute). The centripetal force provided by this circular motion will push the liquid outwards from the centre of the substrate isotopically. The movement of air over the surface of the film aids in solvent extraction, and encourages nucleation of the film. By controlling the speed of rotation, the thickness of the subsequent film can be controlled.

Spin-coating is extremely useful when making PSCs as, under the right conditions, it can produce very smooth films. However, there are some limitations to consider when using spin coating as a primary fabrication technique. Only 10% of the deposited solution ends up forming the spin-coated film with the rest thrown off the substrate due to this centripetal force, so there is significant material waste. Additionally, the technique only works consistently over relatively small areas, so it is not compatible with large area processing.

Spray-Coating

As PSC efficiencies soar and device stability improves, more research is being devoted to the scale-up of PSC fabrication. Spray-coating is an adaptable solution processing technique with low material wastage and it is very well suited to coating large areas. It has been used successfully to fabricate multiple layers within PSC devices [31, 57, 58], and it has recently been demonstrated that spray-coating can be used to fabricate devices over curved surfaces. [68] This demonstrates potential for PSCs to be deposited onto a wide range of new substrates.

Ultrasonic spray-coating (which is used in this work) is a technique which requires the break up of solutions into a mist of droplets via ultrasonic vibration. This mist is then directed at a substrate by a “shaping gas” stream. While this technique is very flexible, it is much less controlled than spin-coating. Therefore, there are many factors to consider when depositing a layer via spray coating. These include optimising spray-speed, distance between spray-head and substrate, substrate temperature and post-deposition annealing techniques. [31, 63] Also, solution wettability of the solvent is of prime importance with spray coating to ensure the individual droplets coalesce into a uniform film.

2.4.6 Solvent Engineering

In both spray-coated and spin-coated perovskite films, solvent engineering is often employed as a way of controlling perovskite crystallisation rate. Solvent volatility, solvent wettability on various transport layers and the co-ordination of the solvent molecules to the various precursor materials all have a significant impact on formation of a perovskite layer. Therefore, choosing an appropriate solvent plays an important role in achieving a high quality PSC.

The simplest solvent system to consider is a single solvent system. Typically, solvents such as dimethylformamide (DMF) or γ-butyrolacetone (GBL) are used as lone solvents. In these solutions, supersaturation and solvent volatility are the most influential properties that will affect perovskite film quality.[69] The crystallisation pathways of these films are fairly straightforward and easy to optimise. For single solvent systems, the solvent must be relatively volatile in order to be fully removed from the film. This can lead to fast, uncontrolled nucleation of the perovskite crystals, resulting in poor film morphology. In binary or even tertiary solvent systems, this process becomes more complex. Often, binary solvent systems used for PSC precursors consist of a highly co-ordinating or ligand solvent together with a more volatile solvent. It has been shown that the "evaporation" qualities of these binary solutions will almost entirely be determined by the most volatile solvent. [69] The ligand solvent co-ordinates more strongly than the volatile solvent to the precursor materials, such as Pb. The presence of this strong co-ordination slows the rate of film crystallisation, often facilitating a more uniform crystal. In the majority of cases, the film will fully convert to a black perovskite only after a post-depostion treatment (such as thermal annealing)- but by tailoring the amount of different solvents in solution, the crystallisation of perovskite can be tightly controlled. This controlled nucleation often leads to a superior film quality and therefore better PSC performance.

To explore the effect of ligand solvents on crystallisation pathways, we will now briefly discuss co-ordination mechanisms. In the theory of Lewis base-acids, a base is an electron-pair donor and an acid is an electron-pair acceptor. Therefore, both Pb^{2+} and A cations such as MA^{+} can engage in Lewis base-acid intermediate phases with Lewis basic additives (LBAs). [71] In solution, it has been proven that PbI_2 forms $[PbI_6]^{-4}$ octahedra, but PbI, PbI_3 and $[PbI_4]^{-2}$ species have also been identified.[72] One theory suggests that more strongly co-ordinating solvent molecules will compete with halides to form complexes with Pb^{2+} such as $[PbIS_5]^{+}$, PbI_2S_4, $[PbI_3S_3]^{-}$, etc, where S is the solvent molecule. However, in less co-ordinating solvents, this affinity with Pb^{2+} is weaker and therefore there is larger presence of $[PbI_6]^{-4}$. [73] This co-ordination of solvent with Pb^{2+} can be quantified by its Donor number (DN). A solvent's DN correlates to the probability that a solvent molecule will form an LBA adduct with the Pb^{2+} cation. Examples of such adducts are $PbI_2 \cdot DMF$, $PbI_2 \cdot NMP$ or $PbI_2 \cdot 2DMSO$.

The co-ordination of solvents to A-cations is sometimes quantified by a solvent's lithium cation affinity (LCA) number.[71, 74] This describes whether a solvent will form an LBA-adduct with the A cation in solution such as $MA_2(DMSO)_2Pb_3I_8$. [71] Additionally, A cations and X ions can form hydrogen bonds with the different functional groups of a solvent. Therefore, a solvents Hansen parameter δ_H can be used to indicate the amount of hydrogen bonding that will occur between AX and solvent molecules. [70] Tutantsev used careful analysis of DN, δ_H and dipole moment of solvent molecules to classify solvents into the following categories: weak, strong, inert and AX-selective. [70] These are summarised in Figure 2.14. It can be seen here that in general, the "strength" of solvent scales with DN, except for the case of AX-selective solvents. With these solvents, the DN and δ_H values are

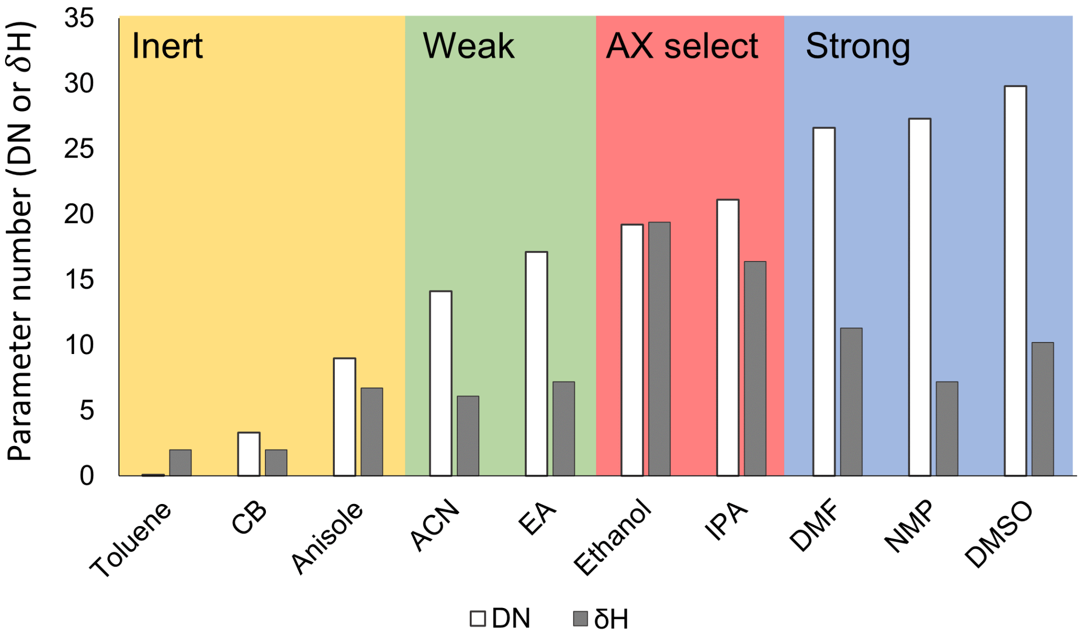

Figure 2.14: Hansen Parameters and Donor Numbers of Perovskite Solvents categorised as inert, weak, AX selective and strong solvents. Figure from data from ref. [70].

approximately equal indicating greater amounts of AX-solvent hydrogen bonding.

We now discuss the various solvents used throughout this work. DMF is the most commonly used solvent for solution processed PSCs. DMF is a polar aprotic solvent with a high DN and δ_H, so will readily dissolve all components within the perovskite precursor. It has been repeatedly reported that films formed from MAI & PbI_2 precursors dissolved in DMF show intermediate phases of DMF-MAI-PbI_2 in pre-annealed films almost immediately after coating. [75–77] When annealed at 100°C, these are fully converted to a black perovskite phase. However, it has been reported that perovskites from systems which use only DMF as a solvent can have a non-uniform, needle-like morphology. [78, 79]. This can lead to inconsistent films and increased shunt pathways reducing device performance. Additionally, colour change in the DMF-based solutions happens almost immediately after deposition, which also indicates a fast crystallisation rate. This is most likely due to the more volatile nature of DMF in comparison to other solvents used for perovskites (such as dimethyl sulfoxide). DMF is also less suitable for practical purposes as it is highly toxic.

Dimethyl sulfoxide (DMSO) can be used as lone solvent for perovskite films [80], but it is largely used as a ligand solvent in addition to other casting solvents (DMF, GBL, etc).[81, 82] In 2014, Jeon et al. discovered that solvent engineering could significantly improve film quality. This study used a $MAPb(I_xBr_{1-x})_3$ precursor in a solvent blend of γ-butyrolactone (GBL) and DMSO, along with a toluene antisolvent quench, and found the films made from solvent blend solutions were much more dense and uniform than those cast from GBL alone. This was attributed to the strong formation of a MAI-PbI_2-DMSO intermediate phase due to the highly coordinating nature of DMSO with Pb^{2+}. Soon after it was reported by Ahn et al. that devices made from DMF/DMSO solvent blends achieved impressive device performances due improved charge carrier properties. [81] It has also been demonstrated that devices made from DMF/DMSO solvent blends show improved device stability, again due to improved film morphology. [83] Although DMF co-ordinates with both A and B cations quite strongly, we can see in Figure2.14 that DMSO has a slightly higher DN than DMF. We also know that DMF is more volatile than DMSO so will act as the "evaporating" solvent in solution. Therefore, in a DMF/DMSO system, DMSO will be the more strongly co-ordinating solvent i.e. the ligand solvent . By varying the ratios of PbI_2:DMSO in DMF, different DMSO intermediates can be formed.[84] Interestingly, DMSO molecules have been found to preferentially bind with Pb^{2+} ions when competing with iodine, only to swap places with the FAI molecule during solvent annealing.[85] This facilitates uniform A-cation integration throughout the perovskite film. For these reasons, DMF-DMSO solvent blends have been used very successfully to create high quality PSCs. [86–88]

N-Methyl-2-pyrrolidone (NMP) has also been used as a solvent for perovskite precursors.[66, 85] Like DMSO, it acts a ligand solvent slowing crystallization of perovskite films, hereby improving film quality and grain size. It has also be demonstrated that unlike DMSO, NMP forms only one intermediate complex no matter how much is added to the precursor. [89] Yang et al. showed that the intermediates phases of films deposited from a DMF:NMP solvent blend were present in the unannealed film for up to 4 times longer than those made from a DMF:DMSO blend. This larger processing window allowed a large area substrate to be coated with an extremely uniform film. [77] Bu et al. study on $CsFAPbI_3$ perovskites reported that when these perovskites are dissolved in DMF, $FA_2Pb_2I_8 \cdot 4DMF$ and $Cs_2Pb_2I_8 \cdot 4DMF$ phases could be identified, and suggested that these facilitated the conversion of the perovskite to the $\delta - FAPbI_3$ and $\delta - CsPbI_3$ phase. However, by using NMP as an additive, this conversion pathway was hindered due to competitive formation of $PbI_2 \cdot NMP$ adducts. DMF/NMP solvent blends have been shown to make the solution processing of PSC more adaptable to industrial applications whilst maintaining high device performance. [64, 77, 89]

The use of solvent additives to slow or halt perovskite crystallisation altogether has faciliated the making of large area devices and mini-modules by creating a larger processing window. [90, 91] Although there are already many dependable solvent systems for making PSCs, there is a drive within the community to make perovskite solutions less hazardous. This would not only decrease the health and environmental risks associated with making and using PSCs, it would also significantly decrease cost of production. One way to do this is by reducing the use of toxic solvents. Current work focusses on replacing toxic solvents with greener alternatives (using acetonitrile solvents [92], triethyl phosphate [93], methylamine formate [94]), looking to reduce the amount of toxic solvent used [95] or diluting these toxic solvents.[96].

2.4.7 Solution Aging

Considering the large quantity of research focussed on PSCs over the past 15 years, relatively few studies have been conducted which examine PSC precursor aging processes.

Understanding the reactions that occur prior to perovskite deposition has been extremely useful for controlling perovskite crystallisation pathways. One example of this is evident in the use of solvent engineering in PSCs. Many believe that studying the precursor solutions themselves will provide insight into how a good perovskite layer is formed. From a more practical stand point, many perovskite stoichiometries do not have a reported shelf-life. This can lead to wastage of time and materials in a research laboratory, and determining a "shelf-life" for PSC solutions is vital if PSCs are to become fully commercialised.

Since the start of this research project, there has been a growing interest in this area and some really interesting results have been observed. There are relatively few methods which are used to study the solution chemistry of PSC precursors. Dynamic light scattering (DLS) is a technique often used to determine colloid sizes within solutions. It has been used to measure the sizes of "colloids" in perovskite precursors [78, 97, 98], but the amount of information that can be extracted with this technique is fairly limited. In the past few years, liquid-state nuclear magnetic resonance (NMR) has been adopted by the perovskite community as an extremely useful tool for examining organic molecules within PSC precursors. [99–102] Additionally, Dutta et al. used cryo-electron microscopy to image the structures formed within a PSC solution.[103] This technique provided not only information about colloid sizes, but also probed the crystalline nature of these colloids. Furthermore in the past few years, several studies have been conducted using small-angle X-ray and small angle neutron scattering to explore the nature of various complexes within precursor solutions. [104–106] This is an exciting area of research as these techniques provide effective, non-invasive methods to probe colloids within solution. However, there is a lot of research to be done in order to standardise these methods and accurately model the colloids.

It has been shown that short term aging (2-24 hours) of some perovskite precursors can result in improved device performance [98, 107–109] and film morphology.[109, 110] However, over long time periods the stability of perovskite precursor solutions can vary significantly. In 2018, Dou et al. reported that triple cation perovskite precursor solutions had poor solution stability. Over a period of 1 month, device performance and film morphology of perovskites made from this stock solution deteriorated significantly. This change was linked to the formation of δ-phases in films made from aged inks.[111] Since then, many studies have shown that double or triple cation perovskite precursors also display this poor solution stability.[99, 112–114] Shin et al. showed that $FAPbI_3$ solutions dissolved in DMF/DMSO solvent blends also exhibited poor solution stability over a period of 1 month. [115] In fact, similar $FAPbI_3$ solutions showed poor stability over a very short period of 48 hours, and this degradation was attributed to the synthesis of 1-3-5-triazine in solution.[101] Again, this study found that maintaining solution stability correlated with preventing the formation of δ-phases forming in films. It has also been shown that FA^+ molecules are not stable in solution under illuminated conditions.[116] Despite this, new research has shown that $CsFAPb(I_xBr_{1-x})_3$ shows increased solution stability compared to TC and $MAPb(I_xBr_{1-x})_3$ solutions.[100] Yu et al. found that films made from aged $MAPbI_3$ and TC solutions exhibited rod-like structures in their surface morphology and speculated that this could explain the poor device performance. Zhan et al. studied the shelf life of $FAPbI_3$ precursor inks which used MACl and CsCl as additives within them. Interestingly, the solutions using MACl as an additive showed poor device stability compared to those which used CsCl as an additive.[117] This indicates that the presence of Cs^+ A-cations in precursor solutions reduces or slows this solution degradation.

There have been several theories proposed to explain why precursor inks may exhibit poor solution stability. The first suggests that solvents significantly contribute to this process. This theory suggests that DMF hydrolyses to form dimethylammonium/dimethylamine and formic acid over time. It was speculated that dimethylammonium (DMA^+) can be incorporated into the perovskite lattice. Due to its large ionic radii, the overall perovskites tolerance factor hereby increases, $t > 1$, which instigates the formation of δ-phases in the film. [111] It has also been reported that the formic acid formed during this hydrolysis could change the pH of precursor solutions, which in turn could affect the size of intermediate colloids. [97, 115] A second theory suggests that a series of addition-elimination reactions between MA^+ and FAI can lead to the formation of two new molecules N-methyl formamidinium iodide (MFAI) and N,N'-dimethyl formamidinium iodide (DMFAI).[99, 100, 118] These organic molecules could also be incorporated into the perovskite crystal as A-cations, having a similar effect to DMA^+, and induce δ-phase formation. Valenzano et al. used NMR to demonstrate that the presence of Cs^+ in double cation films slowed this reaction significantly.[119] Some reports suggest that there is increased formation of higher order iodide complexes such I_2 and I_3^- from free iodine occurs as iodine-based solutions (such as $FAPbI_3$, $MAPbI_3$) age. [94, 113] I_2 species have been shown to accelerate the degradation of both $MAPbI_3$ and $FAPbI_3$ perovskite films, especially under illumination. [120] Therefore, some studies which have attempted to prolong perovskite solution shelf-life have done so by using additives that occupy the free iodine in solution. [112, 113]

Various methods have been used to slow down or halt solution aging. Many studies have used additives to stabilise solutions.[94, 99, 101, 112–114] Alternatively, Shin et al. found that synthesising solutions from single crystals rather than individual powders resulted in better solution stability.[115] This may indicate that stoichiometry plays a key role in extending a precursor solutions useful lifetime. Additionally, Dou et al. observed that perovskites formed through mechanosynthesis can be stored for long periods, and dissolved directly before use, to avoid all solution aging effects entirely.[111]

2.5 Summary

This literature review should outline the relavent concepts and review the appropriate literature to provide context for the work included in this thesis. The atomic qualities discussed in the early parts of this chapter are instrumental in some of the methods described in Chapter 3. The effects of perovskite composition on the formation of various polytypes is an important idea which is explored further in Chapter 4. The effects of solvent co-ordination on subsequent film morphology is studied in Chapter 4 and 7. The ideas discussed in the solvent aging section are revisited in all experimental chapters in this thesis.

Chapter 3

Experimental Methods

This chapter explores the theory and methodology of the experimental techniques and procedures used in this work. Here, we discuss the specifics of fabricating and characterising perovskite devices, as well as discussing the characterisation of perovskite films and precursor solutions. For the most important techniques, we discuss the relevant physics and chemistry that underpins the methods used to understand this complex solution chemistry. Each experimental chapter contains a methods section with specific information about each experiment, whereas this chapter aims to provide a general overview of how the experimental work was conducted.

3.1 Perovskite Devices

Both regular (n-i-p) and inverted (p-i-n) device architecture are used within this work at different points. Both architectures centre a perovskite absorbing layer, but for the inverted devices the position of the electron and hole extraction layers are reversed as discussed in Chapter 2. For devices in Chapter 4 and 6, regular architecture devices were used as the standard devices. Regular architecture devices are fabricated almost entirely from solution processing techniques (except for the evaporated gold electrode). However, these regular devices proved to be unstable under operational stress when used in Chapter 5. Therefore, for stability studies, inverted devices were used.

3.1.1 Materials

Charge transport layers were selected based on device orientation and perovskite composition. Chapters 4 and 6 use regular architecture devices, with SnO_2 as the electron transport layer. SnO_2 has a wider bandgap than TiO_2 [121] and allows efficient charge extraction alongside methylammonium-based perovskites. SnO_2 has been found to have high electron mobility in thin films, is chemically tolerant, and is compatible with a range of low-temperature methods, such as chemical bath deposition [64] , spin-coating, spray-coating or slot die-coating from nanoparticle suspensions[121]. 2,2',7,7'-tetrakis[N,N-di(4-methoxyphenyl)amino]-9-9'-spirobifluorene (Spiro-OMeTAD) was used as the hole transport layer in all regular devices in this work. Spiro-OMeTAD has good hole mobility properties and a conduction band that allows effective electron-blocking. [122] However, this is usually used in combination with several dopants to tune material properties: lithium bistrifluoromethanesulfonimidate (LiTFSI) and tris[2-(1H-pyrazol-1-yl)-4-tert-butylpyridine)cobalt(III) tris(bis(trifluoromethylsulfonyl)imide)] (Fk209) are added to improve conductivity, and 4-tertbutylpyridine (tBP) is added to improve film morphology. As of 2021, an SnO_2 ETL and Spiro-OMeTAD HTL were the transport layers used to achieve the certified world record highest efficiency PSC of 25.5% [88]. The stack most commonly used in Chapter 4 and 6 is ITO-coated glass/SnO_2/perovskite/Spiro-OMeTAD/Au.

Although such materials can be used to create a high efficiency device, we found that regular architecture devices had poor device stability under long term stress. Therefore, in Chapter 5 we used an inverted device stack established by Cassella et al.[31] In this stack, self-assembled monolayers (SAMs) are used as the HTL, namely [2-(3,6-dimethoxy-9H-carbazol-9-yl)ethyl]phosphonic acid (MeO-2PACz) and C_{60} used as the ETL, with an adjacent BCP hole blocking layer.[123]. The full stack for this device was ITO-coated glass/MeO-2PACz/perovskite/C_{60}/BCP/Ag. A Self-Assembled Monolayer is the general name for 2D nanomaterials that are only a few molecules thick and will self-assemble into organized layers. They consist of three parts – the terminal group that interacts with the perovskite or overlayer, an anchor group which attaches the SAM to the ITO layer and a spacer group which acts as the backbone of the molecule connecting the anchor and terminal group.[124] SAMS have revolutionised the p-i-n achitecutre perovskite devices. They are easy to deposit, very high yield and much cheaper than the leading regular architecture HTL, Spiro-OMeTAD. [29] Additionally, they require no extra doping, unlike Spiro-OMeTAD, and they are extremely thin, which reduces parasitic absorption in the device. C_{60} is a fullerene that can be thermally evaporated to produce a dense electron transport layer, with high electron mobility and improved film morphology than other p-i-n ETLs (such as PCBM). Devices using a C_{60} ETL exhibit a low level of hysteresis, which is important for p-i-n perovskite devices. Here, we have used C_{60} in conjunction with a BCP hole-blocking layer, which allows for better charge selection at the electron transport interface.

There are several perovskite compositions used in devices in this work. Firstly, in Chapter 4 and 5, we used a 1.2M stoichiometric triple cation perovskite: $Cs_{0.05}FA_{0.81}MA_{0.14}PbI_{2.55}Br_{0.45}$. In Chapter 6, a 1.1M $CsFAPbI_3$ perovskite doped with small amounts $PbCl_2$ was used. Both of these formulations have been shown to make good PSC devices. [64, 125]. In Chapter 7, film and solutions studies were done using a 0.65M $MAPbI_3$ solution and a 1.3M Pb-excess TC ($Cs_{0.05}FA_{0.79}MA_{0.16}Pb(I_{0.85}Br_{0.15})_3$)) solution.

3.1.2 Solution Deposition Techniques

Spin-Coating

Spin-coating is used throughout this work to deposit ETLs (SnO_2), perovskites (as in Chapter 4, 5 and 6) and HTLs (both SAMs and Spiro-OMeTAD). Substrates were held inside the spin coater using an appropriately sized chuck. Depending on the layer 25-100μl of solution was deposited onto a substrate. This substrate was rotated at several thousand revolutions per minute (rpm) and the centripetal force pushes the solution outwards equally across the substrate as shown in Figure 3.1. Often, additional annealing was needed to

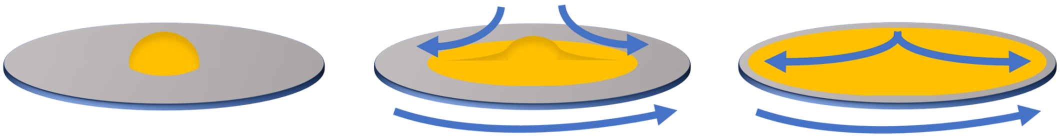

Figure 3.1: Diagram Illustrating Spin Coating. The substrate is rotated causing the solution to be equally distributed across the substrate due to centrepetal force.

ensure complete solvent removal. Most films were spin coated statically (i.e. the substrate is static when the material is deposited). However, Spiro-OMeTAD was coated dynamically - which means the solution was dispensed onto the substrate while it is rotating.

Spray-Coating

Spray coating is a high throughput, high speed deposition technique often used for solution processing over large areas. In Chapter 6, ultrasonic spray-coating was used to deposit the perovskite and transport layers. An ultrasonic spray-coater works by using a piezoelectric transducer to break down a flowing solution into small droplets. A shaping gas is then used to create a direct stream of mist aimed towards a substrate. Ideally, these small droplets coalesce on the substrate to form one uniform film. This process is shown in Figure 3.2. The whole spray head moves in parallel to the substrate in order to coat the surface. There are many variables to optimise when spray-coating, as the process is much less controlled than spin-coating. A few of the variables which need to be defined are: precursor flow speed, distance of spray-head from the substrate, volatility and viscosity (therefore concentration) of precursor solution, spray-head speed, substrate temperature and (most importantly) the wettability of precursor onto the chosen substrate.

3.1.3 Device Fabrication

Substrates: Etching and Cleaning

ITO-coated glass substrates were sourced from Ossila in patterned formation (8 -pixel) or unpatterned. To pattern unpatterned devices, part of the ITO layer was partially etched using a dilution of (1:2) hydrochloric acid to water in combination with Zinc powder. Kapton tape was used to protect the areas where ITO was to be retained.

It was important to clean the substrates thoroughly to ensure uniform performance across the entire device. Therefore, the same cleaning process was used throughout this work and was based on previous work.[126] Firstly, the substrates were massaged with Hellmanex and thoroughly rinsed with water to physically remove dirt from the substrate. The substrates were then sonicated in diluted Helmanex (in deionised -DI- water), DI water and isopropanol for 15 minutes each, with sufficient rinsing between each stage. In some cases, the substrates were stored in IPA until just before deposition. Substrates were then dried using filtered nitrogen gas and the placed in a UV-Ozone cleaner for 25 minutes before depositing any layers. Device fabrication began as quickly as possible after UV-ozone treatment.

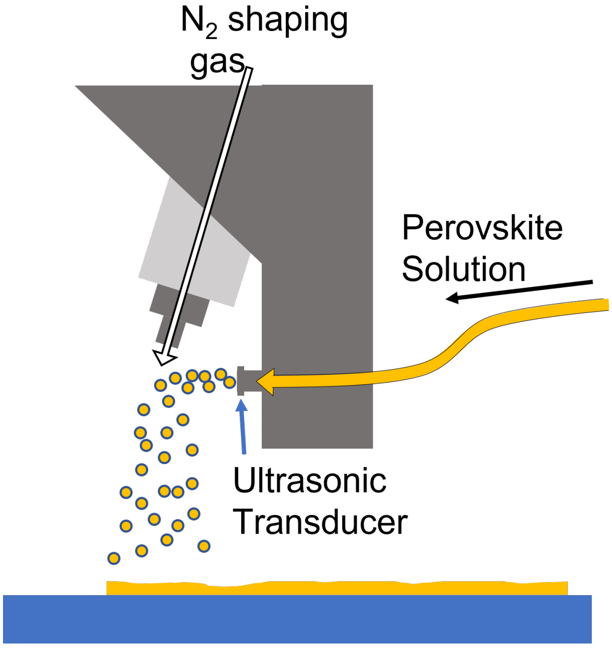

Figure 3.2: Diagram on illustrating spray coating. An ultasonic piezo-electric transducer breaks the solution into droplets, which are then directed towards the substrate using a shaping gas.

Regular Architecture

The SnO_2 layer was spin or spray coated onto clean substrates. A cotton swab soaked in DI water was used to remove some of the SnO_2 to create a contact with the ITO (see Figure 3.3). The SnO_2 layer was annealed for 30-40 minutes at 150°C and was then UV-ozone treated for 25 minutes immediately before perovskite deposition.

All perovskite layers were deposited in a glovebox environment. After transferring substrates into the glovebox, a stream of compressed N_2 was used to remove dust from the substrates. The exact details of perovskite deposition are detailed in each chapter. During deposition and annealing of this layer, there was a distinct colour change from a yellow wet-film to a specular black film, often through a (brown-ish) intermediate phase. For perovskites in Chapter 4, 5 & 7, an antisolvent quench was used to control crystallisation. This involves depositing $\sim 100\mu$l of antisolvent (chlorobenzene, anisole, ethyl acetate) onto the substrate while it is still rotating.

Spiro-OMeTAD was spin coated dynamically or spray coated on top of the perovskite layer, and then taken out of the glovebox to allow oxidisation, improving conductivity of the layer. These devices were placed in a dark dry-box overnight. These devices were then patterned to create an ITO contact with a razor and an acetonitrile wash. Finally, a gold electrode layer (80-100nm) was thermally evaporated onto devices using an Edwards 306 Bell Jar evaporator. The deposition prcoess of n-i-p devices is shown in Figure 3.3

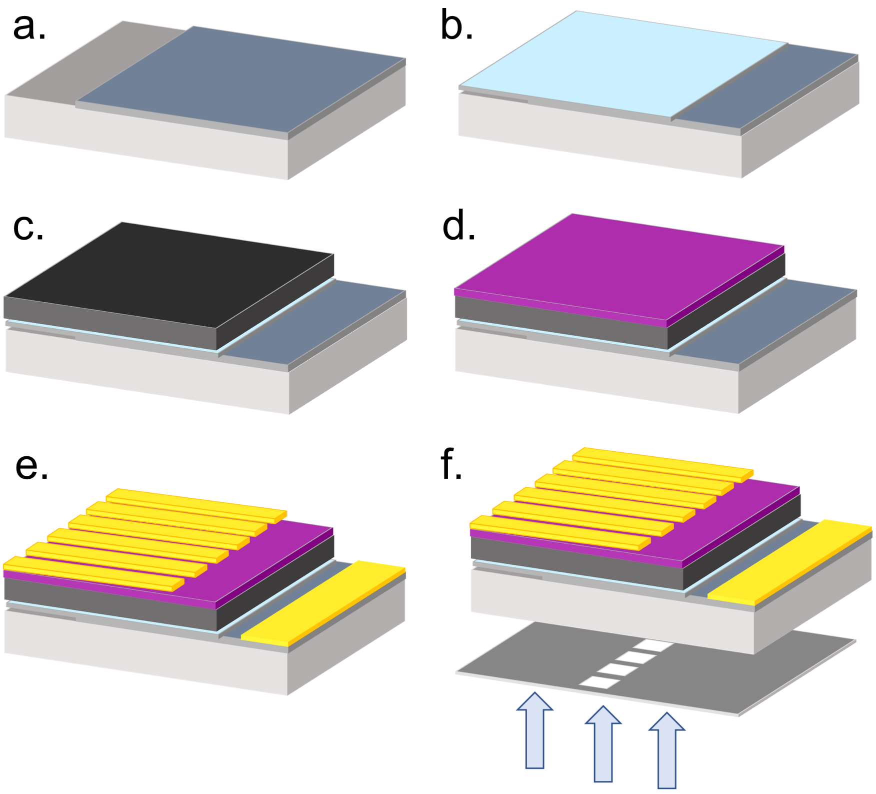

Figure 3.3: Steps involved in Six-Pixel Regular Architecture Device Fabrication. a.) Etch ITO. b.) Deposit and pattern SnO_2. c.) Deposit and pattern perovskite. d.) Deposit and pattern Spiro-OMeTAD, and leave overnight to oxidise. e.) Gold contact thermally evaporated. f.) Device mask used to define device area while testing. Devices are illuminated from the glass-side of the device.

Inverted Architecture

For inverted devices, all layers were deposited in a glovebox environment. 50 μl of 1 mmol MeO-2PACz SAMs solution dissolved in ethanol was spin-coated for 3000rpm for 30s onto clean substrates and annealed for 10 minutes at 100 °C. Perovskite layers deposition details are outlined in Chapter 5 - however due to the low wettability of SAMs, the perovskite material was manually spread across the substrate before spin coating. Devices were patterned at this point, using a razor and acetonitrile wash to create a ITO contact. Then, 23nm and 8nm of C_{60} and BCP were thermally evaporated onto the perovskite stack using an Angstrom thermal evaporator. Finally, 100nm of silver was thermally evaporated onto the devices to form a contact.

3.1.4 Device Characterisation

Initial Measurements

After fabrication, devices were tested on a Newport 92251A-1000 Solar Simulator under AM 1.5 illumination which had been calibrated to $1000Wm^{-2}$ using a silicon reference cell. Six and eight pixel devices were defined by an active area of 0.02506±0.00006 cm^2 and 0.02365±0.00012 cm^2 respectively. This device area was defined using a thin metal sheet mask. J-V sweeps were performed using a Keithley 237 source measure unit. Voltages were varied between -0.2V and 1.2V and back to -0.2V at a speed of 0.1 Vs^{-1}. For power point tracking, the maximum power point voltage (V_{MPP}) was calculated from the J-V curve and the chosen pixel was held at this voltage for ~1 minute and the corresponding PCE output is measured.

3.1.5 Stability Measurements

For stabilised measurements in Chapter 5, devices were encapsulated before initial testing. The full device area was encapsulated using UV-curable Blufixx epoxy and a glass encapsulation slide. To measure aging a device under various conditions, different solar simulators and source meters were used. In some cases, devices were illuminated within an ATLAS Suntest CPS+ with a white light source calibrated to ~ 1 Sun. For these measurements, a Keithley 2400 source meter was used. Voltage was varied between 0 and 1.2 at a scan speed of 0.2 Vs^{-1}. In another case, devices were aged in an inert environment under constant illumination. In this case, Ossila Automated I-V Test System -S2006- was used as a source meter, and devices were continuously illuminated under a LED light source calibrated to 1 Sun. Throughout this device aging, J-V curves were scanned intermittently from 0V to 1.2V at a scan speed of 0.2 Vs^{-1}. In these aging studies, device area was not accurately defined. Therefore, where possible, J-V sweeps were measured before and after device aging using the calibrated set-up described in the previous section.

3.2 Film Characterisation

3.2.1 UV-Vis Absorption and PL

Absorbance measurements were taken using a UV/VIS/NIR light source (Ocean Optics – DH-2000-BAL), collection fibre optic cables (Ocean Optics) and spectrometer (Ocean Optics – HR2000+ES). For PL measurements, films were excited using a 400 nm laser and PL emisson measured with collection fibre optic cables (Ocean Optics) and spectrometer (Ocean Optics -FLAM minature spectrometer). Thin films of perovskite material were prepared on quartz coated substrates and processed using OceanView software. A thin film sample was placed between the focussed UV-Vis light source and the detector, and the relative intensity of the transmitted beam, compared to the original beam was used to measure absorbance through the thin film and PL from the film.

3.2.2 Scanning Electron Microscopy

In scanning electron microscopy (SEM), a beam of electrons are accelerated towards a sample. Electrons have a much smaller wavelength than visible light, so electron microscopy can achieve greater resolution a visible light microscope. This enables imaging of much finer morphological detail of a films surface. In SEM, electrons are produced at the apex of a column and are accelerated through a series of lenses (which are essentially electromagnets) towards a stage with a sample mounted on it. These creates a focussed electron beam. These lenses can control the movement of the beam over the sample, allowing a defined area to be scanned. All of this happens at vacuum pressure. When the electron beam interacts with the sample, backscattered electrons, secondary electrons and various X-rays are produced. Secondary or surface electrons are produced when electrons hit the atoms on the surface of the sample, then absorb the energy from the electron beam and release their own electrons. Alternately, backscattered electrons are electrons from the electron beam itself that are reflected off the surface and can come from deeper within the sample. The quality of image that can be obtained from a given sample can be determined by beam spot size, the acceleration voltage, and by the conductivity and robustness of the sample.

Within this work, we imaged the surface morphology of perovskite films using SEM. As we were mostly interested in surface morphology, back scattered electrons were imaged through an in lens detector. As perovskites conduct electrons, our samples did not require surface pre-treatment - however these are not perfect conductors and the quality of charge transfer depends on the quality of the perovskite material. Hence, we used low acceleration voltages (between 1.0 - 1.5kV) to image these as high voltages results in excessive charging which limited image resolution and effectively "burns" the samples. Samples were connected to sample stubs using silver conductive paint that was extended to the edges of the perovskite film.

3.2.3 X-Ray Diffraction

X-Ray Diffraction (XRD) was conducted on various X-Ray diffractometers to identify perovskite and non-perovskite phases within the perovskite film. In XRD, X-rays are coherently scattered by electrons within the crystal structure. Crystalline material are defined by their repeating molecular structure such as a periodic unit cell. According to Braggs law, a wave with a wavelength λ should scatter from a crystal structure with lattice spacing, d, with constructive interference if:

$$2d\sin\theta = n\lambda \tag{3.1}$$

where n is an integer and θ is the incident (and reflected) angle of the wave. Therefore over a given range of angles, there will be points of constructive interference depending on lattice spacing d, which will give information about the crystal structures present within the perovskite film. In this work, the X-ray diffractometers consist of a X-ray source and a detector on opposite sides of the sample. The X-ray source is directed towards the sample, and the X-ray source and detector move in unison through a series of angles to detect where diffraction occurs. The sample is continually rotated through out measurement to account for anisotropy within the sample's crystal structure.

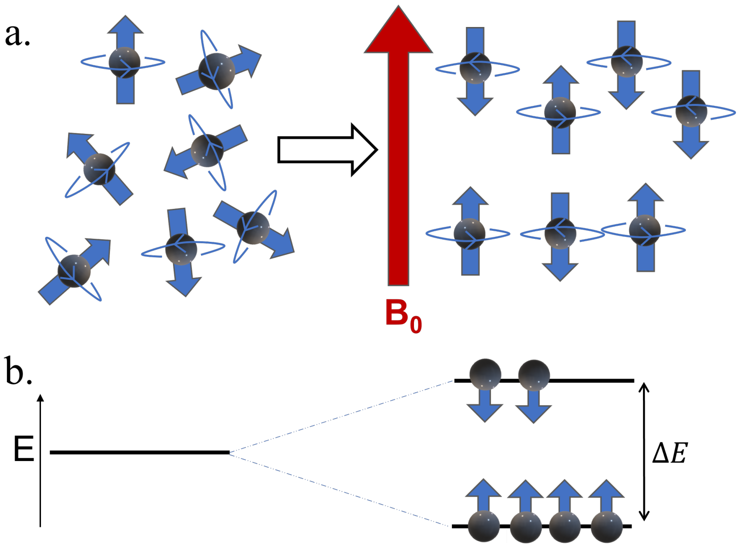

Figure 3.4: a). Orientation of magnetic moments of protons ($I = \frac{1}{2}$) with and without external applied field, B_0. b.) Energy levels associated with protons with and without B_0. Thick arrows represent the magnetic moment of each nucleus.

3.3 Precursor Characterisation

The main focus of this work has been to identify chemical processes within the perovskite precursor solutions and relate this to subsequent film and device properties. There are relatively few methods to examine these perovskite solutions, however we have thoroughly explored the following methods in order to identify aging processes. Nuclear magnetic resonance provided vital insights in Chapters 4 and 6. Various scattering techniques have been used to determine colloid sizes within perovskite precursor inks. The applications, limitations and procedures involved with small-angle neutron scattering, spin-echo small angle neutron scattering and dynamic light scattering are explored in Chapter 7.

3.3.1 Nuclear Magnetic Resonance

Some atoms have a non-zero intrinsic spin, I. This non-zero spin induces a small magnetic field around the nucleus, and the direction of this magnetic field can be described as the magnetic moment of the nuclei (shown in Figure 3.4). For simplicity, this section focuses on the ^1H isotope i.e. protons, but any non-zero spin nucleus containing multiple protons and neutrons will also have a magnetic moment. For an equilibrium state, the protons are randomly aligned as in Figure 3.4a. However, if an external magnetic field (B_0) is applied, spin-$\frac{1}{2}$ nuclei (such as ^1H) have 2 possible spin states they can occupy, as the magnetic field of the ^1H either aligns parallel or antiparallel to B_0. These two spin states have different energy levels - as aligning with B_0 requires less energy than aligning against B_0. Therefore, there is an overall excess of protons which align with B_0 in the low energy spin state.

Nuclear magnetic resonance uses this basic principle to probe the chemical composition of materials without disturbing or damaging them. In ^1H NMR, the sample is held in an applied external field, B_0, and then exposed to various radiofrequency (rf) waves. If an rf wave has an energy equal to the energy difference between these two spin states, the lower energy proton can “flip” states into the higher energy state. Over time, these protons will then precess back to their ”comfortable” alignment, and as they lose this energy, they will emit a photon equal to this energy.

Pulsed NMR is a commonly used experimental technique. The lifetime of this measurement is shown in Figure 3.5 but the underlying principle of this technique relies on one principle: if the magnetic moment of a molecule (or magnetization of a sample - $\mathbf{M}$) is tilted away from B_0, $\mathbf{M}$ will precess with Larmor precession frequency:

$$\nu_0 = -\frac{\gamma B_0}{2\pi} \tag{3.2}$$

where γ is gyromagnetic ratio of the sample and B_0 is a constant applied magnetic field.

In Pulsed NMR, a circularly polarised rf signal is absorbed by proton which “tilts” the magnetic moment (or magnetization $\mathbf{M}$) out of alignment with B_0. This is represented in Figure 3.5a as $\mathbf{M}$ “tilting” into the x-y plane. From here, we will define the z axis as being aligned with B_0. $\mathbf{M}$ will then precess with frequency ν_0. In order to visualise the effect this has on the system, we will now adjust our frame of reference to also rotate with ν_0 as in Figure 3.5b. If the absorbed rf wave is circularly polarised at frequency ν_0, there will be a short-lived magnetic field, B_1, acting down the x-axis in our rotating frame of reference (Figure 3.5b). This pulse therefore causes $\mathbf{M}$ to move out of the z-axis, towards the x-axis. However, once this pulse is over, $\mathbf{M}$ precesses and aligns with B_0 once more along the x-axis. Back in the stationary frame of reference (Figure 3.5a), we see this precession as it spirals around the z-axis with frequency ν_0. While this happens a rf radiation is emitted, which is known as the Free Induction Decay (FID). This emission is measured as in Figure 3.5c.

The relaxation of $\mathbf{M}$ is associated with two relaxation times: T_1 and T_2. T_1 is associated with spin-lattice relaxation and represents the release of energy into the surrounding material. T_2 represents the effect of the magnetic fields of other protons on each other, B_{loc}. This is the spin-spin relaxation time. Both of these decay times can be measured by T_2^* where

$$\frac{1}{T_2^*} = \frac{1}{T_1} + \frac{1}{T_2} + \gamma \Delta B_0 \tag{3.3}$$

Here ΔB_0 is the variation in B_0 over the experiment. This oscillating magnetization will cause an oscillating voltage in a detection coil which is measured as shown in Figure 3.5c. By studying the Fourier transform of this signal, the frequency at which nuclear magnetic resonance occurs can be determined and it is possible to identify the different molecules in the system.[127] T_1 can be separately measured using multiple pulses of rf waves alternating between 180° and 90° signals.

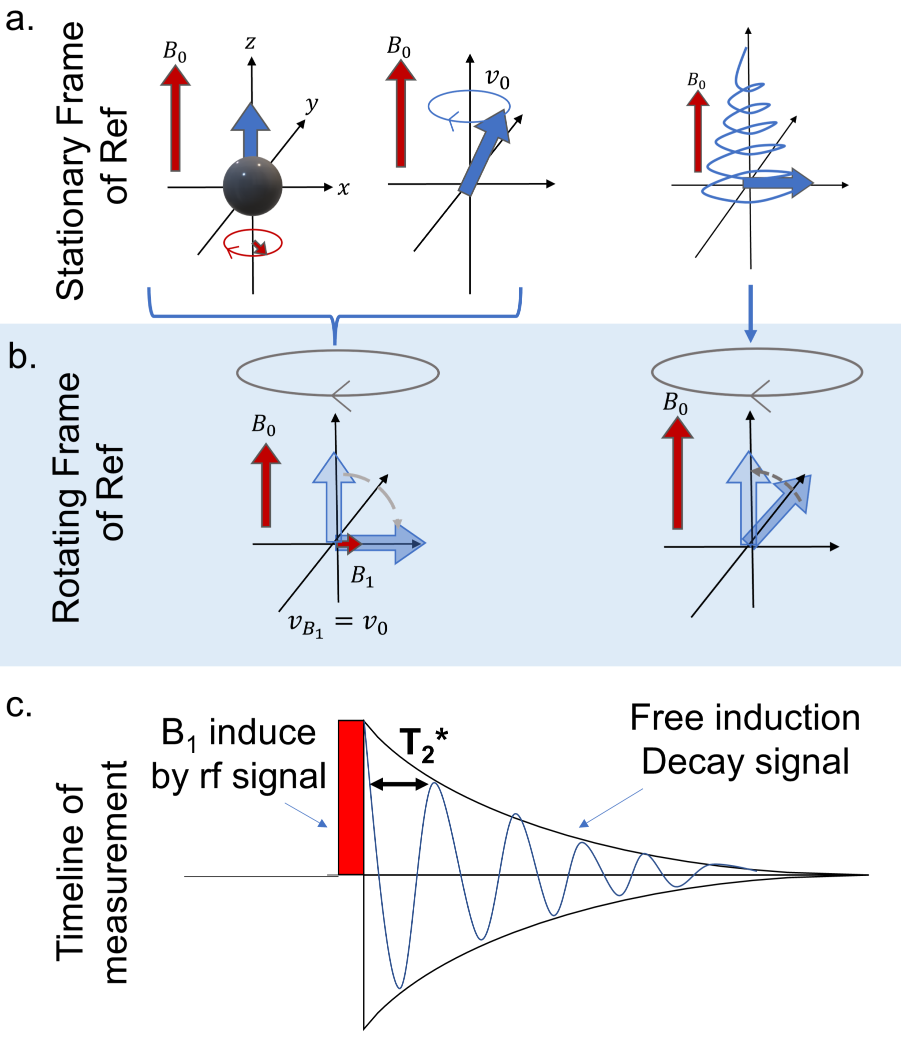

Figure 3.5: Measurement of free-induction decay in pulsed NMR in a stationary (a.) and rotating (b.) frame of reference. c.) Signal measured during Pulsed NMR.

The instrumental configuration of an NMR machine is depicted in Figure 3.6. This generally comprises of a bore hole in which the samples are placed (usually in a thin glass test tube), and this bore hole is surrounded by a radio frequency emitter, and some signal detection coils. Outside of this are superconducting magnets which generate B_0. These superconducting magnets function best in extremely cold environments so are cooled using liquid nitrogen and liquid helium jackets while also maintaining vacuum conditions.

Figure 3.7 shows examples of NMR spectra taken of a perovskite precursor solution. The x-axis of the graph is presented in chemical shift scale, which is measured in parts per million. Parts per million represents resonant frequencies as a fraction of the absolute resonance frequency, which varies with magnet strength. This means that these measurements are independent of magnet strength and can be compared with measurements from other NMR systems. All frequency measurements are made with respect to a reference peak.

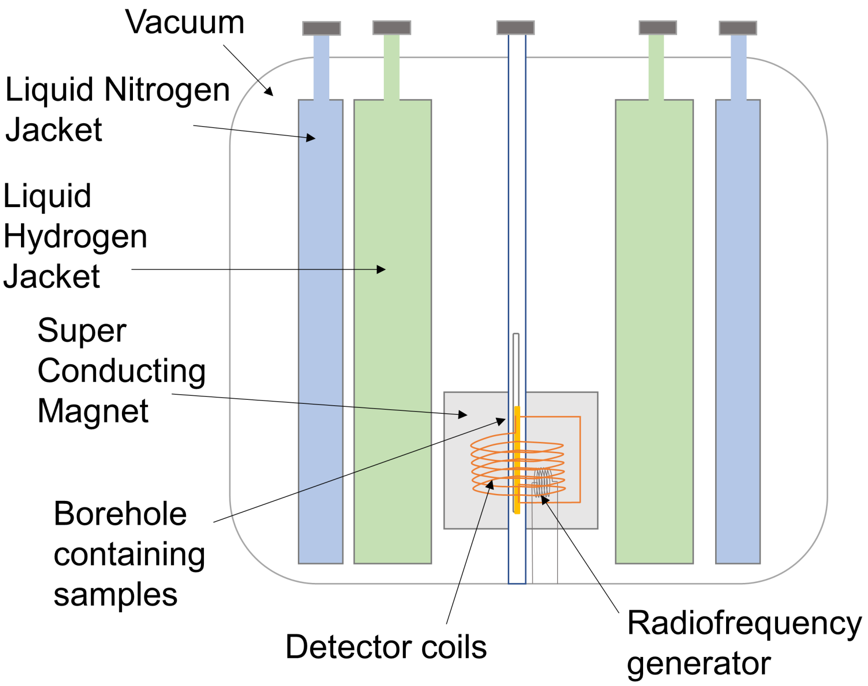

Figure 3.6: Diagram depicting NMR instrumental configuration. Adapted from [127]

In NMR analysis, the integrated area underneath each peak can provide information which helps to identify peak sources and also quantify the relative amounts of each molecule within a solution. For example, in Figure 3.7a (which is the ^{1}H NMR spectra of FAI in d_7-DMF/d_6-DMSO) the peaks at 9.0ppm and 8.1ppm are associated with the NH_2 group and the $C-H$ group of FA molecule $(CH(NH_2)_2)$ respectively. Therefore, their relative integrated ratios are 4:1, representing the 4 protons which contribute to the two NH_2 groups and the 1 proton which makes up of the $C-H$ group. These integrated ratios are measured using TopSpin software. In some of the spectra obtained, there are overlapping peaks as seen in Figure 3.7b. It is possible using TopSpin software to deconvolve these peaks from one another in order to measured their independent integrated areas. In this process, individual Gaussian peaks are fitted to each peak within a specific ppm range and the integrated areas calculated for each case. This is shown in the inset of Figure 3.7b. In order to gain insight into the absolute concentrations of each molecule in solution, an isolated, internal standard of known concentration can be used. By calculating the molarity of this standard, absolute concentrations of the various other molecules can be calibrated during post processing. In both spectra in Figure 3.7, an internal standard is seen at 8.44ppm. By defining the integrated area under this peak as the known concentration of the standard, the absolution concentrations of all molecules can be calculated as is done in Chapter 4 and 6.

One useful characteristic of NMR is that deuterium and hydrogen behave quite similarly chemically. However they have a different intrinsic spin. By replacing all the hydrogen atoms in the solvent molecules with deuterium, i.e. using a deuterated solvent, we can basically remove the solvent signals. Throughout this work, deuterated solvents are used

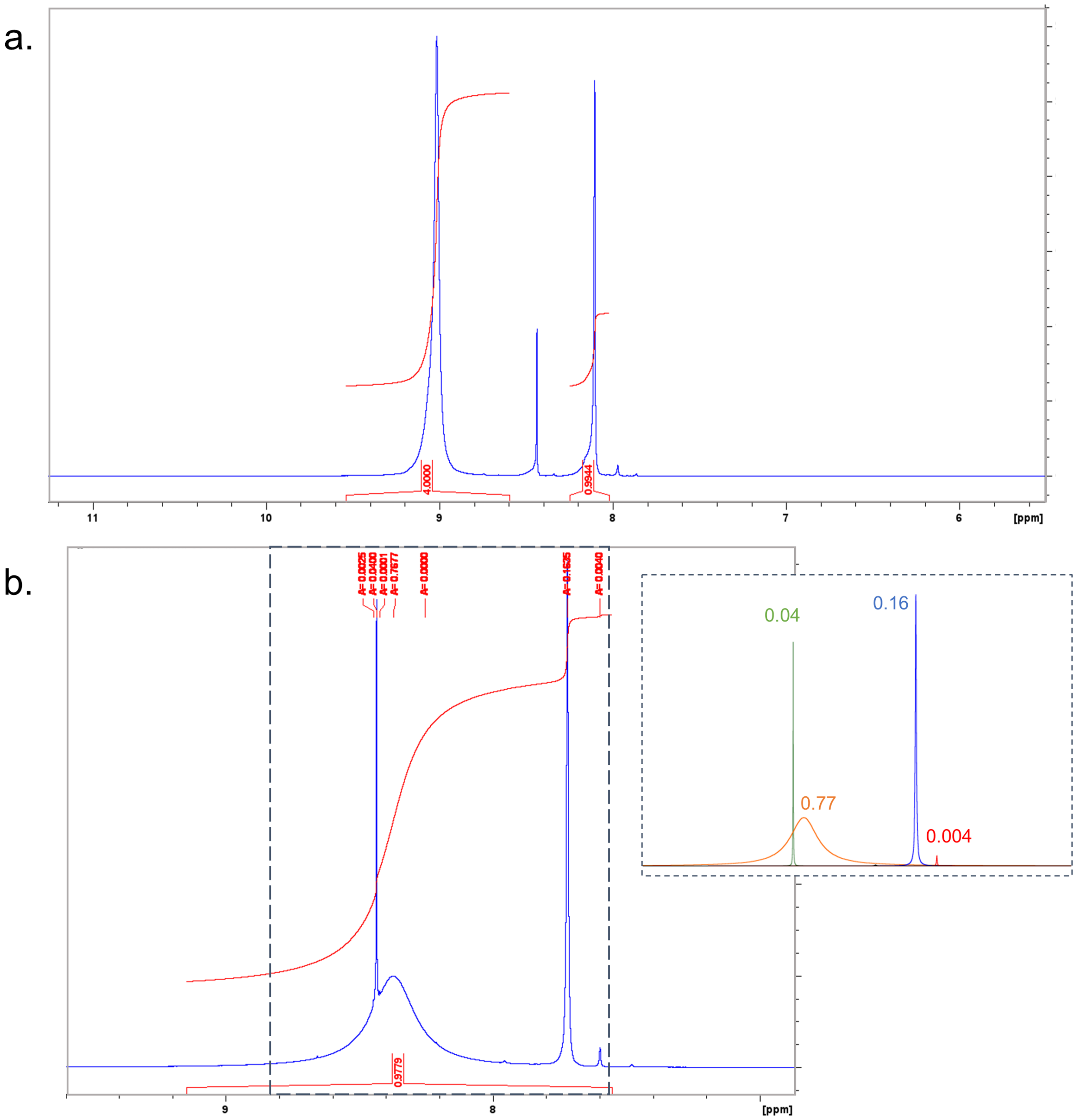

Figure 3.7: a.) ^1H NMR spectrum of FAI precursors in d_7-DMF/d_6-DMSO (4:1) after 7 days aging. b.)^1H NMR spectrum of TC precursors in d_7-DMF/d_6-DMSO (4:1) after 7 days aging. Inset shows deconvoluted fits to indivual peaks, and their respective integrated ratios.

for NMR measurements unless stated otherwise. We also note that the exact chemical shift of any proton environment is highly dependent on its surroundings. This chemical shift can vary due to the due to concentration, pH or altered solvent co-ordination. In this work we found that exact peak locations vary depending on the solvent used. It is very important that peaks are identified through relative peak placement to one another and their integrated ratios, as well as their chemical shift.

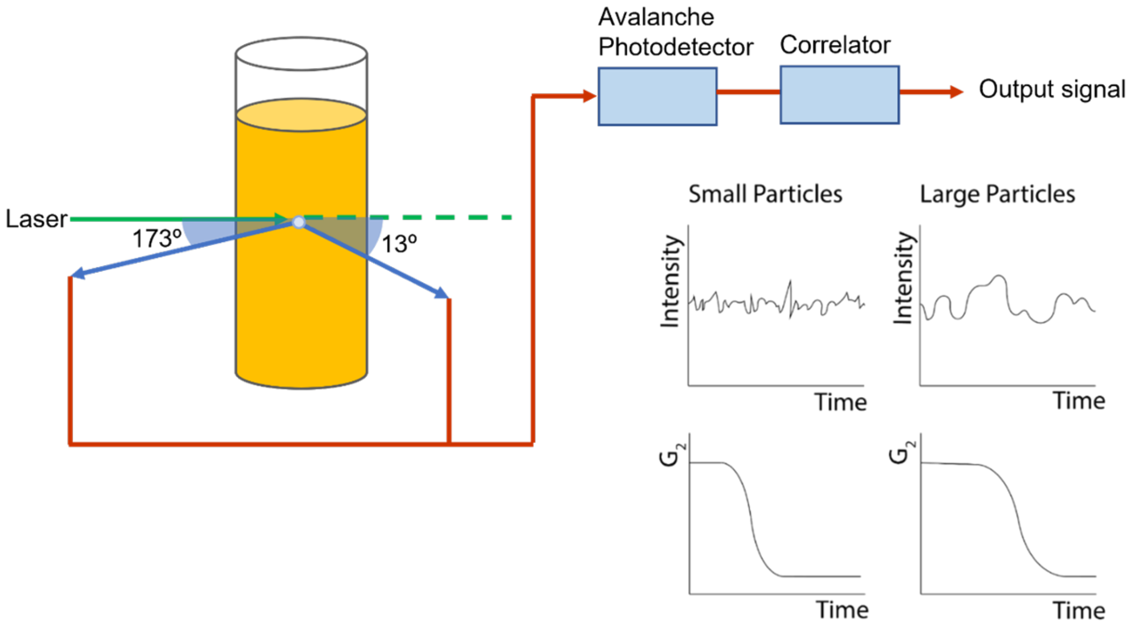

Figure 3.8: Schematic depicting dynamic light scattering from a Zetasizer Nano ZS DLS machine, adapted from [130]

3.3.2 Dynamic Light Scattering

Dynamic light scattering (DLS) is a technique used to determine the hydrodynamic radius of colloids within solution. For the DLS conducted in this work, a laser was directed into the chosen colloidal suspension and the intensity of the scattered light is detected at a set angle as shown in Figure 3.8. At the detector, the detected light will form a pattern of constructive and destructive interference as the light has been randomly scattered off colloids in the dispersion. This interference pattern changes as the particles move due to Brownian motion. The rate of change of these patterns depends on the size of the colloids. Larger particles move more slowly through diffusion. [128, 129] This diffusion rate will also depend on the viscosity and temperature of the solvent used. DLS measures these fluctuations in the interference pattern over time as shown schematically in Figure 3.8. The output of the measurement is an autocorrelation function showing the fluctuation of intensity over time. This is known as G_2 [130]. G_2 is related to the electric field autocorrelation function G_1 which measures the averages motion of particles relative to one another.

G_2 is given by:

$$G_2(\tau) = B + \beta|G_1(\tau)|^2 \tag{3.4}$$

where B is a baseline constant, τ is the lag time between time (t) and (t+ τ) and β is factor associated with the measuring equipment. For a polydisperse system, G_1 can be written as:

$$G_1 = \int_0^{\text{inf}} G(\Gamma)e^{-\Gamma_\tau dt} \tag{3.5}$$

Where

$$\Gamma = -D_\tau q^2 \tag{3.6}$$

Here, Γ is a decay constant that is directly related to the diffusion constant, D_τ, of the colloids in a dispersion over time increment τ. The scattering vector, q, incorporates the information about the refractive index of the solvent[128]).

The hydrodynamic radius R_h of a molecule can be determined through the Stokes-Einstein equation if the diffusion coefficient is known:

$$D_\tau = \frac{k_B T}{6\pi\eta R_h} \tag{3.7}$$

Here T is measurement temperature in Kelvin, k_B is the Boltzmann constant and η is the viscosity of the solvent. Through Equation 3.4-3.7, a series of exponential decays can be fitted to G_2 for each particle population and R_h can be determined for each exponential fit. As can be seen in Figure 3.8, the exponential decay time will be longer for larger colloids [129] Additionally, the more extended the decay appears, the greater the polydispersity of the colloids in the dispersion.

Volume vs. Intensity

Another way of presenting G_2 is as follows:

$$G_2(\tau) = \frac{\langle I(t)I(t+\tau)\rangle}{\langle I(t)\rangle^2} \tag{3.8}$$

where $I(t)$ and $I(t+\tau)$ are the intensities at t and t+τ respectively. Here, we see that the data extracted from DLS is a ratio of scattered intensities, therefore the results from DLS measurements are often presented as Intensity %. In simple terms, this can be interpreted as the percentage of detected light that was scattered from a particle of a certain size. For particles much smaller than the lasers wavelength (d< $\frac{\gamma}{10}$), light is scattered uniformly according to Rayleigh scattering theory. However, for particles comparable in size to γ the scattering can be described by Mie scattering theory, which depends on the refractive index of the scattering colloid and solvent, as well as the shape of the colloid, resulting in a pronounced angular dependence to the scattering [128]. Niskanen et al. demonstrated in 2019 that hydrodynamic radius of polystyrene nanospheres were obtained using both Rayleigh approximation and Mie theory up to a radius of 200nm.[131] Only Mie theory could accurately predict the size of colloids larger than 200nm. The intensity of Rayleigh scattering (I) is proportional to the square of the volume of the colloid and thus to its radius (r) using

$$I \propto r^6 \tag{3.9}$$

This means that a particle with r = 50 nm will scatter with a million times the intensity of a particle with a radius of r = 5 nm. This can be an issue when studying multimodal particle dispersions, as the scattering from a few larger particles will dominate the signal compared to smaller particles which may be the majority population. Mie theory can be used to convert data from this intensity-weighted domain into either a number-weighted or, as here, a volume-weighted domain. [132, 133] For a solution containing N_a particles of size a, and N_b particles of size b, the magnitude of the intensity peak at size a is evaluated using:

$$\%I_a = 100 \times \frac{a^6 N_a}{a^6 N_a + b^6 N_b} \tag{3.10}$$

Using the Rayleigh approximation, in which mass is proportional to r^3, the volume percentage of colloid is

$$\%V_a = 100 \times \frac{a^3 N_a}{a^3 N_a + b^3 N_b} \tag{3.11}$$

Therefore by using volume % data, the relative signal varies with particle size exponentially with a factor of 3, compared to a factor of 6 for intensity weighted data. In this work, spherical geometry is assumed for the conversion from intensity to volume. Dynamic light scattering is used extensively in Chapter 7 and differences in intensity vs. volume weighted distributions are fully explored with relation to perovskite precursor solutions.

3.3.3 Neutron Scattering

Small-Angle Neutron Scattering

In order to understand the movement of neutrons through a sample, we will consider them as steady stream of particles moving with wavelength λ in the x direction as

$$\Psi = \Psi_0 e^{ikx} \tag{3.12}$$

Where $k = 2\pi/\lambda$, $\Psi_0 = \sqrt{\Phi}$ and Φ is incident flux from the neutron beam. If a neutron interacts with a fixed atom and we consider the position of this fixed atom to be the “origin” point. This neutron will scatter radially outwards with waveform

$$\Psi = \Psi_0 f(\lambda, \theta) \frac{e^{ikr}}{r} \tag{3.13}$$

where r is the radial distance from the origin scattering point, Ψ_0 is the waveform of the incident beam and $f(\lambda, \theta)$ is a function which describes the likelihood of a particle with wavelength λ being scattered at angle θ. [134, 135] For a single scattering event this is independent of θ or λ, only to scattering length, b.

Small-Angle Neutron Scattering (SANS) is a technique which is used in this work to probe the size, shape, distribution and number of scattering entities within a liquid samples. In a SANS experiment, a collimated beam of neutrons with initial wave vector ($\overrightarrow{k_i}$) is directed towards a sample and neutrons are scattered from atomic nuclei with wave vector $\overrightarrow{k_f}$ using angle 2θ (see Figure 3.9). The incident angle of these scattered neutrons is measured by a 2D detector, positioned at a large distance from the sample. Typically, this 2D scattering pattern is radially integrated to generate a 1D intensity profile as a function of the scattering vector, $\overrightarrow{q}$. In order to define some important scattering parameters,

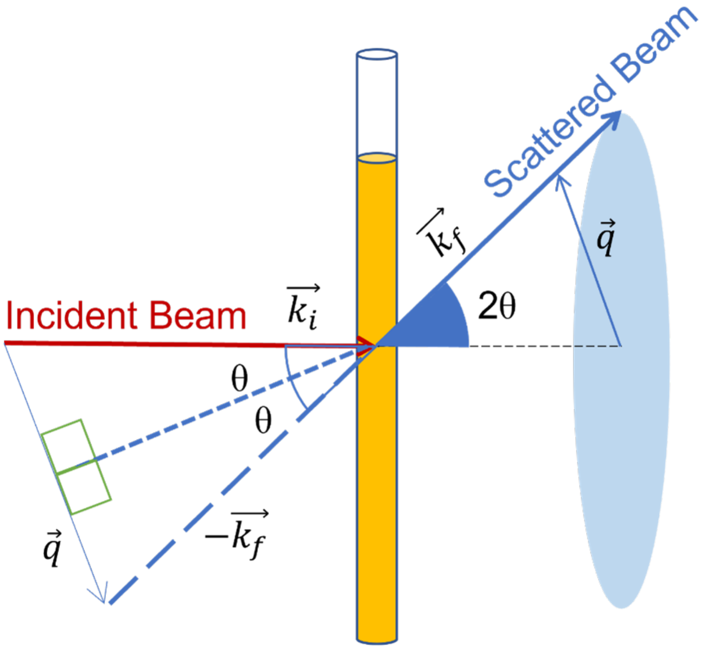

Figure 3.9: An illustration of the typical transmission geometry used for SANS measurements.

we will first consider a single scattering event as in Figure 3.9. At this point we define a scattering vector, $\overrightarrow{q}$ as the difference between wave vectors of the incident and scattered neutrons

$$\overrightarrow{q} = \overrightarrow{k_i} - \overrightarrow{k_f} \tag{3.14}$$

Assuming elastic scattering (i.e. no energy is lost during the collision), the magnitude of the incident wave vector is equivalent to the magnitude of the scattered wave vector. This scattering vector can also be expressed in terms of neutron wavelength, λ, which is calculated from the de Broglie equation ($\lambda = \frac{h}{m_n v}$ where h is Planck's constant, m_n is the mass of the neutron and v is the velocity of the neutron). Therefore we can express this using

$$|\overrightarrow{k_i}| = |\overrightarrow{k_f}| = k = \frac{2\pi}{\lambda} \tag{3.15}$$

As shown in Figure 3.9, we can also define q as

$$q = 2k \sin\theta \tag{3.16}$$

By using equations 3.16 and 3.15, we can define the magnitude of the scattering vector as:

$$q = \frac{4\pi \sin\theta}{\lambda} \tag{3.17}$$

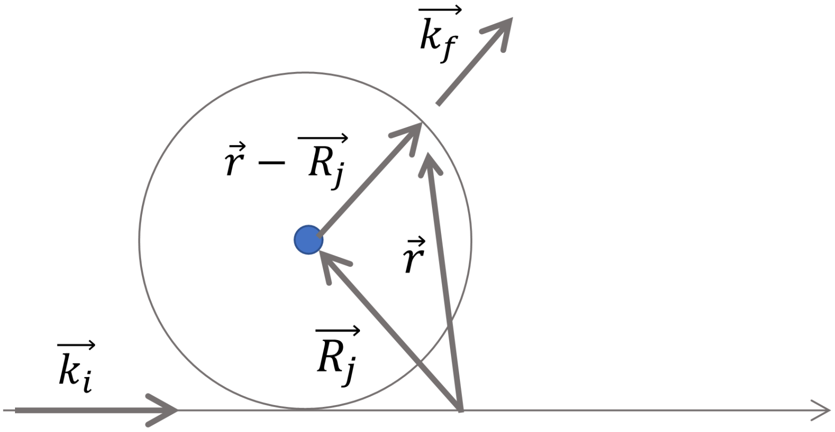

Figure 3.10: Schematic of scattering event which occurs away from the origin at position R_j. Adapted from [134]

The measurable q-range in a SANS experiment is dependent on the wavelength of the neutrons used and the distance L between the detector and the sample. Placing the detector far away from the sample allows small angles to be probed, corresponding to low-q values. Scattering at low-q arises from large length scales, d, according to the reciprocal relationship between real-space and q-space:

$$q = \frac{2\pi}{d} \tag{3.18}$$

We will now consider a scattering event happening at a position, $\overrightarrow{R_j}$, away from the origin point as shown in Figure 3.10. This scattering event will make a contribution to the overall scattered wave of:

$$[\delta\psi_f]_j = \psi_0 e^{i\overrightarrow{k_i}\cdot\overrightarrow{R_j})} f_j \frac{e^{i\overrightarrow{k_f}\cdot(\overrightarrow{r}-\overrightarrow{R_j})}}{|\overrightarrow{r}-\overrightarrow{R_j}|} \tag{3.19}$$

Here f_j represents the interaction characteristics of atom j with a neutron. Within this equation we can see that if $\overrightarrow{R_j} = 0$, this equation simplifies back into 3.13. Equation 3.19 provides a framework which allows the summation of many collision events to contribute to the overall waveform detected

$$\Psi_f = \psi_0 e^{i\overrightarrow{k_f}\cdot\overrightarrow{r}} \sum_{j=1}^{N} f_j(\lambda,\theta) \frac{e^{i\overrightarrow{q}\cdot\overrightarrow{R_j}}}{|\overrightarrow{r}-\overrightarrow{R_j}|} \tag{3.20}$$

where $\overrightarrow{q}$ is defined in Equation 3.14. This summation assumes that the scattering which occurs within the sample is weak.[134] Additionally, if the distance between nuclei is much less than the distance between the sample and the detector, we can assume $|\overrightarrow{r}-\overrightarrow{R_j}| \sim r$.

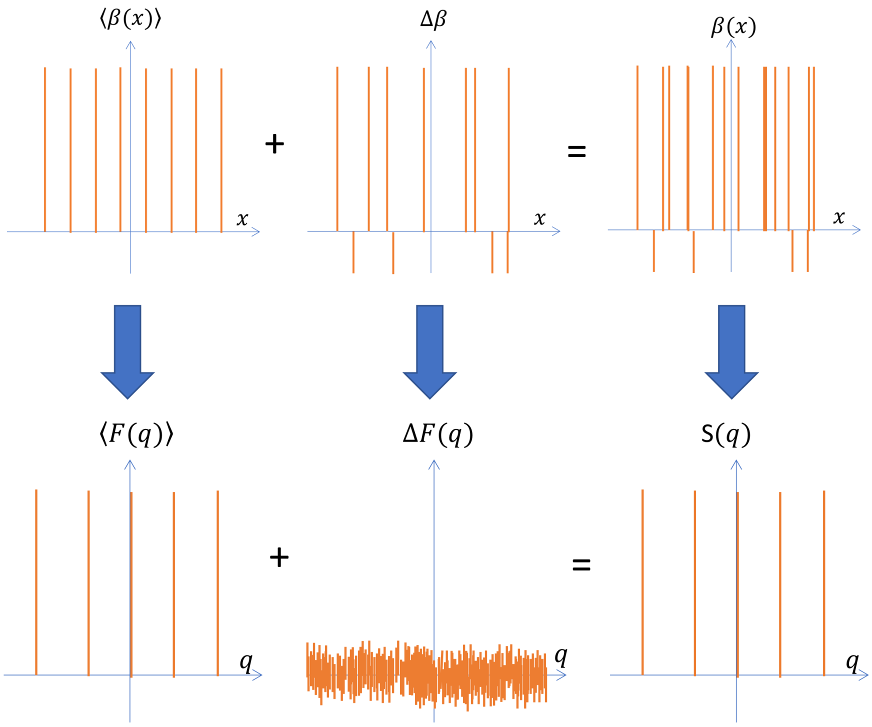

Figure 3.11: SLD variation due to coherent and incoherent scattering in real space (x) and the Fourier transform of this signal. Adapted from [134].

We will use this waveform to define the scattering cross section σ. Physically, σ represents the amount of scattered neutrons which will pass through area dA (the scattering rate, SR) relative to the incident flux of neutrons, Φ (i.e. $\sigma \propto \frac{SR}{\Phi}$). The SR of neutrons at a particular λ and θ can be defined using the square product of Equation 3.13

$$\sigma \propto |\Psi_f|^2 = \Psi_f \Psi_f^* = \frac{\Phi}{r^2}|f(\lambda, \theta)|^2 \tag{3.21}$$

where $\Phi = |\psi_0|^2$. In earlier discussions of f, we assumed the atom causing the scattering is point-like. In reality f is determined by the size and shape of the object which scatters the neutron. It is also known that in neutron scattering, f does not depend on θ or λ. [134] This can be accounted for using a scattering length density (SLD) function, $\beta(x, y, z)$ instead of the simplified scattering length b. The SLD fuction $\beta(\overrightarrow{R})$ can be broken down into coherent and incoherent parts. These are defined as the average and standard deviation of the scattering lengths ($\langle\beta\rangle$ and $\Delta\beta$ respectively)

$$\beta(\overrightarrow{R}) = \langle\beta(\overrightarrow{R})\rangle \pm \Delta\beta(\overrightarrow{R}) \tag{3.22}$$

$\langle\beta(\overrightarrow{R})\rangle$ corresponds to the repeating structures within the wave which result in a tangible pattern, while $\Delta\beta(\overrightarrow{R})$ are random fluctuations. Repeating and random fluctuation in real space can be seen in Figure 3.11 for coherent and incoherent scattering components respectively. However, when these two components are combined it is difficult to discern one from the other. If the Fourier transforms of these signals are studied (shown in q space in Figure 3.11) we see that only the repeating patterns emerge and the contributions from incoherent scattering appear as white noise. In most cases, the coherent scattering contains the desired information (length scales, etc) about a sample, so often incoherent scattering is removed as background. By integrating Equation 3.21 over all angles within an area dA $(= r^2 sin2\theta d\phi d2\theta)$ and including SLD function $\langle\beta\rangle$, we can define the measured intensity as

$$\frac{d\sigma}{d\Omega} \propto I_{el}(\overrightarrow{q})_{coh} \propto \left| \iiint_V \langle \beta(\overrightarrow{R}) \rangle e^{i\overrightarrow{q}\cdot\overrightarrow{R}} d^3R \right|^2 \tag{3.23}$$

where $d\Omega = \frac{dA}{r^2}$ is the solid angle of the detector.

Most systems or molecules consist of numerous atoms. Therefore, within neutron scattering the SLD within a system containing K types of atoms can be represented as:

$$\beta = \frac{\Sigma_{i=1}^{K} \langle b_i \rangle}{V_m} \tag{3.24}$$

where $\langle b_i \rangle$ is the coherent scattering length of atom j and V_m is molecular volume.

For a single solute material dissolved in a solvent, we can consider two different SLDs; the SLD of the solvent, β_0, and the SLD of the solute β_1. If the difference between these two SLDs (i.e. the neutron SLD contrast or $\Delta(SLD)$) is great enough, the colloids within solution can be measured separately from the solvent whilst remaining in solution. One great advantage of neutron scattering techniques is that SLD does not vary linearly across the periodic table as is the case for X-ray scattering lengths. For example hydrogen and deuterium have significantly different neutron SLDs despite exhibiting very similar behaviour. This means that by using deuterated material, ΔSLDs can be increased without impacting chemical properties such as solubility. Having sufficient ΔSLD is vital when measuring colloids in solution.

The intensity profiles of different materials will vary massively depending on size and shape of the "colloids" in solution and will also be influenced by how the colloids interact with each other. These are often shown in the Form and Structure factors of the intensity profiles respectively. Intensity profiles can also be affected by volume % and $\Delta(SLD)$ of the solution. There are many different models which will each predict the intensity profiles that specific colloids exhibit in solution. For example, $\frac{d\sigma}{d\Omega}$ for particles of spherical and cylindrical shape with equal volume and ΔSLD are shown in Table 3.1. Therefore, it is clear that in order to extract physical properties about a system, it is important that the correct model is used to fit the data.

There are several advantages with using neutron scattering to study perovskite solutions compared to conventional small angle X-ray scattering (SAXS) methods. SAXS experiments on perovskite solutions often suffer from low transmission rates as the solutions are very concentrated and Pb has a large scattering cross-section due to its high electron density. SANS overcomes this due to the highly penetrative, weakly interacting nature of neutrons. In contrast to SAXS, which relies on the electromagnetic interaction between the incident

Shape	Differential cross section
Spherical	$\left[V_P\|\beta_1-\beta_0\|\frac{3j_1(qR)}{qR}\right]^2$
Thin Rod	$V_P^2\|\beta_1-\beta_0\|^2\left[\frac{2}{qL}\int_0^{qL}\frac{\sin x}{x}dx-{\frac{4\sin^2(qL)}{qL}}^2\right]$

Table 3.1: Differential cross sections showing q dependence on shape for isotropically distributed particles. R denotes spherical radius, L is length of cylinder, $V_P = 4\pi R^3/3$. [134]

X-ray, and differences in electron density of the sample, neutrons are an uncharged probe so only interact with nuclei within the sample. The significance of ΔSLD in neutron scattering was of great advantage in Chapter 7 for measuring particles in solvents. The SLD of hydrogen and deuterium atoms are $\langle\beta_H\rangle = -0.374^{-14}$m and $\langle\beta_{De}\rangle = 0.403 \times 10^{-14}$m respectively. As mentioned previously, this difference in SLD can be used used to increase ΔSLD between the solvent and the solute in a solution without affecting the solution chemistry of the sample. For example, the SLD of DMF is $0.964\times10^{-6}/\text{Å}^2$, but the SLD of deuterated DMF is $6.33\times10^{-6}/\text{Å}^2$.[134] When examining $MAPbI_3$ perovskite, which has an SLD of $\sim0.75\times10^{-6}/\text{Å}^2$, using d_7-DMF as a solvent instead of DMF increases the ΔSLD significantly ($\Delta SLD_{DMF} = 0.964 - 0.75 = 0.214$, $\Delta SLD_{d_7-DMF} = 6.33 - 0.75 = 5.58$). Increasing this contrast increases the signal measured and facilitates the measurement of solute seperately from solvent as in Chapter 7

Spin-Echo SANS

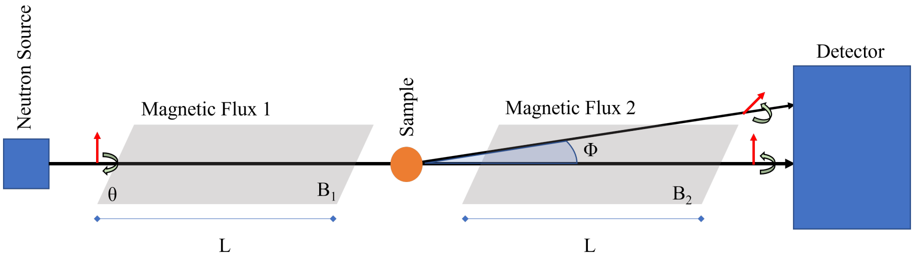

Figure 3.12: A schematic depicting the basic structure of how a SESANS instrument works. [136]

In a Spin-Echo Spin-Angle Neutron Scattering (SESANS) instrument, the scattering angle is encoded using intrinsic neutron spin. As discussed earlier, this is similar to NMR where ^1H nuclear can be measured by exploiting the spin-$\frac{1}{2}$ property of the ^1H nuclei and using Larmor precession in magnetic fields. As neutrons are also spin-$\frac{1}{2}$ particles, we can measure the scattering angle by the use of carefully shaped magnetic fields. The key here is the fact that any accumulated precession is proportional to the strength of the magnetic field and the path traversed by the neutron through the field. In a simplified view we consider the magnetic field arrangement in Figure 3.12 with the field strength in B_2 to be equal and opposite to that in B_1. Here, it can be see that for any unscattered neutron, the field integral comes to zero. However, if the neutron is scattered then the field integral in B_1 is not cancelled out by B_2 and will not come back to the original polarisation (P_0).

Measuring the polarisation of scattered neutrons P_S compared to the polarisation of the unscattered beam P_0 allows for the correction of instrumental effects. The spin-echo lengths that can be probed using this method are determined using the following equation:

$$z = cBL\lambda^2 \cot\theta \tag{3.25}$$

where c is a constant, L is the separation between magnets, θ is the inclination of the magnets, B is magnetic field strength and λ is neutron wavelength[137]. Hence, with a combination of these parameters, we can measure the size of scattering particles in a size range up to 20μm.

The polarisation ($P(z) = \frac{P_s(z)}{P_0(z}$) of the neutrons as a function of the spin-echo length, z is what is measured and is given by;

$$P(z) = e^{\Sigma t[G(z)-1]} \tag{3.26}$$

Where Σ_t is is the fraction of neutrons that are scattered once by a sample of thickness t and G(z) is the projection of the autocorrelation of the density distribution function of the sample[138]. For dilute spheres of radius R (volume fraction (Φ) $\leq$5%) this quantity Σ_t is given by;

$$\Sigma_t = \frac{3}{2}Rt\Phi(1-\Phi)(\rho_a - \rho_b)^2\lambda^2. \tag{3.27}$$

Chapter 4

Perovskites On Ice: An Additive-Free Approach to Increase the Shelf Life of Triple-Cation Perovskite Precursor Solutions

Mary E. O'Kane, Joel A. Smith, Tarek I. Alanazi, Elena J. Cassella, Dr. Onkar Game, Dr. Sandra van Meurs, Prof. David G. Lidzey

ChemSusChem
Chemistry–Sustainability–Energy–Materials
Chemistry Europe
European Chemical Societies Publishing

Volume 14, Issue 12
19th April 2021
DOI: 10.1002/cssc.202100332

4.1 Paper Foreword

The importance of understanding solution chemistry of PSC precursors inks was discussed in Chapter 2 and at the time of publication, a few studies had been conducted to examine the long-term storage of triple cation perovskite precursor inks. It had been shown that they had limited shelf-life in ambient and inert conditions. Some studies had found this lifetime could be prolonged with the use of additives, but we set out to extend this ink lifetime without altering the composition of solutes within solution. We also aimed to explore the role of solvent co-ordination in this aging process. In this chapter, we present a paper published in 2021, which demonstrated that low-temperature storage of triple cation precursors inks could increase usable ink lifetime in triple cation perovskite precursor solutions.

4.2 Author Contributions

MOK coordinated the project, created all samples and PSC devices, and performed the absorbance, SEM and AFM measurements and all data analysis, with help from authors where needed. JAS assisted with the co-ordination of the project and contributed to the analysis and discussion and manuscript considerably. SVM took the NMR measurements and assisted with planning, plotting and analysis of all NMR data. EJC created Scheme 1 and helped identify the chemical reactions therein. TIA performed the XRD measurements and assisted in XRD peak identification. DGL proposed of and supervised the project. My sincerest thanks goes to all contributing authors.

4.3 Main Paper Body

4.3.1 Abstract

The development of stable perovskite precursor solutions is critical if solution-processable perovskite solar cells (PSCs) are to be practically manufacturable. Ideally, such precursors should combine high solution stability without using chemical additives that might compromise PSC performance. Here, we show that the shelf-life of high-performing perovskite precursors can be greatly improved by storing solutions at low-temperature without the need to alter chemical composition. We find that devices fabricated from solutions stored for 31-days storage at 4°C achieve a champion PCE of 18.6% (97% of original PCE). The choice of precursor solvent also impacts solution shelf-life, with DMSO-based solutions having enhanced solution stability compared to those including DMF. We explore the compositions of aged precursors using NMR spectroscopy and analyse films made from these solutions using X-ray diffraction. We conclude that the improvement in precursor solution stability is directly linked to the suppression of an addition-elimination reaction and the preservation of higher amounts of methylammonium within solution.

4.3.2 Introduction

Over the past 10 years, metal-halide perovskite solar cells (PSC) have achieved impressive single-junction power conversion efficiencies (PCEs) of up to 25.5% and 29.5% in tandem architectures with silicon.[7] These perovskites have the general composition ABX_3, where A is a monovalent cation (typically formamidinium ($CH_3NH_2^+, FA^+$), methylammonium

($CH_3NH_3^+, MA^+$) or caesium, Cs^+), B is a divalent metal (such as Pb^{2+} or Sn^{2+}) and X is a halide anion (I^-, Br^- or Cl^-). A significant advantage of this material family is that changes to composition can be used to modify material properties.[40, 46, 49, 139, 140] For example, the pure formamidinium-based perovskite $FAPbI_3$ can exist as a black photo-active alpha-phase, but is metastable at room temperature and will convert to a photo-inactive delta-phase. However, by replacing some fraction of FA with small amounts of Caesium (Cs^+) and methylammonium (MA^+), it is possible to stabilize the black perovskite phase at room temperature.[17, 19, 46, 141] Therefore, FA-rich, triple-cation (TC), mixed-halide perovskites compositions have become a popular choice in the research community.

As both the efficiency and operational stability of PSCs has increased, many researchers increasingly look towards the manufacturing requirements of PSCs using roll-to-roll processing. Here, solution-based manufacture is an attractive prospect as it potentially allows PSCs to be produced using low-cost and high-throughput techniques. Unfortunately, it has been shown that perovskite precursor solutions are often subject to poor long-term storage stability[66, 98, 99, 111, 112, 115] (although short-term aging can improve the performance of resultant PSC devices).[98, 107, 108] This instability presents a significant problem for any practical manufacturing as this will impact on the cost of the process. Indeed, in order to be commercially competitive with vacuum (solvent-free) deposition techniques, solution-processing methods need to demonstrate a similar level of process control, despite the additional chemical challenges. To control solution stability, it is clear that understanding the interplay between the various organo-halides, metal halides and solvents in perovskite precursor solutions is essential.

Certain studies on mixed-cation PSCs have suggested that the poor performance of devices from "aged" solutions result from the degradation of the casting solvents – particularly dimethylformamide (DMF).[142] Indeed, it has been shown that that DMF can hydrolyse into dimethylamine (DMA) and formic acid, especially when accelerated by the presence of lead halides or at high temperature.[92, 111] The DMA formed can then be protonated by formic acid or another Brønsted acid in solution to form dimethylammonium, [DMA^+ or $(CH_3)_2NH_2^+$][92, 143] which can then be incorporated into the perovskite crystal lattice.[111, 142, 144] Similarly, mechanisms have been proposed for DMA^+ formation in $MAPbI_3$ solutions based on the other most commonly used aprotic solvent dimethyl sulfoxide (DMSO). [145]

A different mechanism has however been proposed by Wang et al. [99] to describe the degradation of $MA_{0.5}FA_{0.5}PbI_3$ solutions. Here, it was suggested that the emergence of a non-perovskite δ-phase in films prepared from aged solutions occurred as a result of a series of addition-elimination reactions. In brief, it was proposed that methylammonium is deprotonated to methylamine (CH_3NH_2), which can react with FAI to form the condensation product N-methyl formamidinium iodide (MFAI) and, in a secondary process, N,N-dimethyl-FAI (DMFAI), with both reactions releasing NH_3. Following this, we summarise both degradation pathways in Figure 4.1. In either case, any excess of large organic cations (MFA^+, $DMFA^+$, DMA^+) in the perovskite is expected to modify the Goldschmidt tolerance factor of the perovskite, forcing the material to adopt a non-photoactive phase. For large cations, these $APbI_3$ phases are generally similar to the aforementioned $\delta - FAPbI_3$ (2H polytype) phase, comprising “1D” continuous chains of face-sharing lead-iodide octahedra.[13, 20, 140, 146] The formation of such cationic species in degraded precursor solutions therefore represents an important process that is expected to prevent the crystallisation of the precursor into a light-absorbing perovskite phase.

A number of studies have explored various methods to reduce such solution-aging effects. Kim et al. studied the evolution of $FAPbI_3$ perovskite solutions and proposed that the addition of tri-iodide species can improve the quality of films prepared from aged precursors.[147] Qin et al. have explored the effect of stabilisers on precursor solutions [112], and showed that the addition of the small molecule ITIC-Th to FA-MA-based solutions can improve solution stability. Wang et al. [99] also found that solution-aging effects could be controlled through the addition of the stabiliser triethyl borate (TEB) by withdrawing electrons from I^- , thereby inhibiting the MA deprotonation reaction. Additionally, Shin et al. showed that $FAPbI_3$ solutions made from precursor powders are less stable than those made from $FAPbI_3$ single crystals using the same solvents, [92, 115] with Dou et al. demonstrating that solution decomposition can be prevented by instead storing in their precursor state as ball-milled perovskite powders.[111]

Although PSC precursor stabilisers have been identified, it has been shown that even unintentional variations of stoichiometry can dramatically affect device performance.[55] In order to fabricate the highest performing perovskite materials, it is necessary to maintain tight control over the stoichiometry of the precursor solution. Here, the addition of compounds to enhance precursor stability will affect their solution chemistry, and therefore could inadvertently affect perovskite nucleation or charge transport properties within the resultant perovskite films. This in turn may limit device performance or long-term operational stability. For this reason, the development of methods to enhance solution stability without recourse to molecular stabilisers is seen as a key part of any efficient manufacture process.

In this work, we have examined the effect of long-term storage on TC perovskite precursor solutions, and using an additive-free method, have found a way to significantly increase their solution shelf-life. By studying device performance, the structure of perovskite films fabricated from aged solutions and by directly characterising precursor solutions using nuclear magnetic resonance (NMR) spectroscopy, we identify the formation of both MFA and DMFA in aged perovskite precursors. We show that this reaction results in a significant loss of MA and leads to the formation of non-perovskite polytypes when such solutions are cast into thin films. We then show that by storing solutions at low temperature, their stability can be significantly enhanced without the necessity to alter solution chemistry. Specifically, we find that devices fabricated using a typical TC precursor solution stored for 1 month at approximately 4 °C achieve a champion efficiency of 18.6% with a power output of 18.4% recorded over 1 min. After 2 months storage at approximately 4°C, such precursor solutions used for PSC devices have >97% of the champion device performance of freshly prepared solutions and >85% of this reference device efficiency after 4 months solution storage. Our results also indicate that DMSO-based precursor solutions are more stable than those made from a DMF/DMSO solvent mixture. Indeed, by using a DMSO-based precursor, we have fabricated devices using solutions that have been cold-stored for 4 months, with devices demonstrating a 1 min stabilised PCE of 16.4%; an efficiency equivalent to 92% of devices

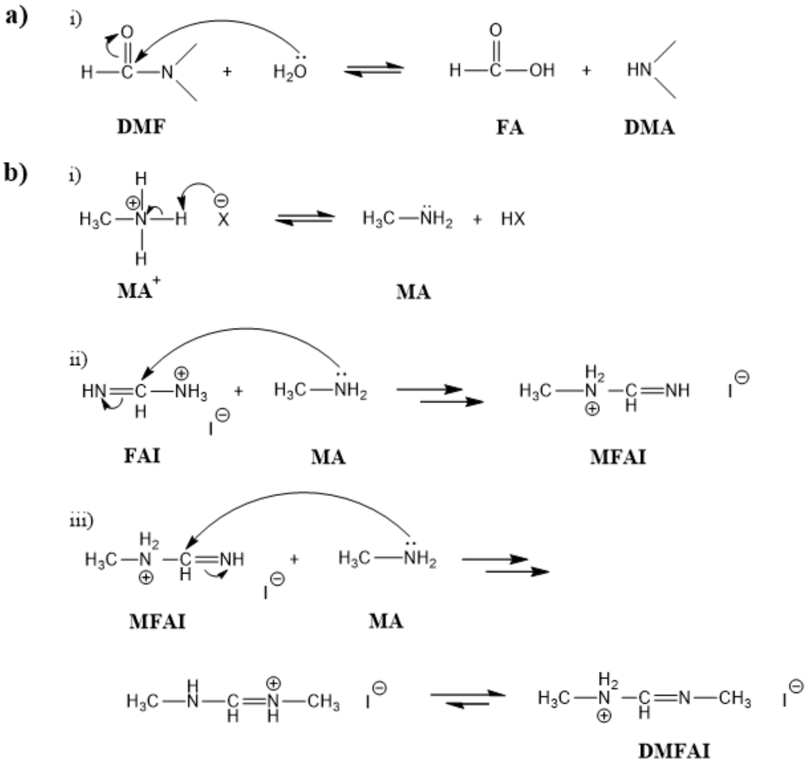

Figure 4.1: (a) Hydrolysis of DMF to produce DMA. (b) i) Deprotonation of prepared from freshly prepared solutions MAX component where X represents a halide ion. ii) Schematic of the addition-elimination reaction producing MFA. iii) Schematic of the addition elimination reaction producing DMFA. For simplicity, the NH_3 reaction products are not shown. Reaction scheme (b) reproduced from [99].

prepared from freshly prepared solution.

4.3.3 Results And Discussion

Device Studies

We have prepared several TC precursor solutions, and explored their shelf life under different conditions. These solutions were used both to prepare perovskite films for morphology studies and to fabricate PSC devices. Here, we concentrate on two main solution compositions: a stoichiometric TC solution in DMF/DMSO (here termed TC-mixed) and a stoichiometric TC in DMSO (termed TC-DMSO). Specifically, the composition of the two solutions fabricated was as follows:

1. TC-mixed: TC solution ($Cs_{0.05}FA_{0.81}MA_{0.14}PbI_{2.55}Br_{0.45}$) dissolved with a typical 4:1 DMF/DMSO solvent volume ratio

2. TC-DMSO: as TC-mixed but containing only DMSO solvent.

Here, all stock solutions were stored in amber vials and sealed in a N_2-filled glovebox environment. Each PSC device had the basic architecture ITO/SnO_2/TC-perovskite/spiro-OMe- TAD/Au [ITO: indium-doped tin oxide; spiro-OMeTAD: 2,2',7,7'-Tetrakis[N,N-di(4-methoxyphenyl)amino]-9,9'-spirobifluorene]. The fabrication and testing of perovskite solutions and devices is described in detail in the Experimental Section. For each time point, a series of control devices were fabricated from an equivalent, freshly prepared precursor solution. These controls allowed us to account for any external factors that occurred at each time point that could have affected device performance. Significantly, we find that the control devices show consistent performance over the duration of the experiment when fabricated using the same bottle of solvent (see Figure 4.9); a result that indicates that the age of the solvent alone does not cause a significant reduction in device efficiency.

To understand the aging of the TC-mixed precursor solution ($Cs_{0.05}FA_{0.81}MA_{0.14}PbI_{2.55}Br_{0.45}$), we first explored the effect of different storage temperatures on device performance. Solutions were stored at 4, 22, 45 and 70°C over a period of 17 days. The metrics of devices prepared from the solutions are shown as a function of solution aging time in Figure 4.10. Here, devices prepared using solutions stored at 70°C for 17 days have deteriorated greatly in performance, with their efficiency reduced to around 30% of the control devices prepared from a freshly made precursor solution. Notably, devices fabricated from solutions stored at 4°C had efficiencies consistent with the experimental controls. We have used this experiment to calculate an effective activation energy for the degradation process of 0.31 eV using the Arrhenius relationship [148] (shown in Figure 4.10). Although, this energy is an order of magnitude larger than room temperature, it is not inconsistent with that determined in other processes that occur over a period of days or weeks at room temperature. [148, 149]

These measurements indicate that storage of the precursor solution at lower temperature increases their useful lifetime. We therefore performed an extended study in which we compared devices fabricated from TC-mixed and TC-DMSO precursor solutions that were either stored in a glovebox at room temperature ($\approx$ 22°C) or refrigerated ($\approx$ 4 °C). These conditions will henceforth be referred to as RT- and LT-aged, respectively. Figure 4.2a shows the PCE of devices fabricated from the RT-aged TC-mixed precursor as a function of storage time. The average and best PCE of devices fabricated from the freshly prepared solution was (18.1 ± 0.5) and 19.0%, respectively. There is a noticeable reduction in the efficiency of devices prepared from solutions stored for approximately 30 days at RT. Devices prepared from solutions stored for four months have an average PCE of (5.0 ± 0.6)% (with 6.1% best sweep). This effect primarily results from a reduction in fill factor (FF) and short-circuit current (J_{SC}) (see Figure 4.11). Notably, devices prepared from solutions stored for 186 days (6 months) demonstrated no photovoltaic response. For completeness, we plot the J-V sweeps for the best performing devices fabricated at each time-point during the storage experiment in Figure 4.2b (see full device metrics in Tables 4.2 and 4.3). Here, a significant hysteresis in the J-V characteristics is observed for devices fabricated from solutions stored for >2 months. The stabilised power output for these devices is shown in Figure 4.2c, where a reduction in PCE is evident. As can be seen in Figure 4.12, we observed similar trends with precursor aging for devices prepared from TC-DMSO solutions; however, when DMSO was used as a primary solvent, we find

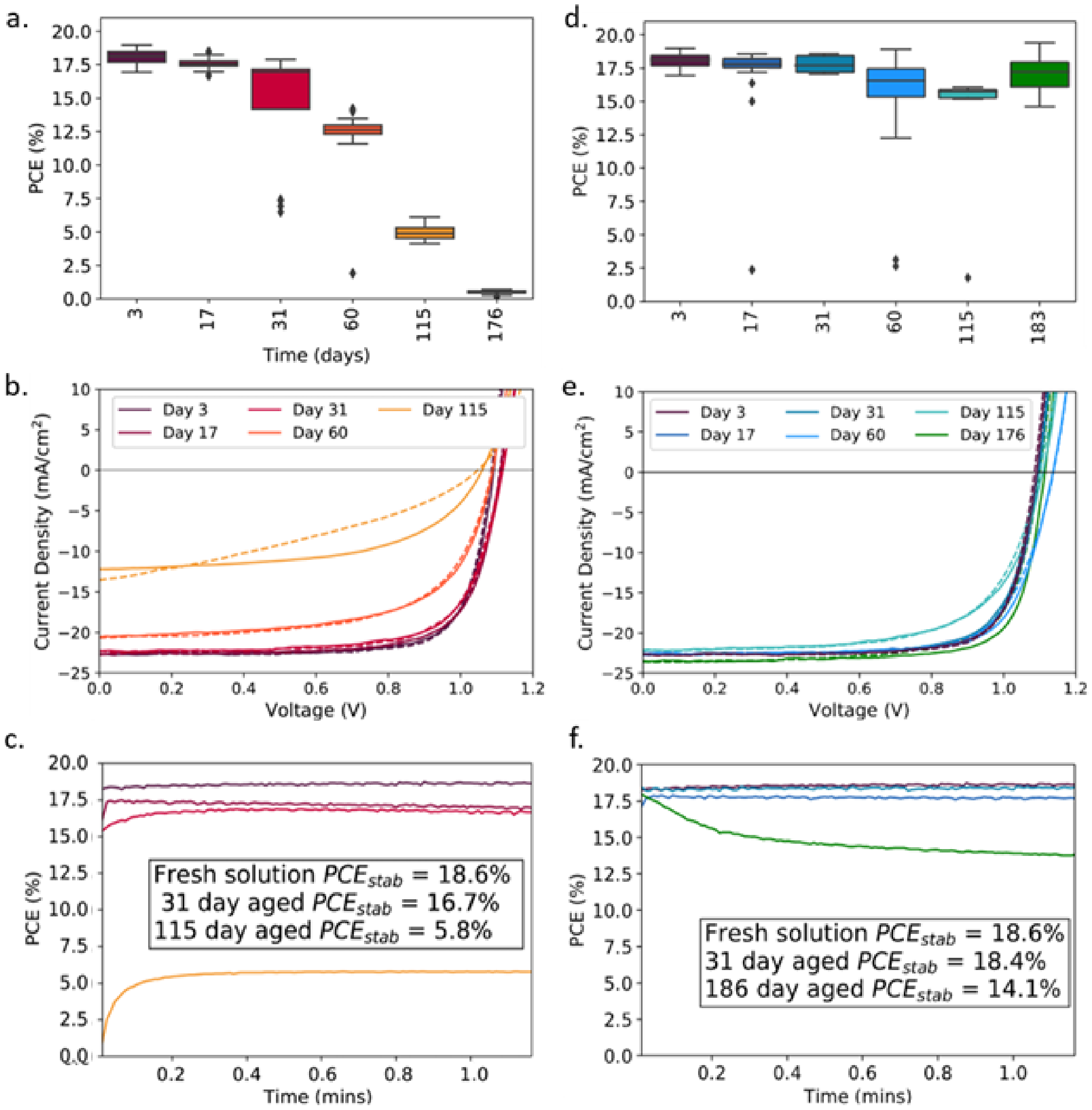

Figure 4.2: (a) PCE of perovskite device with the stack ITO/SnO_2/perovskite/spiro-OMeTAD/Au fabricated from RT-aged TC-mixed (DMF/DMSO) solutions. (b) J-V curves and (c) stabilized power output for the best performing devices from RT-aged solutions. (d) PCE of devices fabricated from low-temperature-aged solutions, with (e) J-V curves and (f) stabilized power output for the best performing cells. Full J-V sweep parameters for (b) and (e) and all device data for boxplots in (a) and (d) are given in Tables 4.2 and 4.3

that the resultant devices had improved performance compared to those prepared from DMF/DMSO precursor that had been aged over 31 and 186 days (see Tables 4.4 and 4.5).

We now discuss the performance of devices fabricated from precursor solutions stored at 4 °C. Figure 4.2d shows device PCE as a function of storage time for the LT-aged TC-mixed solution, with J-V curves and power output for the best devices recorded over a period of 1 min plotted in Figure 4.2e,f, respectively. Here, Figure 4.2 confirms that over a 1-month storage period, there was negligible degradation in device performance compared to RT-aged solutions. Specifically, after 31 days solution-aging, the devices fabricated had an average and best efficiency of (17.8 ± 0.6) and 18.6%, around 97% of the PCEs achieved by devices made from fresh solution. This enhanced stability is reflected in device stabilised power output; here "champion" devices prepared from solutions stored for 3 days and 1 month had stabilised efficiencies of 18.6 and 18.4%, respectively.

We find that devices fabricated from solutions that have been cold-stored for 2 months have some degree of reduced performance; however, this effect is less significant than for those fabricated from RT-aged solutions. Devices fabricated from cold-stored solutions for 4 months had efficiencies that were $\geq$85% of those prepared from freshly made solutions, with average and best PCEs of (15.7 ± 0.3) and 16.0%. Furthermore, after 6 months of cold solution-storage, devices had impressive initial sweeps. It can be seen however that there is a rapid (30 s) burn-in (loss of efficiency) seen in the device made from the 6 month LT-aged solutions (see Figure 4.2f), with the device efficiency not stabilising completely over the course of the measurement. Nevertheless, the champion device made from this solution had a PCE of 14.1% after 1 min. We suspect that even though low-temperature storage significantly slows reaction rates, there is a gradual build-up of degradation products in solution that is likely to have a negative impact on the long-term operational stability of the finished devices. More experiments are planned to explore such effects.

Interestingly, we find a slightly higher level of stability from TC-DMSO solutions stored at 4°C compared to those based on the mixed solvent (see Figure 4.13). Indeed, although devices fabricated from the TC-DMSO solution had a lower initial performance [(16.6 ± 1.7) and 18.0% best efficiency], this solution achieved (16.7 ± 0.6)% PCE after 4 months of LT storage. The champion device fabricated at this 115 day time point had an initial sweep of 17.5% with a stabilised efficiency of 16.4%. This preliminary result suggests that precursor solutions prepared from DMSO may have better intrinsic stability than those based on DMF.

Film Morphology

To explore the origin of the observed changes in device efficiency, we have investigated the optical and structural properties of perovskite films prepared from freshly prepared (control) and aged solutions. Here, Figure 4.3a,b plots the UV/Vis absorption of films made from TC-mixed solutions stored at RT and LT, respectively. It is immediately apparent that films prepared from solutions stored at RT undergo a progressive reduction in optical density. Indeed, the film prepared from the solution stored at RT for 115 days ($\approx$ 4 months) has no clear absorption onset, with an absorption tail that extends to long wavelengths being characteristic of a significant degree of optical scattering. The absorption spectra for films prepared from the LT-aged solution appear much more self-similar; here,

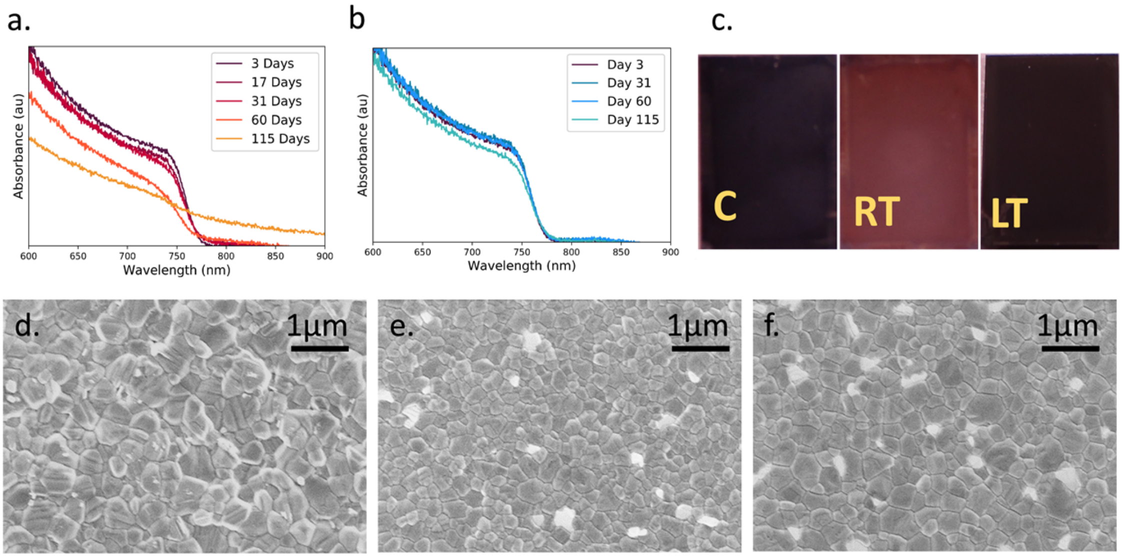

Figure 4.3: UV/Vis absorption spectra of TC-mixed perovskite films prepared from solutions that have been aged at (a) RT and (b) at a low temperature of 4°C. (c) Images of films prepared from a precursor solution aged for 115 days at RT and at 4°C (LT) next to a film fabricated from a freshly prepared control ink (marked C). SEM images comparing films fabricated from (d) RT- and (e) LT-aged (115 days) solutions to those fabricated from a (f) freshly prepared control solution.

a small reduction in optical density is only apparent in the film prepared from the 115-day stored solution.

These observations are confirmed in Figure 4.3c (and Figure 4.14) where we present images of films prepared from a control solution and solutions stored for 115 days at RT or LT. Here, the film prepared from the control solution is black and specular, whereas the film prepared from the solution aged at RT appears cloudy and less optically dense, indicating a rougher film. This roughness is consistent with the increased optical scattering observed in absorption measurements shown in Figure 4.3a. This is further supported by atomic force microscopy (AFM) shown in Figure 4.15, confirming an increase in roughness for films produced from RT-aged precursor solutions. Here, the root mean square (RMS) roughness determined from freshly prepared (control) solutions and solutions aged at LT and RT is 26, 30 and 80 nm, respectively. We also observe similar effects for DMSO-based solutions aged at RT (see Figure 4.16).

Remarkably, in contrast to the RT-aged film, the film prepared from the solution stored at LT is consistent in appearance with the control film and has formed a photoactive perovskite phase. To investigate this effect, we used scanning electron microscopy (SEM). Such grains have a “striped” appearance; an effect consistent with crystallographic twinning. [150, 151] Twinning effects generally result from a local increase in strain during

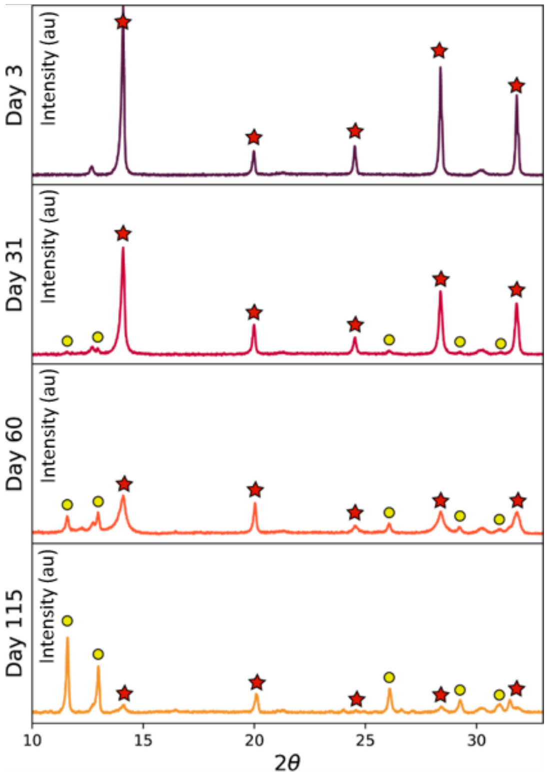

Figure 4.4: XRD patterns for films made from RT-aged TC-mixed solutions after 3, 31, 60 and 115 days. Red stars mark cubic perovskite peaks and yellow circles mark emerging intermediate peaks.

film formation, likely resulting from a lattice mismatch within the crystal. Note that while bright grain boundaries are suggestive of inorganic-rich grain boundaries, we cannot exclude the possibility that such effects result from inefficient charge transfer between the grains. It is apparent, however, that no significant changes in film structure are observed in samples prepared from precursor solutions stored at LT.

Crystal Structure

X-ray diffraction (XRD) was used to explore the crystal structure in films produced from control and aged precursor solutions. Figure 4.4 plots XRD data recorded from films fabricated from the TC-mixed solution aged at RT for 3, 31, 60 and 115 days. Here, peaks consistent with a pseudo-cubic TC perovskite are labelled with red stars, while yellow circles identify new peaks (comparative data recorded from TC-DMSO cast films are shown in Figure 4.17). Figure 4.4 shows there is a significant solution age dependent reduction in scattering from the perovskite 100 reflection at 2θ=14.1°. This process is accompanied by an increase in scattering from new peaks at 11.6°, along with peaks at 12.9, 26.0, 29.2 and 31.5°. This reduction in scattering intensity from the 14.1° peak and the emergence of a peak at 11.6° with those between 25–33° coincide with those expected for a 4H hexagonal polytype (see Figure 4.19). The TC-DMSO sample also exhibits reflections consistent with 6H phases being present in the film. Our

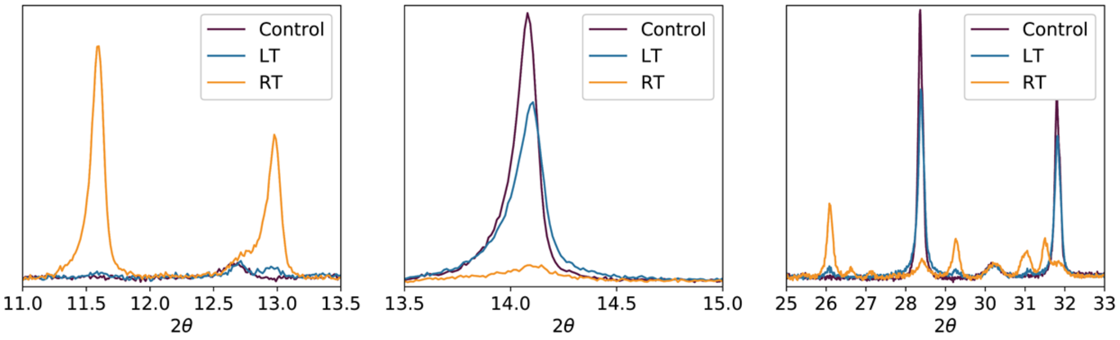

Figure 4.5: XRD highlights for films made from TC-mixed solutions that have been stored for 115 days at RT (yellow) and LT (blue) together with a freshly prepared control film (purple). Here, films from the LT-aged ink still exhibit strong scattering from the perovskite phase, whereas in the RT-aged solution a non-perovskite phase is present (see Figure 4.19).

measurements indicate that these polytypic phases preferentially form in films prepared from RT-aged solutions, with the formation of various polytypes being dependent on the casting solvent, and in turn the degradation of the organo-halide component of the solution.

Figure 4.5 compares XRD scattering patterns from films made with a control TC-mixed precursor solution, with films prepared from solutions aged for 115 days at RT or LT. It can be seen that the reduction of the tetragonal perovskite phase (evidenced by the peak at 14.1°) and the growth of the peaks at 11.6, 12.9 and 26.0° are strongly suppressed when solutions are stored at 4 °C; a result consistent with the thin-film absorption and SEM measurements presented in Figure 4.3 and the device studies shown in Figure 4.2. This same effect is seen for the TC-DMSO solutions stored at low temperatures (Figure 4.20). Our results suggest therefore that storage at low temperature strongly suppresses the formation of undesirable polytype phases.

NMR Solution Study

We have used NMR to analyse the composition of TC solutions as they are aged in d_7-DMF, d_6-DMSO or a d_7-DMF/d_6-DMSO mix. Figure 4.6 shows NMR spectra recorded from a TC precursor dissolved in 4:1 d7-DMF/d6-DMSO, measured weekly over 28 days (full spectra for all solutions can be found in Figures 4.22–4.29). Here, we assign the peaks at 2.2 and 7.7 ppm to the CH_3 and CH protons in MA and FA, respectively. We find a different chemical shift for these peaks in the different solvents (DMF vs. DMSO), which we suspect results from solvent interaction effects.[152, 153] We discuss this effect further in the Supporting Information. Figure 5a,b shows the formation of three new peaks around 2.57, 2.73 and 7.77 ppm as solutions age. As shown in Figure 5c, this growth is correlated with a significant decrease in intensity of the MA CH_3 peak (2.20 ppm) after 28 days aging. On the basis of previous work by Wang et al.,[99] we assign the peaks at 2.57 and

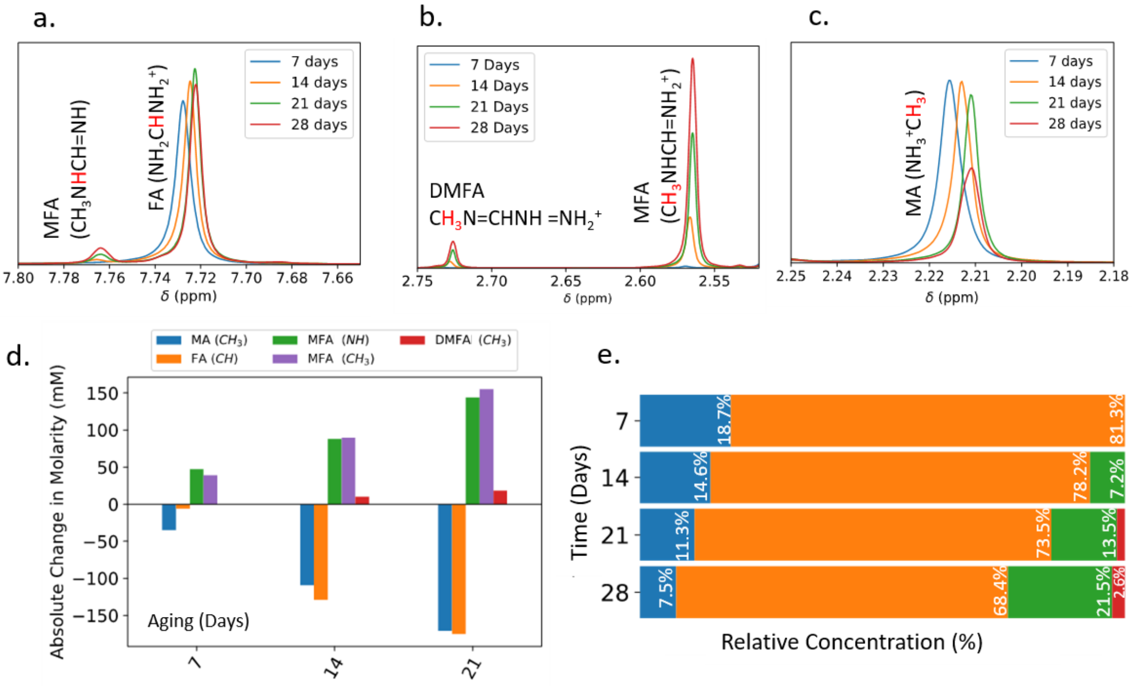

Figure 4.6: (a–c) NMR spectra of TC-mixed solution dissolved in DMF/DMSO measured at several time points over a 1-month period (full spectra in Figures 4.22– 4.25). (d) Absolute change in molarity for the various organic components over time, estimated compared to an internal standard for which the molarity remains constant. (e) Relative concentration of the organic cations over time determined as described in Supporting Information. Here we see a significant reduction in the relative concentration of both MA and FA, along with an increased concentration of MFA and DMFA.

7.79 ppm to the methyl and amine groups of MFA, respectively, with the peak at 2.74 ppm ascribed to the methyl group of DMFA. We note however that previous work has described the hydrolysis of DMF to form DMA, and its subsequent protonation to produce DMA^+. DMA^+ has an ^1H NMR peak at approximately 2.55 ppm [145] (i. e., overlapping with the peak that we assign to the methyl group of MFA). To determine whether DMA does in fact contribute to our measured NMR spectra, we have integrated the area under the peaks at 2.57 and 7.79 ppm and find them to have an area ratio of (3.0 ± 0.3):1. This intensity ratio is consistent with the 3 :1 proton ratio expected for the CH_3 and NH groups in MFA, and thus we conclude that our solutions do not contain a substantial concentration of DMA^+. We can gain further confidence in this conclusion by performing ^2H (deuterium) NMR on precursors (see Figure 4.21). This measurement probes the relative composition of the deuterated solvents and is insensitive to changes in the molecular cations. Figure 4.21 shows NMR spectra for the deuterated DMSO and DMF/DMSO precursor solutions both before and after 6 months storage at RT. Here, no changes are observed in the deuterated spectra after this time period; a result that indicates that any degradation in the precursor solutions does not result from deterioration or chemical changes to the solvent.

We can use our ^1H NMR spectra to gain a quantitative understanding of changes in precursor chemistry. Here, we have used an internal standard of known concentration in an isolated capillary tube (seen at 8.436 ppm) to determine absolute molarity changes of MA, FA, MFA and DMFA in solution as a function of time (full method described in Chapter 3). Absolute molarities of organic component within the TC solution in DMF/DMSO are shown in Figure 4.6d with NMR spectra shown in Figures 4.22–4.25. We find that over a period of 29 days, the quantity of FA and MA both reduce by a similar concentration (170 mM); a finding that may indicate that these components react with each other. Over the same time period, the increase in the integrated area under the peaks at 2.57 and 7.79 ppm indicate the formation of approximately 150 mM of MFA, with the peak at 2.74 ppm indicating the formation of approximately 20 mM of DMFA. The total concentration of MFA and DMFA formed over this time period is thus approximately 170 mM; a value comparable to the molarity loss of MA and FA. This simple analysis confirms the reaction proposed by Wang et al.,[99] and suggests that the main degradation pathway in high-efficiency perovskite precursor solutions involves the deprotonation of methylammonium to methylamine initiating an addition-elimination reaction, thus forming the condensation products MFA and subsequently DMFA.

We have applied the same methodology to explore changes in the chemistry of precursor solutions utilising a DMSO solvent. Here, NMR spectra recorded from DMSO-only precursor solutions are shown in Figure 4.26-4.28. Our analysis indicates that a combined total of approximately 65 mM MFA and DMFA form in the DMSO-only precursor solution after 28 days. This again confirms that the solvent has an impact on the rate of chemical decomposition.

Finally, we have used NMR to examine the effect of storage temperature on the precursor solution degradation process. Figure 4.7 shows the relative intensities of peaks characteristic of MA, MFA, DMFA and FA in either a DMF or DMF/DMSO solvent before and after 6 months (216 days) storage in LT and RT conditions. Here, the relative composition was calculated using the same method as was used in Figure 4.6. In this experiment, however, no internal standard was present, and absolute concentrations cannot be calculated for each species. However, we have referenced the relative intensities of each of the peaks to a residual DMSO peak present in all samples, whose intensity was not found to change over the course of the experiment. We find that a similar amount of MFA and DMFA are formed in DMF/DMSO based solutions regardless of storage conditions. In all cases however, we note a reduction in the relative concentration of MA in the aged solutions, with this effect being most significant in the RT-aged DMF/DMSO TC solution. Indeed, the complete absence of MA in solution correlates with our device studies in which we demonstrated that this precursor solution could not be used to create a perovskite film after storage at RT. It is also apparent that the formation of MFA and DMFA in the DMSO-based precursor solution is significantly suppressed when it is stored at LT. This finding further supports our conclusion that TC perovskites are generally more stable in DMSO-based solutions.

4.3.4 Conclusions

We have studied the aging of high-performance triple-cation (TC), mixed-halide precursor solutions and have found that such effects are strongly dependent on temperature. Using

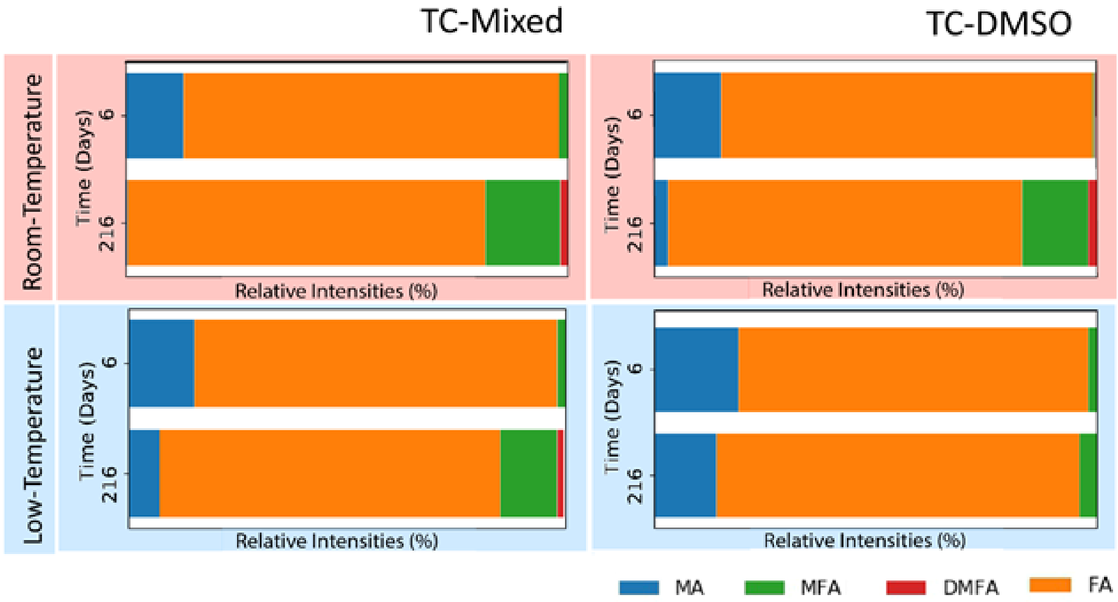

Figure 4.7: Relative intensity of different cationic species in the TC precursor solutions after 6 and 216 days after storing at either RT or 4°C (LT). Data is shown for solutions prepared from a DMF/DMSO solvent mix or DMSO-only.

NMR spectroscopy, we have identified the primary mechanism of degradation in these solutions to be the deprotonation of methylammonium, and the subsequent formation of N-methyl formamidinium (MFA) and N,N-dimethyl formamidinium (DMFA). This change in the proportion of organic components will directly alter the tolerance factor of the perovskites and drive the formation of non-perovskite polytype phases. This is confirmed using X-ray diffraction, which shows that films cast from RT-aged solutions contain a greater fraction of nonperovskite phases, resulting in devices having significantly reduced performance. Furthermore, it appears that the choice of precursor solvent affects the decomposition to larger cations and consequently the polytypes that form.

With low-temperature solution storage, this process can be significantly suppressed without altering the solution chemistry. Specifically, we show that devices that have been fabricated from a TC perovskite dissolved in DMF/DMSO can be stored for 1 month at 4 °C with negligible deterioration in device performance. Indeed, using this approach we show that even after 4 months cold storage, such solutions can be used to fabricate devices with a power conversion efficiency (PCE) of $(15.7 \pm 0.3)\%$ and retain >85% of the efficiency of devices prepared from freshly prepared solutions.

We find that solvent choice has a significant impact on solution stability. For the particular TC perovskite studied, we find DMSO can be used to create a more stable precursor solution than the widely used DMF/DMSO solvent mixture. Although devices prepared from this precursor have lower initial efficiencies, we find that devices fabricated from DMSO only precursor solutions are more stable; for example, they can be stored for 4 months at 4 °C and can then be used to create devices having a champion PCE of 17.1% with a stabilised efficiency of 16.4 %, a value that is ≥90% of devices made from freshly prepared solutions. Previous work has indicated that solvent reactions involving DMSO require a significantly higher temperature[145] than those that occur in DMF-based solvents.[97, 111, 142] We speculate that the observed increased stability may stem from the higher basicity of DMSO. DMSO may establish more hydrogen bonding with methylammonium in solution, supressing the aforementioned addition-elimination reaction. It is also possible the solvent degradation products (even in small amounts) may drive reaction kinetics forwards, however we note that our NMR data shows that no significant amount of these products (namely dimethylamine) are formed during aging. More generally, our results demonstrate that with correct storage conditions, solution stability can be maintained for a significant period without the need to alter solution chemistry. We believe that future work should address the long-term operational lifetime of devices made from aged solutions and also explore the impact of intrinsic factors (such as solvent basicity) on solution stability.

4.3.5 Experimental Details

Precursor Solution Preparation

All solvents were purchased from Sigma Aldrich. PbI_2 and $PbBr_2$ were purchased from TCI Chemicals, MAI and FABr were purchased from Ossila, and Caesium Iodide was purchased from Sigma Aldrich. The stoichiometric inks prepared contained 467.5 $mg.mL^{-1}$ of PbI_2, 167.2 $mg.mL^{-1}$ of FAI, 68.3 $mg.mL^{-1}$ of $PbBr_2$ and 18.8 $mg.mL^{-1}$ of MABr. These were weighed out and dissolved in each of the relevant solvents (DMF/DMSO or DMSO). A stock solution of CsI was prepared in DMSO (389 $mg.mL^{-1}$), with 40 μL of this solution then added to the solution. The final stoichiometry of the resultant solutions was $Cs_{0.05}FA_{0.81}MA_{0.14}PbI_{2.55}Br_{0.45}$.

Device Fabrication

Devices were fabricated on ITO coated glass that was patterned via etching using zinc powder and 4 M HCl. Substrates were cleaned using a surfactant (Hellmanex) solution to remove excess zinc and then sonicated in a Hellmanex solution, deionised (DI) water and isopropyl alcohol (IPA) for 20 min, 5 min and 15 min, respectively.

PSC devices had the following device structure: glass/ITO/SnO2/ perovskite/spiro-OMeTAD/Au. To fabricate devices, substrates were first placed in a UV-ozone cleaner for 20 min. A suspension of 15% SnO_2 nanoparticles in H2O was diluted to 4:1 with H_2O. 50 μL of this solution was then spin coated at 3000 rpm for 30s onto the ITO substrate. These samples were then exposed to a UV-ozone (for 20 min) before being transferred to a nitrogen-filled glovebox. Perovskite layers were then deposited from the precursor solutions via spin coating, with the spin-coating parameters listed in Table 4.1. All perovskites were "quenched" during spin-coating using 100 μL of an ethyl acetate antisolvent to promote crystal nucleation.

A spiro-OMeTAD hole transport layer (85 $mgmL^{-1}$in chlorobenzene) was spun onto the perovskite. The following dopants were added to this solution: 34 μLmL^{-1} TBP, 11 μLmL^{-1} FK209 in ACN (300$mgmL^{-1}$ concentration) and 20μLmL^{-1} of LiTFSI in

ACN ($500mgmL^{-1}$). This solution was filtered directly before use, and was spin coated by dynamically dispensing $25\mu L$ of solution at 4000 rpm and coating for 30 s. The coated substrates were stored in dry air overnight and then placed in an Edwards Auto 306 belljar evaporator. A gold electrode layer (80 nm) was then evaporated onto the substrates through a shadow-mask to create 6 pixels with each pixel having an area of 0.02506 cm^2.

Devices were tested using a Newport 92251A-1000 solar simulator in ambient conditions, with J–V measurements recorded using a Keithley 237 source measure unit. Measurements were made by reverse sweeping the bias between -0.1 and 1.2 V at 100 mVs^{-1}. Device stabilised power output was measured by holding devices for several minutes at a bias voltage defined by the reverse sweep V_{MPP}. All device metrics were typically measured one day after perovskite deposition.

Film Characterisation

UV-Vis measurements were performed under ambient conditions using UV-VIS-NIR light source (Ocean Optics – DH-2000-BAL), collection fibre optic cables (Ocean Optics) and spectrometer (Ocean Optics – HR2000+ES). Samples for absorption measurements were prepared on quartz-coated glass using the same deposition methods as used in device fabrication. Thickness measurements were performed using a DekTakXT surface profilometer to scan over a scratch made in the film. Measurements were made at several places across each film, and an average and standard deviation then determined.

Samples for SEM, AFM and XRD were prepared on ITO coated glass that had been coated with SnO_2 and perovskite films using the same deposition parameters as used to create devices. AFM images were taken using Bruker Dimensions 3100 in Intermittent Contact Mode using BrukerTESPA-V2 cantilevers with a spring constant of 42 N/m. Roughness measurements were taken using Gwyddion image analysis software. SEM imaging was performed using an FEG-Raith SEM operating at a beam energy of 1.5 kV at a working distance of 4-5 mm, with an in-lens detector used to collect backscattered electrons. X-ray Diffraction measurements were performed using a PANalytical X'Pert Pro system. This was equipped with Copper Line Focus X-ray tube run at a voltage of 45 kV with a tube current of 40 mA, with data collected using a 1D-detector, in Bragg-Brentano geometry.

NMR

NMR For solution-NMR measurements, samples were prepared using deuterated solvents sourced from Sigma Aldrich. Peak positions were calibrated with respect to an internal isolated standard of 1,2,4,5-Tetrachloro-3-nitrobenzene (TCNB) at 8.4364 ppm in DMSO-d_6 in a capillary tube. ^{1}H NMR and ^{2}H measurements were performed using a Bruker AVANCE III instrument operating at 400.2 MHz and 61.43Hz respectively at 289K. Spectra were recorded in 16 scans using over a 20ppm spectral width with 64k acquisition points and a relaxation delay of 30s to ensure full quantification. All solutions were sealed into 100 MHz, 7" Standard Series NMR tubes in a Nitrogen-filled glovebox. Molarity changes as shown in Figure 4.6 were estimated using TopSpin software and referenced to the TCNB internal standard that had a molarity of 383 mM. The measurements presented Figure 4.7 were locked onto a DMSO-d_6 solvent peak.

4.4 Supplementary Information

4.4.1 Spin-Coating Parameters Used for Perovskite Films

Solution	Spin Cycle	Quenching Time	Annealing Temp	Annealing Time
TC mixed	Acceleration 200rpm/s for 10s 2000rpm for 10s 4000rpm for 20s	10s before end of last step	100°C	60 min
TC-DMSO	2000rpm for 10s 4000rpm for 28s	15s before end	130°C	10 mins

Table 4.1: Spin coating parameters for PSCs/films described in the study.

4.4.2 Arrhenius Relationship Note

We explored the time-dependent aging of the perovskite precursor solutions at a series of different temperatures. This allowed us to estimate an overall activation energy for the reactions taking place. Here, we used the Arrhenius relationship [148] which we have used to relate the reduction in device efficiency (caused by the degradation of the precursor solution) to its storage temperature.

$$ln(\lambda) = -\frac{E_A}{k_B T} + ln(A) \tag{4.1}$$

Here, E_A is an activation energy, k_B is the Boltzmann constant, T is the solution storage temperature, A is a fitting constant and λ is the degradation rate. Here, we define degradation rate using the following equation

$$\lambda = \frac{1 - (\frac{PCE_n}{PCE_{Initial}})}{n} \tag{4.2}$$

where $PCE_{Initial}$ is the average initial PCE of devices made from freshly prepared solutions and PCE_n is the average PCE for devices that had been prepared from solutions that had been aged for n hours.

4.4.3 NMR: Experimental Details and Molarities

Nuclear magnetic resonance was conducted on 1.3M solutions dissolved in deuterated solutions. All analysis were carried out using TopSpin software. MA and FA peaks were identified by their chemical shift and comparison to ^{1}H reference spectra of individual components. To estimate absolute molarity changes, the area under each peak in the aged precursor solution was integrated and compared with the area under the internal standard. Overlapping peaks were deconvoluted using TopSpin software to extract their individual intensities. The internal standard used was 1,2,4,5-tetrachloro-3-nitrobenzene which was prepared at a concentration of 383 mM in d_6-DMSO. This peak can be seen at 8.436 ppm in Fig 4.21-4.29. This calibration peak however overlaps with a broad peak at ∼8.4 ppm. We speculate this broad peak is made from several unresolved peaks corresponding to the NH components of FA and MA usually found at 9.0 ppm and 8.7 ppm for FA and 7.8ppm for MA. Here, we suspect that significant proton exchange between molecules may cause these peaks to merge and broaden. To isolate the signal corresponding to the TCNB standard (and thereby also determine the area of the other peaks), we have use the deconvolution feature in the TopSpin software. An example of this deconvolution process is shown in Figure 4.8a. Here it can be seen that the individual peaks can be successfully isolated and their integrated area determined. We acknowledge that this deconvolution process may lead to an uncertainty in the integration values which we believe to be around ±10%.

We have also performed a ^1H NMR calibration experiment, measuring TC solutions containing 3 different total solids concentrations: 225mg/ml, 774mg/ml and 901mg/ml. For each of these samples, the integrated areas of the FA-CH and $MA - CH_3$ peaks are calibrated with reference to the area of the (known concentration) TCNB standard, with this process utilised throughout this study. We present the results of this experiment in Figure 4.8b. Figure 4.8b show that the molarities determined scale in an approximately linear fashion with concentration for both the MA and FA peak; a result that indicated that this methodology can accurately measure concentration within solution.

The molarity determined from each peak is detailed in Tables 4.6-4.8. The measured intensities have been scaled where necessary to calculate molarity to compensate for the number of hydrogen atoms (or protons) contributing to it, e.g. in each MA CH_3 group there are three hydrogen atoms which contribute to one peak. Absolute molarity changes shown in Figure 4.6d were calculated using $\delta M = M_{init} - M_P$, where δM is the change between the initial molarity M_{init} and the molarity at time point, M_P. The relative (RM) molarity (expressed as a %) is calculated by normalising individual molarities, M_x, to the total molarity of the A-cations using

$$RM(\%) = \frac{M_x}{M_{MA} + M_{FA} + M_{MFA} + M_{DMFA}} \tag{4.3}$$

Peak positions were calibrated with respect to an internal isolated standard of 1,2,4,5-Tetrachloro-3-nitrobenzene (TCNB) (peak at 8.4364 ppm) in DMSO-d_6 in a capillary tube which was placed inside the sample tube containing the precursor solution being measured. The spectra presented below therefore contain peaks that derive from both the sample and the standard. We highlight peaks associated with the TCNB standard using a blue box.

Note that the standard capillary tube used was washed before use with isopropanol and water. These species inside the capillary can be seen as contamination peaks at 4.3 ppm, 3.8 ppm, 1.0 ppm (for IPA) and 3.3 ppm (for water) in the following ^1H spectra. For the ^1H measurements, we find a chemical shift between the samples that are dissolved in different solvents.

It is important to emphasize that the exact chemical shift of any proton environment is highly dependent on its surroundings and can vary due to the due to concentration, pH or

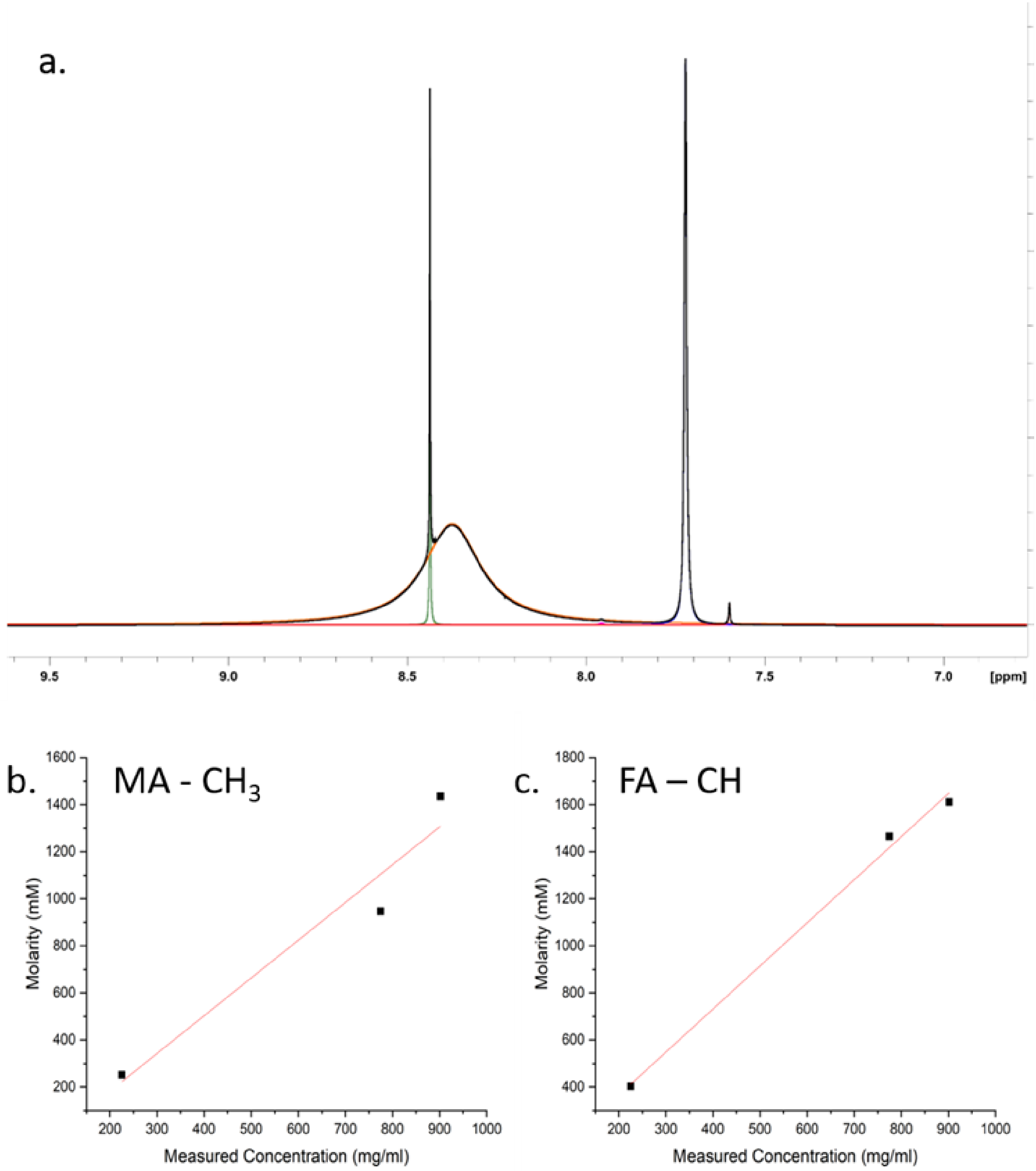

Figure 4.8: Part of NMR spectra for TC-DMF-DMSO sample showing deconvoluted peaks and with the combined line shape (black). b. & c. Concentration calibration experiments conducted for three different sample concentrations. Here, the molarities calculated from the deconvoluted MA- CH^3 peak (b.) and FA-NH peak (c.) are plotted against measured sample concentrations. As expected, there is a linear relationship between sample concentration and integral area. Here the points are black squares with a linear fit in red.

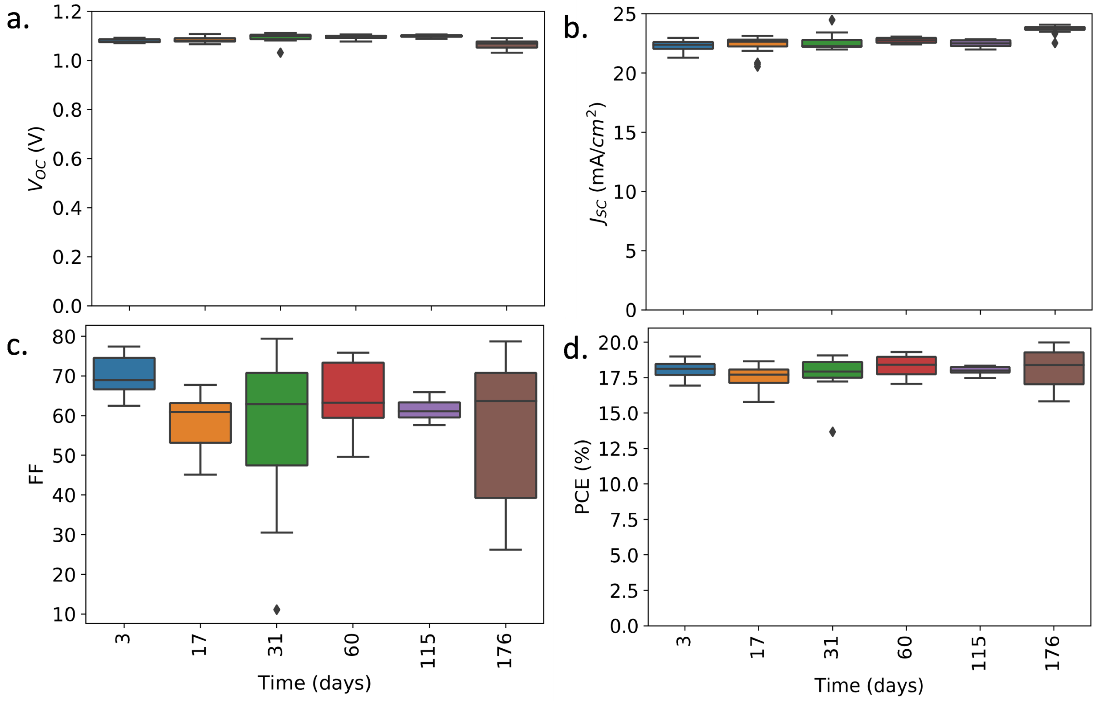

Figure 4.9: Boxplots showing V_{OC} (a), J_{SC} (b), FF (c) and PCE (d) for control devices made from a fresh TC-mixed solution at each time point.

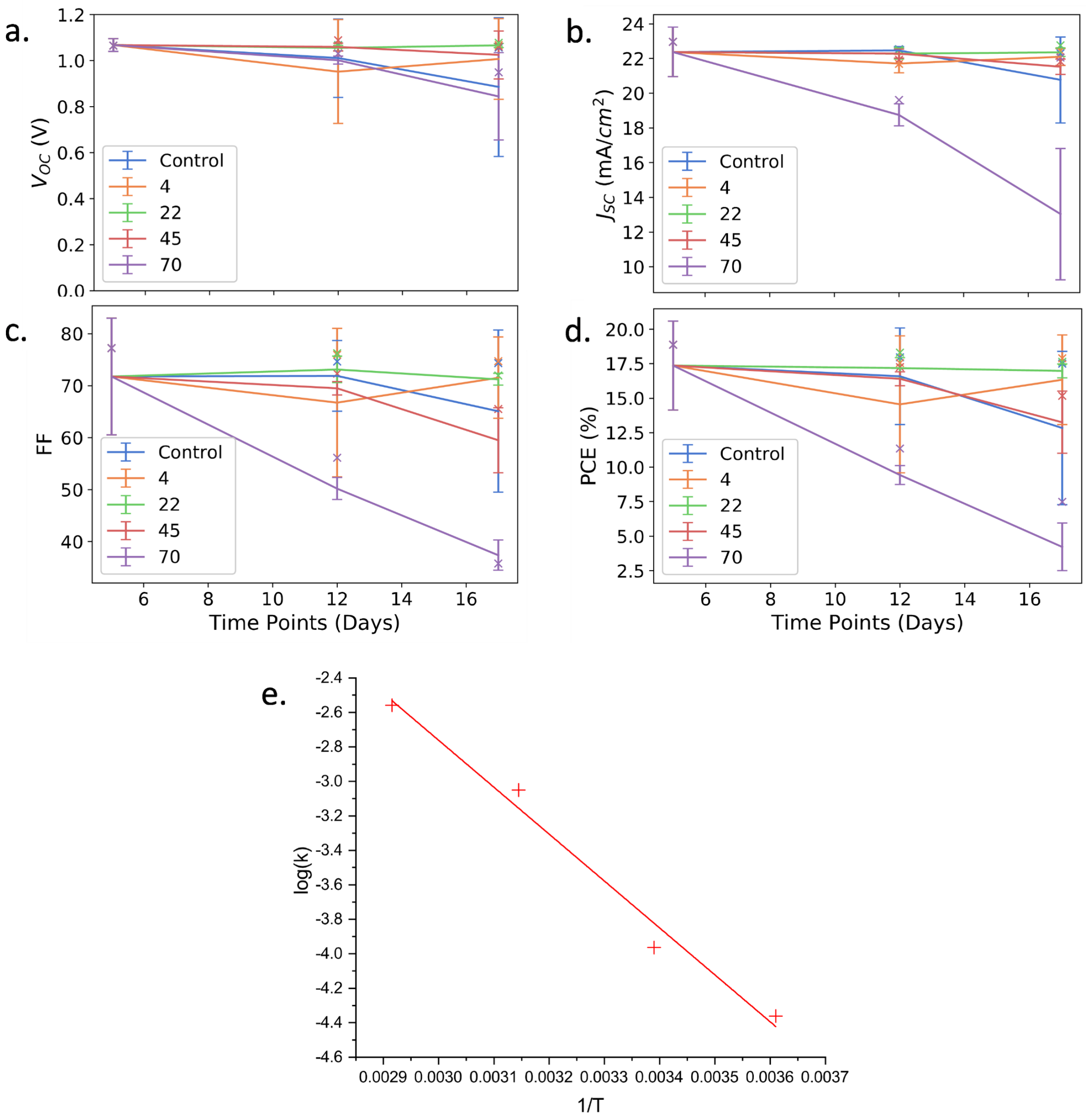

Figure 4.10: Average and standard deviation of the performance metrics for devices made from a TC-mixed (DMF:DMSO 4:1) solution aged at various temperatures over a 3 week period. e) Linear plot of $\log(\frac{\gamma}{t})$ against $\frac{1}{T}$ (see equation 4.1) where $k = \frac{\gamma}{t}$ represents rate of performance reduction per hour and T is temperature in K. Here a best fit to the data gives the activation energy $\frac{E_A}{k_B}$.

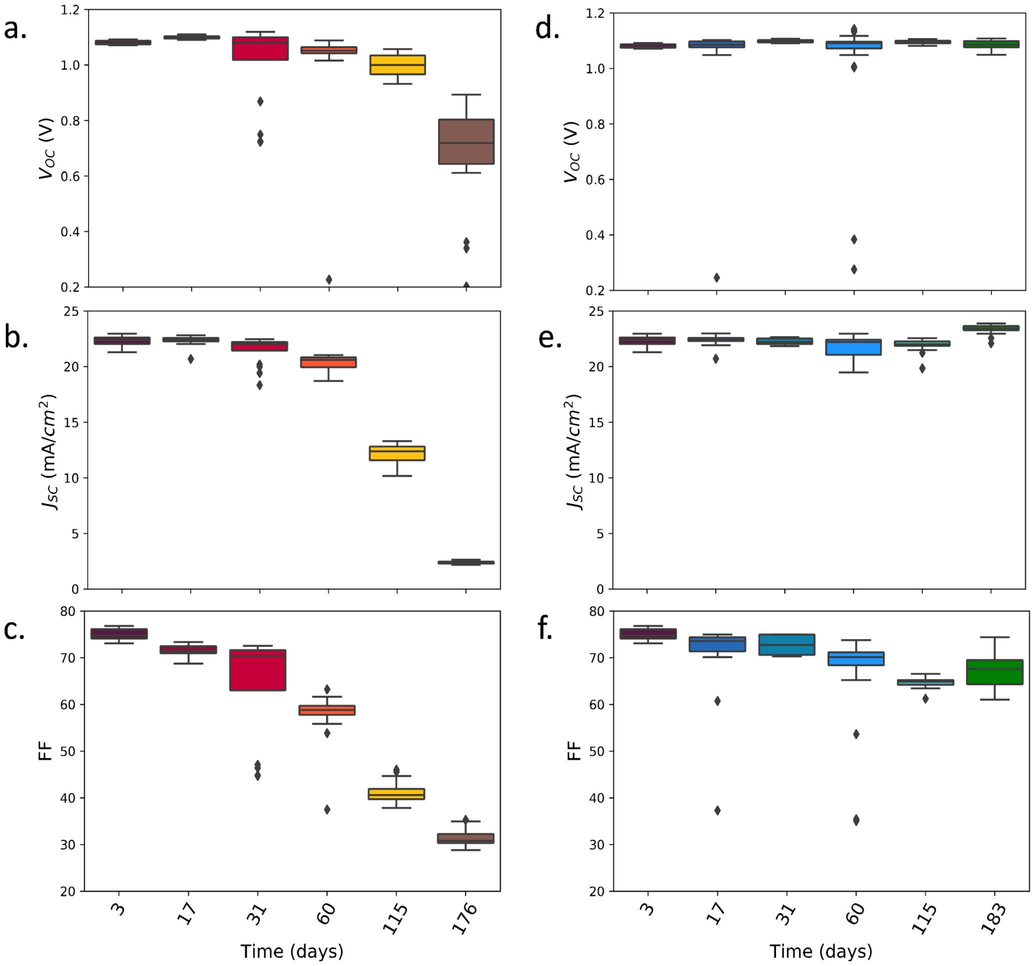

Figure 4.11: V_{OC}, J_{SC}, and FF for devices made from RT- (a-c) and LT-aged (d-f) TC-mixed solutions. Results for the 183- and 176-day time point made from new, undisturbed precursor solutions that were aged under identical conditions to data points presented at the other time points.

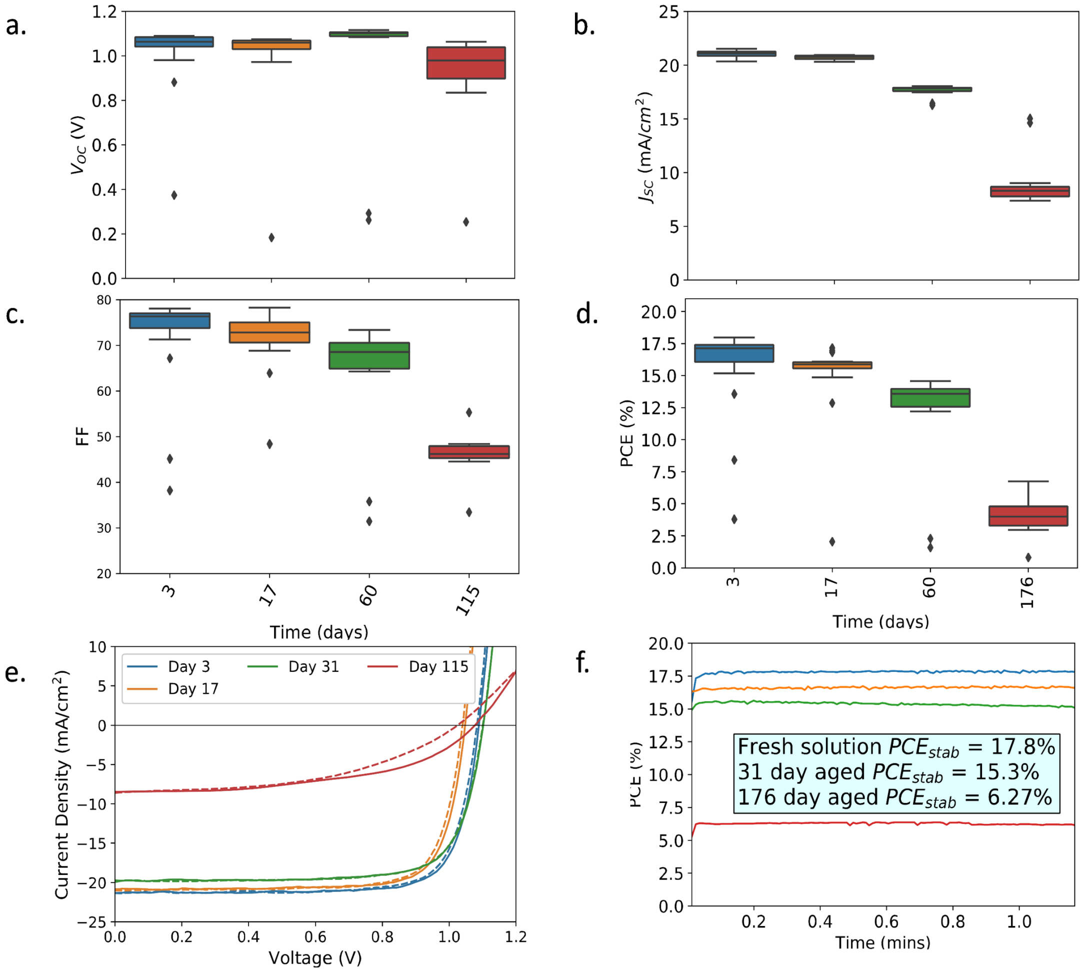

Figure 4.12: RT-aged TC-DMSO device box-plots. (a) V_{OC}, (b) J_{SC}, (c) FF, (d) PCE, (e) J-V curves and (f) stabilised power output measurements for the best performing devices.

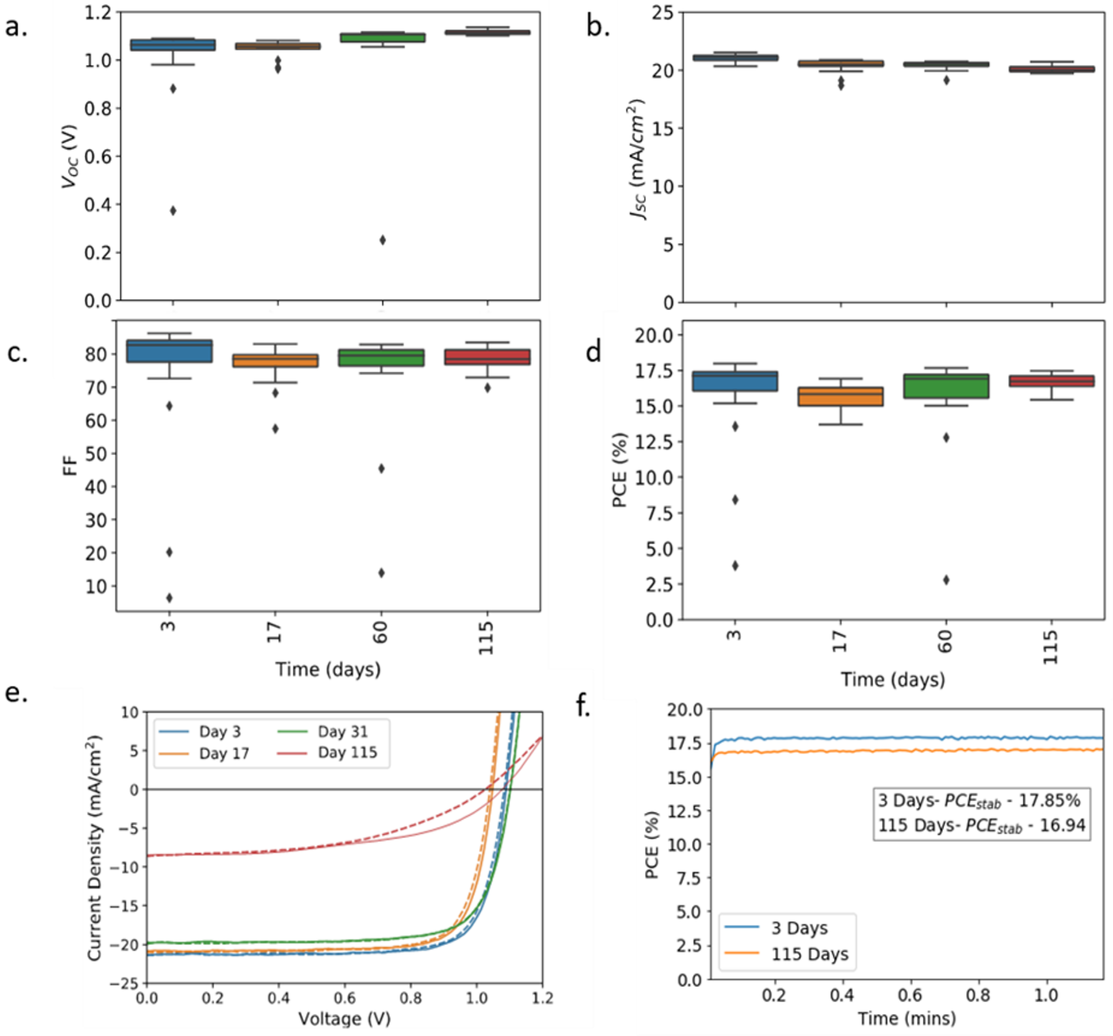

Figure 4.13: LT-aged TC-DMSO device metrics. (a) V_{OC}, (b) J_{SC}, (c) FF, (d) PCE, (e) J-V curves and (f) stabilised power output measurements for the best performing devices..

Storage Time (Days)	V_{OC} (V)	J_{SC} (mA/cm^2)	FF	PCE (%)	Number of devices
Fresh	1.08 ± 0.01 (1.09)	22.3 ± 0.4 (22.7)	75.1 ± 1.1 (76.9)	18.1 ± 0.5 (19.0)	7
17	1.10 ± 0.06 (1.11)	22.3 ± 0.5 (22.7)	71.6 ± 1.2 (73.2)	17.6 ± 1.2 (18.5)	4
31	1.01 ± 0.14 (1.11)	21.5 ± 1.2 (22.3)	64.5 ± 10.9 (71.2)	14.6 ± 4.4 (17.9)	4
60	1.06 ± 0.02 (1.08)	20.4 ± 0.5 (20.6)	58.8 ± 2.0 (63.2)	12.7 ± 0.7 (14.2)	6
115	1.00 ± 0.04 (1.08)	12.1 ± 1.0 (20.6)	41.1 ± 2.2 (63.2)	5.0 ± 0.6 (14.2)	5

Table 4.2: Device parameters: average (best) to accompany Figure 4.2a-c. Here the TC was dissolved in DMF/DMSO solvent and stored at RT. Devices were then made from these solutions at several time points as indicated

Storage Time (Days)	V_{OC} (V)	J_{SC} (mA/cm^2)	FF	PCE (%)	Number of devices
Fresh	1.08 ± 0.01 (1.09)	22.3 ± 0.4 (22.7)	75.1 ± 1.1 (76.9)	18.1 ± 0.5 (19.0)	7
17	1.08 ± 0.02 (1.11)	22.5 ± 0.3 (22.6)	72.6 ± 3.3 (74.9)	17.7 ± 0.8 (18.5)	5
31	1.10 ± 0.01 (1.10)	22.3 ± 0.3 (22.7)	72.7 ± 2.1 (75.0)	17.8 ± 0.6 (18.6)	2
60	1.09 ± 0.03 (1.13)	21.8 ± 1.0 (22.7)	69.7 ± 4.1 (73.2)	16.6 ± 1.5 (18.9)	6
115	1.10 ± 0.01 (1.10)	22.1 ± 0.4 (22.1)	64.9 ± 0.7 (66.6)	15.7 ± 0.3 (16.1)	4

Table 4.3: Device parameters: average (best) to accompany Figure 4.2d-f. Here the TC was dissolved in DMF/DMSO solvent and stored at LT. Devices were then made from these solutions at several time points as indicated.

solvent co-ordination. Indeed, in all solutions (even though such solvents are deuterated), we observe some residual non-deuterated solvent (i.e. DMSO or DMF) that is generated through the replacement of deuterium by a proton. As there is a different chemical environment in the TC solution and TCNB solutions, we observe some shift of the peaks associated with the residual solvents; for example we see peaks at 2.2 and 2.5 ppm which

Storage Time (Days)	V_{OC} (V)	J_{SC} (mA/cm^2)	FF	PCE (%)	Number of devices
Fresh	1.05 ± 0.04	20.7 ± 0.3	74.5 ± 5.8	16.6 ± 1.7	9
	(1.09)	(21.3)	(77.6)	(18.0)	
17	1.05 ± 0.03	20.7 ± 0.2	72.9 ± 3.4	15.8 ± 0.9	5
	(1.06)	(20.9)	(77.4)	(17.1)	
60	1.10 ± 0.01	17.8 ± 0.2	68.9 ± 3.1	13.5 ± 0.7	6
	(1.11)	(17.9)	(75.4)	(14.6)	

Table 4.4: Device parameters: average (best) to accompany Figure 4.12. Here the TC dissolved in DMSO solvent and stored at RT. Devices were then made from these solutions at several time points as indicated.

Storage Time (Days)	V_{OC} (V)	J_{SC} (mA/cm^2)	FF	PCE (%)	Number of devices
Fresh	1.05 ± 0.04	20.7 ± 0.3	74.5 ± 5.8	16.6 ± 1.7	9
	(1.09)	(21.3)	(77.6)	(18.0)	
17	1.04 ± 0.04	21.1 ± 0.6	73.2 ± 3.3	15.5 ± 0.9	4
	(1.09)	(20.7)	(75.5)	(16.9)	
60	1.09 ± 0.03	20.3 ± 0.5	73.0 ± 5.1	16.2 ± 1.5	6
	(1.11)	(20.8)	(76.2)	(17.7)	
115	1.12 ± 0.01	20.1 ± 0.3	74.2 ± 1.8	16.7 ± 0.6	4
	(1.12)	(20.3)	(76.7)	(17.5)	

Table 4.5: Device parameters: average (best) to accompany Figure 4.13. Here the TC dissolved in DMSO solvent and stored at LT. Devices were then made from these solutions at several time points as indicated.

are both associated with DMSO.

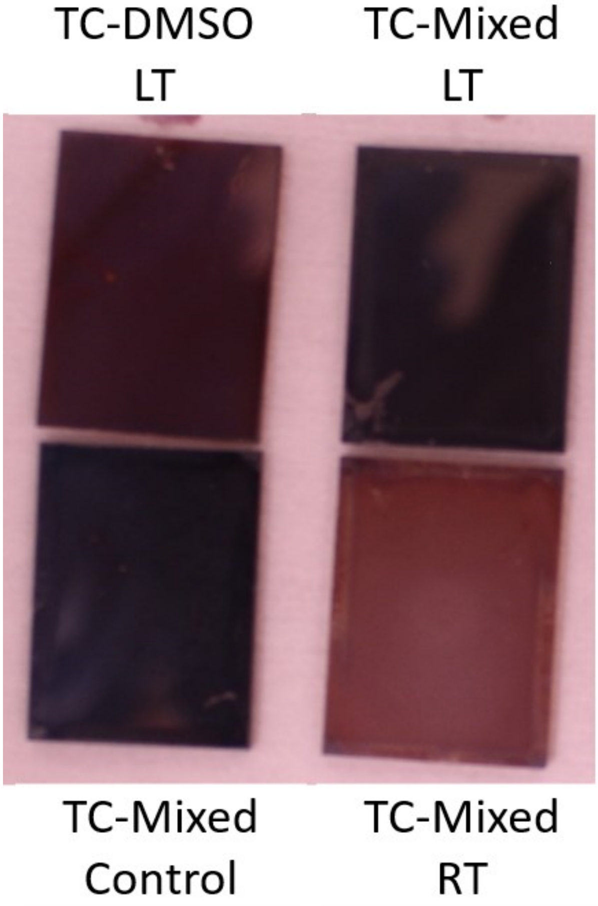

Figure 4.14: Images of all films prepared for solutions aged for 4 months together with a control film prepared from a freshly prepared solution.

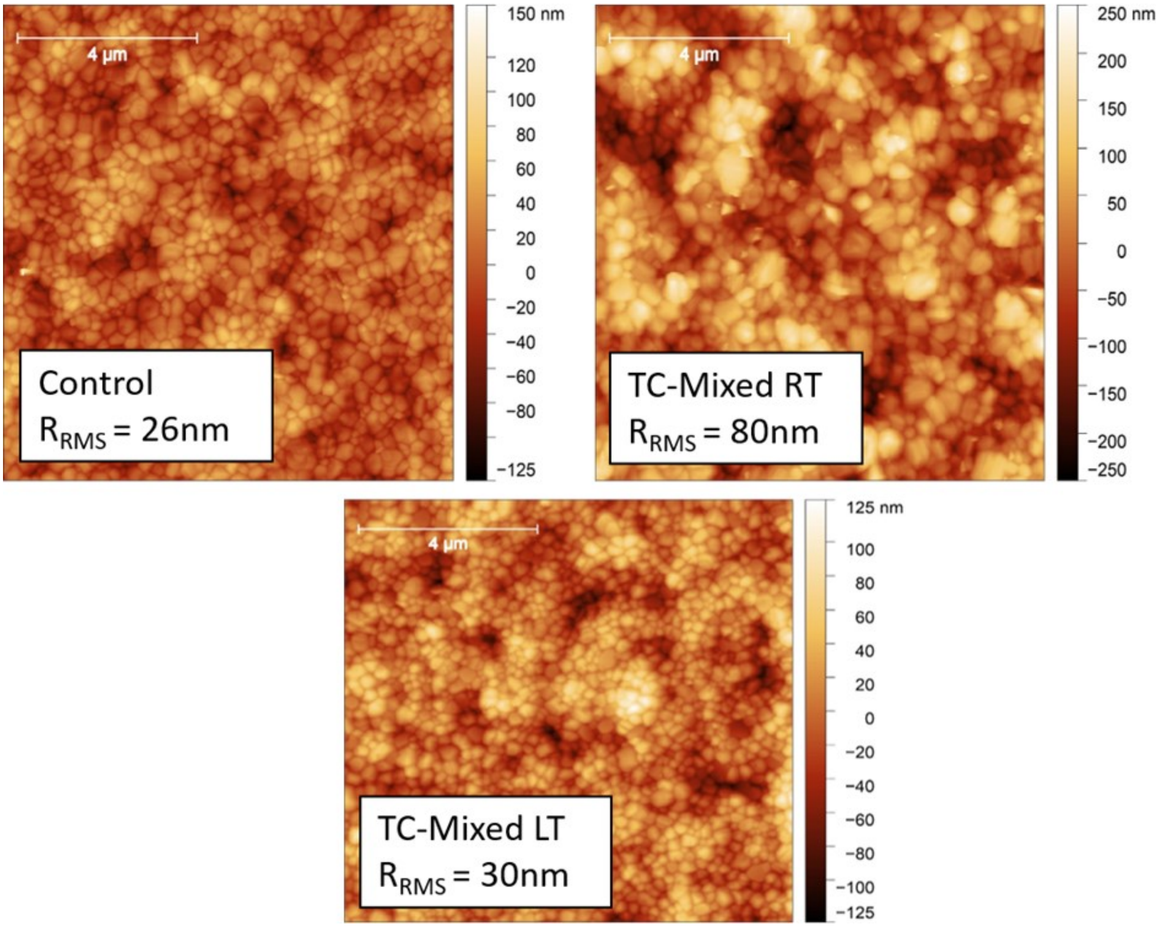

Figure 4.15: AFM height images for films prepared from 115 day aged (LT and RT) TC-mixed precursor solutions, together with a control film prepared from a freshly prepared solution.

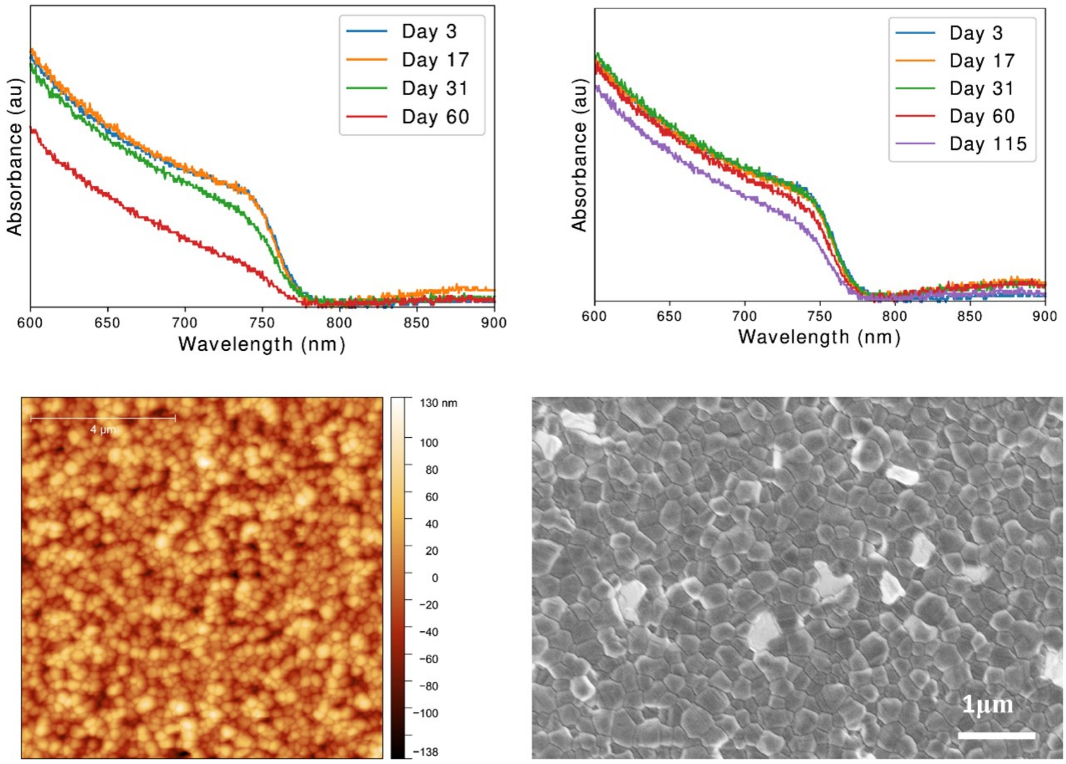

Figure 4.16: UV-Vis absorption recorded from films made from (a) RT-aged and (b) LT-aged TC-DMSO solutions at several time points. (c) AFM and (d) SEM images of films made from 4 month RT-aged DMSO precursor solutions.

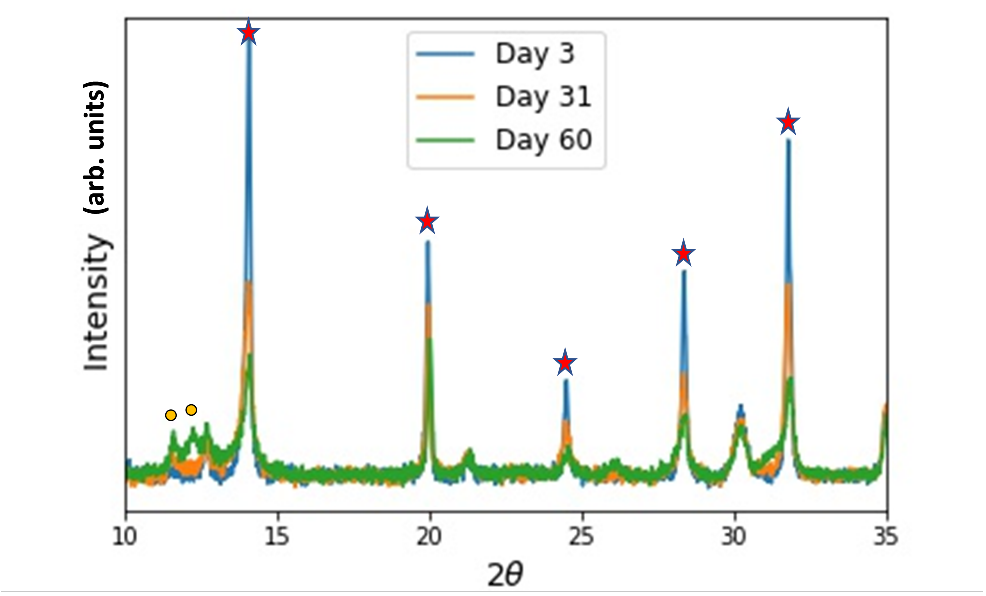

Figure 4.17: XRD patterns recorded from a film prepared from a RT-aged TC-DMSO precursor solution aged for several time points over a 2 month period.

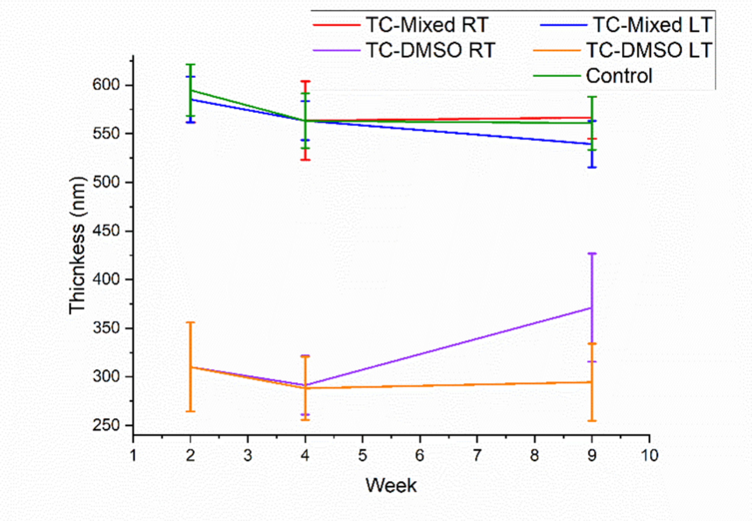

Figure 4.18: Thicknesses of films prepared at various points in time from progressively aged precursor solutions. The composition of the precursor is shown in the figure legend. Thickness was measured at various points across the film using surface profilometry.

Aging (days)	MA CH_3 (2.20 ppm)	FA CH (7.72 ppm)	MFA NH (7.76ppm)	MFA CH_3 (2.57 ppm)	DMFA CH_3 (2.73 ppm)
7	320	1550			
14	290	1550	50	40	
21	219	1430	90	90	10
28	169	1380	145	155	20

Table 4.6: Molarity (in mM) of organic molecules within solution estimated from NMR measurements (within ±10%) of aging TC solutions in DMF-d_7/DMSO-d_6. This was measured using Topspin and referenced to the internal standard TCNB having a molarity of 383mM. Peaks consisting of multiple hydrogen signals have been scaled to reflect their true concentration.

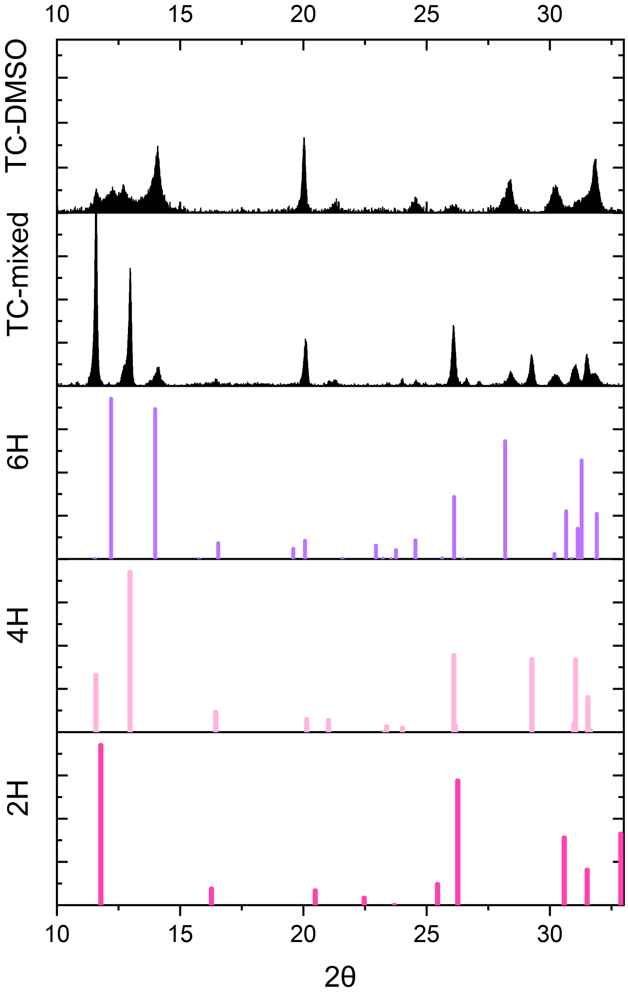

Figure 4.19: Simulated data for different $FAPbI_3$ 2H, 4H and 6H polytypes – based on CIF files from [140] - compared with XRD data from films created from 115-day RT-aged TC-mixed and TC-DMSO solutions. The dashed lines are used to guide the eye. This confirms that different polytypes are present in the films made from aged inks, and the nature of the polytype is apparently dependent on solvents. We find that the DMF/DMSO film exhibits many peaks that clearly align with a 4H polytype, (principally the peaks forming at 29.2° and 31.5°) indicating a combination of corner-sharing and face-sharing Pb-halide octahedra. .

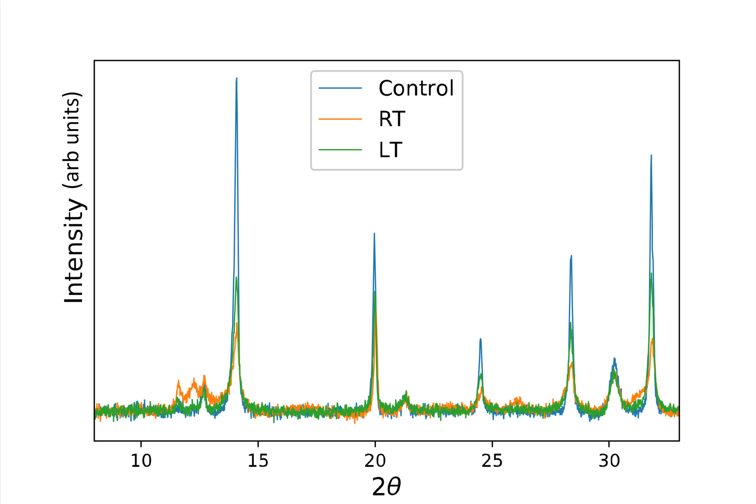

Figure 4.20: XRD patterns for films made from 115-day-aged TC-DMSO solution stored at RT (orange) and LT (green) compared with a control made from a fresh DMSO solution.

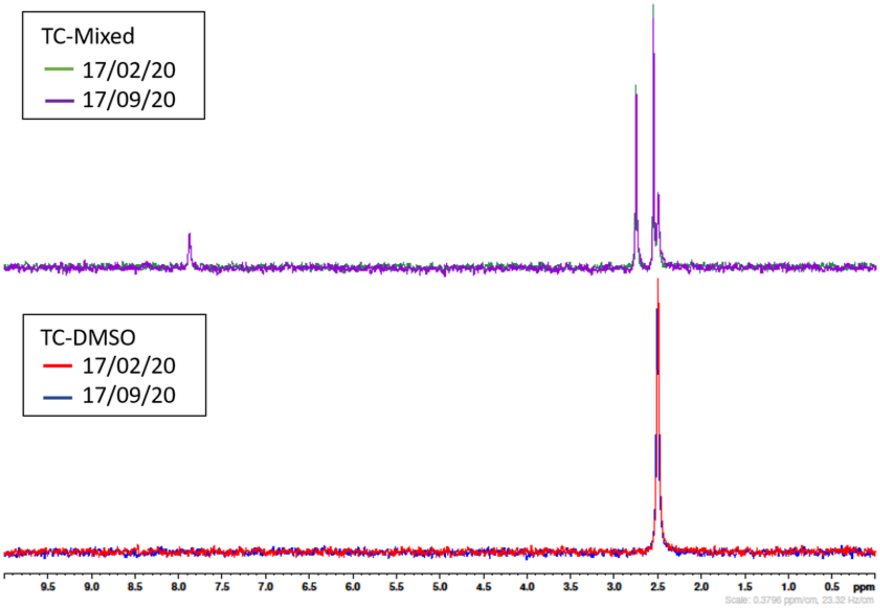

Figure 4.21: ^{2}H spectra of TC solutions dissolved in d_7-DMF /d_6-DMSO (4:1) (above) and d_6-DMSO (below) before and after 6 months storage at RT under nitrogen. Peaks at 2.5 ppm are assigned to d_6-DMSO and those at 2.55 ppm, 2.75 ppm and 7.87 ppm are assigned to DMF-d_7.

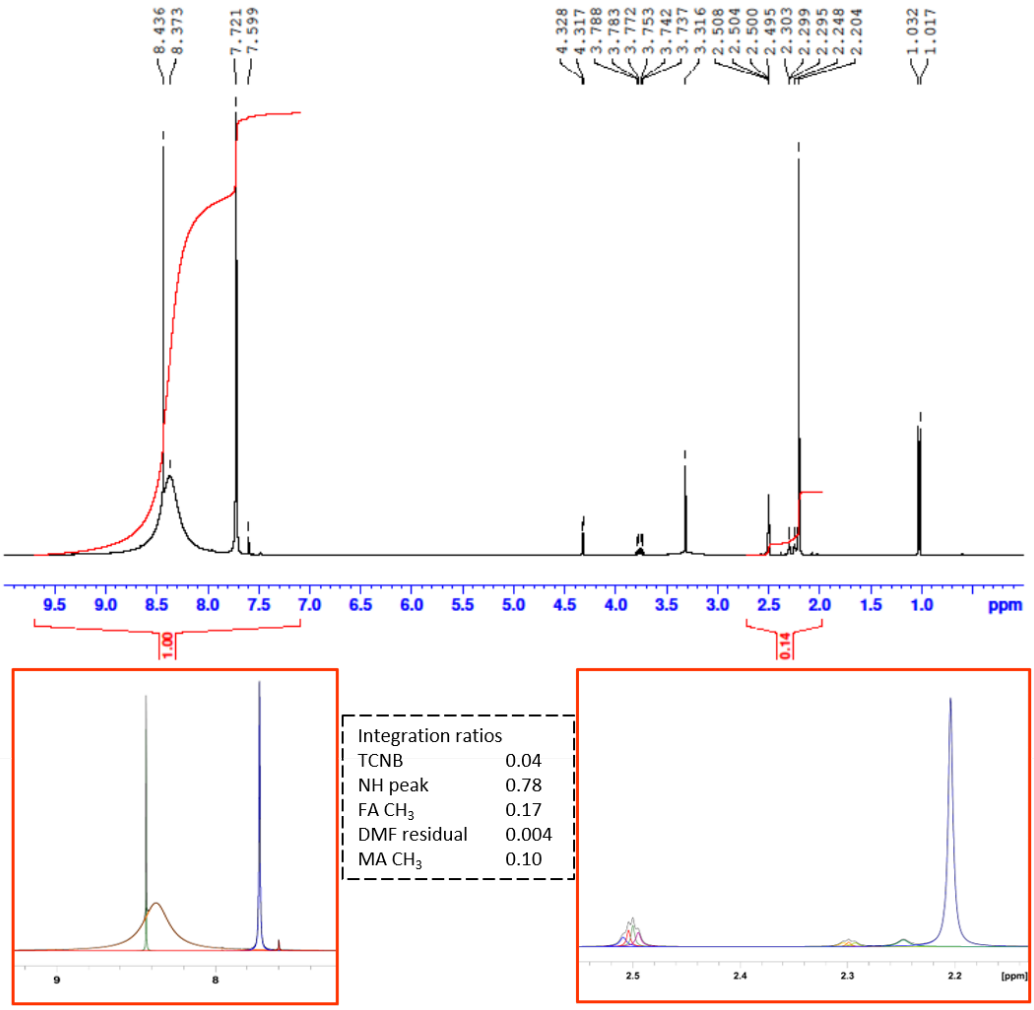

Integration ratios	
TCNB	0.04
NH peak	0.78
FA CH_3	0.17
DMF residual	0.004
MA CH_3	0.10

Figure 4.22: Full ^1H NMR spectrum of TC precursor in d_7-DMF/d_6-DMSO (4:1) after 7 days aging. Peaks at 7.72 ppm and 2.20 ppm are assigned to $C-H$ of FA and CH_3 of MA respectively. Peaks at 7.60 ppm and 2.29ppm are assigned as residual DMF impurities, and 2.24 ppm peak is assigned to residual DMSO impurities, confirmed with ^2H NMR spectra on similar solutions. For completeness, the deconvoluted spectra are also shown in the bottom two panels to show how the area of overlapping peaks are deconovolved.

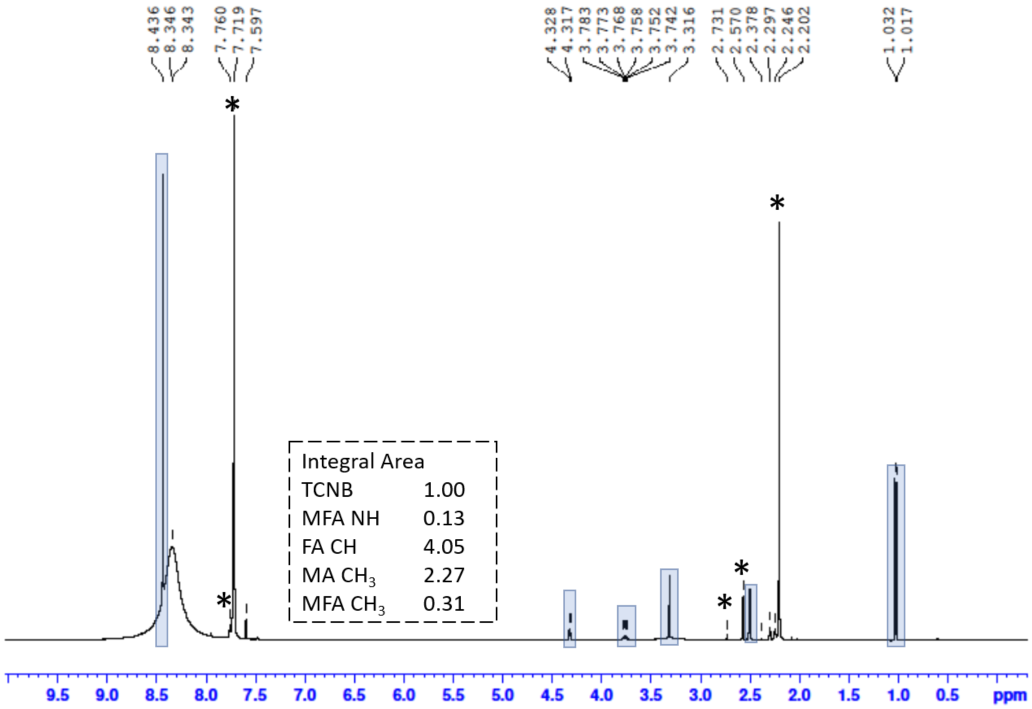

Figure 4.23: Full ^1H NMR spectrum of TC precursor in d_7-DMF/d_6-DMSO (4:1) after 14 days aging. Asterisks denote peaks of interest: Peaks at 7.72 ppm and 2.20 ppm are assigned to the $C-H$ of FA and CH_3 of MA respectively. Emerging peaks at 2.57 ppm and 7.76 ppm are assigned to CH_3 and NH of MFA respectively, with the peak at 2.73 ppm assigned to the CH_3 of DMFA. Peaks at 7.60 ppm and 2.29ppm are assigned as residual DMF impurities, and 2.24 ppm peak is assigned to residual DMSO impurities, confirmed with ^2H NMR spectra on similar solutions. Peaks highlighted in blue are from the internal standard. Integral values, referenced to the TCNB standard as 1.00, are shown in the inset box.

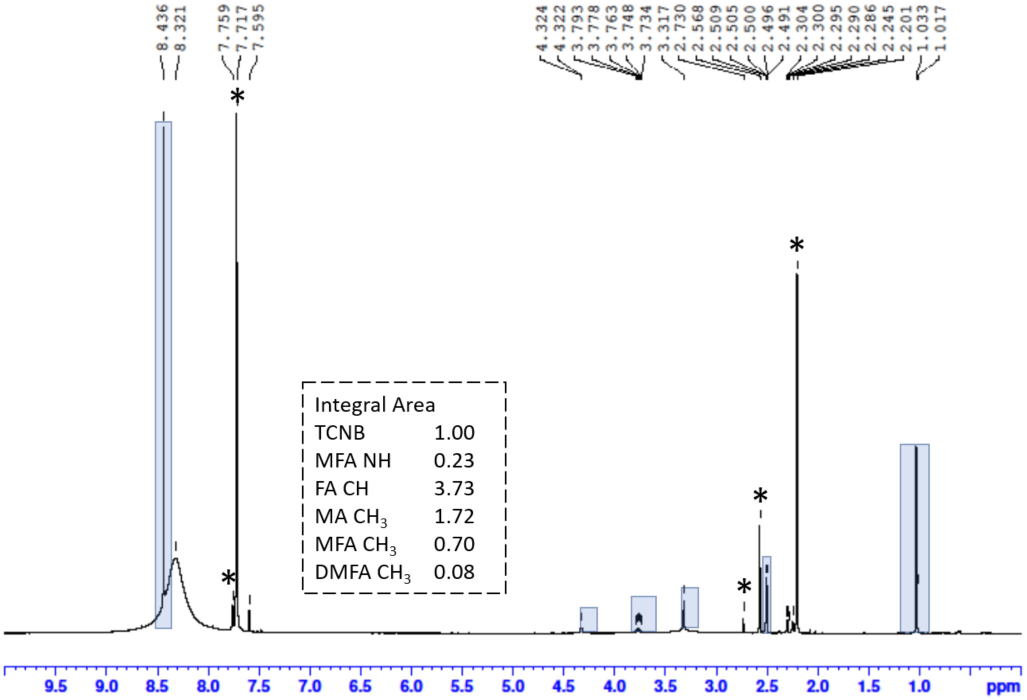

Figure 4.24: Full ^{1}H NMR spectrum of TC precursor in d_7-DMF/d_6-DMSO (4:1) after 21 days aging. Asterisks denote peaks of interest: Peaks at 7.72 ppm and 2.20 ppm are assigned to the $C-H$ of FA and CH_3 of MA respectively. Emerging peaks at 2.57 ppm and 7.76 ppm are assigned to CH_3 and NH of MFA respectively, with the peak at 2.73 ppm assigned to the CH_3 of DMFA. Peaks at 7.60 ppm and 2.29ppm are assigned as residual DMF impurities, and 2.24 ppm peak is assigned to residual DMSO impurities, confirmed with ^2H NMR spectra on similar solutions. Peaks highlighted in blue are from the internal standard. Integral values, referenced to the TCNB standard as 1.00, are shown in the inset box.

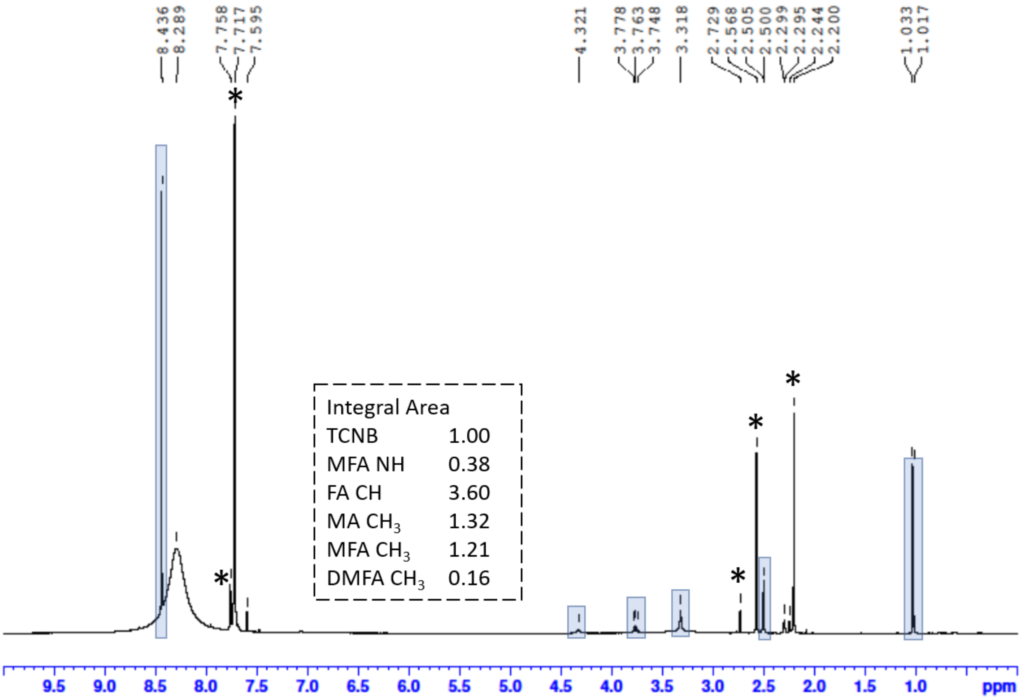

Figure 4.25: Full ^{1}H NMR spectrum of TC precursor in d_7-DMF/d_6-DMSO (4:1) after 28 days aging. Asterisks denote peaks of interest: Peaks at 7.72 ppm and 2.20 ppm are assigned to the $C-H$ of FA and CH_3 of MA respectively. Emerging peaks at 2.57 ppm and 7.76 ppm are assigned to CH_3 and NH of MFA respectively, with the peak at 2.73 ppm assigned to the CH_3 of DMFA. Peaks at 7.60 ppm and 2.29ppm are assigned as residual DMF impurities, and 2.24 ppm peak is assigned to residual DMSO impurities, confirmed with ^2H NMR spectra on similar solutions. Peaks highlighted in blue are from the internal standard. Integral values, referenced to the TCNB standard as 1.00, are shown in the inset box.

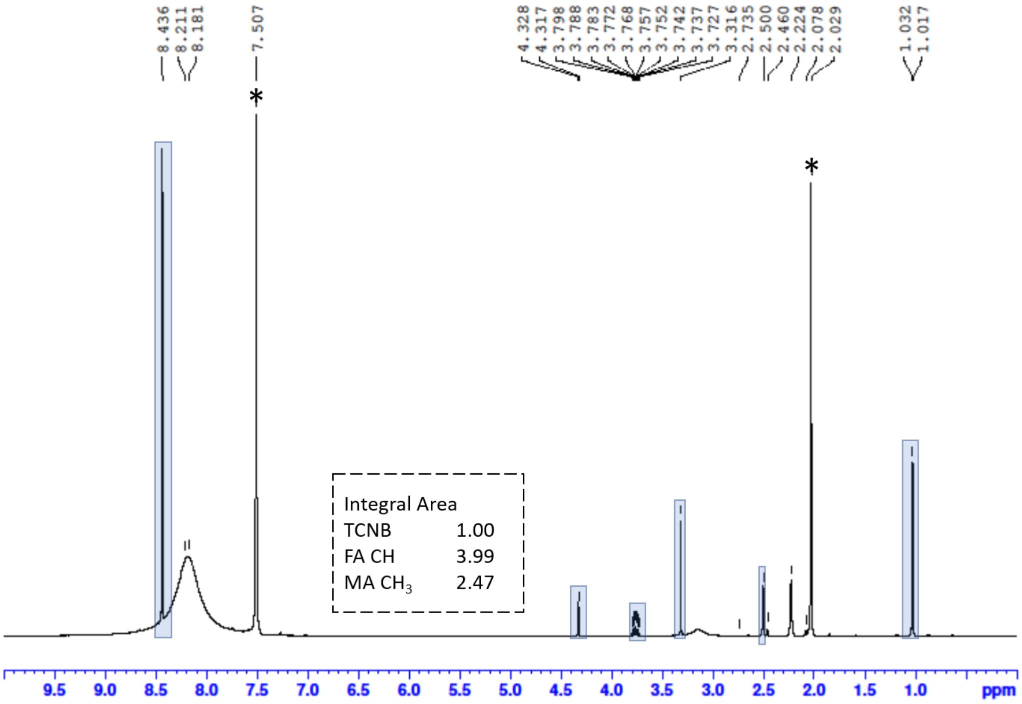

Figure 4.26: Full ^{1}H NMR spectrum of TC precursor in d_6-DMSO after 7 days aging. Asterisks denote peaks of interest: Peaks at 7.51 ppm and 2.02 ppm are assigned to the $C-H$ of FA and CH_3 of MA respectively. The peak at 2.22 ppm is assigned to residual DMSO impurities, confirmed with ^{2}H NMR spectra on similar solutions. Integral values, referenced to the TCNB standard as 1.00, are shown in the inset box.

Aging (days)	MA CH_3 (2.0 ppm)	FA CH (7.5 ppm)	MFA NH (7.6ppm)	MFA CH_3 (2.5 ppm)	DMFA CH_3 (2.6 ppm)
7	315	1527			
14	298	1465	29	28	
21	311	1506	51	50	
28	260	1445	66	66	7

Table 4.7: Molarity (in mM) of organic molecules within solution estimated from NMR measurements (within ±10%) of aging TC solutions in d6-DMSO. This was measured using Topspin and referenced to the internal standard TCNB having a molarity of 383mM. Peaks consisting of multiple hydrogen signals have been scaled to reflect their true concentration.

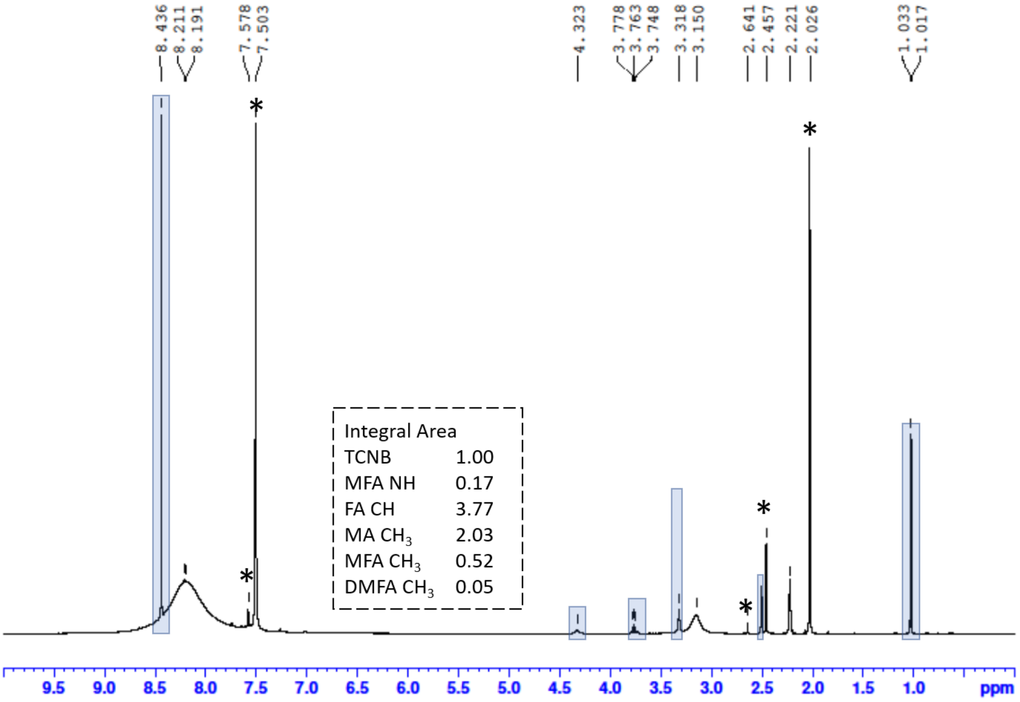

Figure 4.27: Full ^1H NMR spectrum of TC precursor in d_7-DMSO after 28 days aging. Asterisks denote peaks of interest: Peaks at 7.81 ppm and 2.28 ppm are assigned to the $C-H$ of FA and CH_3 of MA respectively. The peak at 2.22 ppm is assigned to residual DMSO impurities, confirmed with ^2H NMR spectra on similar solutions. Integral values, referenced to the TCNB standard as 1.00, are shown in the inset box.

Aging (days)	MA CH_3 (2.0 ppm)	FA CH (7.5 ppm)	MFA NH (7.6ppm)	MFA CH_3 (2.5 ppm)	DMFA CH_3 (2.6 ppm)
7	345	1561			
28	117	1287	161	173	21

Table 4.8: Molarity (in mM) of organic molecules within solution estimated from NMR measurements (within ±10%) of aging TC solutions in DMF-d_7. This was measured using Topspin and referenced to the internal standard TCNB having a molarity of 383mM. Peaks consisting of multiple hydrogen signals have been scaled to reflect their true concentration.

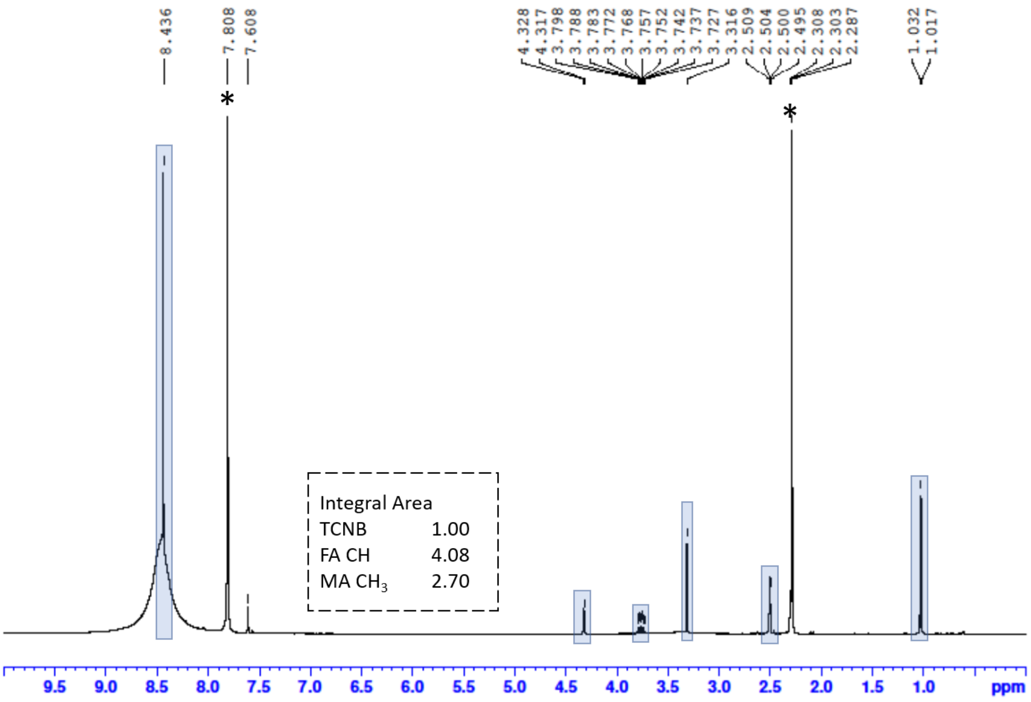

Figure 4.28: Full 1^H NMR spectrum of TC precursor in d_7-DMF after 7 days aging. Asterisks denote peaks of interest: Peaks at 7.81 ppm and 2.28 ppm are assigned to the $C - H$ of FA and CH_3 of MA respectively. Peaks at 7.60 ppm and 2.29 ppm are assigned to residual DMF impurities confirmed with ^2H NMR spectra on similar solutions. Integral values, referenced to the TCNB standard as 1.00, are shown in the inset box.

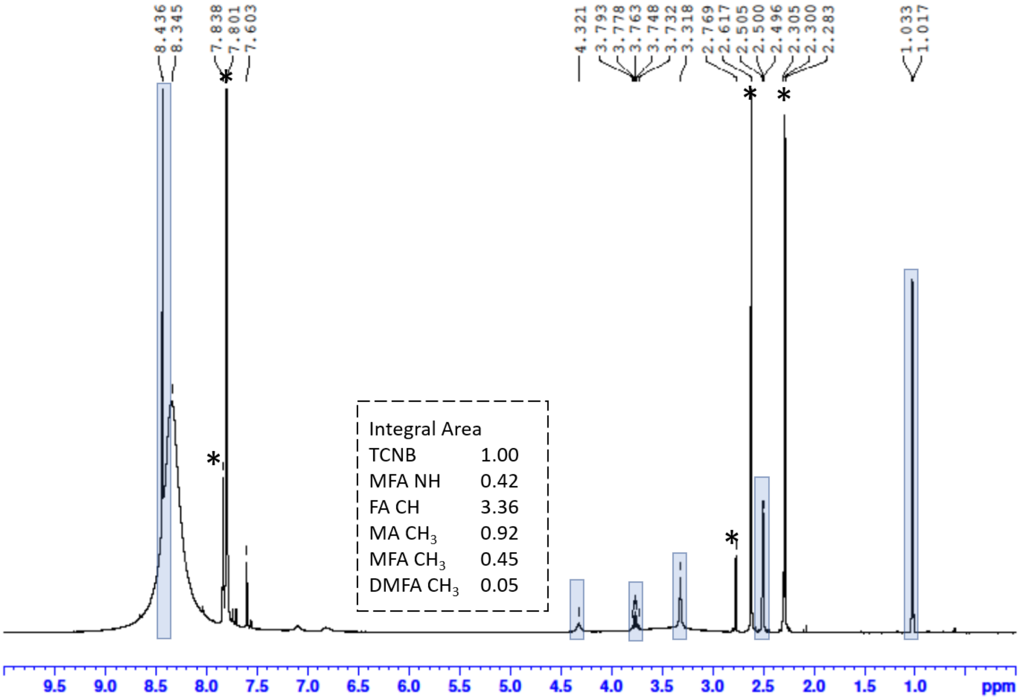

Integral Area	
TCNB	1.00
MFA NH	0.42
FA CH	3.36
MA CH_3	0.92
MFA CH_3	0.45
DMFA CH_3	0.05

Figure 4.29: Full 1^H NMR spectrum of TC precursor in d_7-DMF after 28 days aging. Asterisks denote peaks of interest: Peaks at 7.80 ppm and 2.9 ppm are assigned to the $C-H$ of FA and CH_3 of MA respectively. Emerging peaks at 2.61 ppm and 7.84 ppm are assigned to CH3 and NH of MFA respectively, with the peak at 2.77 assigned to the CH_3 of DMFA. Peaks at 7.60 ppm and 2.29 ppm are assigned to residual DMF impurities confirmed with ^2H NMR spectra on similar solutions. Integral values, referenced to the TCNB standard as 1.00, are shown in the inset box.

Chapter 5

Stability of Devices from Aged Precursor Solutions

5.1 Abstract

We have used this chapter to expand on the results of Chapter 4, and explore the stability of devices made from aged triple-cation inks. Here, we use a variety of device stressing conditions to probe resilience to intrinsic and extrinsic degradation factors. We find that devices made from inks which were stored at low-temperature maintain device performances similar to controls, further supporting the results of Chapter 4. However, we found that devices made from accelerated aged inks have exhibited some photodegradation effects under constant illumination. This effect was exacerbated under ATLAS Lifetime testing. Studies of the optical properties of these perovskite films indicated no change in the perovskite stoichiometry, however there are some indications of increased trap state density within these films. However, more intensive exploration is needed to pinpoint the exact causes of this photo-induced degradation.

5.2 Introduction

Over the past few years, accurately measuring and reporting PSC stability is now considered to be as important as measuring initial device statistics. Adapting to this has been a challenge for many in the community, as the stability of PSCs held under different aging conditions varies significantly based on many factors (device architecture, perovskite composition, etc). Also it is difficult to disentangle the primary degradation routes during such aging studies as there are usually a combination of external stresses (temperature, humidity, light, O_2 etc) in every chosen environment. For this reason, the field has struggled to define standardised stability measurements. The standardised tests set out by the International Electrotechnical Commission are often not suitable for PSC devices as they are designed for the more robust Si-PV. At the International Summit on Organic Stability (2010), organic photovoltaic (OPV) researchers tried to adapt IEC standards to apply to OPVs. These aims of these standards were to evaluate solar cells which are at the lab-scale experimental stage. The goal of setting these standards was to help standardise research metrics, rather than act a "standard qualification test".[154] At 11th International Summit on Organic and Hybrid Photovoltaics stability (2018) [154], a group of PSC researchers tried to achieve the same thing for PSC devices. This report created guidelines which outlined what information should be included for publication with regards to stability testing, defined “inert environment” experiments to test intrinsic stability of PSCs and discussed figures of merit for PSC stability. The experiments conducted in this chapter aim to follow some of these guidelines to the best of our ability and we endeavour to be transparent about our stability testing methods throughout.

While PSCs exhibit impressive device performance, their device stability has always been an issue.[155–158] Stability issues in PSCs fall into two basic categories: intrinsic and extrinsic factors. Intrinsic instabilities include phase instabilities - such as those seen in chapter 4 where non-perovskite polytypes such as δ-$FAPbI_3$ form - and intrinsic defects within the film (e.g. vacancies and interstitials), but can also refer to chemical instabilities within the device such as degradation of materials to produce harmful agents (for example, I_2 ions which can migrate through a device, to cause degradation of Ag contacts). Moreover, the extrinsic factors that can impair device stability include moisture, O_2, light and heat-induced reactions.[159] Many methods are often used in conjunction to improve the stability of PSC devices. Some extrinsic instabilities (such as oxygen and moisture degradation) can be mitigated with proper encapsulation of the PSC device.[158, 160], however these cannot mitigate degradation due to light and heat. Even with encapsulation, inherent instabilities need to be accounted for. For this, additives are often used to passivate defects in the film and prevent ion diffusion throughout the device.[157, 161, 162]

One important factor to consider when optimizing PSC device stability is perovskite composition. This was discussed in Chapter 2 but will be briefly summarized here. MA-based perovskites have been shown to be vulnerable under exposure to moisture [32, 35] and high temperatures [38]. $FAPbI_3$ has better light and temperature stability than $MAPbI_3$ [17] but is inherently phase unstable and also vulnerable to moisture. The incorporation of small amounts Cs^+ and MA^+ has been found to significantly improve the intrinsic stability of FA-based perovskites.[46] Another way to achieve more stable PSCs is optimize the halide composition.[17, 46] It has been demonstrated that $MAPb(I_{1-x}Br_x)_3$ perovskites have increased stability under high humidity when $x \geq 0.2$ [48]. However under light soaking, this mixed-halide phase with higher bromine content tends to phase-separate to an iodide-rich phase and a bromide-rich phase.[51] Despite these inherent instability, it has been demonstrated that mixed-halide mixed-cation perovskites demonstrate markedly improved device stability compared to single cation or single halide stoichiometries. Importantly, Saliba et al showed that triple-cation, mixed halide perovskite compositions (TCs) have increased stability maintaining over 18% PCE after 250 hours being held at maximum power point in an inert environment.[46] It is hereby thought that well encapsulated TC devices should have good device stability.

In order to conduct aging experiments efficiently, “accelerated aging” methods are often used to shorten overall experiment length. [148, 163] These often rely on the Arrhenius principle, which describes the relationship between a reaction rate, the reaction activation energy, E_A (kJ.mol^{-1}), and temperature using:

$$k = A \exp^{-\frac{E_A}{RT}} \tag{5.1}$$

Here, k is reaction rate, A is a constant, R is ideal gas constant, and T is temperature in Kelvin. This allows the relationship between reaction rate k_A at temperature T_A, and reaction rate k_B at temperature T_B to be expressed using:

$$ln(\frac{k_A}{k_B}) \propto -\frac{E_A}{R}(\frac{1}{T_A} - \frac{1}{T_B}) \tag{5.2}$$

This equation indicates that the rate of a specific reaction will increase exponentially as temperature increases. As a general rule of thumb, the rate of a reaction will roughly double for every 10°C/10K increase in temperature.

In Chapter 4, we have shown that low temperature storage of PSC solutions can increase ink lifetime, with these aged solutions being used to create efficient perovskite devices. However, we found that there is an apparent drop in stabilised PCE of devices made from ink stored for 6 months at ~ 4°C or low temperature (LT). Here, we explore the operational stability of devices made from aged inks. Specifically, TC perovskite solutions were aged at a range of temperatures ($4 - 40°C$) for 9 days then made into devices. The stability of these devices were tracked in dark inert conditions (GB Dark), illuminated inert conditions (GB Sol Sim) and "real world" conditions (ATLAS). Additionally, the effect of high stress conditions on the optical properties of films made from the "aged aging" inks were compared. It is found that aging TC perovskite inks does not appear to induce intrinsic instabilities when the devices are stored in GB Dark conditions. It is also found that devices made from LT-stored inks maintain impressive device performance in all aging conditions used here. We do however identify some light-induced instabilities in devices made from the "accelerated aged" solutions. Although the exact cause of these instabilities cannot be presently identified, we speculate that long term storage of inks at room temperature could increase the density of defects within a perovskite film, and reduce long-term device stability.

5.3 Experimental Details

Device Fabrication

In this work, we have studied the stability of devices made from aged TC precursor inks. The ink stock was made as described in Chapter 4, and used a DMF/DMSO (4:1) solvent blend. Initial experiments with n-i-p regular architecture as used in Chapter 4, demonstrated that these devices were not sufficiently stable for this experiment - possibly due to inherent stability issues with Spiro-OMeTAD. We instead used an inverted device structure for these devices consisting of ITO-coated glass/MeO-2PACz/TC perovskite/C_{60}/BCP/Ag.

For the hole transport layer, 60μl of a self-assembled monolayer (SAM), MeO-2PACz, stock solution (1mMol in ethanol), was spin coated at 3000rpm for 30s onto patterned ITO-coated substrates. These were then annealed for 10 minutes at 100°C in ambient conditions. The TC perovskite was filtered then deposited onto the SAM layer. At this point, the perovskite precursor must be spread with a pipette tip due to its low wettability. This was then spin coated with an accelerated rotation of 200rpm/s until 2000rpm, then spun at 2000rpm for 10s and 4000rpm for 20s. An antisolvent quench (100μl anisole) was applied 10s before the end of programme. Films were then annealed for 30 minutes at 100°C. These devices were then patterned in the glovebox. C_{60}, BCP and Ag were then thermally evaporated onto the devices with thicknesses of 23nm, 8nm and 100nm respectively. After fabrication, devices and films were encapsulated in an inert atmosphere using a UV-cured Blufixx LED epoxy and a glass encapsulation slide. In all cases, the epoxy covered the entire active area. Devices were tested with a Newport 92251A-1000 solar simulator calibrated to 1 Sun in ambient conditions, and J–V measurements recorded using a Keithley 237 source measure unit. Measurements were made by reverse sweeping between -0.1V and 1.2V at 100mVs^{-1}.

UV Vis absorption measurements were performed using an Ocean Insight FLAME miniature spectrometer. For PL measurements, films were excited with a 400 nm laser and PL emissions measured with an Ocean Insight FLAME miniature spectrometer.

Solution Aging

Precursor solutions were stored under various conditions before “aged-ink” devices and films were made. All solutions were sealed under an inert environment before storage. LT solutions were stored in ambient conditions at ∼4°C, and RT solutions were stored in a glovebox at ∼20°C. To simulate solution aging, solutions were held at ∼40°C using a temperature calibrated hotplate. Here, a stirrer bar was used to improve temperature uniformity within the solution.

Stability Measurements

The stability of devices made from a fresh stock of TC precursor ink was checked, and devices maintained ≥80% of their initial efficiency over 168h under ATLAS conditions. This ink was then divided and “aged” at various temperatures. The temperatures were 4°C (low-temperature -LT), 20°C (room temperature -RT) and 40°C (accelerated aging). Devices and films were made from solutions after after 1 week, and 2 weeks aging. Here, we assume through the Arrhenius equation that any reactions that occur in the RT (20°C) ink should happen at 4 times the rate when stored at 40°C. This experiment should reveal how long-term storage of precursor inks may affect operational device stability. Devices made from aged precursor inks were encapsulated in all cases and routinely tested over a 15 day period whist undergoing one of the following device aging protocol.

- **Storage in a dark, inert environment** i.e. covered with foil in a nitrogen glovebox (hence referred to as **GB Dark**) This experiment was designed to identify any intrinsic instabilities. J-V sweeps for GB Dark devices were measured intermittently using a Newport 92251A-1000 solar simulator in ambient conditions and a Keithley 237 source measure unit.
- **Aged in inert conditions under constant white LED illumination** (**GB Sol Sim**) This experiment was designed to identify any light induced reactions that may occur in devices. J-V sweeps were recorded intermittently using the Ossila I-V test system in inert conditions under a white Oriel LSH-7320 ABA LED light at 1 Sun. The defined device area is 0.04cm^2 as the device was unmasked. The scan rate was 0.2Vs^{-1} with 0.02V voltage increments.

- **Aged in an Atlas Suntest CPS+ Lifetime Tester** Here, devices were held at open circuit voltage, and constantly illuminated with a ∼1 Sun white light source (**ATLAS**). ATLAS aging is conducted in air and temperatures within the ATLAS can reach up for 50°C. ATLAS measurements were recorded using a Keithley 2400 source measurement under a 1 Sun white light and elevated temperature ($40 - 50$°C).The defined device area is 0.048cm^2 as the device was unmasked. The scan rate was 0.2Vs^{-1} with 0.02V voltage increments.

Test	Temperature	Light	Environment	Holding Bias
GB Dark	Ambient	None	Inert	None
GB Sol Sim	Ambient	White LED light source	Inert	None
ATLAS	Uncontrolled	1Sun White light source	Ambient	V_{OC}
ISOS-D-1I	Ambient	None	Inert	V_{OC}/MPP
ISOS-L-1I	Ambient	Solar Simulator	Inert	V_{OC}/MPP

Table 5.1: Conditions of our device aging protocol compared to the ISOS-D-1I and ISOS-L-1I criteria defined by the ISOS. [154] Inert refers to N_2 filled glovebox. V_{OC} and MPP refers to devices being kept at open-circuit voltage or maximum-power point voltage for the duration of device aging.

We believe that GB Dark and GB Sol Sim conditions meet most of the criteria for the ISOS-D-1I and ISOS-L-1I protocol respectively (see Table 5.1). However we acknowledge that intermittent J-V sweeps can give a misleading representation of true device stability. We also are aware that even with good encapsulation, the true barrier properties of these materials are not known. Therefore, we cannot assume that an encapsulated device in ambient conditions will perform in the same way as a device in an inert environment. Therefore, the ATLAS test conditions allow us to explore the stability of devices under a more high stress environment.

As both the ATLAS and GB Sol Sim could not be accurately corrected for the actual device area (due to lack of a calibrated mask), the results of these processes are normalised to the initial performance of each device. Where possible for GB Sol Sim and ATLAS measurements, external J-V sweeps were measured before and after aging using the Newport 92251A-1000 solar simulator and an appropriate mask to provide more accurate device metrics.

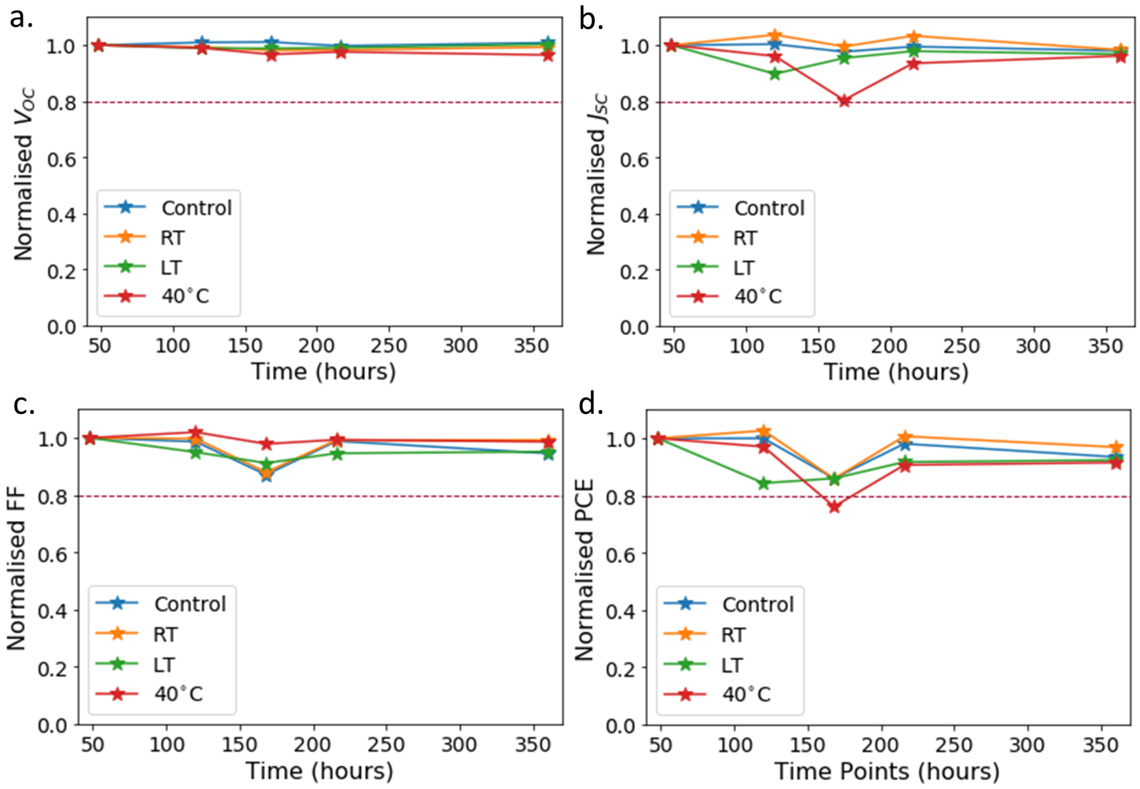

Figure 5.1: Normalised V_{OC} (a), J_{SC} (b), FF (c) and PCE (d) for champion devices stored in "GB dark" conditions. Inks were stored for 2 weeks at various temperatures before deposition (LT, RT, 40°C). At each time point , device metrics are normalised to their initial measurements taken at 48h. The red dotted line corresponds to 80% performance compared to inital device performance.

5.4 Results and Discussion

5.4.1 Intrinsic Stability

Figure 5.1 shows the results of the GB Dark experiment. Inks were stored for 2 weeks at a range of temperatures before devices are made from them. These subsequent devices were stored in GB Dark conditions and were tested periodically over a two week period. The metrics from aged devices were normalised to their initial performances at each time point. Here, it can be seen that there is no significant change in V_{OC} over this period (Figure 5.1a). Although there are some fluctuations in FF and J_{SC}, there is no significant reduction in device performance due to ink aging at any temperature compared to devices made from a fresh control ink. This correlates with the externally measured device metrics shown in Figure 5.8 (accompanying device values are in Table 5.2 and 5.3) for before and after GB-dark device aging. It can be seen in Figure 5.8 that the initial PCEs of devices made from the 40°C ink (champion PCE 16.4%) are lower than those from the control, LT and RT inks and there is a much larger spread in device performance. This is expected as it was seen in Chapter 4 that accelerated aging of this precursor ink leads to lower PCEs in devices.

We also find that the champion pixels for devices made from the 40°C ink maintain similar device metrics after 15 days GB Dark storage (≥80% of their initial PCE). It is noted that the spread in device performance increases drastically after GB dark aging for the device made from 40°C ink. This is due to a large number of non-performing pixels, which indicate these pixels have shunt pathways. However, we reiterate the pixels which have not shunted after aging maintain good device performance over this period.

5.4.2 Light Soaking Effects

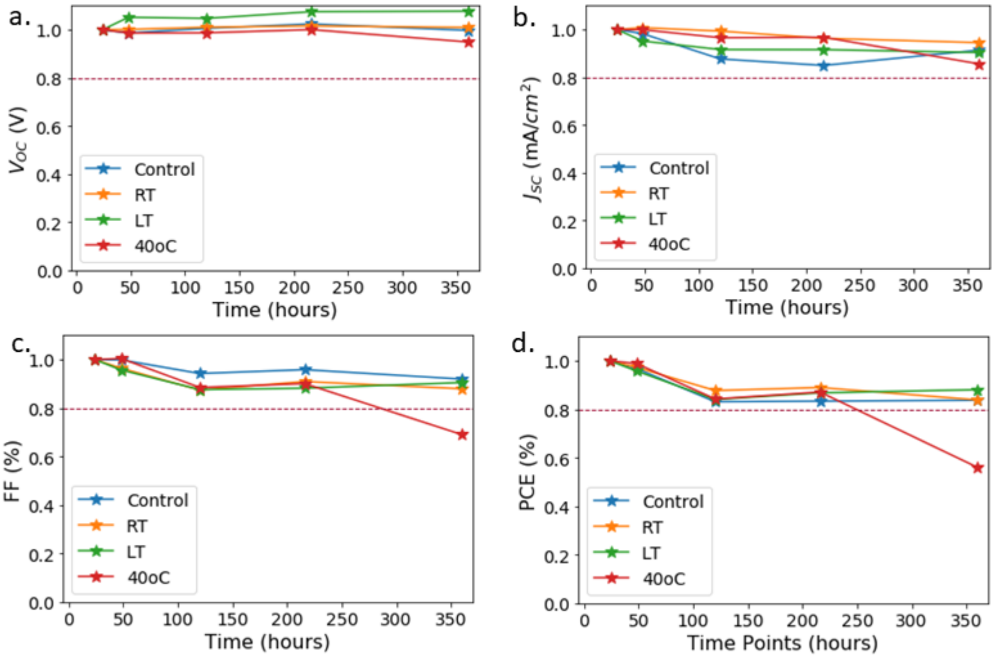

Figure 5.2: Average metrics of devices as they are aged in an inert environment under white light illumination (GB Sol Sim). Devices were made from solutions that had been aged for 2 weeks at LT, RT and 40°C ink.

To investigate any photoactivated instabilities established in devices prepared from aged inks, we exposed devices to a white LED light in inert conditions, and then measured J-V sweeps periodically over 360 hours (15 days). Figure 5.2 shows the normalised average device metrics for devices stored in GB Sol Sim conditions. Excitingly, we find that devices made from LT and RT inks do not show significant deterioration under constant illumination compared to controls, maintaining over 80% of their initial PCE after 360 hours aging. In fact, devices made from LT-stored inks appear to maintain slightly better device performance under GB Sol Sim conditions than the control devices, due to a slightly increased V_{OC}. However, devices made from the 40°C ink (representing accelerated aging) underwent a reduction in device performance after 216 hours. Here we see a drop in all metrics between these time points, but the PCE performance drops with normalised FF which drops by 34% between these timepoints. Figure 5.9 and Table 5.4 and 5.5 show externally measured device metrics taken before and after aging in GB Sol Sim conditions. These con-

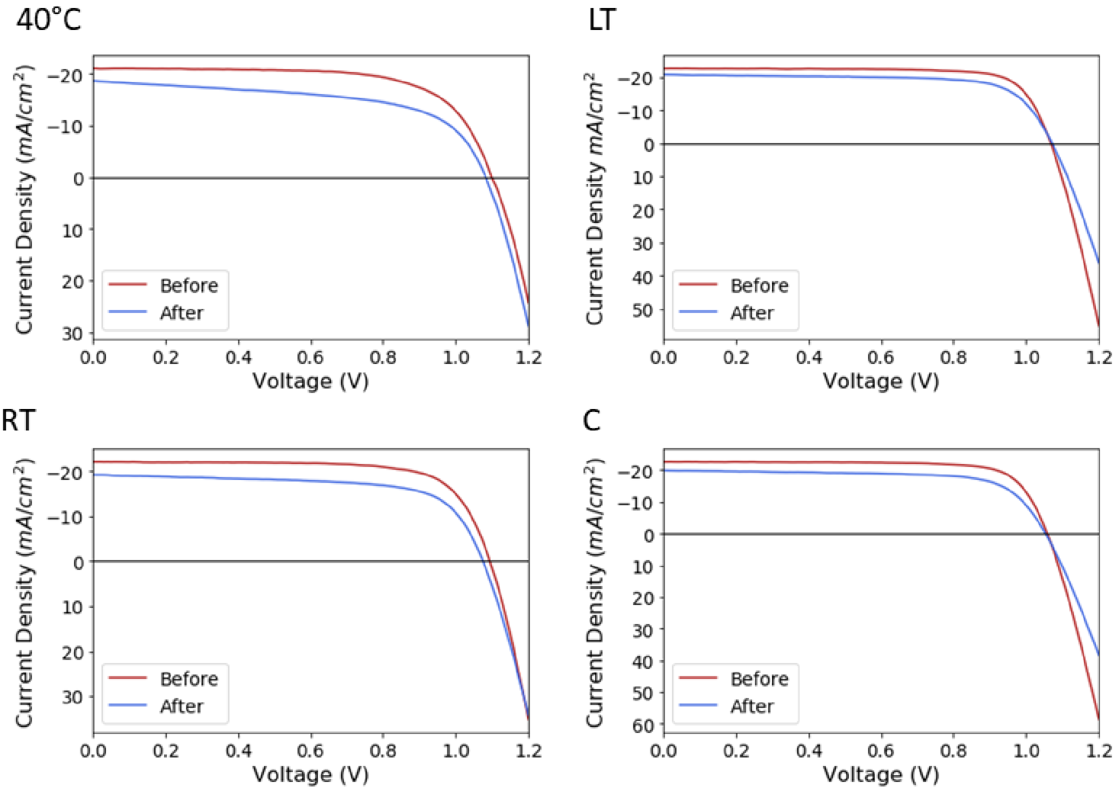

Figure 5.3: Reverse J-V sweeps for the champion devices before and after 15 days device aging under GB Sol Sim conditions.

firm the results in Figure 5.2 are representative of device performances for champion devices.

Figure 5.3 plots J-V sweeps for champion devices before and after 15 days aging under GB Sol Sim conditions. In all cases, we see a slight reduction in J_{SC} after device aging. Additionally, Table 5.4-5.5 (see Supplementary Information) indicates a significant drop in FF after device aging in all cases. This shows that even devices made from freshly-prepared inks are not completely stable under LED illumination. However, we note that for the device made from the 40°C aged ink, there is a slight change in the gradient of the curve near J_{SC} which is normally associated with an increase in shunt resistance (R_{SH}). This will change the area under the curve, and explain the larger reduction in FF. We have seen in Chapter 4, that as solutions age, the surface morphology of films changes, becoming more uneven and having increased roughness. We speculate that there are more "vulnerable" spots in the films made from the 40°C aged ink, which under the operational stress of a device may generate defects or pinholes, increasing the density of shunt pathways in the device. However, this has a relatively small effect on device performance, as even the device made from 40°C aged ink maintains over 70% device performance after such continuous stress. To follow up this work, we note that longer term ink aging experiments are needed to explore this effect fully.

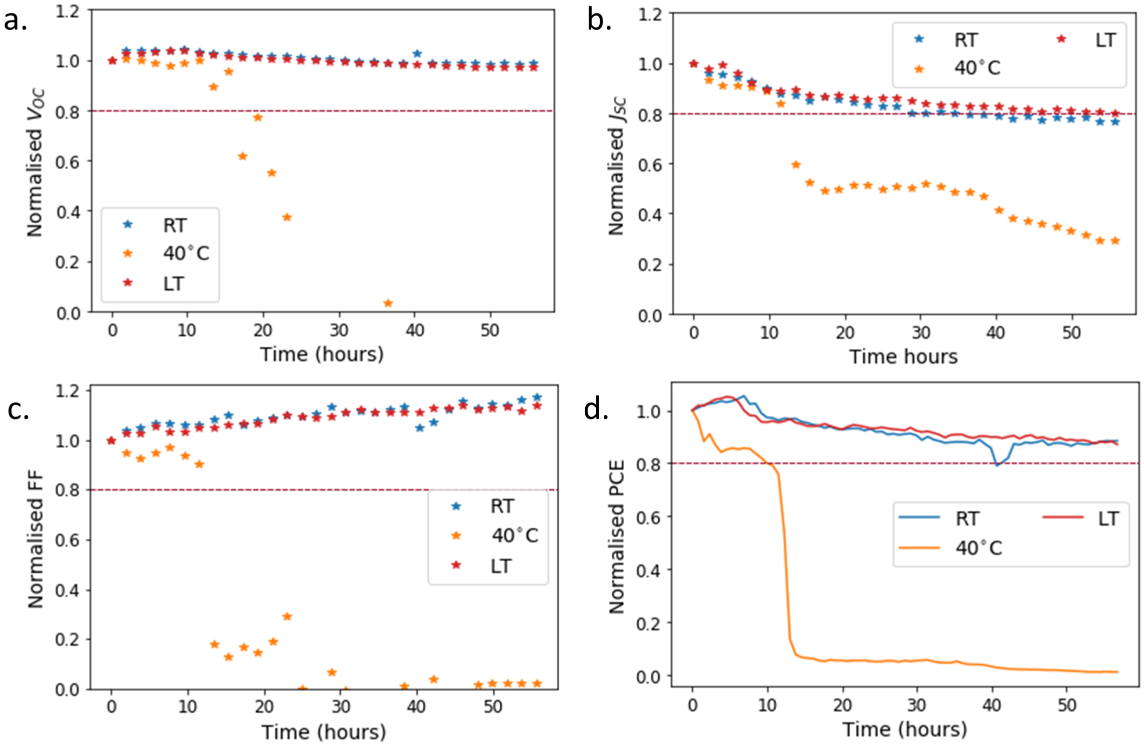

Figure 5.4: Champion pixel metrics of devices aged under ATLAS tester conditions. Devices were made from TC solutions aged for 1 week aged at RT, LT and 40°C.

5.4.3 ATLAS Aging

Devices were aged in an ATLAS lifetime tester to investigate their stability under constant voltage and constant illumination in near ambient conditions. Additionally, we note the temperature of the ATLAS lifetime tester can reach $40-50$°C, although temperature was not carefully controlled during this experiment. Devices were made from solutions that were aged for 1 week at 40°C, RT and LT. Device performance was then tracked over a three day period (around 60 hours). J-V sweeps were sequentially recorded for each pixel on each device, so each device was tested approximately every 20 minutes. This allowed us to establish a clear picture of exactly when device deterioration takes place. For the best pixel from each device, we normalised metrics to the initial ATLAS J-V sweep. This data is shown in Figure 5.4. Tables 5.6 and 5.7 (see Supplementary Information) along with Figure 5.10show externally measured device metrics taken before and after this aging process which confirm these results with accurately represent device performance.

Figure 5.4 shows that for the champion pixels made from RT and LT aged inks demonstrate an impressive device stability over 56 hours, although there is slight reduction in PCE due to a reduction in J_{SC}. It is apparent however, the device made from the 40°C-aged ink undergoes complete failure after 12 hours. Again the J_{SC} is found to dramatically drop, but interestingly the V_{OC} become so erratic we assume this is no longer functioning as a solar cell. To confirm this, Figure 5.5 shows the J-V sweeps taken during

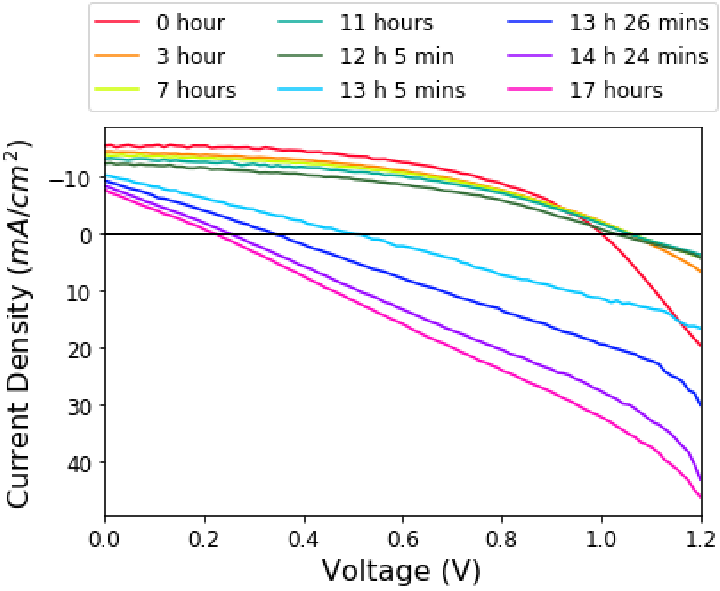

Figure 5.5: J-V sweeps taken for the champion pixel of the device made from 40°C aged inks. Measurements were taken within the ATLAS lifetime tester during ATLAS aging.

device aging in the ATLAS tester. It can be seen that as the device ages both J_{SC} and FF reduce significantly and the J-V curve loses it characteristic shape. Between 12-13 hours, the device loses all diode behaviour. This indicates the shunt density pathway has increased throughout the device and the device is now acting as a resistor. These conclusions are again supported by the external device metrics measured after ATLAS aging (see Figure 5.10, Table 5.6 and Table 5.7 in Supplementary Information). However, we can see that even devices made from RT and LT aged inks have an increased amount of device shortages after undergoing ATLAS testing.

This study was then repeated using precursor inks which had been aged for 2 weeks at various temperatures (Figure 5.6). Unfortunately, due to issues with the Keithley 2400 J-V sweeping, this data is somewhat intermittent with gaps in the data between hour 1-18 and hours 55-90. However, these devices were still held under illumination and ambient conditions throughout the experiment. It can be seen that 100 hours aging in the ATLAS tester caused device failure for devices made from both the RT and 40°C aged inks. For devices made from 40°C stored ink, we see a similar trend as seen in Figure 5.4 where device failure correlates with erratic V_{OC} measurements. Interestingly, the dramatic deterioration in the device made from the RT ink is due to a reduction in FF. We note it is possible the device encapsulation failed leading to device failure. More rigorous study of these conditions including more devices and a more continuous testing environment is needed to fully confirm what is causing this degradation. Nevertheless, we can confirm from this experiment that only devices prepared from the LT-aged inks can maintain a high stability, similar to the control devices under these conditions. This further confirms the necessity of low temperature storage of perovskite precursor inks as shown in Chapter 4.

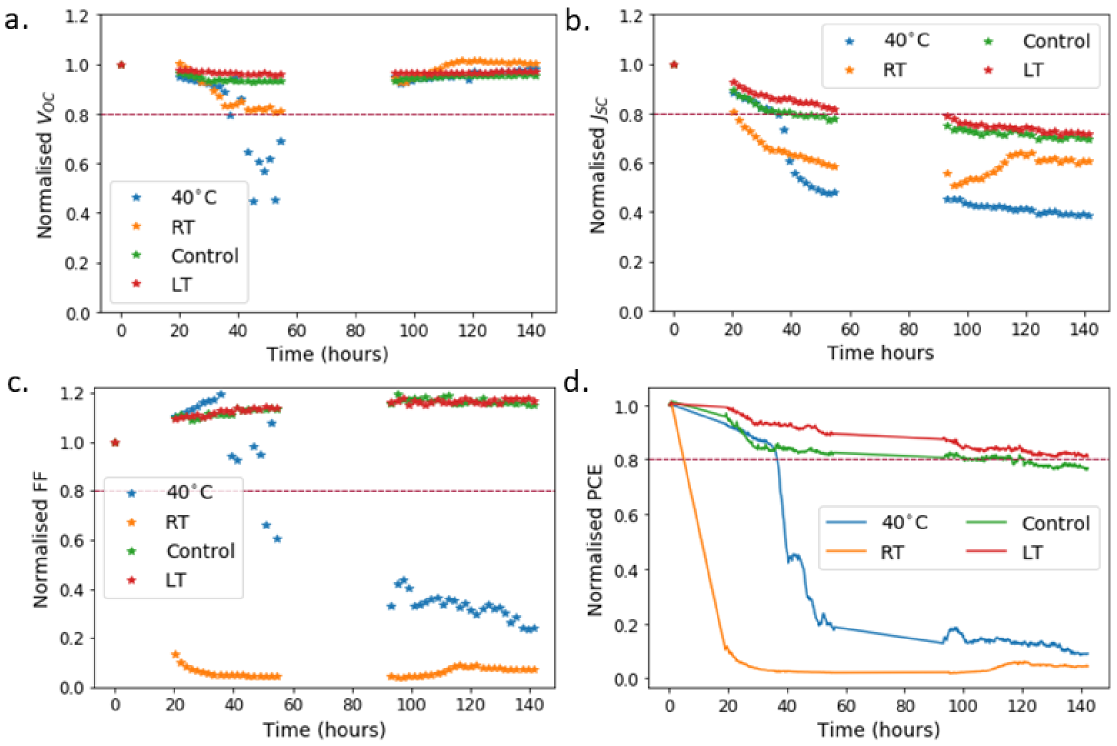

Figure 5.6: Device metrics for devices aged in the ATLAS lifetime tester. These devices made from TC solutions aged for 2 week aged at RT, LT and 40°C. Control devices were made from a freshly-made TC solution.

5.4.4 Film Study

To investigate whether the photo-induced degradation is due to changes in the perovskite layer or whether it was caused by an interaction with a transport layer, we conducted aging studies on isolated perovskite films. Films were made from a freshly prepared TC ink, encapsulated and placed in GB dark, GB Sol Sim or ATLAS aging conditions for 5 days. The remaining TC precursor ink was then aged for 9 days at 40°C and films were made from these solutions, encapsulated and measured as with the freshly prepared ink.

Figure 5.7 a-b show the UV-Vis absorption and PL spectra of films made from fresh inks. These films were then aged under GB Dark, GB Sol Sim or ATLAS conditions. It can be seen that the films from the freshly prepared ink show no significant difference in absorption or PL profiles after GB dark and GB Sol Sim stressing. However, there is a significant reduction in PL intensity for the films aged under ATLAS conditions. This is not unexpected as it is likely these films will experience high temperatures as well as constant illumination during this aging. We also acknowledge that imperfect encapsulation, or deterioration of the encapsulation material over time, could potentially expose the perovskites to moisture or oxygen, which could accelerate this deterioration. However, any

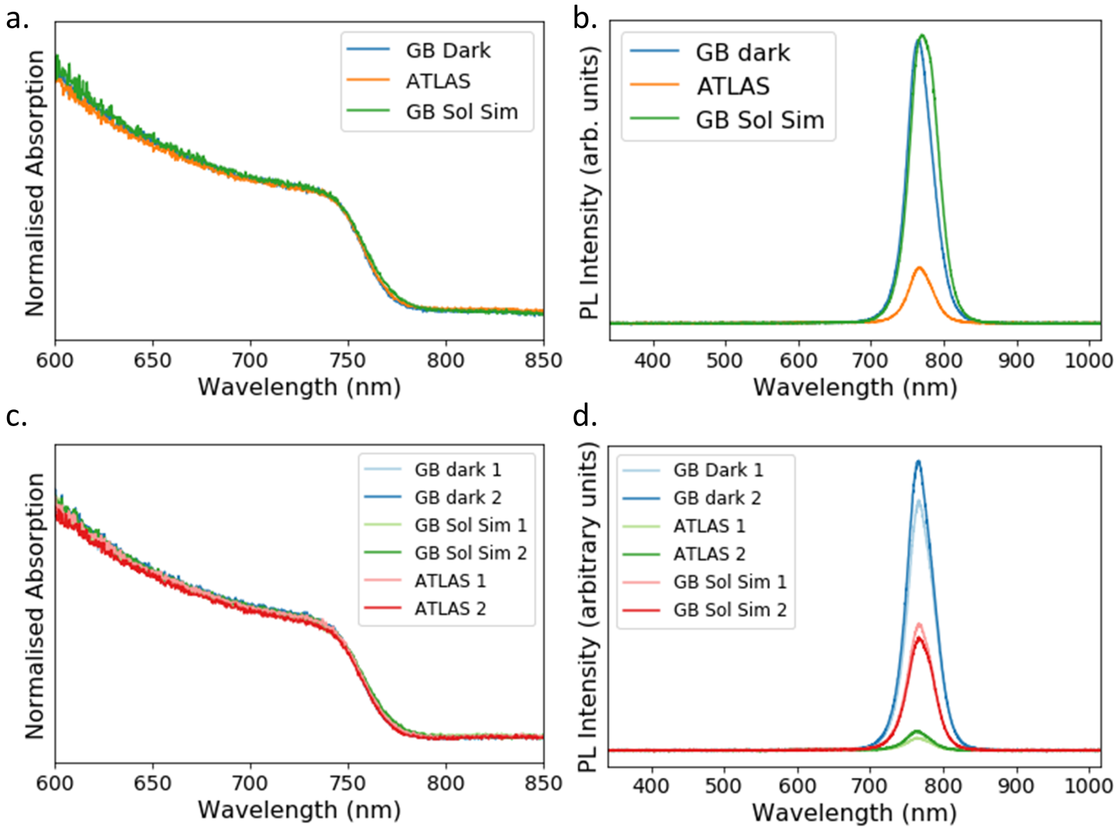

Figure 5.7: UV-Vis Absorption (a) and PL (b) spectra for films made from a freshly made TC ink. UV-Vis Absorption (c) and PL (d) data for films made from TC inks that had been aged for 9 days at 40°C. In all circumstances, films were encapsulated after deposition films were aged in either GB dark, GB Sol Sim or ATLAS conditions for 5 days.

change in composition or phase of the perovskite layer would be evident in changes in the absorption profile. We therefore speculate that trap states may be generated in the perovskite layer during ATLAS aging, which could result in non-radiative recombination routes, quenching PL intensity.

Figure 5.7 c-d show UV-Vis absorption and PL spectra for films prepared from aged inks. These films were then aged for 5 days under GB Dark, GB Sol Sim and ATLAS conditions. Here, as was seen for the films prepared from fresh solutions, we see no real difference in the absorption profile over time. However, we observe an interesting phenomenon in the PL emission intensity. After GB dark aging, there is still a high level of radiative emission from films made from these aged inks, but the GB Sol Sim aged-films shows significantly reduced PL intensity, and the ATLAS films are even less emissive. This is the same effect as seen in Figure 5.7a-b for the ATLAS aged films and hereby suggests it results from the same degradation mechanism. Therefore, this cannot be an effect due solely due to oxygen or moisture ingression, as the GB Sol Sim films were not exposed to ambient conditions for long periods of time.

We note that these measurements were taken after 5 days (120 hours) of film aging. It can be seen in Figure 5.2 that devices prepared from inks aged at 40°C maintain good device performance for over 200 hours under the GB Solar Sim. We conclude therefore that any perovskite deterioration for GB Sol Sim aged-films after 120 hours is not yet significant enough to inhibit device performance. However, we see in Figure 5.4 that devices made from 40°C aged inks exhibit device failure well before this 120 hour time point in the ATLAS tester. It is therefore possible that in this case, PL quenching results from an increase in trap states within the perovskite film and therefore an increase in non-radiative recombination; an effect which has been reported previously.[164, 165] This could also explain the erratic V_{OC} observed in the Figure 5.4. However, in order to specifically disclose the mechanisms responsible for such effects in these films will require an intensive study with longer ink aging times, longer device tracking and with more extensive study of materials post-device aging. We also note that the PL measurements taken during this study were only measured at one angle and no quantification data can be extracted from this. Therefore to further confirm and explore this effect, we would recommend that collecting time-resolved photoluminescence (TRPL) or photoluminescence quantum yield (PLQY) data on these films. These techniques could illuminate more about if and when there are trap states forming in films made from aged TC solutions. At the very least, further measurements of this should be taken using an integrated sphere.

5.5 Conclusions

We have examined the stability of devices made from TC inks aged at various temperatures. We have used three different device aging conditions (GB Dark, GB Sol Sim, ATLAS) to explore the intrinsic and extrinsic vulnerabilities of devices and films made from aged inks. We found that champion devices made from aged inks show no increased degradation after GB dark aging. This indicates that the intrinsic stabilities of these perovskite films (such as phase instabilities) are not affected significantly as a result of solution aging. We also found that devices made from LT-stored inks maintain impressive device performances under all aging conditions studied. This confirms that ink stability can be prolonged by storing precursor inks at low temperatures as described in Chapter 4. We identified however that devices made from inks that has undergone accelerated aging (at 40°C) show reduced device performance after continuous illumination in a glovebox environment (GB Sol Sim). This is linked with a reduction in FF from aged devices and J-V sweeps show a potential increase in shunt pathway density as these devices age.

We have also found that after 12 hours aging in the ATLAS tester, devices made from accelerated aged ink exhibit device failure. J-V sweeps indicate this is due to defects forming in the film, causing shunt pathways and hence the device loses all solar cell function. By studying isolated perovskite films, we found that films made from aged inks show a decrease in PL intensity under increasing film stress. However there is no change in PL peak wavelength or absorption profile. This could indicate an increase in non-radiative recombination is likely at play. We hereby speculate that in films prepared from accelerated-aged ink, there is a higher concentration of “vulnerable points” in the film that, under increased operational stress, can act as trap states or eventually shunt pathways through the perovskite layer.

Due to several circumstances, the length of this experiment was shorter than ideal. In order to elaborate on these results, more work is needed, both with longer ink aging times and longer device testing periods. Additionally, in further work we would reccomend exploring the interactions between the various layers of the perovskite device to further probe how the perovskite layer changes under these various aging conditions.

5.6 Supplementary Information

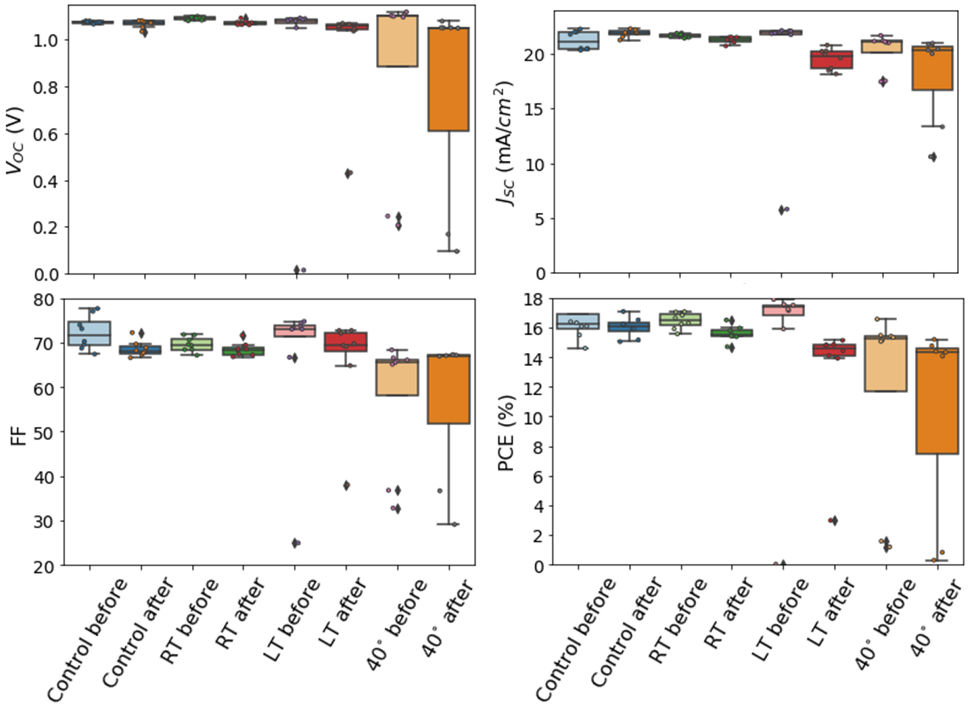

Figure 5.8: Device metrics before and after GB Dark device aging for 15 days.

Ink	V_{OC} (V)		J_{SC} (mA/cm^2)		FF		PCE (%)	
	Average	Best	Average	Best	Average	Best	Average	Best
40°C	1.10	1.11	21.1	21.8	66.2	67.6	15.4	16.4
LT	1.08	1.09	21.9	22.0	73.9	75.5	17.5	18.0
RT	1.09	1.10	21.2	22.3	70.5	72.4	16.6	17.2
Control	1.07	1.07	21.2	22.3	73.4	77.7	16.7	18.5

Table 5.2: Table showing average and best device metrics for champion PCE devices measured before aging in GB Dark conditions. These devices made from inks that had been stored at various temperatures for two weeks.

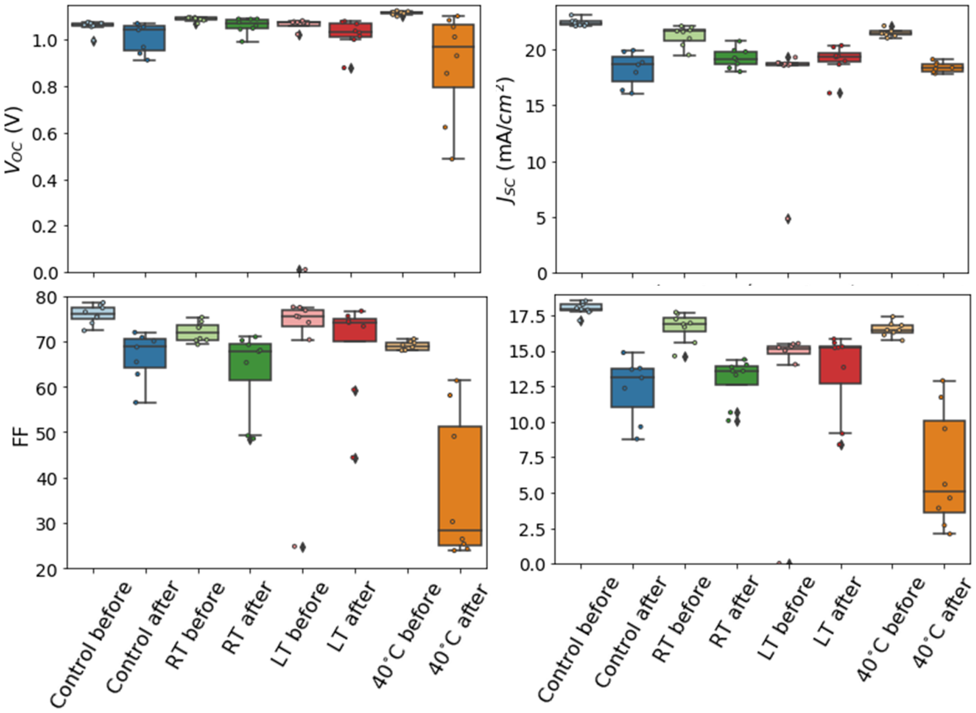

Figure 5.9: Device metrics before and after GB Solar Sim device aging for 15 days.

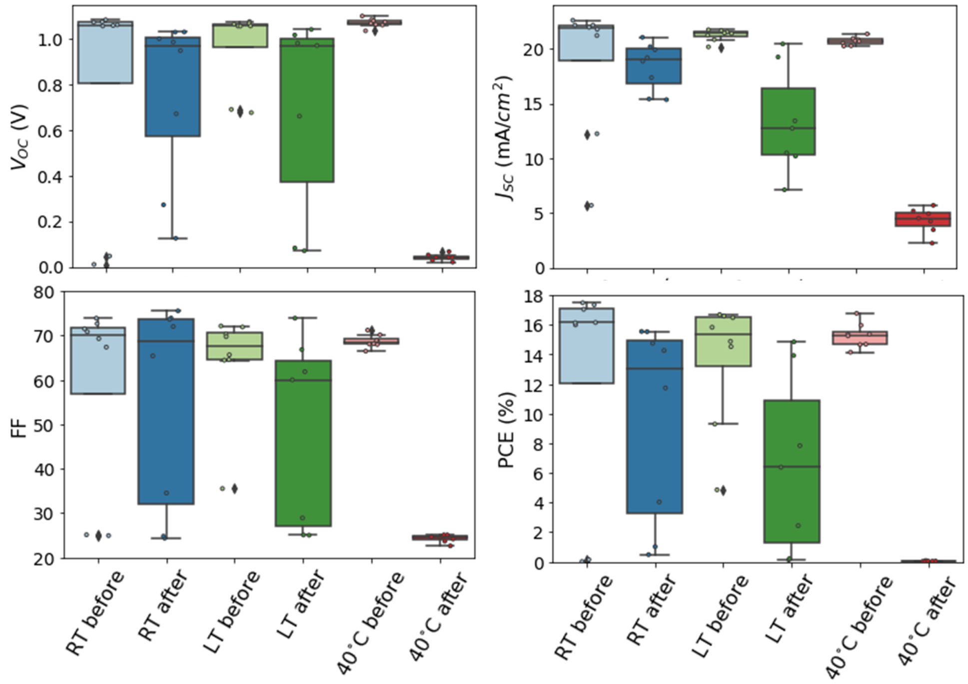

Figure 5.10: Device metrics before and after ATLAS device aging for several days.

Ink	V_{OC} (V)		J_{SC} (mA/cm^2)		FF		PCE (%)	
	Average	Best	Average	Best	Average	Best	Average	Best
40°C	1.05	1.08	20.5	20.9	66.4	66.6	14.3	15.0
LT	1.06	1.06	19.7	20.2	71.1	72.4	14.8	15.5
RT	1.07	1.09	21.3	21.3	69.0	71.9	15.8	16.7
Control	1.07	1.08	21.8	21.9	69.6	73.5	16.2	17.3

Table 5.3: Table showing average and best device metrics for champion PCE devices after aging for 2 weeks in GB Dark conditions. These devices are made from inks that had been stored at various temperatures for 2 weeks.

Ink	V_{OC} (V)		J_{SC} (mA/cm^2)		FF		PCE (%)	
	Average	Best	Average	Best	Average	Best	Average	Best
40°C	1.11	1.11	21.5	22.1	69.0	70.5	16.5	17.4
LT	1.00	1.07	19.7	22.5	71.7	78.4	15.7	18.8
RT	1.02	1.09	19.9	22.1	68.7	73.3	14.9	17.7
Control	1.05	1.05	20.4	22.3	75.3	78.5	16.2	18.5

Table 5.4: Table showing average and best device metrics for champion PCE devices before aging in GB Sol Sim conditions. These devices are made from inks that had been stored at various temperatures for 2 weeks.

Ink	V_{OC} (V)		J_{SC} (mA/cm^2)		FF		PCE (%)	
	Average	Best	Average	Best	Average	Best	Average	Best
40°C	0.89	1.10	18.4	19.1	37.3	61.3	6.6	12.9
LT	1.04	1.07	19.3	20.8	69.4	72.6	14.1	16.1
RT	1.05	1.09	19.3	19.6	59.1	70.7	11.9	15.0
Control	1.01	1.05	17.8	19.9	61.6	70.9	11.2	14.9

Table 5.5: Table showing average and best device metrics for champion PCE devices after aging for 2 weeks in GB Solar Sim conditions. These devices are made from inks that had been stored at various temperatures for 2 weeks.

Ink	V_{OC} (V)		J_{SC} (mA/cm^2		FF		PCE (%)	
	Average	Best	Average	Best	Average	Best	Average	Best
40°C	1.07	1.10	20.7	21.4	68.7	71.2	15.3	16.8
LT	0.97	1.07	21.3	21.7	64.2	71.9	13.6	16.7
RT	1.07	1.10	22.0	22.2	70.9	72.7	16.7	17.4

Table 5.6: Device metrics for champion PCE devices before aging in ATLAS lifetime tester.These devices are made from inks that had been stored at various temperatures for 2 weeks.

Ink	V_{OC} (V)		J_{SC} (mA/cm^2		FF		PCE (%)	
	Average	Best	Average	Best	Average	Best	Average	Best
40°C	0.04	0.05	4.2	5.7	24.0	24.2	0.04	0.07
LT	0.69	1.04	12.8	19.3	49.6	73.9	6.33	14.9
RT	0.76	1.00	18.4	21.1	49.6	73.7	9.7	15.6

Table 5.7: Device metrics for champion PCE devices after 2 days aging in ATLAS lifetime tester. These devices are made from inks that had been stored at various temperatures for 2 weeks.

Chapter 6

Methylammonium-Free Precursors - The Perfect Solution?

6.1 Abstract

In this work, we explore the stability of $CsFAPI_3$ precursor solutions. We here find these inks are more stable than the triple cation solutions which were the examined in Chapter 4 and 5. Using ^{1}H, ^{13}C and ^{207}Pb NMR, we identify little change in the $CsFAPbI_3$ solutions, except for the formation of a small quantity of 1-3-5-triazine after several weeks storage. Therefore, we find that high quality films and consistent devices were produced from aging $CsFAPbI_3$ inks for up to 6 weeks. This solidifies one hypothesis postulated from results of Chapter 4, that without the presence of the unstable MA^+, the main degradation reactions are prevented and solution stability is greatly improved.

6.2 Introduction

It is already well known that the hydroscopic nature of methylammonium (MA^+) is a major source of instability in $MAPbX_3$ devices.[32–34, 48] Furthermore, $MAPbI_3$ is known to degrade at high temperatures.[38] Therefore, $MAPbI_3$ perovskites have limited stability under working operational conditions. Formamidinium (FA^+) based matierials do not suffer the same thermal instabilities as MA-based perovskites and have a band gap of 1.48 eV which is much closer to the ideal band gap for maximum photovoltaic performance (1.33 eV). However as discussed in Chapter 2, $FAPbI_3$ perovskite compositions can be phase unstable. It has been reported that MA-based perovskites (such as $MAPbBr_3$) can be used to stabilise a perovskite $\alpha-$phase.[19] A commonly used composition is the triple-cation, mixed-halide stoichiometry ($CsFAMAPb(I_{1-x}Br_x)_3$) as used in Chapter 4.[46] However, these mixed-halide stoichiometries often compromise the band gap of $FAPbI_3$ and still contain MA^+ and therefore have inherent vulnerabilities. It was shown in Chapter 4 that MA^+ is particularly reactive when in solution. Namely, we found that MA reacts with FAI to form new organic compounds, resulting in MA^+ is completely disappearing from the precursor. Subsequently, these TC solutions have a limited shelf life.

MA^+-free ($CsFAPI_3$) devices were first fabricated in 2015.[17] However, they exhibited lower device performances than devices which incorporated MA^+, as they had imperfect band gap. Xie et al. proposed that depositing an MACl layer on top of a $FAPbI_3$ film could recrystalise the perovskite layer to encourage $\alpha - FAPbI_3$ nucleation.[166] Concurrently, MACl has been used as an additive or dopant within the perovskite precursor solution, often in quite large concentrations (35-50 mol%) to aid in crystallisation of a stable $\alpha - FAPbI_3$ phase.[167–170] It has been reported that no matter what quantity of MACl is added to the precursor, only 6% of MA^+ stays in the perovskite layer.[171] The rest leaves the film during thermal annealing due to the volatile nature of MA^+. These are therefore still be considered to be "MA-free" devices. It is worth noting many previous studies have used Cl^- as a dopant to improve perovskite performances. Excess Cl^- ions can be hugely beneficial as a passivating agents at perovskite/transport later interfaces. In fact, a recent study has found that these ions in Cl^--containing perovskites form an interlayer with a chlorine-doped SnO_2 ETL which significantly aids charge carrier transport through a PSC device.[88] Min et al. reported that the $\alpha - FAPbI_3$ phase could be stabilised by using small amounts (3.8 mol%) of $MDACl_2$ as an additive to the precursor solution. This addition stabilised the $\alpha - FAPbI_3$ phase in high humidity conditions. [87] Work by Bu et al. [64] reports impressive device performances - 23% PCE on small devices, with over 19% PCE over $65cm^2$ area devices- using an entirely MA-free $CsFAPb(I_xCl_{1-x})_3$ perovskite composition. It is this composition that we have examined in this work.

In Chapter 4, we observe there is an increase in the non-perovskite δ-phase in films made from aged triple-cation precursor solutions. We subsequently discovered that maintaining solution stability depended on the retention of MA^+ ions within precursor solutions. Yu et al. has shown that $CsFAPI_3$ solutions are stable for up to 21 days.[100]. We hereby hypothesise that without the inclusion of MA^+ in $CsFAP(I_xCl_{1-x})_3$ precursors, the main degradation mechanism will be hindered, and these precursor inks will have better long term stability alongside impressive device performance.

Therefore, in this chapter we examined the optical and electronic properties of films made from aged $CsFAPb(I_xCl_{1-x})_3$ precursors, and studied the performance of devices made from a stock solution at significant timepoints over a 7 week period. We also use ^1H, ^{13}C and ^{207}Pb NMR to explore any changes in these solutions over this 6 week period. We found there to be little significant change in any film or solution measurements over this extended period, and hereby we see that the device performance stays consistent for up to 6 weeks. This supports our hypothesis that without the presence of MA^+ to react with FAI, the main degradation pathway can be avoided. We believe this is an extremely promising results for the potential of PSC scalability and we have shown impressive ink stability can be achieved with this high performance PSC ink.

6.3 Experimental Details

Materials and Solution Preparation

For characterisation of films and solutions, we prepared 2M $CsFAPbI_3$ stock solution. This consisted of dissolving 285.47mg/ml FAI, 922.02mg/ml PbI_2, 55.62mg/ml $PbCl_2$, 88.34mg/ml CsI and 192.86μl/ml NMP in DMF. For devices, 1.1M solutions were used in order to be adequately spray coated. For this, 25ml of stock solution was made to the following recipe: 157mg/ml FAI, 507.12mg/ml Pb_2, 30.6mg/ml $PbCl_2$, 48.58mg/ml CsI and 106μl/ml NMP in DMF.

Devices

Devices described later on in this chapter have the following device structure: ITO-coated glass/SnO_2/$CsFAPbI_3$/Spiro-OMeTAD/Au. A 0.2% SnO_2 nanoparticle suspension was prepared in DI water. Before deposition of the SnO_2 layer, substrates were heated to 30°C and this temperature was maintained throughout deposition. The nanoparticle SnO_2 layer was spray-deposited using a Prism Ultra-coat 300 ultrasonic spray coater with a spray-head velocity of 180 mm/s at a height of 30 mm above the substrate. Fluid flow rate was controlled by a 10 mbar nitrogen feed. After 45 seconds drying time, these substrates were annealed at 150°C for 30 minutes.

The perovskite layer were spray-coated from the 1.1M stock solutions with gas-assisted spray processing, with a spray head-speed of 80 mms^{-1} and an air blade speed of 30 mms^{-1}. This layer is deposited under inert conditions. During perovskite depositions, substrates were maintained at 30°C, and there was a delay time between spray deposition and application of the air blade of 25 sec. These perovskites are then annealed for 5 minutes at 70° in inert conditions, and then for 150°C for 10 minutes in ambient conditions A spiro-OMeTAD HTL (86mg/ml in chlorobenzene) was spray coated onto the perovskite layer. The following dopants were added to this solution: 34 μ/ml TBP, 11μl/ml Fk209 in ACN (300 mg/ml concentration) and 20μl/ml of LiTFSI in ACN (500mg/ml concentration). Spiro-OMeTAD was spray-coated using an Prism Ultracoat 300 spray coater with a spray-head speed of 150 mms^{-1} at a height of 60mm. Fluid flow rate was controlled with a 20 mbar nitrogen feed. Devices are placed in dry, ambient conditions overnight to allow oxidisation of the Spiro-OMeTAD layer. A 100nm gold layer is then deposited onto the device using an Edwards 306 Vacuum Thermal Evaporator.

Devices were tested using a Newport 92251A-1000 solar simulator in ambient conditions, with J–V measurements recorded using a Keithley 237 source measure unit. Measurements were made by reverse sweeping the bias between -0.1V and 1.2V at 100 mV/s. All data is processed and plotted in Python and devices with PCEs below 10% have been excluded from the full dataset. Normalised data is normalised to the initial metric values for each timepoint.

Film Fabrication and Characterisation

For film characterisation measurements, 60μl of 2M $CsFAPbI_3$ solutions was spin coated onto quartz substrates at 5000 rpm for 50 seconds. These were then annealed for 5 minutes at 70°C under inert conditions, then for 10 minutes at 150°C in ambient conditions. UV-Vis absorption, XRD and SEM measurements were conducted using the same procedures as those described in Chapter 4 with following amendments. SEM imaging was performed using an FEI Nova NanoSEM 450. UV Vis absorption measurements were performed using an Ocean Insight FLAME miniature spectrometer. For PL measurements, films were excited with a 400 nm laser and PL emissions measured with an Ocean Insight FLAME miniature spectrometer. ImageJ software was used to measure grain size from SEM images.

NMR

For solution-NMR measurements, samples were prepared using deuterated solvents (d_7-DMF, N-Methyl-d_3-2-pyrrolidinone-d_6) sourced from Sigma Aldrich. ^1H, ^{13}C and ^{207}Pb measurements were performed using a Bruker AVANCE III instrument operating at 400.2 MHz, 83.7MHz and 100.6MHz respectively at 289K. ^1H spectra were recorded in 64 scans using over a 20ppm spectral width with 64k acquisition points and a relaxation delay of 30s to ensure full quantification. ^{207}Pb spectra were recorded in 256 scans over a 402ppm spectral width with a relaxation decay of 2s. ^{13}C spectra were recorded in 1024 scans over a 238ppm spectral width with a relaxation decay of 10s. 64k acquisition points were taken for each measurement. For individual cation measurements, peak positions and absolute molarities were calibrated to an internal reference standard (1,2,4,5-tetrachloro-3-nitrobenzene, TCNB) of 383mM at 8.4364ppm. All solutions were sealed into 100 MHz, 7" Standard Series NMR tubes in a Nitrogen-filled glovebox. Molarity changes as shown in Figure 5 were estimated using TopSpin software. The measurements presented in Figure 6.6 were locked onto a DMF-d_7 solvent peak.

6.4 Results and Discussion

6.4.1 Film study

We first explored how $CsFAPbI_3$ ink aging affected film crystallisation. A large stock of $CsFAPbI_3$ ink was made, and films were fabricated from this solution at regular intervals over a 7 week period. These films were characterised using UV-Vis absorption and PL measurements, XRD and SEM. Figure 6.1 shows normalised UV-Vis absorption and PL spectra of films made from $CsFAPbI_3$ ink that had been aged for various lengths of time. It can be seen that the optical properties of the film remain constant, regardless of $CsFAPbI_3$ ink age. This is confirmed in Figure 6.2, which shows XRD spectra taken of films made from this $CsFAPbI_3$ stock solution at various timepoints. Here, no new peaks are observed, and interestingly there is no sign of the δ-phase (11.6°) often found in $FAPbI_3$-based perovskites. This unstable phase was observed in films made from aged TC inks in Chapter 4. This supports the conclusions of Chapter 4 that the main cause of degradation in triple-cation solutions was due to a reaction between MA^+ cations and FAI. This also indicates that a stable α-phase perovskite can be fabricated from aged $CsFAPbI_3$ solutions.

We do however identify a change in the intensity of the PbI_2 peak (12.7°) in films made from aged solutions as shown in Figure 6.2. Figure 6.3 plots the intensity ratio of the PbI_2 peak (at 12.7°) compared to the perovskite (110) peak (at 14.1°) for each timepoint. Taking the ratio of these intensities should account for any uncontrolled intensity differences between measurements. Figure 6.3 shows a decrease in this relative amount of PbI_2 in films made from aged inks, compared to films made from a fresh solution. It has been suggested that excess amounts of PbI_2 can have a passivating effect on PSC devices or can lead to increase grain size.[172, 173] It is possible that this reduction in concentration of unreacted PbI_2 in films from aged inks may affect subsequent device performance.[173] It has also been suggested that the amount of unreacted PbI_2 present in devices can also affect device stability. However, as we discuss layer in this chapter, we do not see of these evidence of these effects in the device data presented in this work.

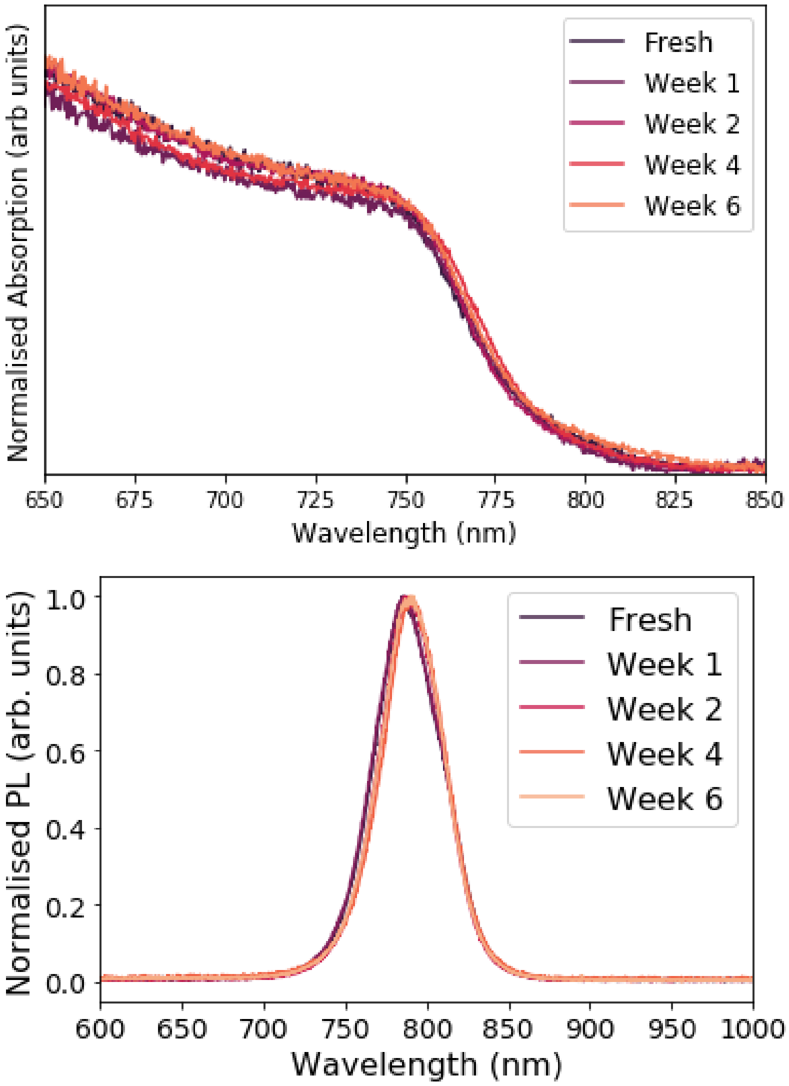

Figure 6.1: UV-Vis Absorption (a) and PL (b) spectra for films made from $CsFAPbI_3$ solutions aged for various times up to 6 weeks.

Figure 6.4a shows SEM images of films made from $CsFAPbI_3$ ink aged for different lengths of time. There appears to be no striking change in these images (for example grain appearances, etc) that would indicate a change in film morphology as the precursor ink ages for 4 weeks. However, some alterations in these films occur after 6 weeks aging, there appears to be a slight charge build up at the grain boundaries (indicated by bright regions) and the appearance of larger pinholes. However, since we do not see any major changes in XRD or UV-Vis absorption profiles at 6 weeks, it is not clear that this this significantly affects optical properties or crystal structure of the perovskite film. Figure 6.4b shows grain size analysis of the images in Figure 6.4a. Here, two structures are considered. The apparent "grains" appear as various shades of grey in Figure 6.4a, and "bright spots" which are much smaller and brighter. It has been previously suggested that such small bright grains are likely PbI_2.[172] Interestingly, we observe a larger average grain size in

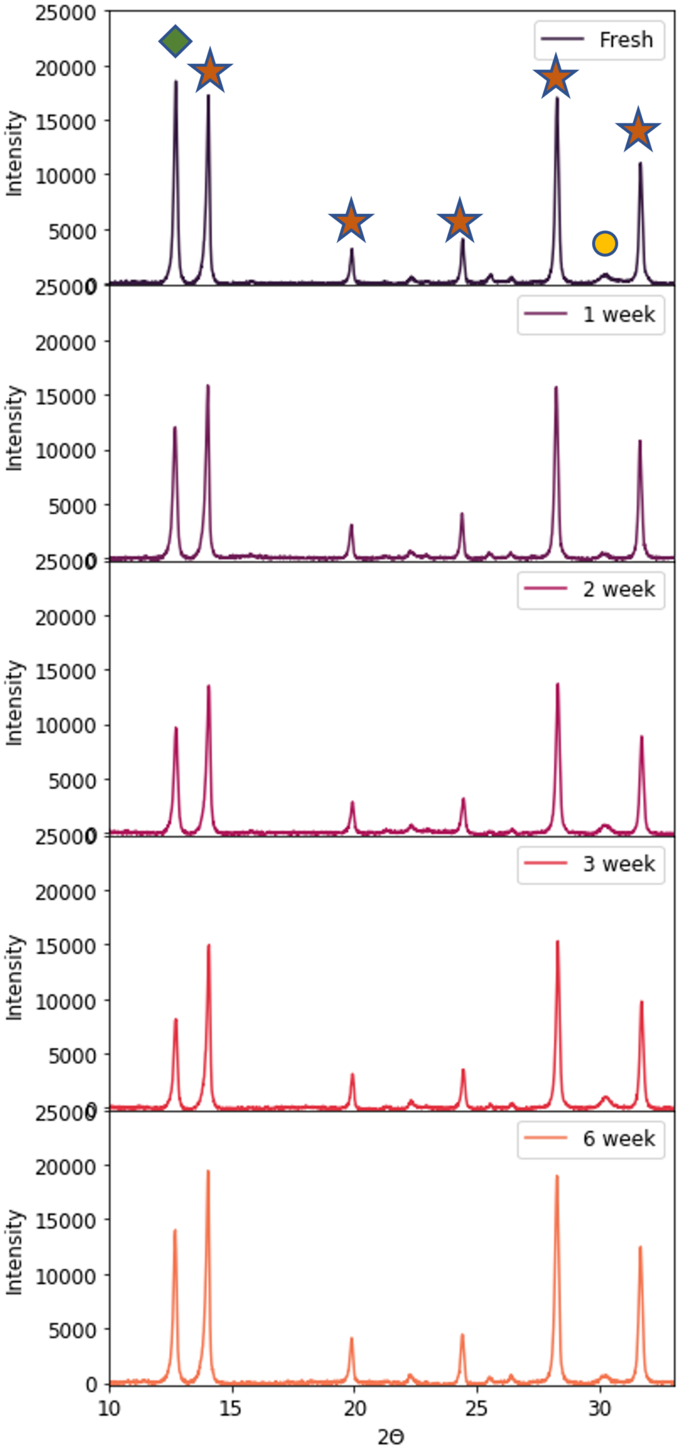

Figure 6.2: XRD profiles of films which were fabricated from $CsFAPbI_3$ inks that had been aged for 6 weeks. Orange stars mark peaks assigned as $\alpha - CsFAPbI_3$, green diamonds identify the PbI_2 peak and yellow circles correspond to ITO. $CsFAPI_3$ peaks assigned from ref [64]

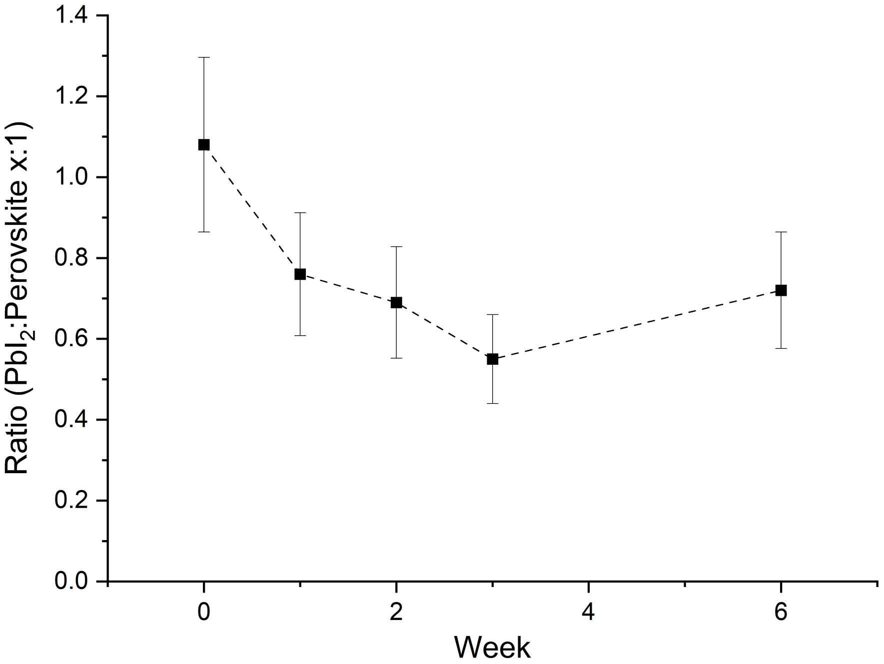

Figure 6.3: Intensity ratio of PbI_2 peak to perovskite (110) peak (x:1 PbI_2:perovskite) for films made from inks of various ages. Data taken on the basis of Figure 6.2

films made from precursor inks that have been aged for 6 weeks - which may explain the larger pinholes. However, there is notable variation in the average grain size at each time point, so this could be a process dependent effect. It is also apparent that the size of the "bright spots" is unchanged as the solution ages. In future, it would be interesting to study the morphology of such films further (for example with atomic force microscopy) to see if the films are less uniform when prepared from aged inks. This is an effect seen with $MAPbI_3$ perovskites in Chapter 7.

6.4.2 Solution Chemistry

We have used liquid-state ^1H, ^{13}C and ^{207}Pb NMR to explore the solution chemistry of a $CsFAPbI_3$ precursor ink over a period of 7 weeks. The molecular structure of the FA^+ ion is shown in Figure 6.5, and results from the ^1H NMR measurements are shown in Figure 6.6. Firstly, there appears to be an increase in signal intensity of the peak at 8.2ppm as solutions age. This peak is associated with the methyl group of FA $(C - H)$ i.e. the Group 1 proton in Figure 6.5. Figure 6.6a(i) and 6.6b show that this apparent signal increase is actually a reduction in the full-width half-maximum (FWHM) of this peak. It has been reported that the chemical exchange of protons can cause line broadening in NMR spectra [174] and previous studies have shown that the linewidth of all ^1H NMR peaks decrease when HI is added to perovskite solutions. This is due to increased ^{1}H-^{1}H bonding with exchangeable protons, reducing proton exchange.[102] We speculate therefore that as the $CsFAPbI_3$ solutions age, there is less chemical exchange occurs with or around such Group

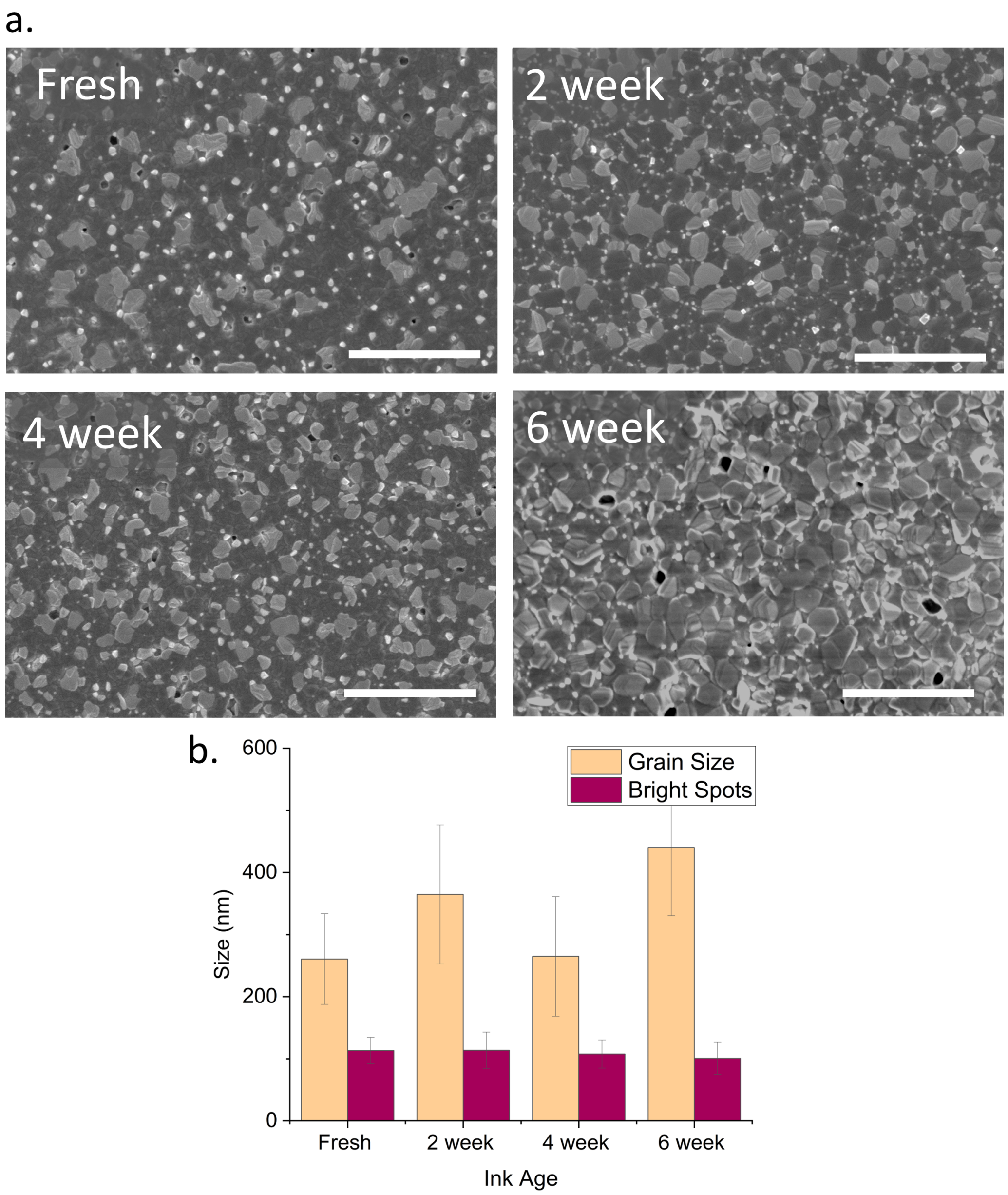

Figure 6.4: a.) SEM images showing the surface of $CsFAPI_3$ films made from inks aged for different lengths. (b.) Grain analysis of images in (a). Sizes of "Grains" and "Bright spots" are measured separately as they are assumed to be different structures.

1 protons, reducing the line broadening.

This effect is combined with a small chemical shift in the broad peak at 8.8-9.0ppm (Figure 6.6ii). This peak corresponds to the amine groups of the FA molecule, which consists of 2 separate NH_2 groups (Group 2 and 3 in Figure 6.5). The magnetic fields experienced by Group 2 and Group 3 protons is not equal due to the diamagnetic anisotropy of FA^+ associated with the partial double bond. In other words, Group 2

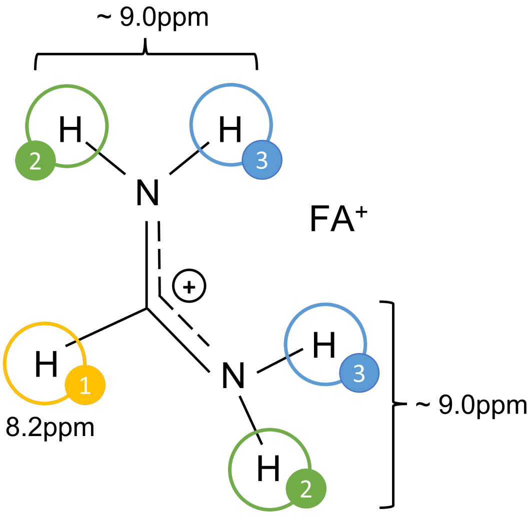

Figure 6.5: FA^+ molecule. The different proton "groups" are assigned as to how they will contribute to an ^1H NMR spectra. The Group 1 proton is assigned to the peak at 8.2ppm in Figure 6.6, while protons from Group 2 and 3 contribute to the broad peak at 8.8-9.0ppm. Adapted from [102]

protons in Figure 6.5 will experience a slightly different magnetic field that Group 3 protons. Therefore, the signal from these amine groups are usually split into two peaks where the Group 2 protons have a higher chemical shift than Group 3 protons.[102] In high resolution measurements, it has been shown that the peak assigned to Group 3 protons will also be slightly split, due to the proximity of each proton to the double bond. We assume that due to the large amounts of proton exchange that occurs within $CsFAPbI_3$ solution at these concentrations, these peaks cannot be resolved from one another. Therefore, Group 2 and Group 3 protons instead contribute to one very broad peak at 8.8-9.0ppm. This movement of the broad amine peak as the solutions age solutions was also seen for TC solutions as discussed in Chapter 4. We have measured the integrated ratio of the $(NH_2)_2$:$C-H$ peak in Figure 6.6 and find it is 4:1 in all cases. We conclude therefore that the same quanitity of protons contribute to this peak as solutions age (i.e. this is not a deprotonation effect). If NMR peaks move towards a lower ppm, this might indicate the protons are becoming more shielded due to an increased number of electrons that surround each molecule. It has been reported that FAI forms via hydrogen bonding between the I^- ion and the "Group 2" hydrogen in FA^+.[175] We tentatively speculate that this shift towards lower ppm could indicate increased hydrogen bonding between I^- ions and Group 2 hydrogens as the solution ages. This would shield the Group 2 protons from the magnetic field experienced during NMR measurements, lowering the shift of the $(NH_2)_2$ peak. This would also explain the narrowing of the $C-H$ peak, as it has already been reported that increase iodide (namely HI) in a perovskite solution can cause this effect.[102] However, it is difficult to make definite conclusions about this peak as it is unresolved and combines the contributions of multiple hydrogens within the FA^+ molecule.

Most interestingly, our NMR data shown in Figure 6.6 does not indicate the formation

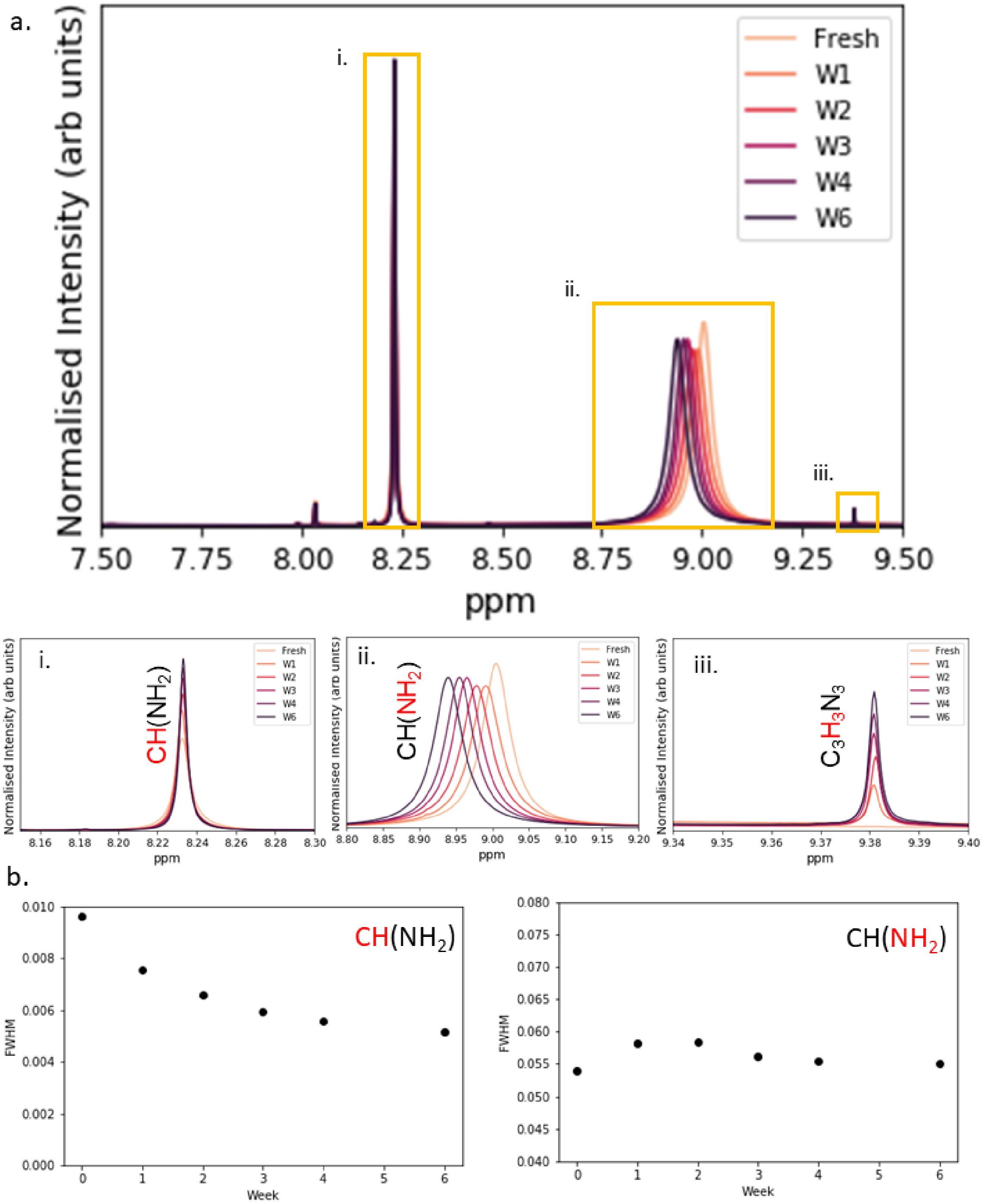

Figure 6.6: a) ^{1}H NMR spectrum from $CsFAPbI_3$ solutions measured at several time points over 6 weeks (labelled W1 for week 1, etc). Insets show zoomed in areas outlined with yellow boxes in main figure. These areas correspond to C-H group of FA (i), NH_2 groups of FA (ii) and ^1H ions associated with 1,3,5-triazine (iii). b) Full-Width Half-Maximum values for the peaks for CH and NH_2 of FA^+ at each timepoint. This data is taken from the peaks shown in part (a).

of new molecules in any great quantity. A new peak at 9.3ppm associated with 1,3,5-triazine ($C_3H_3N_3$) [99, 102] is found as $CsFAPbI_3$ inks age. This molecule is formed through degradation of formamidinium ions along with the formation of ammonia (NH_4) [176]. However, the concentration of this molecule in aged solutions is found to be very low and will likely not affect the overall stoichiometry in $CsFAPbI_3$ ink (unlike MFA and DMFA that were found at high concentration in aged TC perovskite solutions).

To confirm this, we find very little change in the ^{13}C and ^{207}Pb NMR over time (see Figure 6.7). This peak at 158ppm in C^{13} spectra is assigned to the $C-H$ group of FA^+, and Figure 6.7a shows little changes in this peak over the course of 6 weeks. Again, the only new peak to emerge throughout this time is at 166.7ppm, due to the creation of 1,3,5-triazine (Figure 6.7b). If the environment surrounding the Pb atom changes, the spectral linewidth can be affected. Figure 6.7 shows no such effect happening as solutions age. These results support those from the film study, that without the presence of MA^+, there are no substantial degradation mechanisms for $CsFAPI_3$ inks within this time frame.

To explore whether organic A-cations alone are stable in solution, we measured the organic components (MAI and FAI) individually in DMF/DMSO at several timepoints during a 1 month period with ^1H NMR. In each case, the molecules were identified in the NMR spectra by peak placement, and confirmed by calculating their relative intensities through peak integration. For FA^+, the $C-H$ and $(NH_2)_2$ peaks should have an integrated ratio of 1:4, and MA should have a ratio of 1:1 for the CH_3 and NH_3 peaks. This is confirmed from the data shown the Supplementary Information in Table 6.1 and 6.2. In these measurements, we used an internal standard of known concentration to measure absolute molarities of each molecule in solution. This allowed us to track changes in the concentration of FA^+ and MA^+ over time. Figure 6.10 in the SI shows ^1H NMR spectra of FAI in solution. Here, we find a similar up shift of the broad $(NH_2)_2$ peak as can be seen as in Figure 6.6. This confirms that this is an aging effect that occurs to the FAI molecule alone. Indeed Table 6.1 confirms that the concentration of FA in solution does not change significantly over a 28 day period indicating there is no significant change to the FA^+ cation over this time period. In Figure 6.11, we see a completely different aging effect for the NH_3^+ peak in MAI. Here, it can be seen that the linewidth of the NH_3^+ peak significantly broadens until it disappears completely. However, as shown in Table 6.2, it appears that the concentration has not changed. This implies that unlike FA^+, MA^+ engages in a significant amount of proton exchange as time goes on. This could explain why such $CsFAPbI_3$ solutions are much more stable over time compared to the FAMA- or MA-based perovskites.

6.4.3 Device Study

Figure 6.8a-d show normalised device metrics for PSCs made from fresh and aged $CsFAPbI_3$ solutions. We note here that the overall performance of these devices are significantly lower than previously reported for this perovskite stoichiometry [64] and that there may be subtle differences in the high performance devices made from these aged inks which are missed by this study. We suspect that this lower device performance could be due to the fact these devices are spray-coated rather than spin-coated and that there was no passivating layer used in these devices as is done in literature. However, we believe that our results are useful in indicating the relative performance of devices made from aged inks. For this

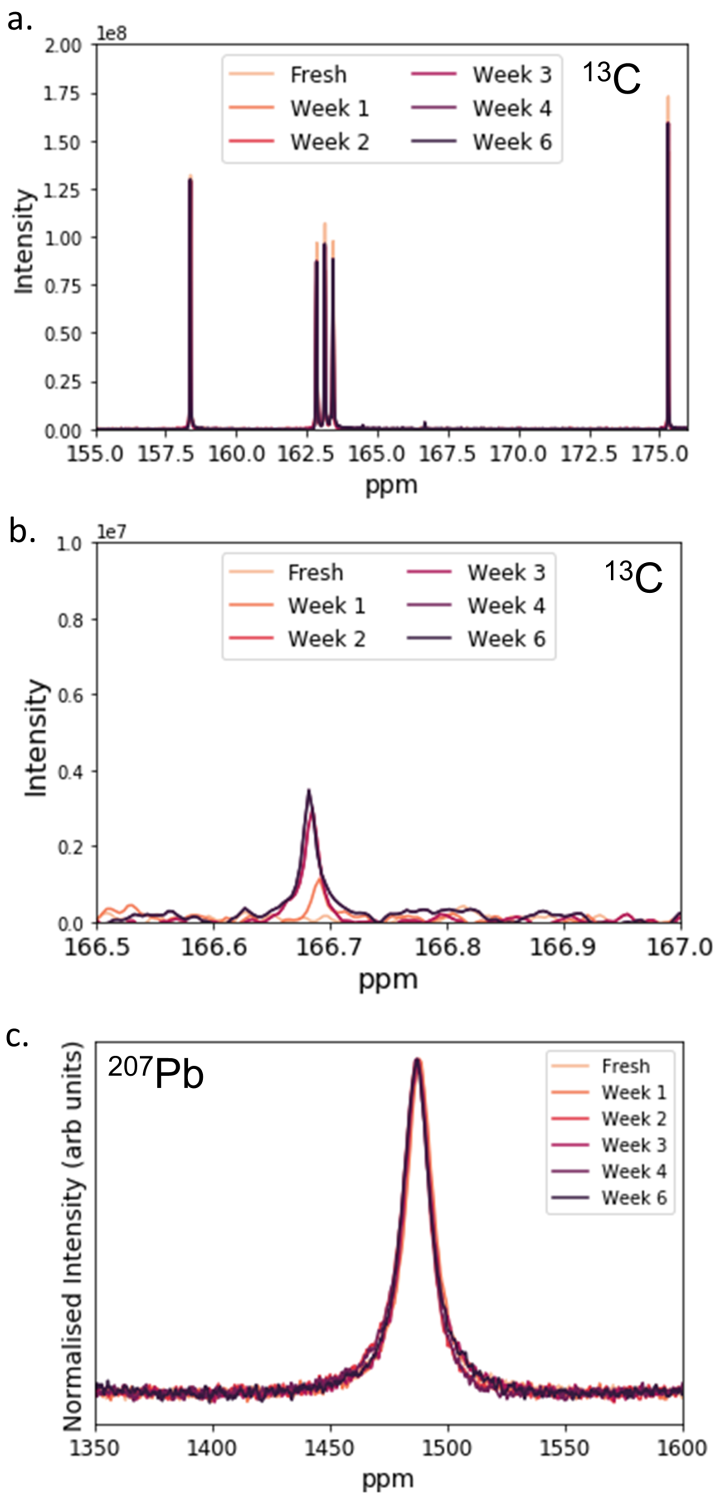

Figure 6.7: a.)^{13}C spectra of $CsFAPbI_3$ inks taken at several timepoints over 6 weeks. (b.) Magnified spectra of (a.) showing development of 1,3,5-triazine.(c.) ^{207}Pb spectra for $CsFAPbI_3$ solutions. Measured at several points over a 6 week period.

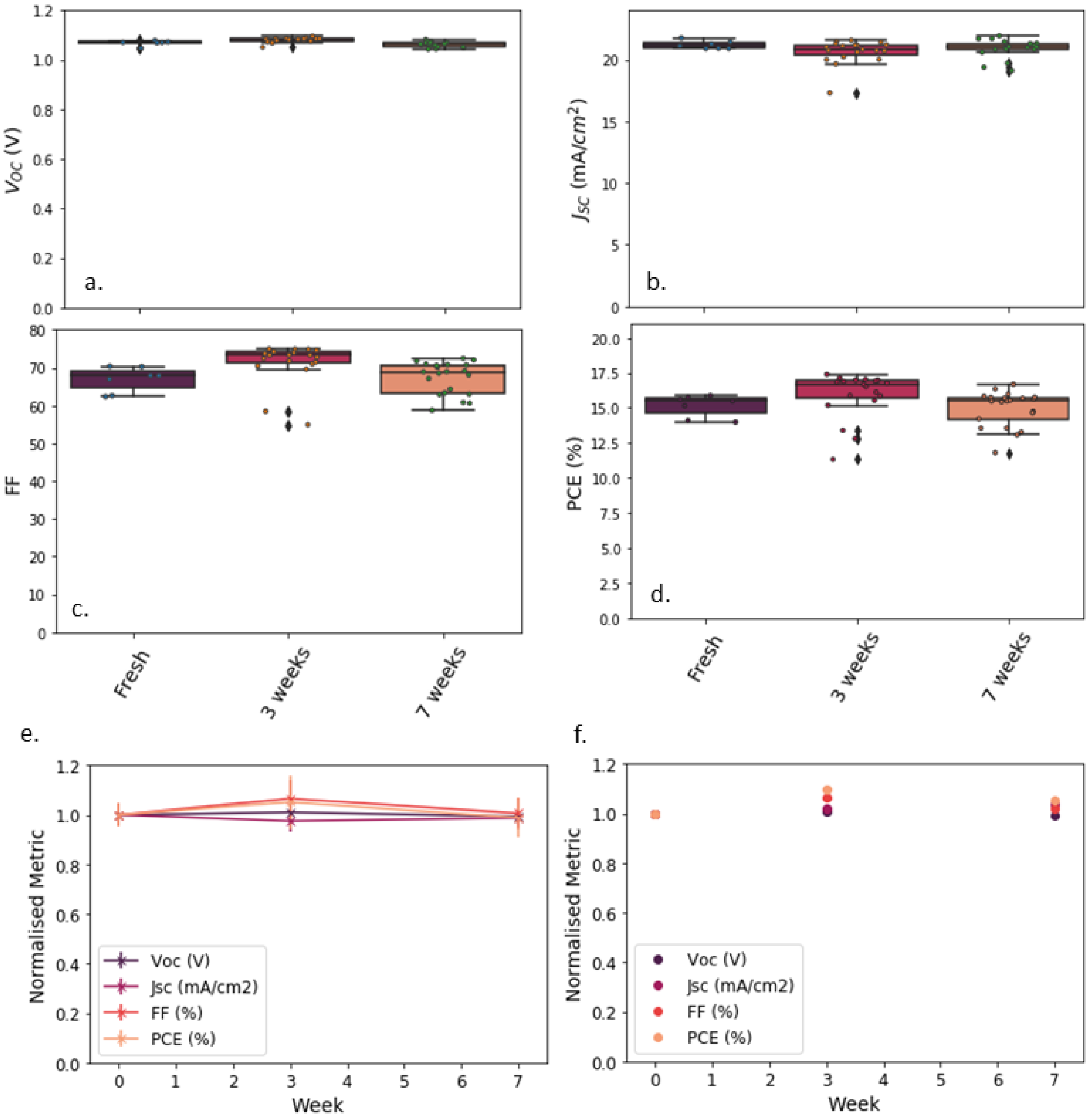

Figure 6.8: Boxplots showing a) V_{OC}, b) J_{SC}, c) FF and d) PCE of devices made from $CsFAPbI_3$ ink over 7 weeks. Normalised device metrics for the average of devices (e) and champion devices (f). For (e), error bars are normalised standard deviation from 5-6 devices for each time point.

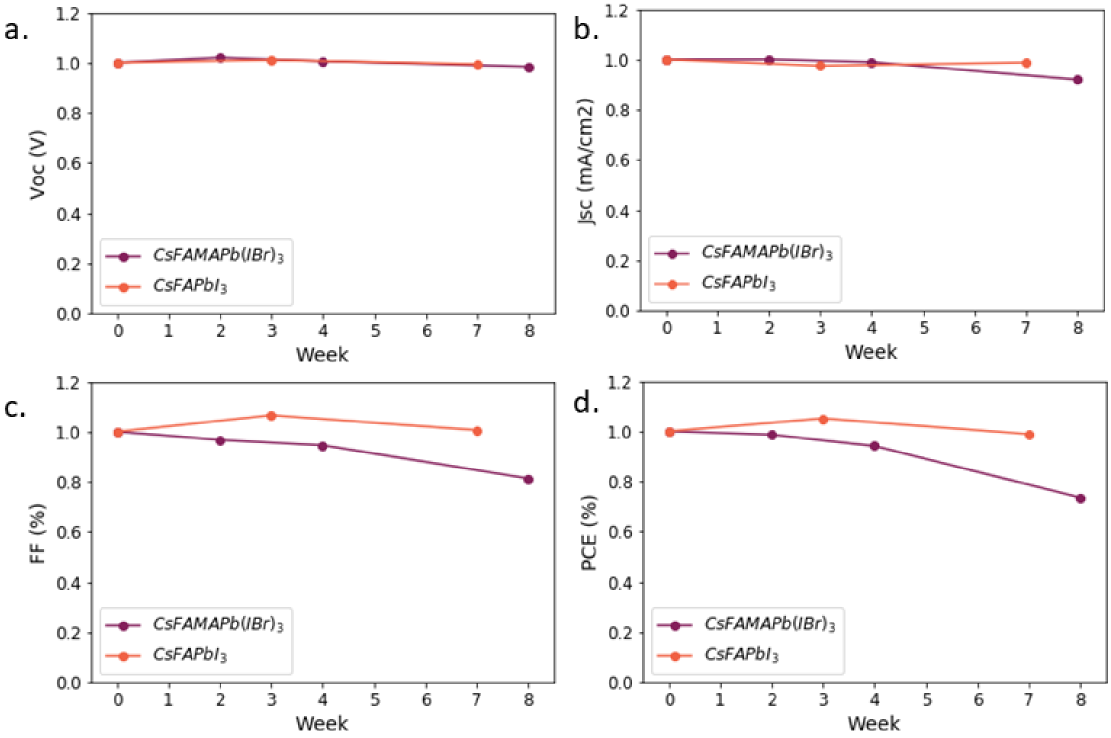

Figure 6.9: Normalised device metrics for the average V_{OC} (a), J_{SC} (b), FF (c) and PCE (d) of devices made from aging TC (labelled $CsFAMAPb(I_xBr_{1-x})_3$) and $CsFAPbI_3$ solutions.

reason, we have normalised the average and champion metrics from each time point to the average and champion result from the fresh $CsFAPbI_3$ ink in Figure 6.8 e and f respectively.

Promisingly, these results show a consistent device performance over a 7 week period across all metrics. In fact, devices made from solutions that had been aged for 3 weeks appear to have a slightly improved PCE compared to the initial control devices, due to a slightly higher FF. We believe this shows that aged $CsFAPI_3$ inks have the potential to perform just as well as their fresh counterparts, and with further device optimisation, we should consistently reach high performing PCEs with this solution.

To validate this idea, we compare our normalised device study to the study in Chapter 4. Here, we normalise the results from aged TC ($CsFAMAPb(I_{1-x}Br_x)_3$) solutions to the devices made from the fresh TC ink. Figure 6.9 shows the normalised average metrics over time for both $CsFAPbI_3$ ink and the TC ink. It can be seen that after 4 weeks aging of the TC ink, the relative PCE of subsequent devices begins to drop, and after 8 weeks aging, the normalised PCE of devices has dropped to less than 80% of its original efficiency. In contrast the device made from 7 week aged $CsFAPbI_3$ inks maintain close to their initial performance. In the TC study, we see this reduction in performance continue rapidly over the next few months. It would therefore be interesting to extend this study on $CsFAPbI_3$ storage, to explore how long these solutions can maintain this impressive stability. Nevertheless, our initial data suggests that perovskite precursor solutions that exclude MA^+ have very high levels of stability.

6.5 Conclusions

Here, we have shown using UV-Vis absorption and PL measurements, SEM and XRD that the optical and morphological properties of films made from $CsFAPb(I_xCl_{1-x})_3$ precursors are not significantly altered as these inks age. Devices made from these solutions perform consistently over a 7 week aging period, but we note the initial PCE of these devices was lower than expected. We also show using ^1H, ^{13}C and ^{207} NMR that the solution chemistry of these $CsFAPbI_3$ solutions does not change significantly in comparison to the TC solutions in Chapter 4. This confirms the hypothesis that without the presence of MA^+ in solutions, the main degradation pathway for $FAPbI_3$ based solutions can be avoided. However, a more in-depth study is needed to determine the long term stability of these solutions and to confirm the results of this study for devices with a PCE over 20%.

6.6 Supplementary Information

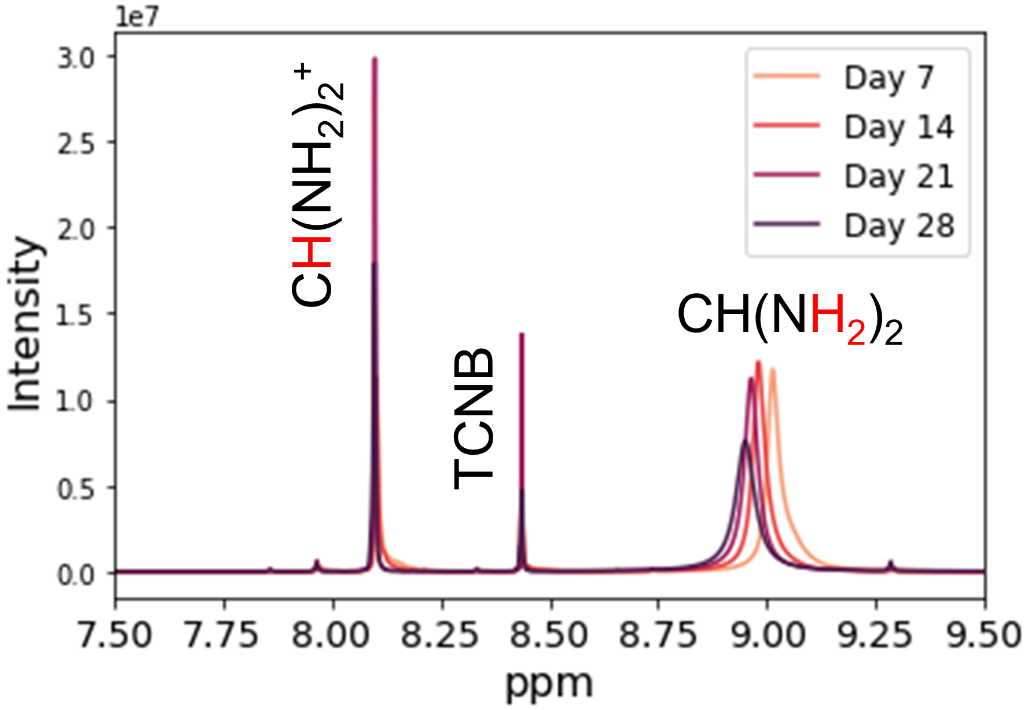

Figure 6.10: ^1H NMR of FAI in 4:1 d_7-DMF d_6-DMSO taken at several time points over a 28 day period. CH and $(NH_2)_2$ have been assigned to 8.1ppm and 8.9-9.0ppm. The peak at 8.4ppm is assigned to an internal standard TCNB in d_6-DMSO.

Day	Concentration from NH (mM)	Concentration from CH_3 (mM)	Integrated Ratio CH:$(NH_2)_2$ (1:x)	Normalised Concentration
7 days	1733	1824	4.2	1
14 days	1987	2000	4.0	1.12
21 days	1521	1523	4.0	0.86
28 days	1652	1656	4.0	0.93

Table 6.1: Data extracted from the ^1H NMR spectra in Figure 6.10 for FAI in $d_7 - DMF/d_6 - DMSO$. Molar concentrations are measured in comparison to an internalised internal standard of known concentration. Normalised concentrations are normalised to the average molar concentration at the 7 day time point.

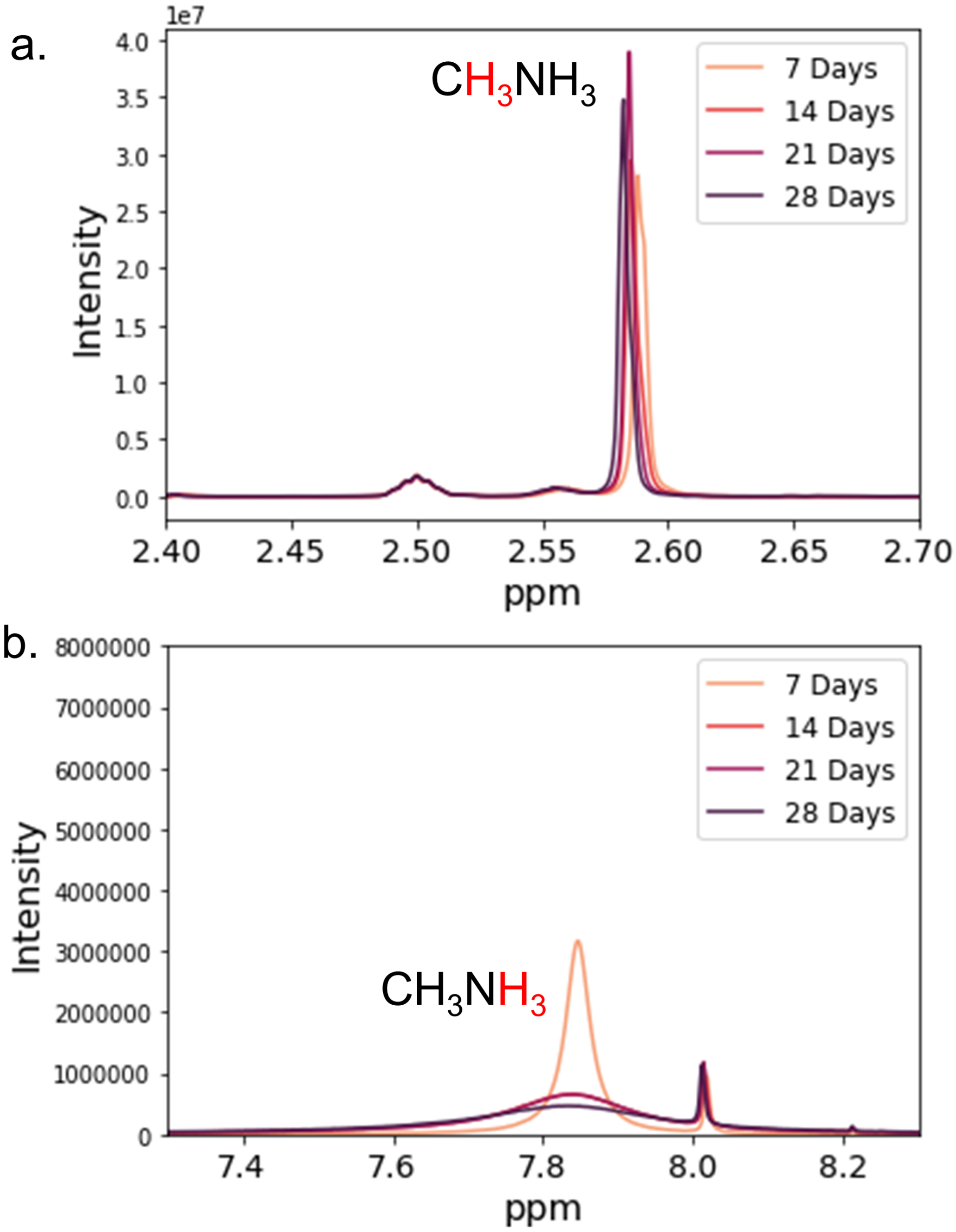

Figure 6.11: ^1H NMR of MAI in 4:1 d_7-DMF d_6-DMSO taken at several time points over a 28 day period. NH_3 (a) and CH_3 (b) have been assigned to 7.9ppm and 2.6ppm. Peak at 8.5ppm is assigned to an internal standard TCNB in d_6-DMSO.

Day	Concentration from NH_3 (mM)	Concentration from CH_3 (mM)	Ratio :CH_3:NH_3 (1:x)	Normalised Concentration
7 days	332	359	0.926	1
14 days	325	336	0.97	0.96
21 days	364	379	0.96	1.05
28 days	304	383	0.79	0.99

Table 6.2: Data extracted from the ^1H NMR spectra in Figure 6.11. Molar concentrations are measured in comparison to an internalised internal standard of known concentration. Normalised concentrations are normalised to the average molar concentration at 7 days.

Chapter 7

Exploring Nanoscale Structure in Perovskite Precursor Solutions Using Neutron and Light Scattering

Mary E. O'Kane, Joel A. Smith, Rachel C. Kilbride, Emma L. K. Spooner, Chris P. Duif, Thomas E. Catley, Adam L. Washington, Stephen M. King, Steven R. Parnell*, and Andrew J. Parnell*

Volume 34, Issue 16
3^{rd} August 2022
DOI: 10.1021/acs.chemmater.2c00905

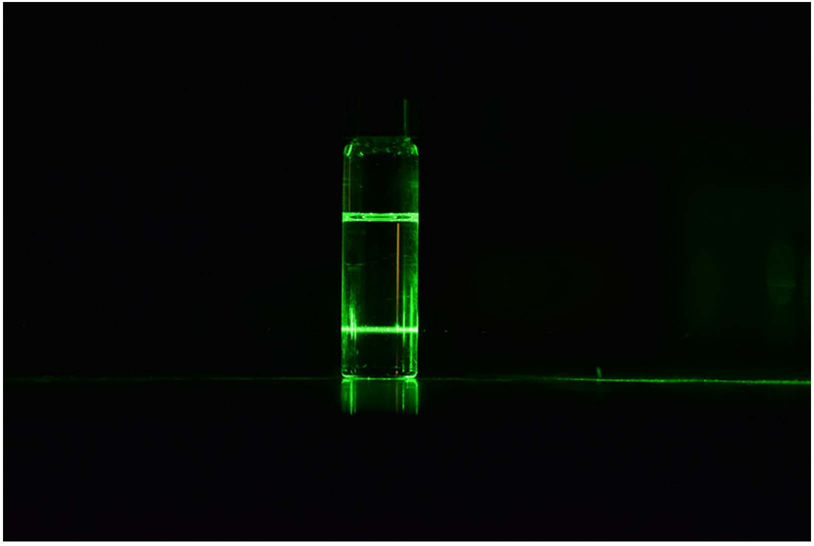

7.1 Paper Foreword

In order to achieve optimum device performance, it would be invaluable to thoroughly understand preliminary co-ordination which occurs within solutions and relate this to film formation. Many people have used Dynamic Light Scattering to study precursor solutions to find an estimated colloid size. In this work, we explore the benefits and limitations in using DLS to study particle size in PSC precursor solutions.

Additionally, we explore Small-Angle Neutron scattering (SANS) and Spin-Echo SANS as techniques for studying perovskite precursor solutions. Interestingly, we find through simple modelling that we can accurately measure colloid size, whilst also probing colloid composition. We do this by modelling the Scattering Length Density of the solute material, and we believe we present an interesting framework for studying these solutions in the future. Additionally, using SESANS we prove that if there are large colloids in these solutions, they must be present in very small quantities. To our knowledge, this is the first example of SESANS being used to examine colloids in PSC solutions.

7.2 Authors Contributions

M.O.K. co-ordinated the project, created all samples, performed the DLS, SEM and SANS measurements and analysed the perovskite film results. J.A.S. assisted with data analysis and contributed meaningfully to the discussion of these results. T.E.C. performed the AFM measurements and performed the height analysis. R.C.K. facilitated and assisted on the beam time for the SANS data, and contributed meaningfully to the model discussion. E.L.S., C.P.D. and A.D.W helped with the beam times for the SANS and SESANS data. S.M.K. contributed considerably to the analysis and discussion of the SANS and SESANS data. S.R.P performed and analysed the SESANS data and supervised throughout the project. AJP co-coordinated the project, analysed the SANS data and supervised throughout the project. My sincerest thanks goes to all contributing authors.

7.3 Main Paper Body

7.3.1 Abstract

Tailoring the solution chemistry of metal halide perovskites requires a detailed understanding of precursor aggregation and co-ordination. In this work, we use various scattering techniques, including dynamic light scattering (DLS), small angle neutron scattering (SANS) and spin-echo SANS (SESANS) to probe the nanostructures from 1 nm to 10 µm within two different lead-halide perovskite solution inks ($MAPbI_3$ and a triple-cation mixed-halide perovskite). We find that DLS can misrepresent the size distribution of the colloidal dispersion and use SANS/SESANS to confirm that these perovskite solutions are mostly comprised of 1-2 nm sized particles. We further conclude that if there are larger colloids present, their concentration must be less than 0.005% of the total dispersion volume. With SANS, we apply a simple fitting model for two component microemulsions (Teubner-Strey), demonstrating this as a potential method to investigate the structure, chemical composition and colloidal stability of perovskite solutions, and we here show that $MAPbI_3$ solutions age more drastically than triple cation solutions.

7.3.2 Introduction

Halide perovskites have emerged as one of the most exciting new hybrid organic-inorganic photovoltaic material systems, capable of producing power conversion efficiencies of up to 25.7%[88] due to several ideal material characteristics[40, 41, 177–179]. A huge benefit of perovskite solar cells (PSCs) is that they can be processed at scale via low-cost solution processing techniques that are compatible with roll-to-roll manufacturing, such as spray coating, inkjet printing, and contact methods like slot-die, gravure and blade coating[57, 180–182]. However, in order to achieve the highest quality perovskite films, every step of the crystallization process must be tightly controlled- from ink creation to device encapsulation. For these materials to be reliably cast from solution on an industrial scale, the structures and compositions formed within the precursor solutions, along with their usable lifetimes, must be more thoroughly understood. To do this requires characterization methods with suitable figures of merit, that can relate a solution's physical and chemical properties to their final material function in thin films. These insights could aid the rational design of new and improved perovskite precursor inks and the overall coating processes.

In 2015, Yan et al. [78] used light scattering techniques to study $MAPbI_3$ (methylammonium lead iodide) precursor solutions. This work concluded that PSC precursors are not in fact "pure" solutions, in the sense that the precursors are not dissolved as ions or complexes. Instead, they suggested that these solutions were colloidal suspensions with colloids ranging in size from 10-1000 nm[78]. Since this study, various scattering techniques and measurements have been used to investigate precursor solutions, including dynamic light scattering (DLS) and Tyndall scattering [95, 97, 98, 147, 183–187]. Most of these studies revealed a bimodal size distribution within the precursor solutions. The bulk of PSC precursor solutions appear to be made up of ~2 nm sized particles, with a second peak often seen at a much longer length scale, assigned to the presence of larger particles. However, the placement and intensity of this "larger colloid" peak varies significantly between solutions that are similar in composition, and there is still debate as to how much these colloids affect subsequent film structure, formation and performance. For example, while some studies show the disaggregation of large colloids/aggregates leads to improved device performance [98, 147, 188], others show an optimum amount of large colloids results in the formation of a more stable precursor [95]. In contrast, some studies using DLS were not able to measure particles greater than 10 nm [187] and a study by Dutta et al.[103] examining perovskite colloids using cryo-electron microscopy of $MAPbI_3$ solutions found the dominant species to be small colloids. Consequently, it is reasonable to ask exactly what DLS is measuring in these solutions.

Firstly, DLS or any form of light scattering from a polydisperse - or bimodal - system must always be interpreted with caution. According to Rayleigh scattering, the intensity of the scattered light scales with d^6, where d is the diameter of a particle[128] – (DLS theory is explored further in the Chapter 3). Thus, even a small number of large particles will dominate the measured signal in a way that is disproportionate to their volume fraction. This makes it inherently hard to study dispersions with a bimodal distribution. Additionally, with DLS there are potential complications that can arise from the inverse relationship between the derived size and the measured diffusion coefficient, because the intensity autocorrelation functions will decay at different rates over different ranges of delay times. The presence of unwanted contaminants such as dust particles can also impact results.

Small-Angle Neutron Scattering (SANS) and Small-Angle X-ray Scattering (SAXS) are powerful and proven techniques used for characterizing the size and shape of colloids in dispersion and macromolecules in solution[189–191], and can readily cope with optically opaque samples, as the scattering results from periodic variations in nuclear scattering length and electron density, respectively. In 2021, Flatken et al.[105] published a study examining perovskite precursor solutions using both SAXS and SANS, which enabled them to confirm the presence of particles at the nm length scale in $MAPbI_3$ solutions. They modelled their small angle data using a cylindrical form factor of dimensions 0.5 nm x 0.7 nm (diameter x length), coupled with a hard sphere structure factor, i.e., a lead-halide octahedra presenting as a cylinder. Their analysis also gave the spacing between the cylindrical particles as 2 nm. Given the limitations on the observable length scales with conventional SANS and SAXS measurements, DLS was used to confirm the presence of $\sim$2 μm colloids in solution.

Spin echo SANS (SESANS) is an exciting neutron scattering development which combines the benefits of a neutron scattering technique with the ability to probe length scales from $100nm \geq x \geq 20\mu m$ [192–194], and if necessary, also analyze highly concentrated systems as multiple scattering is accounted for.[195] The SESANS technique 'encodes' angular information arising from the scattering process in the precession of neutrons in a polarized beam (much like ^1H NMR as neutrons are also spin-1/2 particles), thereby circumventing the strict geometrical limitations of conventional SANS/SAXS or Ultra Small-Angle Scattering (USANS/USAXS). SESANS has been previously used to study a number of soft matter systems[193], aggregates in solution,[196] and colloidal particles [192, 194]. More recently Bernardo et al. used the technique to study the degree of dissolution of a range of organic photovoltaic relevant fullerenes ($PC_{61}BM$ and $PC_{71}BM$) to ascertain the maximum solubility in these highly opaque solutions[137]. They were able to observe the presence of colloidal aggregates in solution arising from incomplete dissolution of the fullerene species as they went beyond the solubility limit.

In this current work, we have investigated the aging of two common perovskite precursor systems; a triple cation (TC) perovskite precursor ($Cs_{0.05}FA_{0.79}MA_{0.16}Pb(I_{0.85}Br_{0.15})_3$), where FA is formamidinium and MA is methylammonium, and a $MAPbI_3$ solution, using both SANS and DLS to study the solution length scales. To cross-check these results and investigate further the presence of dispersed larger colloids, we have measured these same solutions using SESANS over a period of 9 days.

Through the combination of these three techniques, we are able to compare and contrast the length scales and size distributions of dispersed colloids present in perovskite precursor inks. Importantly we conclude that there are only very small amounts of the large (μm-sized) colloids or equivalently sized contaminants. To assess the possible impact of the large colloids in thin films, we calculate a possible number of the micron sized particles in a wet film, deducing that they are unlikely to act as nucleation sites and therefore are probably contaminants or defects.

By further analyzing the SANS data, we also reveal some interesting properties of the nm-sized colloids and observe that $MAPbI_3$ solutions change drastically in chemical composition over a 3 month period, while the colloids dispersed within TC solutions remain relatively stable. This paper shows that the combined use of SANS and SESANS is a novel way of directly studying the structure of precursor perovskite species in solution across a broad length scale range and as a proof of concept, we have shown that SANS could be a useful tool in further solution studies and – in conjunction with other techniques such as NMR – we could obtain a more complete picture of how these precursors evolve over time.

7.3.3 Experimental Methods

Precursor Solution and Film Preperation

All solvents were purchased from Sigma Aldrich (Gillingham UK). Pb-excess triple cation solutions, of 1.2 M:1.3 M and between 12-14 vol%, were made using the following concentrations: 507 mg/ml PbI_2, 171 mg/ml FAI, 73.4 mg/ml $PbBr_2$ and 22.3 mg/ml MABr in 4:1 DMF/DMSO with 50 µl of CsI added from a 1.5 M stock solution. $MAPbI_3$ samples were made at 0.65 M and 8-9 vol% using the following concentrations: 300.8 mg/ml PbI_2 and 103.8 mg/ml MAI in DMF. In both cases, these solutions are stirred overnight at room temperature to dissolve. Samples for absorption measurements were prepared on quartz-coated glass. All other characterization was conducted on ITO-coated glass. Glass substrates were purchase from Ossila.

All perovskite films were deposited in an inert environment. For $MAPbI_3$ films, 50μl of precursor was statically spin-coated using a two step process – 1000rpm for 10s, then 5000 rpm for 30s. 100μl of Ethyl Acetate was smoothly deposited onto this films 10s from the end of deposition. For TC films, 35μl of precursor was statically spin coated using a two step process – 1000rpm for 10s, then 6000 rpm for 20s. 100μl of chlorobenzene was deposited onto the film 5s from the end of deposition. In both cases, films were annealed at 100°C for 20 minutes.

DLS

All the DLS measurements were acquired using a Zetasizer Nano-ZS (Malvern Panalytical, UK). Measurements were taken on the undiluted samples at 1.3 M for the TC solution and 0.65 M for the $MAPbI_3$ solution as has been the standard practice for previous DLS studies on perovskite precursor solutions in literature. The viscosity of the solvents used was calculated as 0.678 MPa.s. The absorption coefficients for PbI_2 and $MAPbI_3$ are very similar for the wavelength used (633 nm) so absorption coefficients for solutes in the solution was estimated to be 0.7. For each measurement, 10 scans each lasting 10 seconds were averaged to produce an intensity weighted size distribution profile. This was repeated 3 times and the scans were averaged for each perovskite precursor ink solution. The intensity-weighted size distributions were then converted to volume-weighted size distributions using Mie theory.

SANS

The majority of SANS measurements were carried out on the LOQ diffractometer[197] at the ISIS Spallation Neutron Source (STFC Rutherford Appleton Laboratory, Didcot, UK). LOQ is a fixed-geometry, time-of-flight instrument, which simultaneously records scattered neutrons with wavelengths $2 \leq \lambda \leq 10$ Å on two separate two-dimensional neutron detectors to provide a total q-range of 0.006 – 1.4 Å^{-1}. For the solvent study on $MAPbI_3$ precursors, SANSXpress measurements were carried out on the beamline SANS2D at ISIS. For the SANS measurements the perovskite precursor materials were prepared in deuterated DMF (DMF-d_7) and DMSO (DMSO-d_6) solvents to provide the necessary neutron scattering length density contrast and contained in 2 mm pathlength cylindrical quartz cuvettes (Hellma UK, Type 120; Starna Scientific Ltd., Type 32) which were mounted on a temperature-controlled sample changer. The solvent scattering length density (SLD) contrast for $MAPbI_3$ was (ΔSLD = (SLD_{solute} – $SLD_{solvent}$) ~ 4.7x10^{-6} Å^{-2}), whilst for the TC solution ΔSLD ~ 4.5x10^{-6} Å^{-2} (see Table 7.2). The incident neutron beam was collimated such that it was 10 mm diameter at the sample position. Each raw 2D scattering data set was corrected for the detector efficiency and spatial linearity, and the measured neutron transmissions, before being azimuthally integrated and converted to the 1D coherent elastic scattering cross-section – herein referred to as the intensity – as a function of the scattering vector q (where q=$4\pi \sin \frac{\theta}{\lambda}$ and 2θ is the scattering angle) using the Mantid framework (version 4.2.0). This data was then placed on an absolute scale (cm^{-1}) by comparison with the scattering from a partially deuterated polystyrene blend of known molecular weight measured with the same instrument configuration. Background corrections arising from the quartz cuvette and the solvent were made in SasView version 4.2.235. The model-fitting was also performed with SasView using the peak_lorentz and teubner_strey models. During aging the solutions were stored in sealed, amber vials under ambient conditions.

Film Characterisation

UV/Vis measurements were performed under ambient conditions using a UV/VIS/NIR light source (Ocean Optics – DH-2000-BAL), collection fiber optic cables (Ocean Optics) and spectrometer (Ocean Optics – HR2000+ES).

AFM measurements were obtained using a Veeco Dimension 3100 in intermittent contact (Tapping) Mode with a NuNano Scout 350 cantilever (nominal spring constant 42 N/m, resonant frequency 350 kHz). Each sample was scanned over three 10x10μm areas. Data was analyzed using the open-source software Gwyddion[198] to obtain roughness measurements. Height histograms were plotted and all bearing analysis was completed using Nanoscope 1.9. SEM imaging was performed using an FEI Nova Nano450 SEM operating at a beam energy of 1.5 kV at a working distance of 4–5 mm, with an in-lens detector used to collect backscattered electrons. Grain sizes were processed using ImageJ software (Version 1.52a). XRD measurements were performed usinga PANalytical X'Pert^3 Powder system. This was equipped with CopperLine Focus X-ray tube run at a voltage of 45 kV with a tube current of 40 mA, with data collected using a 1D-detector, in Bragg Brentano geometry.

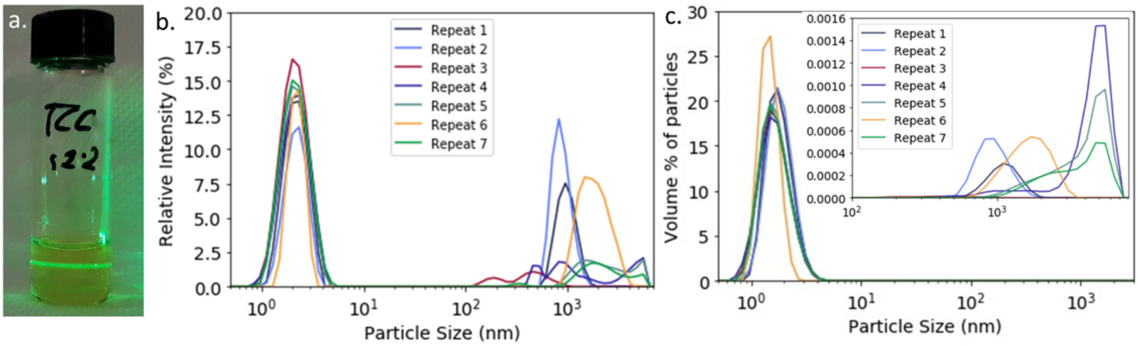

Figure 7.1: a) Tyndall scattering from a triple-cation (TC) perovskite solution, showing the presence of particles / colloids in suspension. And the DLS size distribution data for seven distinct but compositionally identical TC solutions plotted in b) Intensity-weighted and c) Volume-weighted representations. The inset in c) highlights the actual contribution from the larger colloids /particles.

SESANS

The SESANS dynamics measurements were undertaken at the Reactor Institute Delft (RID) at TU Delft, Netherlands. The instrument is described in Rekveldt et al.[136] The solutions were again contained in cylindrical "banjo" quartz cuvettes (Hellma). These were mounted in a bespoke sample rotator to compensate for any sedimentation and to ensure that if there had been large "aggregates" or dispersed colloidal assemblies present they would still have been measured using SESANS. The measured data were scaled relative to a non-scattering empty sample position - this is referred to as having the polarization P0, as there is no length scale (within the spin echo length probed) able to depolarize the beam. This reference incorporates all the instrumental polarization as function of spin echo length. In a sample with length scales in the spin-echo range of the instrument, this results in a deviation from this reference state. Each of the perovskite solution SESANS measurements took 2 hours and measurements were regularly repeated up to a maximum of 9 days post dissolution. The SESANS data presented is displayed as the ratio of the sample to the P_0 divided by the wavelength squared. At RID the neutron wavelength used is 2.06 Å. The colloidal silica comparison sample was measured on the LARMOR beamline at the ISIS Pulsed Neutron & Muon Source[199] from 12 nm to 4 μm and at the RID up to 10 μm (the plotted data is a composite of both datasets). The sample was rotated at 3 RPM for both measurements to avoid sedimentation effects.

7.3.4 Results and Discussion

Dynamic Light Scattering

Figure 7.1 a clearly shows the path of a green laser through a 30 wt% TC solution. In accordance with Tyndall scattering, this proves that this perovskite precursor is a colloidal suspension. However, we cannot deduce the particle size or concentration in solution from this simple qualitative observation. Figure 7.1b. shows the DLS size distributions for seven distinct TC solutions with identical chemical composition – labelled Repeat 1, 2 & 3, etc.,– plotted in terms of intensity. All three solutions give a bimodal distribution, consistently centered around 1-3 nm and with a secondary population at 100-8000 nm. Given that they have the same chemical composition and stoichiometry, these solutions should have the same or very similar populations of particles when measured using this technique. However, Repeats 1, 2 and 6 have a much greater proportion of larger colloids than were measured for other solutions. This may be due to differences in dissolution of the material related to the initial size of the dry material powder. We notice a wide variation in both peak shape and location for these larger colloids. In fact, most solutions show multiple peaks at this length scale. To investigate this further we look more stringently at the data. Each measurement shown in Figure 7.1 is averaged over 3 individual measurements taken successively. If we examine the individual measurements (as shown in Figure 7.7), we see the placement of these peaks changes even over the course of the measurement. This gives us cause to believe these "large colloids" are diffusing in and out of the incident light pathway, leading to these very varied measurements. We believe therefore these particles are quite sparse in the solution. Additionally, Figure 7.8 shows that these larger peaks disappear after filtration, indicating that this is not a measurement artifact. We discuss this further in the Supplementary information, as small amounts of large particles can distort the DLS intensity-weighted size distribution.[128, 129] In order to further understand the true significance of this bimodal distribution, the DLS data must be volume-weighted to give an accurate representation of colloid size by volume fraction. Volume percentage distributions of the solutions are also shown in Figure 7.1c. We see that the peaks in Figure 7.1b derive from a near negligible volume-percentage of larger colloids.

It has been suggested that these μm-sized colloids can influence the subsequent perovskite thin film grain size, by acting as nucleation sites for the perovskite phase during crystallisation.[188] We have investigated this idea with calculations based on our DLS measurements (calculation specifics are detailed in Supplementary Information). Using SEM images of annealed perovskite films made with TC solutions, we find the average grain density and compare this to the number of particles in solution. We assume that to spin coat a perovskite film requires an initial wet film thickness of 10μm. We approximate a total solute concentration of 14 vol% within our TC solutions and assume the particles are spherical. We used the solution with the highest volume fraction of larger particles (Repeat 1). According to our DLS data, 0.000024 vol% of the solutes in this solution have a diameter of ~920 nm and the other 99.999976% of these particles have a diameter of 1.6 nm. If this is the case, then in 1 mL of the TC solution there are $\sim 8 \times 10^6$ μm-sized particles, compared to $\sim 5.4 \times 10^{19}$ nm-sized particles. If these particles are distributed uniformly throughout all precursor material, a wet film with an area of $1cm^2$ and thickness of 10 μm would therefore contain 8000 large particles and $\sim 5.8 \times 10^{16}$ small particles.

Figure 7.2 explores what these numbers mean physically in an annealed perovskite film. Figure 7.2a shows an optical image of a perovskite film at 50x magnification. According to our calculation there would be 10 large colloids in this area. Figure 7.2b shows an example of an SEM image of a TC film. Here we see that neither the large nor the small particles sizes align with grains in the final perovskite film in either density or scale. Given the size and distribution of these large colloids, they are more likely to appear as defects than to enhance film crystallization, and are too few in number to be responsible for the observed

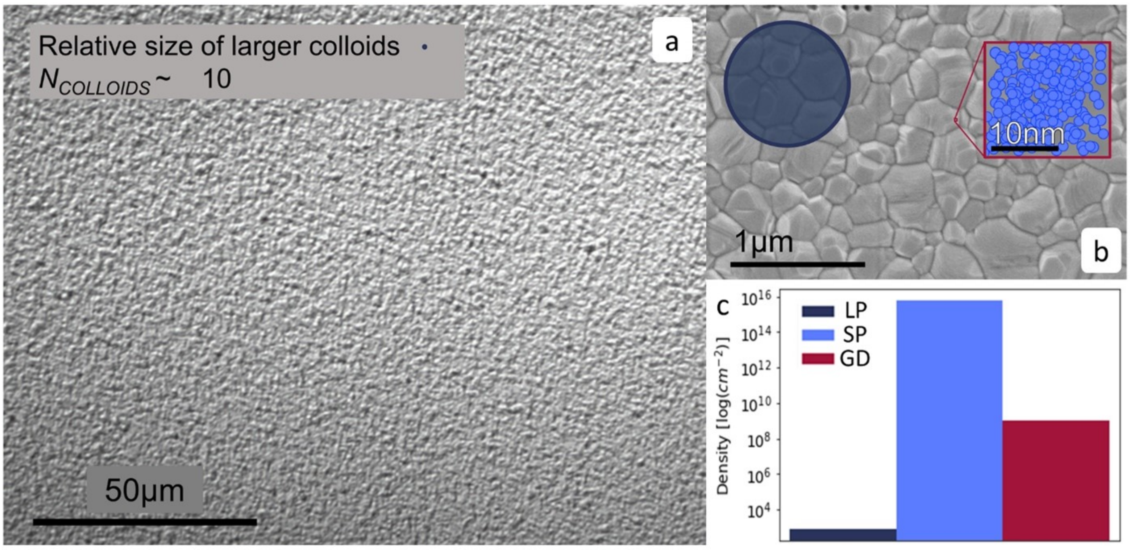

Figure 7.2: An optical microscope image (a) and an SEM image (b) of a thermally annealed perovskite film with an average grain size of 200-600 nm. For both images, a micron sized particle is shown for reference (dark blue). In (b), the inset contains a magnified area of this image along a schematic illustration showing the relative size and density of the smaller particles (light blue). c) Estimated number density of large and smaller particles dispersions in a wet film of 10 μm thickness (LP and SP respectively), compared to the average grain density (GD) in the final annealed perovskite film, this data is plotted on a log scale.

perovskite grain size. We therefore postulate that these grains must instead result from nucleation from the dominant population of smaller 1.7 nm particles.

Neutron Scattering: SANS

To further investigate the dispersed structures in solution, we conducted SANS and SESANS measurements on both the TC precursor (molarity 1.3 M) and a $MAPbI_3$ precursor solution (0.65 M). To provide suitable neutron contrast between the bulk medium and PbI_2 we used deuterated solvents, d_7-DMF and d_6-DMSO (see Table 7.2). This has the added benefit of reducing the incoherent background scattering level, thereby improving the signal-to-noise ratio. This is important because the molar concentrations of our precursor solutions constitute very dilute systems in volume fraction terms and means the SANS intensities are correspondingly low. However, the contrast in our systems is better than that in a silica/D_2O dispersion, a colloidal system that has been widely studied with SANS40. Thus, we can have high confidence that our SANS/SESANS measurements will be sensitive to lead based dispersed colloids or aggregates at low concentrations if they are present in our samples.

To explore if the SANS technique could map changes in the perovskite solutions, we measured two different perovskite precursors (TC and $MAPbI_3$) before and after

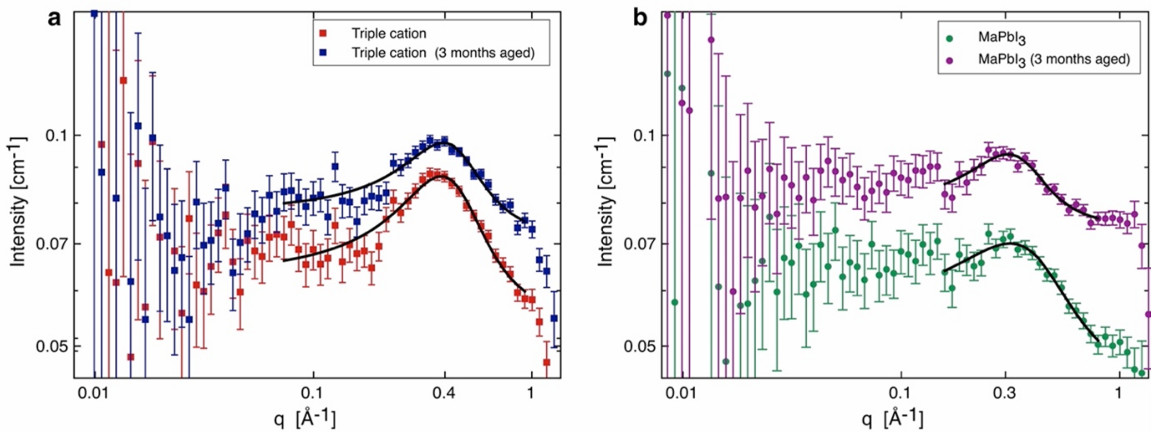

Figure 7.3: SANS data for a.) TC and b.) $MAPbI_3$ perovskite precursor solutions fitted with a Lorentzian peak model (black line). The data in each plot compares the 3 months aged solutions that correspond to the samples measured by SESANS and fresh solutions measured soon after dissolution.

3 months of solution aging. The results are shown in Figure 7.3. As anticipated, the absolute scattering intensities are very small with a concomitant degree of statistical uncertainty, particularly at smaller scattering vectors where there are relatively fewer neutrons. Nevertheless, at larger scattering vectors each set of data clearly shows a broad peak. These peaks were initially fitted to a Lorentzian function to ascertain their position. The TC system (in Figure 7.3a) has peaks positioned at q values of 0.394 $Å^{-1}$ for the aged sample and 0.385 $Å^{-1}$ the fresh sample, corresponding to length scales ($= \frac{2\pi}{q_{peak}}$) of 1.59 nm and 1.63 nm, respectively. These length scales reassuringly agree with the DLS results attained earlier, which give a particle size of 1.6nm for the TC system. For the $MAPbI_3$ solutions, the same analysis gave peak q values at 0.315 $Å^{-1}$ for the fresh repeat and 0.308 $Å^{-1}$ for the aged sample. These smaller q values correspond to slightly larger length scales of 1.99 nm for the repeat and 2.04 nm for the aged sample, respectively.

The broad nature of the peaks indicates that there is no regular repeating structure or single fixed distance. Furthermore, the absence of any power law regions in the data at low q indicates an absence of both mass fractal (e.g., cluster aggregation gives Intensity q^{-2}) and surface fractal (yielding $q^{-3} - q^{-4}$ depending on the surface roughness) behaviour within the SANS measurement range. The latter is indirect corroboration of the DLS findings: namely, that if any micron-sized aggregates dispersed in solution are present, they are so few as to have a negligible impact on the SANS.

In order to reduce the number of assumptions made about the structure of these nanoparticles, we have taken a simple approach to modelling this, employing the model developed by Teubner & Strey.[200, 201] The Teubner-Strey formalism models the scattering of an interacting two-phase system without long-range order characterized by a correlation length, ξ - the length scale beyond which correlations die out- and domain size/periodicity, d. This is discussed further in the Supplementary Information. Below is the formula used to fit the SANS data [200]:

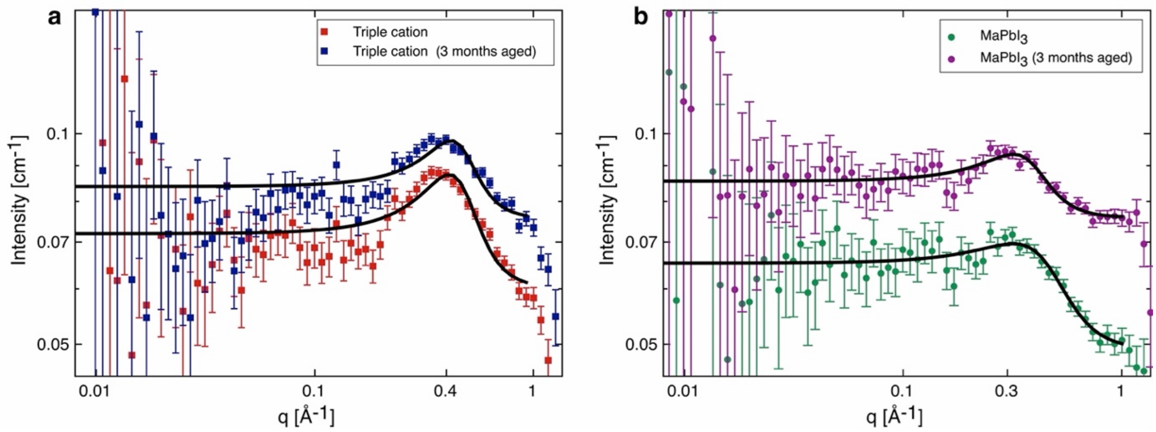

Figure 7.4: SANS data for a.) TC and b.) $MAPbI_3$ perovskite precursor solutions. The data in each plot compares the 3 month aged solutions (corresponding to samples measured for SESANS) and fresh solutions measured soon after dissolution. The continuous lines are fits with the Teubner-Strey model.

$$I(q) = \frac{8\pi\Phi_a(1-\Phi_a)(\rho_a-\rho_b)^2 c_2/\xi}{a_2 + c_1 q^2 + c_2 q^4} \tag{7.1}$$

$$a_2 = [1 + (\frac{2\pi\xi}{d})^2]^2 c_1 = -2\xi^2(\frac{2\pi\xi}{d})^2 + 2\xi^2 c_2 = \xi^4 \tag{7.2}$$

The domain sizes compare favourably with our own DLS data and agree well with other SANS measurements from the literature.[105] However, the simplicity of this model allows the SLD of this “solute domain” to be optimized and the composition determined, and this has provided us with an intriguing insight into the structure of these precursor solutions. Apart from the fresh $MAPbI_3$ sample, the SLD values for the perovskite components are found to be higher than the calculated values for the pure phases or their mixtures likely to be present (see Table 7.2). There are several possible explanations for this: firstly, that our SLD calculations have under-estimated the bulk densities of the different components, although variations in material density will only give relatively small and linearly proportional changes in the SLD. Secondly, that the solute-rich domains have coordinated/entrained (deuterated) solvent molecules. We consider the latter of these to be more likely.

In the $MAPbI_3$ solution both the size and SLD (composition) of the solute-phase changes substantially over the ~3 months aging period. These changes in the solution structure suggest that the solute-rich domains we observe are metastable states, that can change in size or composition over time. This aligns with previous work which has identified that acidity, solvent decomposition and additives can all affect perovskite solution structures.[97, 147, 188] This increase in the domain size and correlation length implies that over time these nm-sized aggregates are growing.

In contrast, we can see that after 3 months of aging, neither the correlation length, nor the domain size have substantially changed in the TC system. But, once again, the SLD of the solute-rich phase giving rise to the scattering does not correspond to that of any of

Sample	Perovskite vol fraction (solute phase)	Perovskite (solute phase) SLD 10^{-6} Å^{-2}	Correlation length ξ (nm)	Domain size, d (nm)
Triple Cation (fresh)	0.140 ± 0.007	2.66 ± 0.07	0.59 ± 0.03	1.41 ± 0.02
Triple Cation (Aged)	0.121 ± 0.007	2.89 ± 0.19	0.64 ± 0.05	1.40 ± 0.02
$MAPbI_3$ (fresh)	0.059 ± 0.005	1.51 ± 0.18	0.41 ± 0.03	1.56 ± 0.03
$MAPbI_3$ (aged)	0.078± 0.006	3.53 ± 0.10	0.63 ± 0.05	1.76 ± 0.04

Table 7.1: Teubner-Strey model parameters derived from fits to the SANS data for $CsFAMAPb(Br_xI_{x-1})_3$ in d_7-DMF:d_6-DMSO solvent blend, and $MAPI_3$ perovskite precursor solutions dissolved in pure d_7-DMF shown in Figure 7.4. The SLD of the solvent bulk phase was fixed at its calculated value, this was 6.3x10^{-6}Å^{-2} for $MAPbI_3$ and 6.12x10^{-6}Å^{-2} for the triple cation solutions.

the individual components shown in Table 7.2. This again suggests that there must be one or more intermediate complexes forming within the solutions with dimensions 1.3-1.4 nm. This size value also correlates well with the DLS results.

There are many differences between these two systems which could result in these different aging processes (this includes solvent blend, molarity and solids composition). Based on what we have found previously[125] we speculate that deprotonated methylammonium (MA^+) is very unstable in TC solutions. We hereby note that additional molecules in the TC sample (formamidinium, bromine, cesium) could potentially have a stabilizing effect on some of the intermediate complexes formed. We also note that in this study, the TC solution is dissolved in a DMF:DMSO solvent blend, while the $MAPbI_3$ sample is dissolved purely in DMF. It has been shown that solvent co-ordination can affect the crystallization rate for perovskite films - for example, DMSO can form strong intermediate phases with different iodoplumbate species during crystallization[70–72, 81, 82, 84, 202] and this stronger co-ordination can reduce some preliminary Pb-I coordinating and bridging interactions.[69, 72] Initially we suspected that, this reduced solvent co-ordination lead to the solute domains in the $MAPbI_3$ sample being more dynamic over time. To explore this idea further, we have aged $MAPbI_3$ solutions in a DMF/DMSO solvent blend as with the TC solutions, and detected the change in colloid populations using SANS. The results are shown in Figure 7.15 and we again find flat scattering at low q, however the Teubner-Strey fits give unphysical volume fractions which may mean that they are not simple two phase solutions. This demonstrates that solvent choice plays an interesting role in the formation of these dispersions, we simply conclude here that these systems are much more complex than we originally suspected. However, we remark that SANS is an valuable tool to compare the composition of these different solutions and this should be the subject of future studies.

We have demonstrated that these small particles are unlikely to be pure Pb-halide aggregates, and appear to contain some entrained/complexed solvent molecules. By studying these two different systems, we have highlighted that SANS can be a useful tool to explore the size and – using a simple model - the composition of these nm-sized dispersions. We have also shown that in this instance, precursor dispersions are more stable for the triple cation-based solutions than for $MAPbI_3$.

Film Morphology

We will now explore what affect these evolving dispersions have on the resulting perovskite films. Figure 7.10 show that the absorption spectra and the positions of XRD peaks for these films do not shift as the solutions age, indicating that there is little change to the perovskite film composition over this time. The only remarkable change is in the TC films, in the reduction of the PbI_2 peak at 12.8° over time. This is expected as there is an excess of Pb in these solutions. Figure 7.11 and 7.14 shows SEM and AFM images of films made from different solutions for $MAPbI_3$ and TC precursors respectively. We see here that the $MAPbI_3$ films have extremely different structures compared to TC films, as expected as they are such different systems. This $MAPbI_3$ structure is explored in Figures 7.12 and 7.13, which contain height histograms and bearing analysis data taken from aged and fresh $MAPbI_3$ AFM images.

In Figure 7.11, we can see $MAPbI_3$ films show a characteristic “plank” structure that has been seen before where DMF is the lone solvent for $MAPbI_3$ perovskites.[78, 203] We find as these solutions age, the surface morphology of the subsequent film changes. Figure 7.11a-b show the films from fresh solutions contain very broad structures, although there are significant pinholes. Figure 7.11a also show striking bright spots, which could imply significant charge build-up within these pinholes. Figure 7.11b show that all of these plank-like features are at a similar height and we see a clear grain structure can be detected within them. In Figure 7.12, the height histogram for fresh $MAPbI_3$ show a single height average at around 400nm, which also suggests a uniform height profile.

Figures 7.11c-d show some interesting changes to this morphology. These structures are still present after ink aging, however they appear to be a lot more disordered. We can see in Figure 7.11d, these fragmented structures lead to a much more varied film. This observation is supported by the roughness measurements taken from this AFM data. The films made from aged $MAPbI_3$ solutions are significantly rougher than their fresh counterparts – we measured RMS roughness of 137 ± 4 nm and 91 ± 8 nm for aged and fresh $MAPbI_3$ respectively. Additionally, this is confirmed by the height histograms in Figure 7.12, which show a much broader peak for the aged ink than for fresh $MAPbI_3$ samples. To probe this in more detail, we analyzed the bearing data for these height histograms. By integrating the area under these histograms, we can find what percentage of the overall film lies at various heights from the top surface of the film (Fig 7.13a). Figure 7.13b shows that for both films, the bulk of perovskite material lies between 300-700nm. However, while the sample from a fresh solution shows a steep change in the curve at around 400nm, the aged $MAPbI_3$ sample shows a shallower gradient between 300-700nm. This indicates the features in the film made from aged $MAPbI_3$ solutions are arranged at random heights, leading to a much less orderly film. We believe this all indicates that there is an altered crystallization pathway for the film made from aged $MAPbI_3$ solution compared to the fresh $MAPbI_3$ solutions – and this change is linked to the larger precursor dispersions seen in Table 7.1.

To substantiate this, we refer to the SEM and AFM for the TC films. In Figure 7.14, we can see that grain size is significantly smaller after solution aging – but otherwise the structure of the perovskite film remains largely the same and produces a dense, uniform film. To confirm these results, we have measured the roughness for these films and found there was no significant difference between the two films- 17.5±0.7 nm and 15.8±0.4 nm for fresh and aged TC respectively.

We therefore believe these precursor dispersions affect perovskite formation pathways, hence the change in $MAPbI_3$ precursors correlates with a change in film morphology. However, we acknowledge that more work should be done to understand how this will impact devices with more long term aging. We also realize there are numerous other factors that are at play here – and further study should include a more comprehensive sample selection, alongside a more comprehensive device study.

SESANS

SESANs uses a polarized beam of neutrons travelling through a series of magnetic fields. By measuring the polarization of scattered neutrons which have interacted with the sample relative to those from the unscattered beam, we can measure the volume fraction of larger colloids in a solution (this is discussed in detail in Chapter 3). The SESANS data for the two distinct perovskite compositions are shown in Figure 7.5. This data was acquired continuously over a long period of time - from the initial dissolution of the perovskite powder precursor for a total of 9 days- with the solutions being measured at intervals throughout this period. To avoid sedimentation of these larger aggregates, these solutions were slowly rotated (3 rpm) as they were measured. While we acknowledge there is a chance that this rotation could break up the larger colloids dispersion, we reason that this disturbance would be no more violent than moving a solution from vial to cuvette before DLS measurements or before perovskite deposition. Additionally, as these solutions are measured over a long period – if these aggregates are going to form, they probably would form to some degree in these conditions -even with minor disturbances. These measurements should be sensitive to a concentration above 0.005 vol% for particles of radius 500 nm and 0.001 vol% for particles of radius 1 μm.[137] The SESANS measurements unequivocally support the volume-weighted DLS results in that they both show a very low or effectively zero volume fraction of dispersed lead based colloids present at larger particles size. To validate our approach, and to illustrate what would be seen if such dispersed particles were present in solution, we have included SESANS data for a 3 μm diameter silica particle dispersion in D_2O, this was at 0.1% by volume. Here we can see a signal with a sharp drop in the polarization and a constant total scattering value at high spin-echo length $\sim 2\mu$m – 10μm.

7.3.5 Conclusions

Within this paper, we have come to three main conclusions. The first is that DLS alone should be used cautiously when analyzing particle sizes within perovskite precursor solutions. While there is reliable and useful information in the “small particle” data, the intensity of light scatting from the large particles can lead to misinterpretations of the quantity of “large particles” present. It is therefore important that the volume-weighted size distributions are studied, in addition to the intensity-weighted size distributions routinely provide by DLS measurements if a true representation of the size distribution in these precursor solutions is to be obtained. We have also outlined the physical significance of these particle sizes and their role in the context of an annealed perovskite film and shown that if these larger particles are there (making up less than 0.0001% of the solution

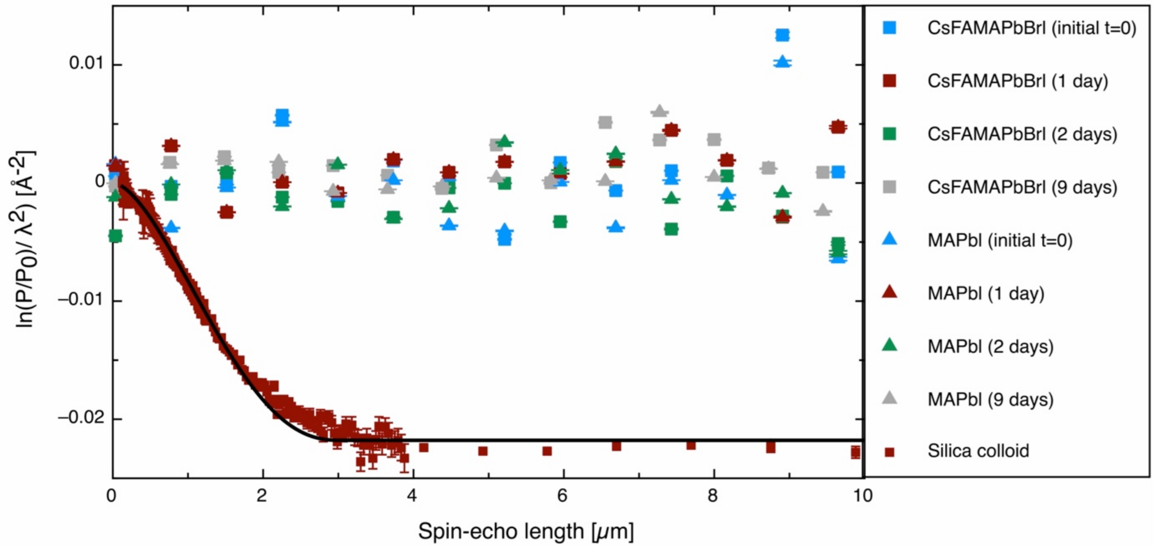

Figure 7.5: SESANS data for the triple cation (labelled as CsFAMAPbBrI) and *MAPbI* precursor solutions (labelled as $MAPbI_3$) measured at various times as indicated in the legend, from the point after dissolution (t=0) and up to 9 days after dissolution. For comparison a SESANS measurement of silica spheres in D_2O showing scattering up to a length scale characteristic of the particle diameter 3µm is also shown, this was 0.1% by volume.

volume) it is unlikely that they have a beneficial effect on grain sizes or film quality – more likely introducing inhomogeneities or defects in the film.

We have also shown that both SANS and SESANS can be valuable tools when probing dispersed colloidal material within perovskite solutions. Using both techniques, we can span the length scales 1 nm -10μm. By applying the Teubner-Strey model to our SANS data and fixing the known SLD of the majority solvent phase, we have revealed that these nm-sized particles are not uniquely Pb-halides but more like perovskite-solvent complexes. Further experiments should help illuminate how these components interact within these complex systems. Indeed, it may be possible to use a whole series of SLD solution contrasts to unambiguously determine the composition of these species. Additionally, SESANS has shown that there are vanishingly small amounts of the dispersed large colloids, being below the level of detection within either of the precursor solutions studied, agreeing with the conclusions found from DLS. We believe that both these techniques could - in conjunction with other techniques such as NMR – help us fully understand these precursor dispersions.

Lastly, through aging of two perovskite solutions (TC and $MAPbI_3$) we have examined solution chemistry over long time periods (3 months). The size and SLD of the nm-sized particles within the aged $MAPbI_3$ sample is significantly different to the fresh $MAPbI_3$ sample, whereas the TC sample stayed relatively consistent, and we have related this to a change in surface morphology for the subsequent films. While there are many factors which could contribute to this observation, we note that the crystallization formation dynamics are altered after for films made from aged $MAPbI_3$, which we think relates to the change in precursor solutions seen with SANS. Exploring this relationship should be the aim of future studies.

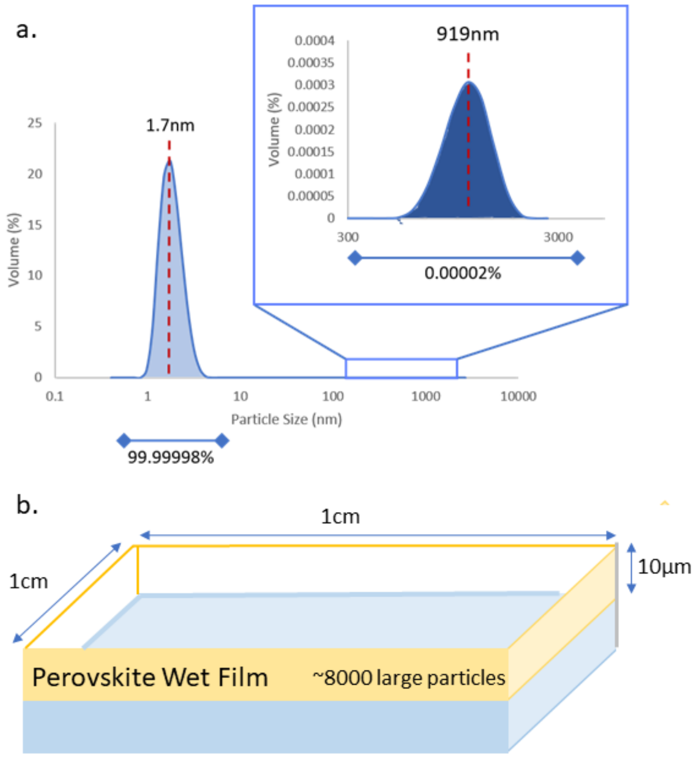

Figure 7.6: a.) Volume Percentage Distribution from DLS measurements on TC 2. Integrated percentages measured as the area beneath the curve. (b.) Schematic of the "wet film" used in the DLS

7.4 Supplementary Information

7.4.1 Film Calculations

From the volume-weighted DLS size distributions, we assume a Gaussian distribution around a mean particle size and use the area underneath this curve to find the Vol% of a particular particle size as shown in Figure 7.6.

This data represents the hydrodynamic diameter of these particles therefore the particle radius is half this. If we assume these are spherical colloids, then the volume of a large and small particle is $4.1\text{x}10^{-13}\text{cm}^{-3}$ and $2.6\text{x}10^{-21}cm^{-3}$, respectively. The total solute vol% of these TC solutions is roughly 14% and from the DLS we can tell that of this 0.0000235% is made up of large particles. Therefore, in any volume of TC solution, $3.291\text{x}10^{-6}$ % of that will made up of large particles. So given the volume of a particle and how much volume they all occupy, we can estimate how many there are. Following through, we find that there are $8.11\text{x}10^{6}$ large particles in 1ml. In a wet film of average thickness 10μm, this would lead to 8150 large particles/cm^2. By the same logic, we calculate that there are

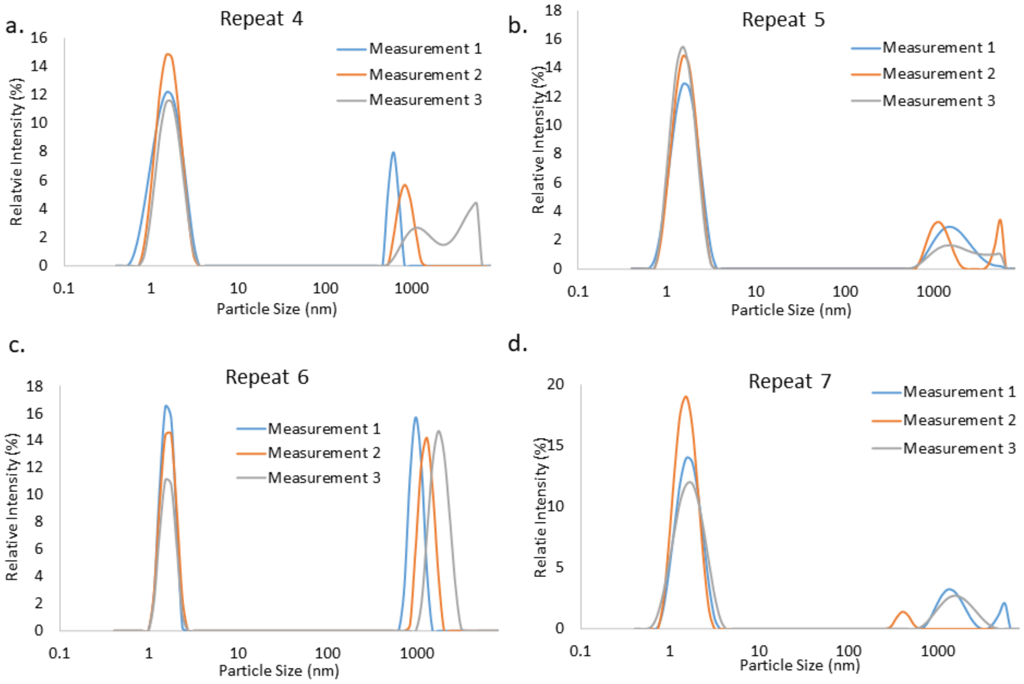

Figure 7.7: Individual Intensity-weighted DLS size distribution graphs for Repeat 4 (a), 5 (b), 6 (c) and 7 (d). Three intensity profiles are taken over the course of a measurement (Measurements 1, 2 and 3) and these are averaged to provide the results in Figure 7.1a.

5.4x10^{19} small particles in 1ml and therefore 5.78x10^{16} small particles/cm^2 in the same wet film.

7.4.2 Tuebner Strey Model

There are many models to describe small angle scattering from different types of nanostructure. Here, the Teubner-Strey model is used to characterise the perovskite precursor solutions. The Teubner-Strey model assumes a two phase system.[200] In this system, the solvent and solutes are the majority and minority phases respectively. The scattering intensity profile over a given q-space can be described using Equation 7.1 and 7.2.

This depends on the domain size d, correlation length, ξ, volume fraction, Φ_a, and respective scattering length densities, $\rho_{a/b}$. In neutron scattering the phase problem means that d can be the domain size or periodicity between particles. We here argue that the d from the Teubner-Strey model corresponds to the average domain size of any solute phase and the correlation length, ξ, is the average length scale before a phase change. The scattering length densities (SLDs) and volume fraction of the solvent and solute

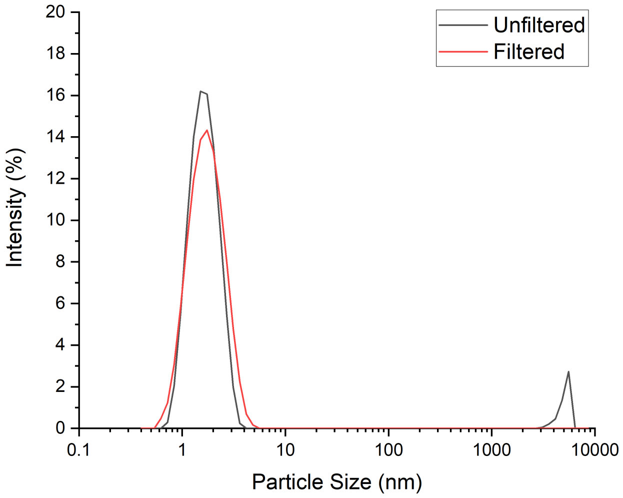

Figure 7.8: Intensity-weighted DLS size distributions from unfiltered (black line) and filtered through a 0.2 μm filter (red line) fresh TC perovskite precursor solutions at 1.3M.

particles can also be extracted using this model. To explore what this could represent in our systems, we refer to Figure 7.9. Here, we can see that if phase B (the solute) is formed of large aggregates (as seen in 7.9a), both the domain size d and average distance between phases (ξ ($= \Sigma\xi_n/\text{n}$)) is larger than for a dispersed solution of nanoparticles (Fig. 7.9).

Neutron scattering lengths do not vary linearly across the periodic table as for X-ray scattering lengths - for example hydrogen and deuterium have significantly different neutron SLDs despite having very similar chemical properties. This property was exploited in this work, by preparing samples in deuterated solvents. This provides a large neutron SLD contrast between the solvent and solute in the solution. The calculated SLDs of solvents, perovskite materials and precursor components are shown in Table 7.2.

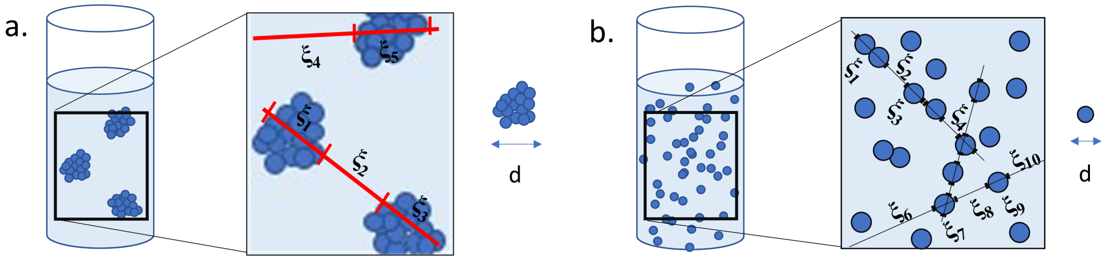

Figure 7.9: An illustration of large aggregates (a) and disperse nanoparticles (b) in a solvent material. The solute material representing the minority phase within the Teubner-Strey model is shown in with dark blue circles, with the solvent (i.e., the majority phase) shown in light blue. Insets show the average spacing between "phase changes" for each system, ξ_n, which is averaged to give the correlation length ξ ($= \frac{\Sigma\xi_n}{n}$). The domain size of the minority phase is shown for each case as d.

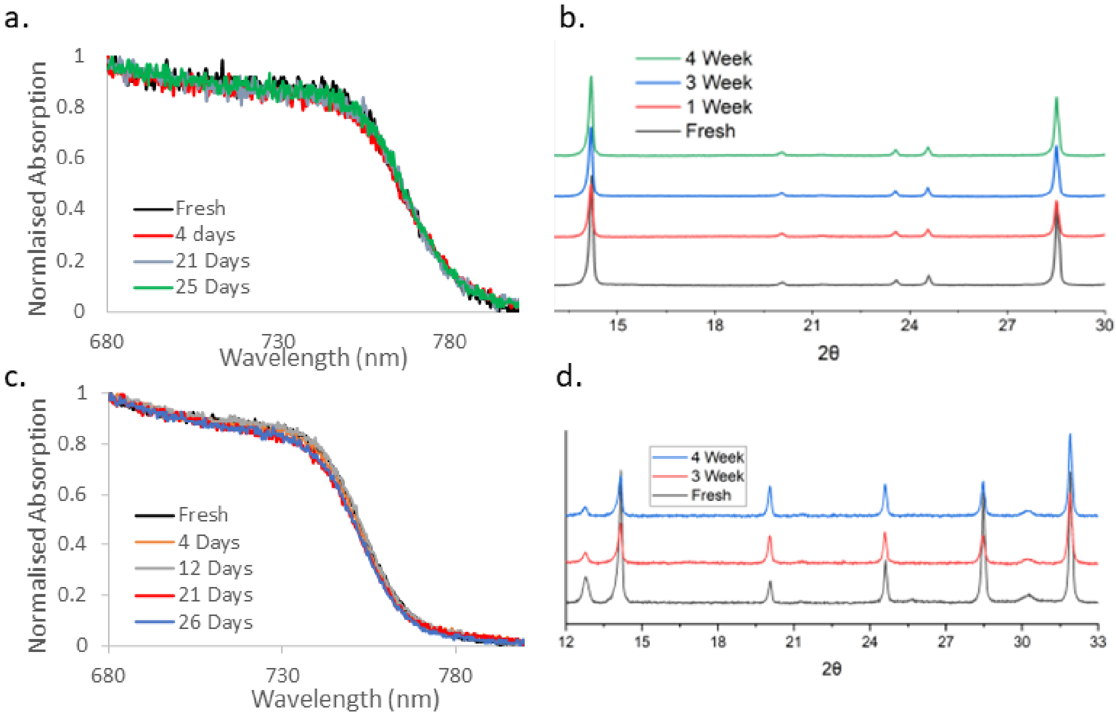

Figure 7.10: UV-Vis absorption spectra (a) and XRD profiles (b) of films made from a $MAPbI_3$ solution aging over a 1 month period. UV-Vis absorption profiles (c) and XRD profiles (d) of films made from a TC solution aging over a 1 month period.

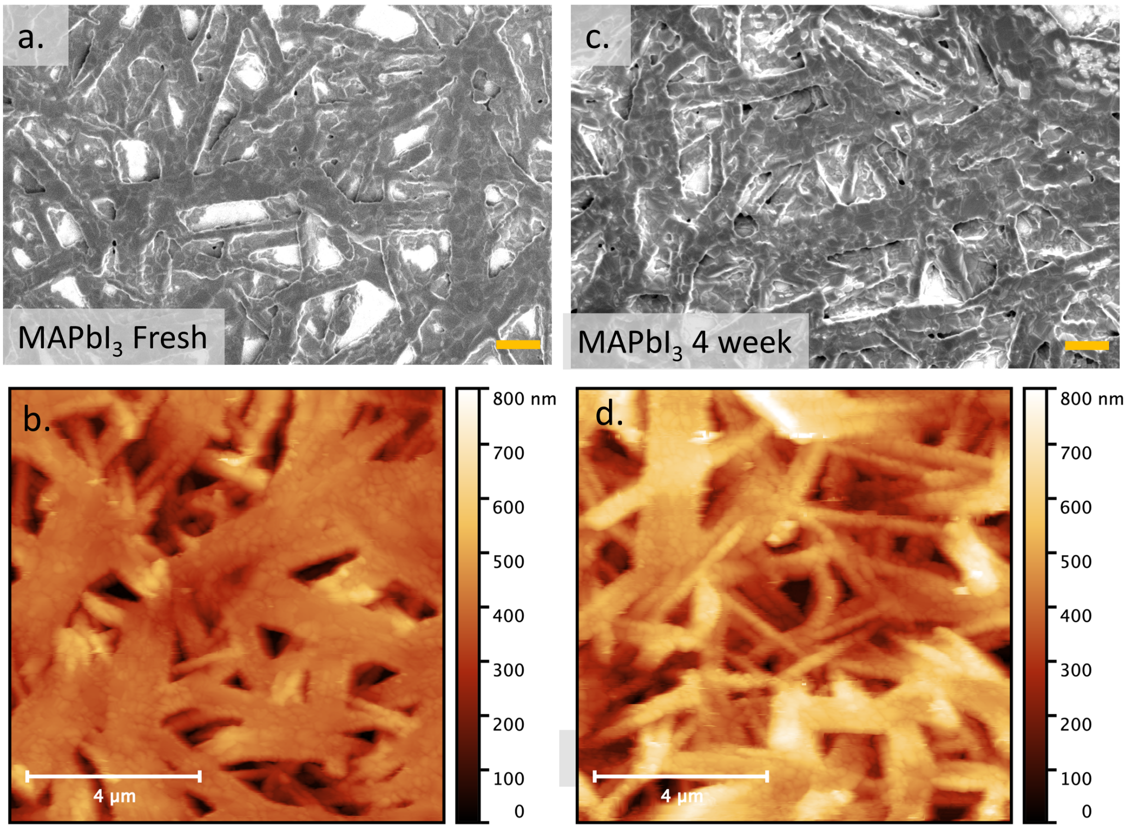

Figure 7.11: SEM and AFM images of fresh and aged $MAPbI_3$ films. SEM (a) and AFM images (b) of $MAPbI_3$ films made from fresh solution. SEM (c) and AFM images (d) of $MAPbI_3$ films made from solutions aged for 1 month. In the SEM image the scale bars in the bottom right represent 1μm.

Material	Chemical Formula	Mass Density (g/cm^3	Neutron SLD
Deuterated dimethyl sulphoxide (DMSO-d_6)	$(CD_3)_2SO$	1.19	5.28
Deuterated dimethylformamide (DMF-d_7)	$(CD_3)_2NC(O)D$	1.03	6.33
4:1 DMF-d_7:DMSO-d_6	$(CD_3)_2NC(O)D : (CD_3)_2SO$	1.06	6.12
Lead Iodide	PbI_2	6.16	1.61
Lead Bromide	$PbBr_2$	6.66	2.51
Formamidinium Iodide	FAI	2.23**	0.93
Methylammonium Bromide	MABr	1.64**	0.03
Methylammonium Iodide	MAI	2.00**	-0.07
Cesium iodide	CsI	4.51	1.11
$MAPbI_3$ perovskite	$CH_3NH_3PbI_3$	4.1-4.2 [15, 204]	0.75
$FAPbI_3$ perovskite	$HC(NH_2)_2PbI_3$	4.1 [15]	1.24
$MAPbBr_3$ perovskite	$CH_3NH_3PbI_3$	3.8 [204]	1.20

Table 7.2: A summary of chemical formulae, mass densities and neutron scattering length densities (SLDs) of the solvents, perovskite compositions and respective perovskite precursor materials used in this work. * Scattering length densities determined using [205]. ** Organic material densities estimated using [206].

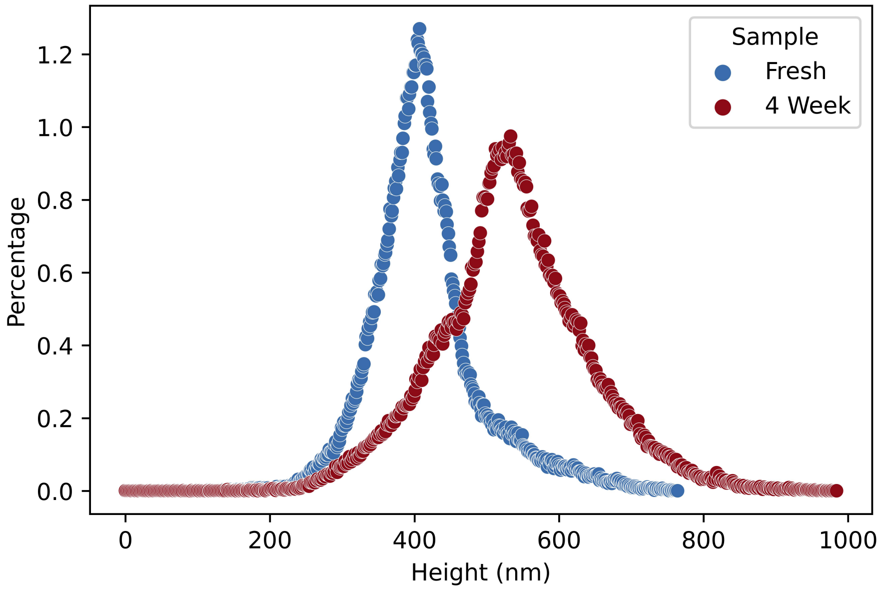

Figure 7.12: Height histograms taken from AFM images of a film made from a fresh $MAPbI_3$ ink (blue circles) and an aged $MAPbI_3$ ink (red circles).

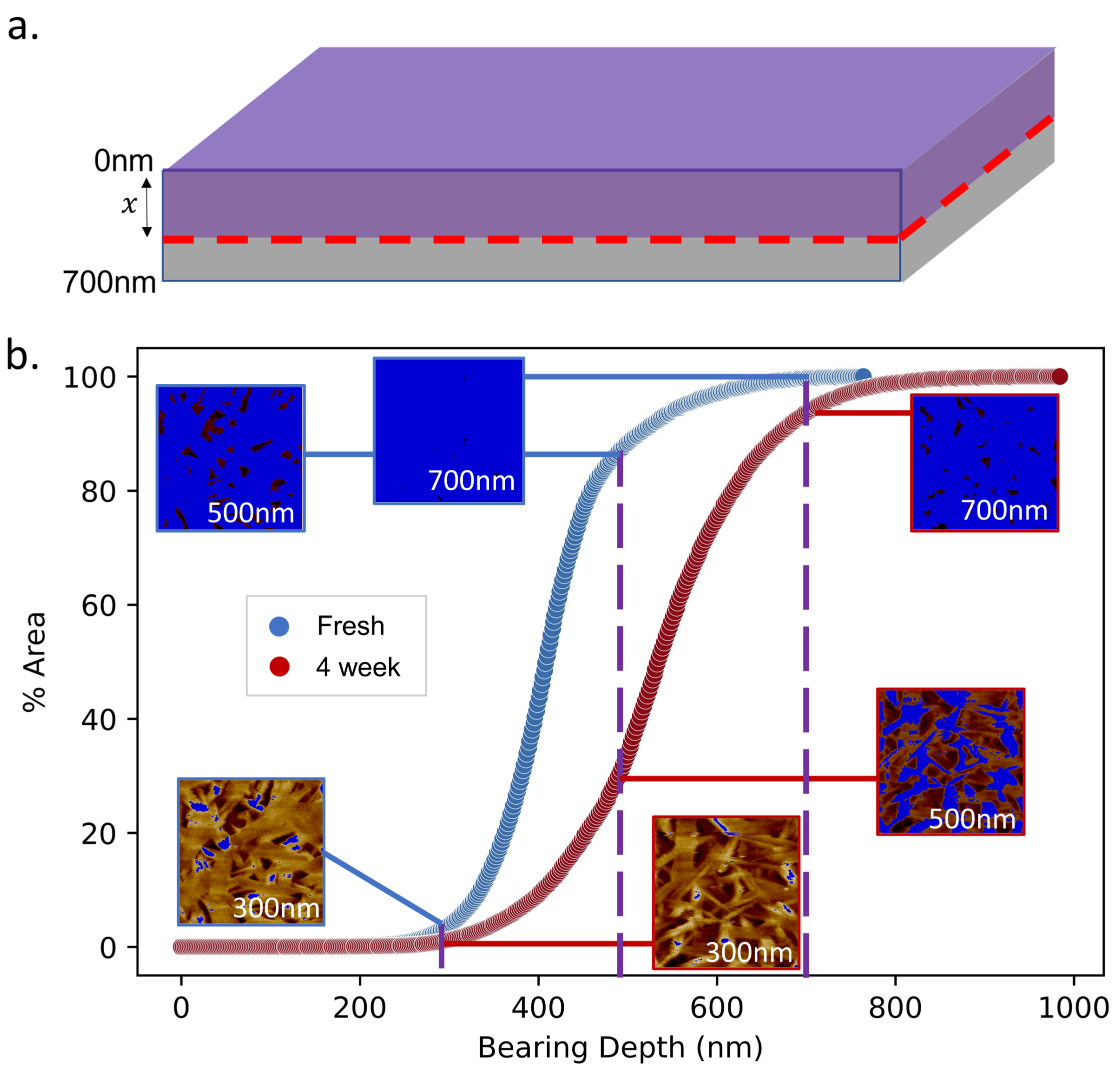

Figure 7.13: a.) A diagram showing the penetrating height of bearing analysis. Data given is the percentage area of the film that lies within the bearing depth (marked x) from the top of the film surface. (b.) Bearing analysis data taken from AFM images made from a fresh $MAPbI_3$ ink (blue circles) and an aged $MAPbI_3$ ink (red circles). Insets show % area of the image within the bearing depth from the film surface for fresh $MAPbI_3$ (blue) and aged $MAPbI_3$ (red). This data is calculated from the histograms in Fig. 7.12.

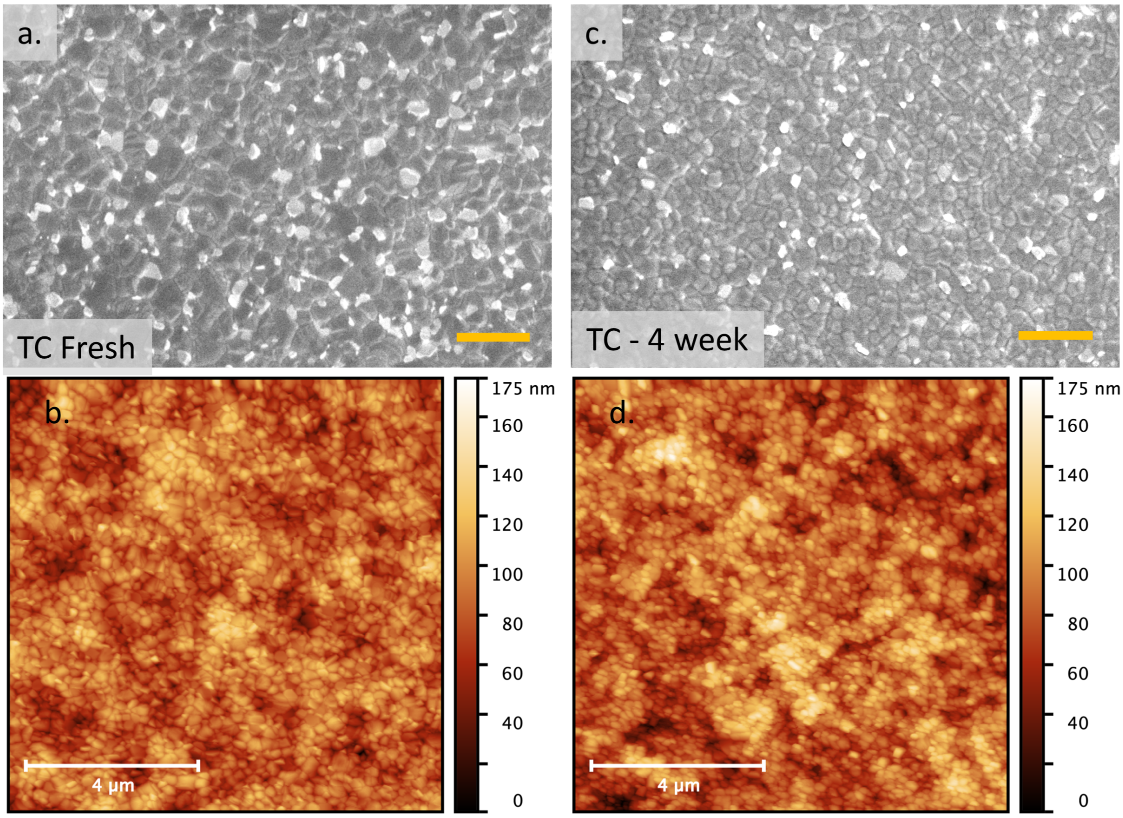

Figure 7.14: SEM (a) and AFM images (b) of TC films made from fresh solutions. SEM (c) and AFM images (d) of TC films made from aged solutions aged for 1 month. In the SEM image the scale bar in the bottom right represents 1μm.

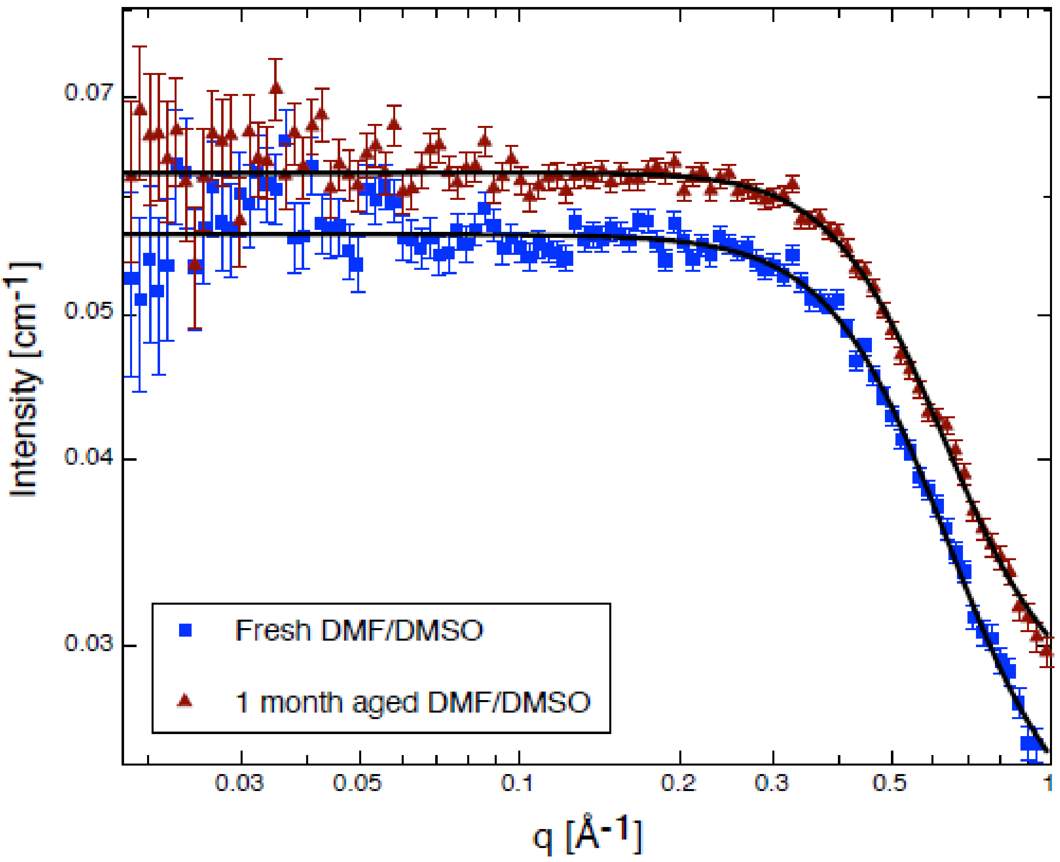

Figure 7.15: SANS data for $MAPbI_3$ in the same solvent mixture (DMF/DMSO) as that used for the $CsFAMAPb(Br_xI_{x-1})_3$ solutions.

Chapter 8

Conclusions and Future Work

8.1 Summary of Results

The concluding remarks from this thesis are as follows:

- In Chapter 4, we identified the primary degradation mechanism within stoichiometric triple-cation mixed-halide solutions to be the deprotonation of methylammonium, and the subsequent formation of N-methyl formamidinium (MFA) and N,N-dimethyl formamidinium (DMFA) through a series of addition-elimination reactions. This reaction consumes MA^+ within the solution inducing the formation of non-perovskite δ-phases within the perovskite films. As this effect worsens, devices made from 6 month aged TC inks show no photovoltaic activity. We found this reaction could be slowed effectively by storing the solutions at low temperature. This prolongs usable shelf-life of the precursor ink without changing the perovskite stoichiometry. Finally, we probe the solvents role in this reaction. By varying the amount of DMF present in solution, we find that solutions using only DMSO as a solvent have a higher solution stability. We attribute this to the higher levels of co-ordination DMSO has with molecules in solution. For example, DMSO molecules may establish more hydrogen bonding with methylammonium in solution, supressing the aforementioned addition-elimination reaction.

- In Chapter 5, we continue to study the triple-cation precursor solutions used in Chapter 4. We aim to explore the device stability of PSCs made from aged precursor inks. We found that champion devices made from all aged inks maintain close to their initial device performances after being storage in dark, inert conditions - indicating that no inert film instabilities are introduced. However, we note that devices made from inks aged at room temperature and 40°C displayed photoinstability in both inert and ambient conditions. Although the cause of this instability could not be specifically identified, we linked this reduction in device performance to a decrease in FF and a possible increase in shunt resistance. To expand on this, we conducted a study of the optical properties of films made from inks aged at 40°C, then stressed under various conditions. Here, we found no significant change in absorption profile of these films that would indicate stoichiometric changes. However, we do find that there is a reduction in PL intensity with increased film stress, which could imply that a small number of trap states are forming. Much more work is needed in order to identify and quantify this effect in relation to device performance. Importantly, we find that all devices made from LT-stored inks maintain a similar performances to control devices throughout all device stressing. This agrees with the results of Chapter 4 that LT storage of inks increases their usable lifetime significantly.

- In Chapter 6, we explore whether methylammonium-free inks have a longer lifetime than the TC inks used in Chapter 4 and 5. Specifically, we examine a $CsFAPbI_3$ ink dissolved in DMF/NMP. We find that high quality films and devices can be made from aging $CsFAPbI_3$ solutions for a period of over 7 weeks. Nuclear magnetic resonance (NMR) showed little change in the solutions over time, except for some indication of increased hydrogen bonding between I^- and FA^+, and the formation of a small amount of 1-3-5-triazine. More study is needed to confirm these effects over a longer timeline, but this is a promising initial study for a stable, high performance PSC precursor solution.

- In Chapter 7, we explore some of the methods used to examine perovskite precursor solutions. We find that DLS is useful for characterising the size of 1-2 nm particles, however for intensity-weighted data, the amount of large colloids within solution is grossly over-represented. The sizes of these 1-2 nm particles was confirmed using small-angle neutron scattering, and the absence of large quantities of large colloids is proven with spin-echo small-angle neutron scattering. We also propose a new model for analysing these complexes, which presents the solution as a two-phase system containing “particle” and “solvent”. Using this Tuebner-Strey approach, we can probe not only the domain size of these particles but the composition of them. Using these results, we speculate that these 1-2nm particles appear to be comprised of both Pb-based material and solvent molecules. This work provides an interesting new framework to study intermediate particles forming in perovskite precursor solutions. We hereby studied the aging process of two completely different precursor solutions (TC and $MAPbI_3$) and interestingly found the SLD and domain size of $MAPbI_3$ particles to change significantly over time compared to those in the TC solutions. This was linked to morphological changes in the films made from aged $MAPbI_3$ ink, which indicates these colloids could provide key insight into the crystallisation pathways within the perovskite films.

8.2 Future Work

This thesis begins to explore the aging qualities of PSC perovskite inks. We have identified some key degradation pathways within mixed-cation mixed-halide PSC solutions, and linked aged $MAPbI_3$ solutions to a change in film morphology. However, there is still much work to be done to fully characterise perovskite precursor ink aging.

The role of halides and inorganic cations in this aging process should be more thoroughly explored. Device stability made from aged inks should be more rigorously explored to pinpoint the cause of the photo-degradation shown in Chapter 5. The stability of methylammonium-free inks could be studied over longer time frames to confirm the results shown in Chapter 6.

Chapter 7 demonstrates the exciting potential of using SANS to study perovskite precursor solutions. We have demonstrated that we can use the Teubner-Strey model to probe the composition and sizes of complexes within precursor solutions. In future, we would like this model to be confirmed, by measuring for a larger range of different perovskite compositions. We suspect there are multiple mechanisms at play within these triple-cation mixed halide precursors, so it would be interesting to examine a wider range of more simple systems ($MAPI_3$, $FAPbI_3$, $MAPbBr_3$, $MAPbCl_3$) and "build-up" to the more complex solutions. Additionally, by varying the deuterated material between samples (i.e. using DMF-d_7 and un-deuterated DMSO vs. DMSO-d_6 and un-deuterated DMF), we could analyse the impacts of different solvent co-ordination within the intermediate complexes.

More broadly the future of solution processing perovskite devices relies on the scaling-up of high performing PSCs. Many changes will need to be made to PSC precursor solutions to optimise them for large scale depositions. For example, different solvents are often used to alter a precursors wettability on a substrate or its volatility after deposition. Addionally additives can be used to control perovskite crystallisation, and optimised perovskite stoichiometries should be explored in order to maximise PSC device performance. In all these cases, it is important to quantify the usable lifetime of these PSC inks, and it is useful to extend this lifetime as much as possible. It is the hope that this thesis demonstrates how the lifetime of these solutions can be measured, evaluates the methods used to examine this solution chemistry and provides a simple method of extending ink lifetime (through low-temperature ink storage). In future, we propose that ink lifetime is an important measurement, which should be reported alongside device data, especially in papers which focus on the scalability of a particular perovskite ink.

Bibliography

[1] W. E. Forum, *The Global Risks Report 2022*, **2022**.

[2] H.-O. Pörtner, D. C. Roberts, H. Adams, C. Adler, P. Aldunce, E. Ali, R. A. Begum, R. Betts, *Climate Change 2022 - Impacts, Adaptation and Vulnerability - Summary for Policymakers*, Publication Title: IPCC, **2022**.

[3] S. N. Islam, J. Winkel, **2018**, Publisher: United Nations, Department of Economic and Social Affairs ISBN: 9781315103358, 1–247.

[4] Renewable Power Generation Costs in 2021 - Executive Summary, en, tech. rep., IRENA, **2021**, p. 4.

[5] Energy Trends renewables tables (ODS), **2022**.

[6] F. Ise, P. P. GmbH, Photovoltaics Report, en.

[7] Best Efficiency Chart, Publication Title: National Renewable Energy Laboratory, **2022**.

[8] J. Nelson, *The Physics of Solar Cells*, World Scientific Publishing Company, **2003**.

[9] J. Singleton, *Band Theory and Electronic Properties of Solids*, Oxford University Press, **2001**.

[10] Reference Air Mass 1.5 Spectra (astmg173).

[11] S. Rühle, *Solar Energy* **2016**, *130*, 139–147.

[12] H. D. Megaw, *Proceedings of the Physical Society* **1946**, *58*, 340–340.

[13] Z. Li, M. Yang, J.-s. Park, S.-h. Wei, J. J. Berry, K. Zhu, *Chemistry of Materials* **2016**, *28*, 284–292.

[14] V. M. Goldschmidt, *Die Naturwissenschaften* **1926**, *14*, 477–485.

[15] C. C. Stoumpos, C. D. Malliakas, M. G. Kanatzidis, *Inorganic Chemistry* **2013**, *52*, 9019–9038.

[16] T. M. Koh, K. Fu, Y. Fang, S. Chen, T. C. Sum, N. Mathews, S. G. Mhaisalkar, P. P. Boix, T. Baikie, *The Journal of Physical Chemistry C* **2014**, *118*, 16458–16462.

[17] J.-W. Lee, D.-H. Kim, H.-S. Kim, S.-W. Seo, S. M. Cho, N.-G. Park, *Advanced Energy Materials* **2015**, *5*, 1501310.

[18] A. Binek, F. C. Hanusch, P. Docampo, T. Bein, *The Journal of Physical Chemistry Letters* **2015**, *6*, 1249–1253.

[19] N. J. Jeon, J. H. Noh, W. S. Yang, Y. C. Kim, S. Ryu, J. Seo, S. I. Seok, *Nature* **2015**, *517*, Publisher: Nature Publishing Group, 476–480.

[20] C. J. Bartel, C. Sutton, B. R. Goldsmith, R. Ouyang, C. B. Musgrave, L. M. Ghiringhelli, M. Scheffler, *Science Advances* **2019**, *5*, eaav0693.

[21] A. Kojima, K. Teshima, U. Shirai, T. Miyasaka, *Journal of the American Chemical Society* **2009**, *131*, 6050–6051.

[22] H.-S. Kim, C.-R. Lee, J.-H. Im, K.-B. Lee, T. Moehl, A. Marchioro, S.-J. Moon, R. Humphry-Baker, J.-H. Yum, J. E. Moser, M. Grätzel, N.-G. Park, *Scientific Reports* **2012**, *2*, 591.

[23] M. M. Lee, J. Teuscher, T. Miyasaka, T. N. Murakami, H. J. Snaith, *Science* **2012**, *338*, 643–647.

[24] J. Burschka, N. Pellet, S.-J. Moon, R. Humphry-Baker, P. Gao, M. K. Nazeeruddin, M. Grätzel, *Nature* **2013**, *499*, 316–319.

[25] J. J. Yoo, G. Seo, M. R. Chua, T. G. Park, Y. Lu, F. Rotermund, Y. K. Kim, C. S. Moon, N. J. Jeon, J. P. Correa-Baena, V. Bulović, S. S. Shin, M. G. Bawendi, J. Seo, *Nature* **2021**, *590*, Publisher: Springer US, 587–593.

[26] D. Yang, R. Yang, K. Wang, C. Wu, X. Zhu, J. Feng, X. Ren, G. Fang, S. Priya, S. Liu, *Nature Communications* **2018**, *9*, 3239.

[27] H. Kim, K.-G. Lim, T.-W. Lee, *Energy & Environmental Science* **2016**, *9*, 12–30.

[28] T. Webb, S. J. Sweeney, W. Zhang, *Advanced Functional Materials* **2021**, *31*, 2103121.

[29] A. Magomedov, A. Al-Ashouri, E. Kasparavičius, S. Strazdaite, G. Niaura, M. Jošt, T. Malinauskas, S. Albrecht, V. Getautis, *Advanced Energy Materials* **2018**, *8*, 1801892.

[30] S. Gharibzadeh, P. Fassl, I. M. Hossain, P. Rohrbeck, M. Frericks, M. Schmidt, T. Duong, M. R. Khan, T. Abzieher, B. A. Nejand, F. Schackmar, O. Almora, T. Feeney, R. Singh, D. Fuchs, U. Lemmer, J. P. Hofmann, S. A. L. Weber, U. W. Paetzold, *Energy & Environmental Science* **2021**, *14*, 5875–5893.

[31] E. J. Cassella, E. L. K. Spooner, T. Thornber, M. E. O'Kane, T. E. Catley, J. E. Bishop, J. A. Smith, O. S. Game, D. G. Lidzey, *Advanced Science* **2022**, *9*, 2104848.

[32] J. Yang, B. D. Siempelkamp, D. Liu, T. L. Kelly, *ACS Nano* **2015**, *9*, 1955–1963.

[33] J. A. Christians, P. A. Miranda Herrera, P. V. Kamat, *Journal of the American Chemical Society* **2015**, *137*, 1530–1538.

[34] A. M. A. Leguy, Y. Hu, M. Campoy-Quiles, M. I. Alonso, O. J. Weber, P. Azarhoosh, M. van Schilfgaarde, M. T. Weller, T. Bein, J. Nelson, P. Docampo, P. R. F. Barnes, *Chemistry of Materials* **2015**, *27*, 3397–3407.

[35] G. Niu, W. Li, F. Meng, L. Wang, H. Dong, Y. Qiu, *J. Mater. Chem. A* **2014**, *2*, 705–710.

[36] Q.-M. Hong, R.-P. Xu, T.-Y. Jin, J.-X. Tang, Y.-Q. Li, *Organic Electronics* **2019**, *67*, 19–25.

[37] E. J. Juarez-perez, *Journal of Materials Chemistry A* **2018**, *6*, Publisher: Royal Society of Chemistry, 9604–9612.

[38] B. Conings, J. Drijkoningen, N. Gauquelin, A. Babayigit, J. D'Haen, L. D'Olieslaeger, A. Ethirajan, J. Verbeeck, J. Manca, E. Mosconi, F. D. Angelis, H. G. Boyen, *Advanced Energy Materials* **2015**, *5*, ISBN: 16146832, 1–8.

[39] H. X. Dang, K. Wang, M. Ghasemi, M.-c. Tang, M. D. Bastiani, E. Aydin, E. Dauzon, D. Barrit, J. Peng, D.-m. Smilgies, S. D. Wolf, A. Amassian, *Joule* **2019**, *3*, Publisher: Elsevier Inc., 1746–1764.

[40] G. E. Eperon, S. D. Stranks, C. Menelaou, M. B. Johnston, L. M. Herz, H. J. Snaith, *Energy & Environmental Science* **2014**, *7*, ISBN: 1754-5706, 982.

[41] A. A. Zhumekenov, M. I. Saidaminov, M. A. Haque, E. Alarousu, S. P. Sarmah, B. Murali, I. Dursun, X.-H. Miao, A. L. Abdelhady, T. Wu, O. F. Mohammed, O. M. Bakr, *ACS Energy Letters* **2016**, *1*, 32–37.

[42] Q. Han, S.-H. Bae, P. Sun, Y.-T. Hsieh, Y. (Yang, Y. S. Rim, H. Zhao, Q. Chen, W. Shi, G. Li, Y. Yang, *Advanced Materials* **2016**, *28*, 2253–2258.

[43] B.-w. Park, S. I. Seok, *Advanced Materials* **2019**, *31*, 1805337.

[44] Z. Yao, W. Zhao, S. (Liu, *Journal of Materials Chemistry A* **2021**, *9*, 11124–11144.

[45] A. Saparbaev, M. Zhang, V. Kuvondikov, L. Nurumbetova, I. O. Raji, I. Tajibaev, E. Zakhidov, X. Bao, R. Yang, *Solar Energy* **2021**, *228*, Publisher: Elsevier Ltd, 405–412.

[46] M. Saliba, T. Matsui, J.-Y. Seo, K. Domanski, J.-P. Correa-Baena, M. K. Nazeeruddin, S. M. Zakeeruddin, W. Tress, A. Abate, A. Hagfeldt, M. Grätzel, *Energy & Environmental Science* **2016**, *9*, Publisher: Royal Society of Chemistry ISBN: 1215421109, 1989–1997.

[47] T. Matsui, J.-y. Seo, M. Saliba, S. M. Zakeeruddin, M. Grätzel, *Advanced Materials* **2017**, *29*, 1606258.

[48] J. H. Noh, S. H. Im, J. H. Heo, T. N. Mandal, S. I. Seok, *Nano Letters* **2013**, *13*, ISBN: 1530-6984, 1764–1769.

[49] D. P. McMeekin, G. Sadoughi, W. Rehman, G. E. Eperon, M. Saliba, M. T. Horantner, A. Haghighirad, N. Sakai, L. Korte, B. Rech, M. B. Johnston, L. M. Herz, H. J. Snaith, *Science* **2016**, *351*, ISBN: 9788578110796, 151–155.

[50] S. D. Stranks, G. E. Eperon, G. Grancini, C. Menelaou, M. J. P. Alcocer, T. Leijtens, L. M. Herz, A. Petrozza, H. J. Snaith, *Science* **2013**, *342*, ISBN: 1095-9203 (Electronic)0036-8075 (Linking), 341–344.

[51] E. T. Hoke, D. J. Slotcavage, E. R. Dohner, A. R. Bowring, H. I. Karunadasa, M. D. McGehee, *Chemical Science* **2015**, *6*, Publisher: Royal Society of Chemistry ISBN: 2041-6520, 613–617.

[52] A. J. Knight, J. Borchert, R. D. J. Oliver, J. B. Patel, P. G. Radaelli, H. J. Snaith, M. B. Johnston, L. M. Herz, *ACS Energy Letters* **2021**, *6*, 799–808.

[53] W. Rehman, D. P. McMeekin, J. B. Patel, R. L. Milot, M. B. Johnston, H. J. Snaith, L. M. Herz, *Energy & Environmental Science* **2017**, *10*, 361–369.

[54] Y. Vaynzof, *Advanced Energy Materials* **2020**, *10*, 2003073.

[55] P. Fassl, V. Lami, A. Bausch, Z. Wang, M. T. Klug, H. J. Snaith, Y. Vaynzof, *Energy & Environmental Science* **2018**, *11*, Publisher: Royal Society of Chemistry, 3380–3391.

[56] A. T. Barrows, A. J. Pearson, C. K. Kwak, A. D. F. Dunbar, A. R. Buckley, D. G. Lidzey, *Energy Environ. Sci.* **2014**, *7*, ISBN: 9780816911127, 2944–2950.

[57] J. E. Bishop, C. D. Read, J. A. Smith, T. J. Routledge, D. G. Lidzey, *Scientific Reports* **2020**, *10*, Publisher: Springer US, 6610.

[58] H. Cai, X. Liang, X. Ye, J. Su, J. Guan, J. Yang, Y. Liu, X. Zhou, R. Han, J. Ni, J. Li, J. Zhang, *ACS Applied Energy Materials* **2020**, *3*, 9696–9702.

[59] L. Vesce, M. Stefanelli, J. P. Herterich, L. A. Castriotta, M. Kohlstädt, U. Würfel, A. D. Carlo, *Solar RRL* **2021**, *5*, 1–11.

[60] Z. Yang, W. Zhang, S. Wu, H. Zhu, Z. Liu, Z. Liu, Z. Jiang, R. Chen, J. Zhou, Q. Lu, Z. Xiao, L. Shi, H. Chen, L. K. Ono, S. Zhang, Y. Zhang, Y. Qi, L. Han, W. Chen, *Science Advances* **2021**, *7*, 1–14.

[61] F. D. Giacomo, S. Shanmugam, H. Fledderus, B. J. Bruijnaers, W. J. H. Verhees, M. S. Dorenkamper, S. C. Veenstra, W. Qiu, R. Gehlhaar, T. Merckx, T. Aernouts, R. Andriessen, Y. Galagan, *Solar Energy Materials and Solar Cells* **2018**, *181*, Publisher: Elsevier B.V., 53–59.

[62] X. Dai, Y. Deng, C. H. Van Brackle, S. Chen, P. N. Rudd, X. Xiao, Y. Lin, B. Chen, J. Huang, *Advanced Energy Materials* **2020**, *10*, 1903108.

[63] Z. Saki, M. M. Byranvand, N. Taghavinia, M. Kedia, M. Saliba, *Energy & Environmental Science* **2021**, *14*, 5690–5722.

[64] T. Bu, J. Li, H. Li, C. Tian, J. Su, G. Tong, L. K. Ono, C. Wang, Z. Lin, N. Chai, X.-L. Zhang, J. Chang, J. Lu, J. Zhong, W. Huang, Y. Qi, Y.-B. Cheng, F. Huang, *Science* **2021**, *372*, 1327–1332.

[65] H. Chen, F. Ye, W. Tang, J. He, M. Yin, Y. Wang, F. Xie, E. Bi, X. Yang, M. Grätzel, L. Han, *Nature* **2017**, *550*, Publisher: Nature Publishing Group, 92–95.

[66] M. Jung, S.-G. Ji, G. Kim, S. I. Seok, *Chemical Society Reviews* **2019**, *48*, Publisher: Royal Society of Chemistry, 2011–2038.

[67] B. Ding, Y. Li, S.-Y. Huang, Q.-Q. Chu, C.-X. Li, C.-J. Li, G.-J. Yang, *Journal of Materials Chemistry A* **2017**, *5*, 6840–6848.

[68] T. Thornber, O. S. Game, E. J. Cassella, M. E. O'Kane, J. E. Bishop, T. J. Routledge, T. I. Alanazi, M. Togay, P. J. M. Isherwood, L. C. Infante-Ortega, D. B. Hammond, J. M. Walls, D. G. Lidzey, *ACS Applied Materials & Interfaces* **2022**, acsami.2c05085.

[69] O. Shargaieva, H. Näsström, J. A. Smith, D. Többens, R. Munir, E. Unger, *Materials Advances* **2020**, *1*, 3314–3321.

[70] A. S. Tutantsev, N. N. Udalova, S. A. Fateev, A. A. Petrov, A. A. Petrov, W. Chengyuan, E. G. Maksimov, E. A. Goodilin, E. A. Goodilin, A. B. Tarasov, A. B. Tarasov, A. B. Tarasov, A. B. Tarasov, *Journal of Physical Chemistry C* **2020**, *124*, 11117–11123.

[71] X. Huang, F. Cheng, B. Wu, N. Zheng, *The Journal of Physical Chemistry Letters* **2022**, *13*, 1765–1776.

[72] E. Radicchi, E. Mosconi, F. Elisei, F. Nunzi, F. D. Angelis, *ACS Applied Energy Materials* **2019**, *2*, Publisher: American Chemical Society, 3400–3409.

[73] S. Rahimnejad, A. Kovalenko, S. M. Forés, C. Aranda, A. Guerrero, *ChemPhysChem* **2016**, *17*, 2795–2798.

[74] O. Romiluyi, Y. Eatmon, R. Ni, B. P. Rand, P. Clancy, *Journal of Materials Chemistry A* **2021**, *9*, 13087–13099.

[75] X. Guo, C. McCleese, C. Kolodziej, A. C. S. Samia, Y. Zhao, C. Burda, *Dalton Transactions* **2016**, *45*, ISBN: 1477-9234 (Electronic) 1477-9226 (Linking), 3806–3813.

[76] A. A. Petrov, I. P. Sokolova, N. A. Belich, G. S. Peters, P. V. Dorovatovskii, Y. V. Zubavichus, V. N. Khrustalev, A. V. Petrov, M. Grätzel, E. A. Goodilin, A. B. Tarasov, *Journal of Physical Chemistry C* **2017**, *121*, 20739–20743.

[77] M. Yang, Z. Li, M. O. Reese, O. G. Reid, D. H. Kim, S. Siol, T. R. Klein, Y. Yan, J. J. Berry, M. F. A. M. V. Hest, K. Zhu, *Nature Energy* **2017**, *2*, 1–9.

[78] K. Yan, M. Long, T. Zhang, Z. Wei, H. Chen, S. Yang, J. Xu, *Journal of the American Chemical Society* **2015**, *137*, ISBN: 0002-7863, 4460–4468.

[79] Y. J. Jeon, S. Lee, R. Kang, J. E. Kim, J. S. Yeo, S. H. Lee, S. S. Kim, J. M. Yun, D. Y. Kim, *Scientific Reports* **2014**, *4*, ISBN: 2045-2322 (Electronic) 2045-2322 (Linking), 26–28.

[80] Y. Wu, A. Islam, X. Yang, C. Qin, J. Liu, K. Zhang, W. Peng, L. Han, *Energy Environ. Sci.* **2014**, *7*, 2934–2938.

[81] N. Ahn, D. Y. Son, I. H. Jang, S. M. Kang, M. Choi, N. G. Park, *Journal of the American Chemical Society* **2015**, *137*, 8696–8699.

[82] N. J. Jeon, J. H. Noh, Y. C. Kim, W. S. Yang, S. Ryu, S. I. Seok, *Nature Materials* **2014**, *13*, 897–903.

[83] Y. Rong, Z. Tang, Y. Zhao, X. Zhong, S. Venkatesan, H. Graham, M. Patton, Y. Jing, A. M. Guloy, Y. Yao, *Nanoscale* **2015**, *7*, 10595–10599.

[84] J. Cao, X. Jing, J. Yan, C. Hu, R. Chen, J. Yin, J. Li, N. Zheng, *Journal of the American Chemical Society* **2016**, *138*, 9919–9926.

[85] Y. Jo, K. S. Oh, M. Kim, K.-H. Kim, H. Lee, C.-W. Lee, D. S. Kim, *Advanced Materials Interfaces* **2016**, *3*, 1500768.

[86] M. Jeong, I. W. Choi, E. M. Go, Y. Cho, M. Kim, B. Lee, S. Jeong, Y. Jo, H. W. Choi, J. Lee, J.-H. Bae, S. K. Kwak, D. S. Kim, C. Yang, *Science* **2020**, *369*, 1615–1620.

[87] H. Min, M. Kim, S. U. Lee, H. Kim, G. Kim, K. Choi, J. H. Lee, S. I. Seok, *Science* **2019**, *366*, 749–753.

[88] H. Min, D. Y. Lee, J. Kim, G. Kim, K. S. Lee, J. Kim, M. J. Paik, Y. K. Kim, K. S. Kim, M. G. Kim, T. J. Shin, S. I. Seok, *Nature* **2021**, *598*, Publisher: Springer US, 444–450.

[89] F. Cheng, X. Jing, R. Chen, J. Cao, J. Yan, Y. Wu, X. Huang, B. Wu, N. Zheng, *Inorganic Chemistry Frontiers* **2019**, *6*, Publisher: Royal Society of Chemistry, 2458–2463.

[90] H.-H. Huang, Q.-H. Liu, H. Tsai, S. Shrestha, L.-Y. Su, P.-T. Chen, Y.-T. Chen, T.-A. Yang, H. Lu, C.-H. Chuang, K.-F. Lin, S.-P. Rwei, W. Nie, L. Wang, *Joule* **2021**, *5*, 958–974.

[91] J.-W. Lee, D.-K. Lee, D.-N. Jeong, N.-G. Park, *Advanced Functional Materials* **2019**, *29*, 1807047.

[92] N. K. Noel, S. N. Habisreutinger, B. Wenger, M. T. Klug, M. T. Hï¿½rantner, M. B. Johnston, R. J. Nicholas, D. T. Moore, H. J. Snaith, *Energy and Environmental Science* **2017**, *10*, Publisher: Royal Society of Chemistry ISBN: 1754-56921754-5706, 145–152.

[93] X. Cao, L. Hao, Z. Liu, G. Su, X. He, Q. Zeng, J. Wei, *Chemical Engineering Journal* **2022**, *437*, Publisher: Elsevier B.V., 135458.

[94] W. Hui, L. Chao, H. Lu, F. Xia, Q. Wei, Z. Su, T. Niu, L. Tao, B. Du, D. Li, Y. Wang, H. Dong, S. Zuo, B. Li, W. Shi, X. Ran, P. Li, H. Zhang, Z. Wu, C. Ran, L. Song, G. Xing, X. Gao, J. Zhang, Y. Xia, Y. Chen, W. Huang, *Science* **2021**, *371*, 1359–1364.

[95] B. Wilk, S. Öz, E. Radicchi, F. Ünlü, T. Ahmad, A. P. Herman, F. Nunzi, S. Mathur, R. Kudrawiec, K. Wojciechowski, *ACS Sustainable Chemistry & Engineering* **2021**, *9*, 3920–3930.

[96] H. Zhang, K. Darabi, N. Y. Nia, A. Krishna, P. Ahlawat, B. Guo, M. H. S. Almalki, T.-s. Su, D. Ren, V. Bolnykh, L. A. Castriotta, M. Zendehdel, L. Pan, S. S. Alonso, R. Li, S. M. Zakeeruddin, A. Hagfeldt, U. Rothlisberger, A. D. Carlo, A. Amassian, M. Grätzel, *Nature Communications* **2022**, *13*, Publisher: Springer US ISBN: 4146702127, 89.

[97] N. K. Noel, M. Congiu, A. J. Ramadan, S. Fearn, D. P. McMeekin, J. B. Patel, M. B. Johnston, B. Wenger, H. J. Snaith, *Joule* **2017**, *1*, Publisher: Elsevier Inc. ISBN: 25424351, 328–343.

[98] P. Boonmongkolras, D. Kim, E. M. Alhabshi, I. Gereige, B. Shin, *RSC Advances* **2018**, *8*, Publisher: Royal Society of Chemistry, 21551–21557.

[99] X. Wang, Y. Fan, L. Wang, C. Chen, Z. Li, R. Liu, H. Meng, Z. Shao, X. Du, H. Zhang, G. Cui, S. Pang, *Chem* **2020**, *6*, Publisher: Elsevier Inc., 1369–1378.

[100] J. C. Yu, B. Li, C. J. Dunn, J. Yan, B. T. Diroll, A. S. R. Chesman, J. J. Jasieniak, *Advanced Science* **2022**, 2201487.

[101] C. Chen, Y. Rao, Z. Li, X. Wang, G. Cui, W. Wang, S. Pang, *Solar RRL* **2021**, *5*, 2000715.

[102] W. T. M. Van Gompel, R. Herckens, G. Reekmans, B. Ruttens, J. D'Haen, P. Adriaensens, L. Lutsen, D. Vanderzande, *The Journal of Physical Chemistry C* **2018**, *122*, 4117–4124.

[103] N. S. Dutta, N. K. Noel, C. B. Arnold, *The Journal of Physical Chemistry Letters* **2020**, *11*, 5980–5986.

[104] J. Li, J. Dagar, O. Shargaieva, M. A. Flatken, H. Köbler, M. Fenske, C. Schultz, B. Stegemann, J. Just, D. M. Többens, A. Abate, R. Munir, E. Unger, *Advanced Energy Materials* **2021**, *11*, 2003460.

[105] M. A. Flatken, A. Hoell, R. Wendt, E. Härk, A. Dallmann, A. Prause, J. Pascual, E. Unger, A. Abate, *Journal of Materials Chemistry A* **2021**, *9*, 13477–13482.

[106] H. Gu, T. Niu, S. Zuo, Y. Cai, L. Chao, P. Müller-Buschbaum, Y. Xia, J. Zhang, G. Xing, Y. Chen, *CCS Chemistry* **2022**, 1–11.

[107] H. Tsai, W. Nie, Y.-H. Lin, J. C. Blancon, S. Tretiak, J. Even, G. Gupta, P. M. Ajayan, A. D. Mohite, *Advanced Energy Materials* **2017**, *7*, ISBN: 1614-6840, 1602159.

[108] G. S. Shin, S.-g. Kim, Y. Zhang, N.-g. Park, *Small Methods* **2020**, *4*, 1900398.

[109] T. Liu, Y. Zong, Y. Zhou, M. Yang, Z. Li, O. S. Game, K. Zhu, R. Zhu, Q. Gong, N. P. Padture, *Chemistry of Materials* **2017**, *29*, 3246–3250.

[110] R. Xing, N. Tang, K. Ding, X. Wang, Z. Wang, *Chemical Physics Letters* **2018**, *711*, 194–198.

[111] B. Dou, L. M. Wheeler, J. A. Christians, D. T. Moore, S. P. Harvey, J. J. Berry, F. S. Barnes, S. E. Shaheen, M. F. A. M. van Hest, *ACS Energy Letters* **2018**, *3*, 979–985.

[112] M. Qin, J. Cao, T. Zhang, J. Mai, T.-K. Lau, S. Zhou, Y. Zhou, J. Wang, Y.-J. Hsu, N. Zhao, J. Xu, X. Zhan, X. Lu, *Advanced Energy Materials* **2018**, *8*, 1703399.

[113] S. Chen, X. Xiao, H. Gu, J. Huang, *Science Advances* **2021**, *7*, 1–7.

[114] H. Min, G. Kim, M. J. Paik, S. Lee, W. S. Yang, M. Jung, S. I. Seok, *Advanced Energy Materials* **2019**, *9*, 1803476.

[115] G. S. Shin, Y. Zhang, N.-g. Park, *ACS Applied Materials & Interfaces* **2020**, *12*, 15167–15174.

[116] H. Wei, S. Chen, J. Zhao, Z. Yu, J. Huang, *Chemistry of Materials* **2020**, *32*, 2501–2507.

[117] Y. Zhan, W. Chen, F. Yang, Y. Li, *Chinese Physics B* **2021**, *30*, 088803.

[118] Q. Dong, W. Shang, X. Yu, Y. Yin, C. Jiang, Y. Feng, J. Bian, B. Song, S. Jin, Y. Zhou, L. Wang, Y. Shi, *ACS Energy Letters* **2022**, *7*, 481–489.

[119] V. Valenzano, A. Cesari, F. Balzano, A. Milella, F. Fracassi, A. Listorti, G. Gigli, A. Rizzo, G. Uccello-Barretta, S. Colella, *Cell Reports Physical Science* **2021**, *2*, 100432.

[120] S. Wang, Y. Jiang, E. J. Juarez-Perez, L. K. Ono, Y. Qi, *Nature Energy* **2017**, *2*, 16195.

[121] J. A. Smith, O. S. Game, J. E. Bishop, E. L. K. Spooner, R. C. Kilbride, C. Greenland, R. Jayaprakash, T. I. Alanazi, T. I. Alanazi, E. J. Cassella, A. Tejada, A. Tejada, G. Chistiakova, M. Wong-Stringer, T. J. Routledge, A. J. Parnell, D. B. Hammond, D. G. Lidzey, *ACS Applied Energy Materials* **2020**, *3*, 5552–5562.

[122] F. M. Rombach, S. A. Haque, T. J. Macdonald, *Energy & Environmental Science* **2021**, *14*, 5161–5190.

[123] H. Yoon, S. M. Kang, J.-K. Lee, M. Choi, *Energy & Environmental Science* **2016**, *9*, Publisher: Royal Society of Chemistry, 2262–2266.

[124] S. Y. Kim, S. J. Cho, S. E. Byeon, X. He, H. J. Yoon, *Advanced Energy Materials* **2020**, *10*, DOI `10.1002/aenm.202002606`.

[125] M. E. O'Kane, J. A. Smith, T. I. Alanazi, E. J. Cassella, O. Game, S. Meurs, D. G. Lidzey, *ChemSusChem* **2021**, *14*, 2537–2546.

[126] M. Saliba, J. P. Correa-Baena, C. M. Wolff, M. Stolterfoht, N. Phung, S. Albrecht, D. Neher, A. Abate, *Chemistry of Materials* **2018**, *30*, ISBN: 0711232105, 4193–4201.

[127] F. A. Bovey, P. A. Mirau, *NMR of polymers*, Academic Press, San Diego, **1996**.

[128] J. Stetefeld, S. A. McKenna, T. R. Patel, *Biophysical Reviews* **2016**, *8*, Publisher: Biophysical Reviews, 409–427.

[129] M. Instruments, Technical Note: Dynamic Light Scattering, Pages: 1-8, **2010**.

[130] MALVERN, *Malvern Instruments Ltd* **2014**, 20.

[131] I. Niskanen, V. Forsberg, D. Zakrisson, S. Reza, M. Hummelgård, B. Andres, I. Fedorov, T. Suopajärvi, H. Liimatainen, G. Thungström, *Chemical Engineering Science* **2019**, *201*, 222–229.

[132] M. Instruments, Dynamic Light Scattering: An Introduction in 30 Minutes, Technical Note.

[133] M. Kaszuba, D. McKnight, M. T. Connah, F. K. McNeil-Watson, U. Nobbmann, *Journal of Nanoparticle Research* **2008**, *10*, 823–829.

[134] D. S. Sivia, *Elementary scattering theory: for X-ray and neutron users*, OCLC: ocn694227131, Oxford University Press, Oxford ; New York, **2011**.

[135] R. J. Roe, *Methods of X-ray and neutron scattering in polymer science*, Oxford University Press, New York, **2000**.

[136] M. T. Rekveldt, J. Plomp, W. G. Bouwman, W. H. Kraan, S. Grigoriev, M. Blaauw, *Review of Scientific Instruments* **2005**, *76*, 33901.

[137] G. Bernardo, M. Melle-Franco, A. L. Washington, R. M. Dalgliesh, F. Li, A. Mendes, S. R. Parnell, *RSC Advances* **2020**, *10*, 4512–4520.

[138] M. Mulder, X. X. Li, M. M. Nazim, R. M. Dalgliesh, B. Tian, M. Buijse, J. van Wunnik, W. G. Bouwman, *Colloids and Surfaces A: Physicochemical and Engineering Aspects* **2019**, *575*, Publisher: Elsevier, 166–175.

[139] X. Zheng, C. Wu, S. K. Jha, Z. Li, K. Zhu, S. Priya, *ACS Energy Letters* **2016**, *1*, 1014–1020.

[140] P. Gratia, I. Zimmermann, P. Schouwink, J.-H. Yum, J.-N. Audinot, K. Sivula, T. Wirtz, M. K. Nazeeruddin, *ACS Energy Letters* **2017**, *2*, 2686–2693.

[141] S.-H. Turren-Cruz, A. Hagfeldt, M. Saliba, *Science* **2018**, *362*, 449–453.

[142] W. M. J. Franssen, B. J. Bruijnaers, V. H. L. Portengen, A. P. M. Kentgens, *ChemPhysChem* **2018**, *19*, 3107–3115.

[143] R. A. Kerner, T. H. Schloemer, P. Schulz, J. J. Berry, J. Schwartz, A. Sellinger, B. P. Rand, *Journal of Materials Chemistry C* **2019**, *7*, Publisher: Royal Society of Chemistry, 5251–5259.

[144] W. Ke, I. Spanopoulos, C. C. Stoumpos, M. G. Kanatzidis, *Nature Communications* **2018**, *9*, Publisher: Springer US, 4785.

[145] J. C. Hamill, J. C. Sorli, I. Pelczer, J. Schwartz, Y.-L. Loo, *Chemistry of Materials* **2019**, *31*, 2114–2120.

[146] A. García-Fernández, J. M. Bermúdez-García, S. Castro-García, A. L. Llamas-Saiz, R. Artiaga, J. López-Beceiro, S. Hu, W. Ren, A. Stroppa, M. Sánchez-Andújar, M. A. Señarís-Rodríguez, *Inorganic Chemistry* **2017**, *56*, 4918–4927.

[147] J. Kim, B.-w. Park, J. Baek, J. S. Yun, H.-w. Kwon, J. Seidel, H. Min, S. Coelho, S. Lim, S. Huang, K. Gaus, M. A. Green, T. J. Shin, A. W. Y. Hobaillie, M. G. Kim, S. I. Seok, *Journal of the American Chemical Society* **2020**, *142*, 6251–6260.

[148] C. Avenel, O. Raccurt, J.-L. Gardette, S. Therias, *npj Materials Degradation* **2019**, *3*, Publisher: Springer US, 27.

[149] O. Sanni, A. P. I. Popoola, O. S. I. Fayomi, *Journal of Bio- and Tribo-Corrosion* **2019**, *5*, Publisher: Springer International Publishing ISBN: 0123456789, 88.

[150] M. Liu, K. Wang, L. Wang, S. Han, H. Fan, N. Rowell, J. A. Ripmeester, R. Renoud, F. Bian, J. Zeng, K. Yu, *Nature Communications* **2017**, *8*, Publisher: Nature Publishing Group, 1–12.

[151] M. U. Rothmann, W. Li, Y. Zhu, U. Bach, L. Spiccia, J. Etheridge, Y.-B. Cheng, *Nature Communications* **2017**, *8*, Publisher: Nature Publishing Group, 14547.

[152] A. D. Buckingham, T. Schaefer, W. G. Schneider, *The Journal of Chemical Physics* **1960**, *32*, 1227–1233.

[153] J. A. S. Cavaleiro, *Journal of Chemical Education* **1987**, *64*, 549.

[154] M. V. Khenkin, E. A. Katz, A. Abate, G. Bardizza, J. J. Berry, C. Brabec, F. Brunetti, V. Bulović, Q. Burlingame, A. Di Carlo, R. Cheacharoen, Y.-B. Cheng, A. Colsmann, S. Cros, K. Domanski, M. Dusza, C. J. Fell, S. R. Forrest, Y. Galagan, D. Di Girolamo, M. Grätzel, A. Hagfeldt, E. von Hauff, H. Hoppe, J. Kettle, H. Köbler, M. S. Leite, S. Liu, Y.-L. Loo, J. M. Luther, C.-Q. Ma, M. Madsen, M. Manceau, M. Matheron, M. McGehee, R. Meitzner, M. K. Nazeeruddin, A. F. Nogueira, Ç. Odabaşı, A. Osherov, N.-G. Park, M. O. Reese, F. De Rossi, M. Saliba, U. S. Schubert, H. J. Snaith, S. D. Stranks, W. Tress, P. A. Troshin, V. Turkovic, S. Veenstra, I. Visoly-Fisher, A. Walsh, T. Watson, H. Xie, R. Yıldırım, S. M. Zakeeruddin, K. Zhu, M. Lira-Cantu, *Nature Energy* **2020**, *5*, 35–49.

[155] M. K. Rao, D. Sangeetha, M. Selvakumar, Y. Sudhakar, M. Mahesha, *Solar Energy* **2021**, *218*, 469–491.

[156] H. J. Snaith, *Nature Materials* **2018**, *17*, Publisher: Springer US ISBN: 0878494197, 372–376.

[157] T. Wu, Z. Qin, Y. Wang, Y. Wu, W. Chen, S. Zhang, M. Cai, S. Dai, J. Zhang, J. Liu, Z. Zhou, X. Liu, H. Segawa, H. Tan, Q. Tang, J. Fang, Y. Li, L. Ding, Z. Ning, Y. Qi, Y. Zhang, L. Han, *Nano-Micro Letters* **2021**, *13*, 152.

[158] L. Duan, A. Uddin, *Materials Chemistry Frontiers* **2022**, *6*, Publisher: The Royal Society of Chemistry, 400–417.

[159] S. Mazumdar, Y. Zhao, X. Zhang, *Frontiers in Electronics* **2021**, *2*, 712785.

[160] Y. Jiang, L. Qiu, E. J. Juarez-Perez, L. K. Ono, Z. Hu, Z. Liu, Z. Wu, L. Meng, Q. Wang, Y. Qi, *Nature Energy* **2019**, *4*, 585–593.

[161] Y.-H. Lin, N. Sakai, P. Da, J. Wu, H. C. Sansom, A. J. Ramadan, S. Mahesh, J. Liu, R. D. J. Oliver, J. Lim, L. Aspitarte, K. Sharma, P. K. Madhu, A. B. Morales-Vilches, P. K. Nayak, S. Bai, F. Gao, C. R. M. Grovenor, M. B. Johnston, J. G. Labram, J. R. Durrant, J. M. Ball, B. Wenger, B. Stannowski, H. J. Snaith, *Science* **2020**, *369*, Publisher: American Association for the Advancement of Science, 96–102.

[162] A. R. b. Mohd Yusoff, M. Vasilopoulou, D. G. Georgiadou, L. C. Palilis, A. Abate, M. K. Nazeeruddin, *Energy & Environmental Science* **2021**, *14*, Publisher: The Royal Society of Chemistry, 2906–2953.

[163] K. C. Waterman, R. C. Adami, *International Journal of Pharmaceutics* **2005**, *293*, 101–125.

[164] V. Sarritzu, N. Sestu, D. Marongiu, X. Chang, S. Masi, A. Rizzo, S. Colella, F. Quochi, M. Saba, A. Mura, G. Bongiovanni, *Scientific Reports* **2017**, *7*, 44629.

[165] C. M. Wolff, P. Caprioglio, M. Stolterfoht, D. Neher, *Adv. Mater.* **2019**, 21.

[166] F. Xie, C.-C. Chen, Y. Wu, X. Li, M. Cai, X. Liu, X. Yang, L. Han, *Energy & Environmental Science* **2017**, *10*, Publisher: Royal Society of Chemistry, 1942–1949.

[167] Y. Zhao, K. Zhu, *The Journal of Physical Chemistry C* **2014**, *118*, 9412–9418.

[168] Y. Zhao, K. Zhu, *Journal of the American Chemical Society* **2014**, *136*, 12241–12244.

[169] C. Zhang, Z. Li, J. Liu, Y. Xin, Z. Shao, G. Cui, S. Pang, *ACS Energy Letters* **2018**, *3*, 1801–1807.

[170] Y. Fan, X. Wang, Y. Miao, Y. Zhao, *The Journal of Physical Chemistry Letters* **2021**, *12*, 11636–11644.

[171] T. Zhu, D. Zheng, M.-N. Rager, T. Pauporté, *Solar RRL* **2020**, *4*, 2000348.

[172] Y. Chen, Q. Meng, Y. Xiao, X. Zhang, J. Sun, C. B. Han, H. Gao, Y. Zhang, Y. Lu, H. Yan, *ACS Applied Materials & Interfaces* **2019**, *11*, 44101–44108.

[173] S. Shukla, S. Shukla, J. Haur, S. S. H. Dintakurti, *ChemSusChem* **2017**, *10*, 3804–3809.

[174] Y. Li, A. G. Palmer, *Journal of the American Chemical Society* **2010**, *132*, 8856–8857.

[175] A. A. Petrov, E. A. Goodilin, A. B. Tarasov, V. A. Lazarenko, P. V. Dorovatovskii, V. N. Khrustalev, *Acta Crystallographica Section E Crystallographic Communications* **2017**, *73*, 569–572.

[176] F. C. Schaefer, I. Hechenbleikner, G. A. Peters, V. P. Wystrach, *Journal of the American Chemical Society* **1959**, *81*, 1466–1470.

[177] M. Saliba, J.-P. Correa-Baena, M. Grätzel, A. Hagfeldt, A. Abate, *Angewandte Chemie International Edition* **2018**, *57*, 2554–2569.

[178] R. D. Schaller, V. I. Klimov, *Physical Review Letters* **2004**, *92*, 186601.

[179] C. Wehrenfennig, G. E. Eperon, M. B. Johnston, H. J. Snaith, L. M. Herz, *Advanced Materials* **2014**, *26*, 1584–1589.

[180] M. Fievez, P. J. Singh Rana, T. M. Koh, M. Manceau, J. H. Lew, N. F. Jamaludin, B. Ghosh, A. Bruno, S. Cros, S. Berson, S. G. Mhaisalkar, W. L. Leong, *Solar Energy Materials and Solar Cells* **2021**, *230*, 111189.

[181] N. Zarabinia, G. Lucarelli, R. Rasuli, F. D. Rossi, B. Taheri, H. Javanbakht, F. Brunetti, T. M. Brown, *iScience* **2022**, *25*, Publisher: The Author(s), 103712.

[182] A. Gusain, A. Thankappan, S. Thomas, *Journal of Materials Science* **2020**, *55*, Publisher: Springer US, 13490–13542.

[183] H. B. Lee, N. Kumar, M. M. Ovhal, Y. J. Kim, Y. M. Song, J.-W. Kang, *Advanced Functional Materials* **2020**, *30*, 2001559.

[184] S. Masi, A. Rizzo, F. Aiello, F. Balzano, G. Uccello-Barretta, A. Listorti, G. Gigli, S. Colella, *Nanoscale* **2015**, *7*, 18956–18963.

[185] Q. Han, Y. Bai, J. Liu, K.-z. Du, T. Li, D. Ji, Y. Zhou, C. Cao, D. Shin, J. Ding, A. D. Franklin, J. T. Glass, J. Hu, M. J. Therien, J. Liu, D. B. Mitzi, *Energy & Environmental Science* **2017**, *10*, Publisher: Royal Society of Chemistry, 2365–2371.

[186] L. Chao, Y. Xia, B. Li, G. Xing, Y. Chen, W. Huang, *Chem* **2019**, *5*, Publisher: Elsevier Inc., 995–1006.

[187] L. Meng, Q. Wei, Z. Yang, D. Yang, J. Feng, X. Ren, Y. Liu, S. (Liu, *Journal of Energy Chemistry* **2020**, *41*, Publisher: Elsevier B.V. and Science Press, 43–51.

[188] D. P. McMeekin, Z. Wang, W. Rehman, F. Pulvirenti, J. B. Patel, N. K. Noel, M. B. Johnston, S. R. Marder, L. M. Herz, H. J. Snaith, *Advanced Materials* **2017**, *29*, ISBN: 1521-4095 (Electronic) 0935-9648 (Linking), 1607039.

[189] B. Jacrot, G. Zaccai, *Biopolymers* **1981**, *20*, 2413–2426.

[190] M. Ballauff, *Current Opinion in Colloid & Interface Science* **2001**, *6*, 132–139.

[191] K. M. Kareh, S. Whitham, *Nature Reviews Methods Primers* **2021**, *1*, ISBN: 0123456789, 69.

[192] T. Krouglov, W. H. Kraan, J. Plomp, M. T. Rekveldt, W. G. Bouwman, *Journal of Applied Crystallography* **2003**, *36*, 816–819.

[193] W. G. Bouwman, *Food Structure* **2021**, *30*, Publisher: Elsevier Ltd, 100235.

[194] G. N. Smith, V. J. Cunningham, S. L. Canning, M. J. Derry, J. F. K. Cooper, A. L. Washington, S. P. Armes, *Soft Matter* **2019**, *15*, Publisher: Royal Society of Chemistry, 17–21.

[195] M. T. Rekveldt, W. G. Bouwman, W. H. Kraan, O. Uca, S. V. Grigoriev, *Neutron Spin Echo Spectroscopy Viscoelasticity Rheology*, *Vol. 134*, Publication Title: Neutron Spin Echo Spectroscopy Viscoelasticity Rheology, Springer Berlin Heidelberg, **1997**.

[196] T. Krouglov, W. G. Bouwman, J. Plomp, M. T. Rekveldt, G. J. Vroege, A. V. Petukhov, D. M. E. Thies-Weesie, *Journal of Applied Crystallography* **2003**, *36*, 1417–1423.

[197] Loq, Publication Title: ISIS Neutron and Muon Source.

[198] D. Nečas, P. Klapetek, *Open Physics* **2012**, *10*, 181–188.

[199] Larmor, Publication Title: ISIS Neutron and Muon Source.

[200] Teubner Strey Model, Pages: Teubner Strey Publication Title: SASView.

[201] M. Teubner, R. Strey, *The Journal of Chemical Physics* **1987**, *87*, 3195–3200.

[202] W. S. Yang, J. H. Noh, N. J. Jeon, Y. C. Kim, S. Ryu, J. Seo, S. I. Seok, *Science* **2015**, *348*, 1234–1237.

[203] Y. Li, Z. Zhao, F. Lin, X. Cao, X. Cui, J. Wei, *Small* **2017**, *13*, 1–7.

[204] A. Jaffe, Y. Lin, C. M. Beavers, J. Voss, W. L. Mao, H. I. Karunadasa, *ACS Central Science* **2016**, *2*, 201–209.

[205] M. Doucet, SASView Version 4.2.2.

[206] Densities of Pure Liquid Organic Compounds, Publication Title: University of East Anglia.